Geochemical characterization of ca. 2680 Ma pillow lavas at Sharrie Lake, southern Slave Province, Northwest Territories

B.Sc. Honours Thesis

Siobhan S.G. McGoldrick
4/28/2014

Distribution License

DalSpace requires agreement to this non-exclusive distribution license before your item can appear on DalSpace.

NON-EXCLUSIVE DISTRIBUTION LICENSE

You (the author(s) or copyright owner) grant to Dalhousie University the non-exclusive right to reproduce and distribute your submission worldwide in any medium.

You agree that Dalhousie University may, without changing the content, reformat the submission for the purpose of preservation.

You also agree that Dalhousie University may keep more than one copy of this submission for purposes of security, back-up and preservation.

You agree that the submission is your original work, and that you have the right to grant the rights contained in this license. You also agree that your submission does not, to the best of your knowledge, infringe upon anyone's copyright.

If the submission contains material for which you do not hold copyright, you agree that you have obtained the unrestricted permission of the copyright owner to grant Dalhousie University the rights required by this license, and that such third-party owned material is clearly identified and acknowledged within the text or content of the submission.

If the submission is based upon work that has been sponsored or supported by an agency or organization other than Dalhousie University, you assert that you have fulfilled any right of review or other obligations required by such contract or agreement.

Dalhousie University will clearly identify your name(s) as the author(s) or owner(s) of the submission, and will not make any alteration to the content of the files that you have submitted.

If you have questions regarding this license please contact the repository manager at dalspace@dal.ca.

Grant the distribution license by signing and dating below.

_____   _____

Name of signatory   Date

DALHOUSIE UNIVERSITY

Inspiring Minds

DATE: _____

AUTHOR: _____

TITLE: _____

_____

_____

_____

Degree: _____   Convocation: _____   Year: _____

    Permission is herewith granted to Dalhousie University to circulate and to have copied for non-commercial purposes, at its discretion, the above title upon the request of individuals or institutions.

_____

Signature of Author

ABSTRACT

Neoarchean (ca. 2680 Ma) transitional to calc-alkaline volcanic rocks in the Tumpline Lake subarea of the Cameron River - Beaulieu River volcanic belt in the southern Slave Province are being assessed to determine their potential as a prospective volcanogenic-hosted massive sulphide (VMS) environment. Bedrock mapping at Sharrie Lake, approximately 70 km ENE of Yellowknife, was completed at 1:7500 in 2012 and 2013. Samples of mafic and intermediate pillow lava flows from this strongly bimodal suite were collected for further study. In addition to some true pillow basalts and andesites, many flows have basalt-like textures yet have the weathered appearance and silica values of a dacite or rhyolite. The VMS-potential of these pillow lava flows will be assessed by characterizing the rock geochemistry and alteration characteristics, and constraining the timing of alteration and deformation relative to metamorphism.

Geochemical discrimination diagrams demonstrate that primary lithology varies from basalt to andesite, and several flows can be identified based on their distinct geochemical signatures. Lava flows have variable trace element patterns although all show arc-like characteristics. The secondary mineralogy is dominated by carbonate, quartz, epidote, chlorite, and minor sericite. In thin section, disseminated matrix carbonate is common and ovoid aggregates of quartz and carbonate, interpreted as deformed amygdules, display textures indicating pre-kinematic origin and recrystallization during regional metamorphism. Lithogeochemical characterization of least altered - most altered sample pairs indicates that alteration is pre-metamorphic and possibly syn-volcanic. The principal components gained or lost in the metasomatic alteration reactions vary between flows of different primary lithology. The relative timing of some secondary minerals is ambiguous owing to the effects of heterogeneous strain. Sericite and some chlorite are generally present replacing earlier phases such as plagioclase, amphibole, and biotite, and both are interpreted to be late. If the secondary mineral assemblage represents the alteration assemblage, the Sharrie Lake samples have undergone carbonate propylitic alteration related to diagenetic (seafloor) alteration processes. It is more likely, however, that the secondary assemblage represents the early seafloor alteration mineralogy overprinted by the later amphibolite facies metamorphic assemblage. Peak lower amphibolite facies metamorphism (~500 °C and 4.0 ± 2 kb) was syn- to post-kinematic based on syn- to post-foliation hornblende growth and post- foliation garnet growth.

Although the alteration mineralogy and geochemistry of the samples in this study do not appear to indicate a strong hydrothermal alteration signature, other characteristics of the Tumpline Lake subarea, such as the geochemistry of felsic volcanic rocks and proximity to known VMS-type showings and deposits, demonstrate that this belt warrants further study as a VMS-potential environment.

Keywords: geochemistry - alteration - greenstone belt - Archean - thermobarometry - Slave Province - Northwest Territories

TABLE OF CONTENTS

TABLE OF FIGURES

TABLE OF TABLES

TABLE OF MINERAL ABBREVIATIONS

Abbreviation	Mineral
Act	Actinolite
Amph	Amphibole
Ap	Apatite
Bt	Biotite
Carb	Carbonate
Cc	Calcite
Chl	Chlorite
Ep	Epidote
Grt	Garnet
Hbl	Hornblende
Ilm	Ilmenite
Mus	Muscovite
Plag	Plagioclase
Qtz	Quartz
Ser	Sericite
Ttn	Titanite

ACKNOWLEDGEMENTS

Thank you to Valerie Jackson and Luke Ootes for giving me the opportunity to conduct field work through the Banting-VMS project and for encouraging me to present my preliminary results at the Yellowknife Geoscience Forum. Thank you to Dr. Rebecca Jamieson, Dr. Martin Gibling, Luke Ootes, and Valerie Jackson for their valuable feedback and guidance throughout the writing of this thesis. Additional thanks to Gordon Brown, for thin section preparation, and Dan MacDonald, for assistance in obtaining EMP data. Thank you to the Government of Canada (Aboriginal Affairs and Northern Development Canada) and to the Government of the Northwest Territories for supporting my field work, analytical work, and travel to the Yellowknife Geoscience Forum.

Thank you to my wonderful roommates (official and un-official) for your support this year. You are amazing people, and your patience and understanding were outstanding.

CHAPTER 1: Introduction

1.1 Introduction

Volcanogenic-hosted massive sulphide (VMS) deposits are important sources of Zn, Cu, Pb, Au and Ag, among other metals, and are particularly abundant in Canada where approximately 350 such deposits have been identified (Galley *et al.,* 2007). These polymetallic ore deposits are found in early Archean to modern submarine volcanic sequences and many Canadian deposits are hosted within Archean greenstone belts (Galley *et al.,* 2007). The Archean Slave Province in the Canadian Shield (Fig 1.1) contains some of Canada's least developed VMS deposits (Bleeker & Hall, 2007). Constraining the greenstone belts in this craton that have VMS potential is a vital step towards increasing exploration activity in the Northwest Territories and Nunavut. The Cameron River - Beaulieu River volcanic belt (CBVB) is one of several belts across the Slave Province that is being evaluated by the Northwest Territories Geoscience Office (NTGO) to determine its prospectivity to host VMS mineralization. Near Sharrie Lake in the CBVB (62° 36' 13" N, 112° 57' 32" W) distinct and varied alteration textures in pillow lava flows suggest the possibility of extensive alteration that could be associated with a VMS-potential environment. Known mineralization in the Sharrie Lake area is generally hosted in gossanous zones between flows, and therefore a detailed petrographic and geochemical study of the mafic to intermediate volcanic rocks is valuable for understanding the alteration and metamorphism of this belt. The unusual appearance of some of the variably deformed altered mafic pillow lava flows around Sharrie Lake (Fig. 1.2) has been subject to previous interpretations that will be reassessed in this study.

This thesis reports on field work from the segment of the CBVB around Sharrie Lake, which was mapped in 2012 and 2013 by Valerie Jackson of the NTGO. Figure 1.3 presents the

2013 map of Sharrie Lake with annotated sample locations. A map of this locality had previously been produced at 1:50000 scale by Lambert in 1972 and 1973 and was used as a base map for the 2012 and 2013 mapping.
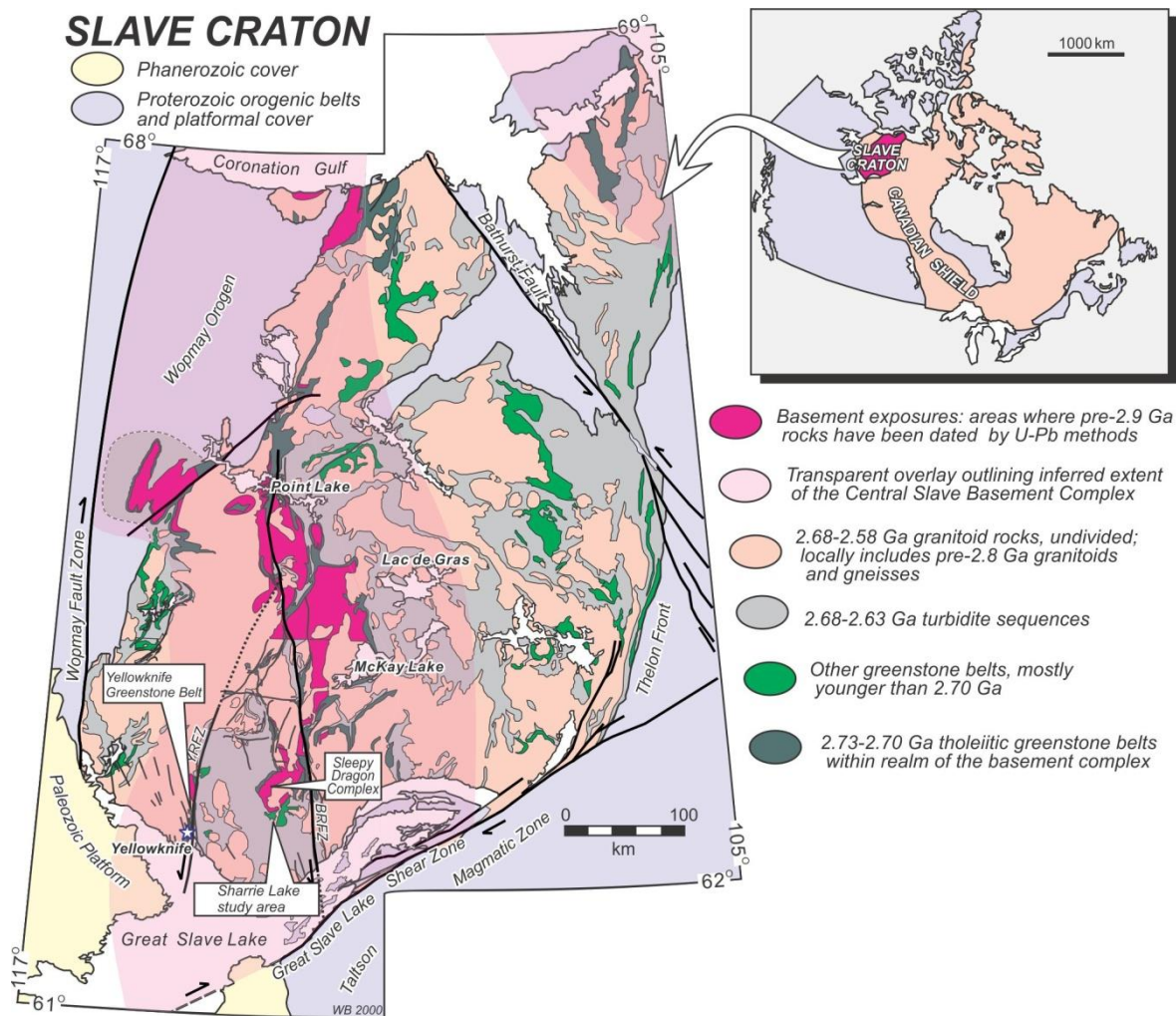
Figure 1.1: Simplified geological map of the Slave Province highlighting the Sharrie Lake study area, the Yellowknife Greenstone belt and the Sleepy Dragon Complex. Modified after a figure courtesy of W. Bleeker, unpublished.

Figure 1.2: Mafic pillows with altered cores, previously interpreted as blocks of trapped felsic volcanic rock (Lambert, 1988).

1.2 Exploration history and VMS potential of the Banting Group volcanic rocks

The Archean Slave Province represents an economically important province in the Canadian Shield. Mineral resources in the Slave Province include undeveloped and underdeveloped VMS deposits, shear- and vein-hosted gold deposits within deformed greenstone belts, banded iron formation-trapped epigenetic gold within turbidite packages, Proterozoic magmatic-related mineralization, and Phanerozoic diamondiferous kimberlite pipes (Bleeker & Hall, 2007). The Banting Group and Banting-like volcanic rocks dated at 2687 to 2660 Ma host a number of known VMS-type deposits including Hackett River, High Lake, Izok Lake, Sunrise, Gondor, and Kennedy Lake (Bleeker & Hall, 2007). These deposits are generally hosted in felsic volcanic rocks proximal to the upper contact with the overlying turbidites (Bleeker & Hall, 2007). The interpreted tectonic setting for the Banting Group of active extension, faulting, volcanism, and the high geothermal gradient associated with this regime is consistent with accepted models for VMS systems (Bleeker & Hall, 2007; Galley *et al.,* 2007; Franklin *et al.,* 2005).
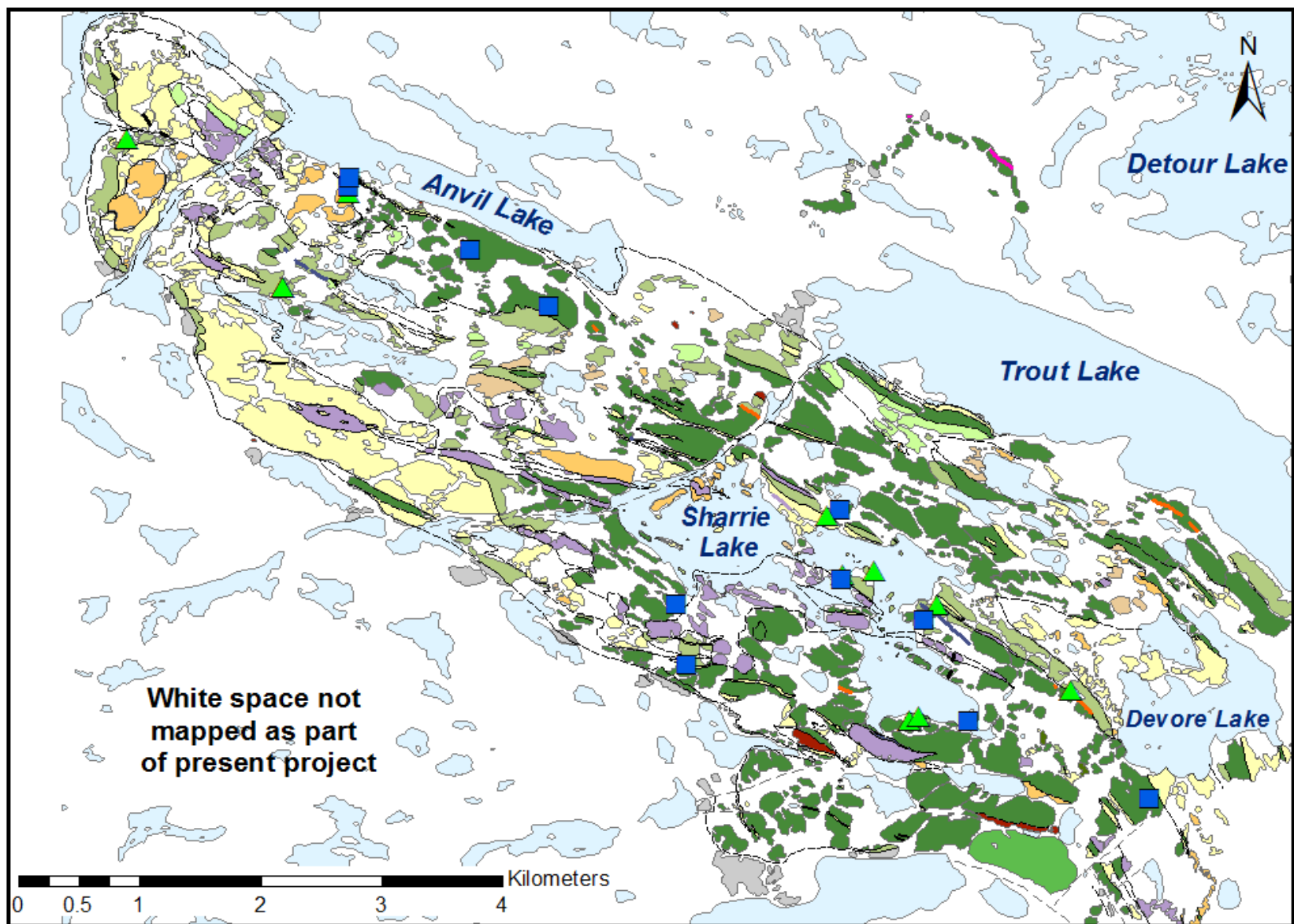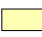
Figure 1.3: Geological map of Sharrie Lake (after V.A. Jackson, unpublished data). See Appendix A for a list of samples and explanation of sample numbering.

<u>Legend</u>

—— Stream

Lake

—— Quartz Veins

– – – Lineaments

— — – Faults

Contacts

– – – – Assumed

—— Defined

Mafic Sample

Intermediate Sample

LITHOLOGICAL UNITS

VOLCANIC

Mafic volcanic; pillow lava (±altered (felsic) cores), flow top breccia, massive, layered

Intermediate volcanic; pillow lava, flow top breccia, massive, layered,

Felsic volcanic; volcaniclastic (ash, lapilli, block), massive

Felsic volcanic; massive

Volcanic; undifferentiated, mixed on a scale too fine to differentiate

Volcanic; mixed felsic and intermediate rocks, commonly layered, commonly volcaniclastic

SEDIMENTARY

Greywacke-mudstone; biotite, cordierite-grade

Shale-siltstone, typically rusty, graphitic

Conglomerate

PLUTONIC

Diabase, likely Proterozoic (includes Mackenzie dyke)

Granitic

Felsic

Mafic ±columnar/polygonal cooling fractures

Ultramafic

OTHER

Gossan

It has long been recommended that a detailed study of the Archean greenstone belts in the Slave Province be undertaken to produce integrated bedrock maps, geochronological, geochemical, and isotopic data in order to constrain the original tectonic setting of these volcanic sequences (Card & King, 1992). This thesis stems from the larger scale Banting-VMS project run by the NTGO that aims to fulfill this long-standing recommendation. Detailed bedrock mapping for the Banting-VMS project was conducted by the NTGO during the summers of 2012 and 2013 in various volcanic belts at 1:7500 scale. Previous exploration projects targeting Banting-hosted deposits in the Beaulieu River volcanic belt have been undertaken by Cominco Limited, and the Yellowknife Syndicate, a group venture by Yellowknife Bear Mines Limited, Long Lac Mineral Exploration Limited, Hydra Explorations Limited, and Keevil Mining Group Limited (NTGO Showing Report, 2011). Drill programs, airborne geophysical surveys, and ground data acquisition were executed by Geophysical Engineering and Surveys Limited (NTGO Showing Report, 2011). Previous bedrock mapping around Sharrie Lake was conducted at 1:250000 and 1:50000 scales, respectively, by Henderson (1985b) and Lambert (1988).

1.3 Objectives

The objectives of this study are:

1) to determine the primary lithological and geochemical characteristics of the pillow lava flows from the CBVB around Sharrie Lake;

2) to compare and contrast the primary lithology, mineralogy, textures, and alteration of the mafic and intermediate pillow lava flows;

3) to determine the origin of the pale mafic pillow cores;

4) to characterize the alteration assemblages of the mafic and intermediate pillow lava flows;

5) to interpret this alteration in the context of a VMS-potential environment; and

6) to determine the relative timing and P-T conditions of metamorphism.

1.4 Scope and organization of this study

This thesis is divided into four sections as follows:

1) review of relevant and available data for the the south-central Slave Province and the Sharrie Lake study area (Chapters 1 and 2);

2) detailed petrography, mineral chemistry from electron microprobe analyses, geochemistry, and presentation of petrological and geochemical data in the context of alteration and metamorphism, including P-T estimates (Chapters 3 and 4);

3) discussion of results, conclusions drawn, and recommendations for further study (Chapters 5 and 6).

CHAPTER 2: Geologic Setting

2.1 Regional geology

As the Sharrie Lake study area lies close to a large basement exposure, the overview of regional geology described herein will focus specifically on the south-central Slave Province, and the domains underlain by the basement. More in-depth overviews of the geology and tectonic history of the Slave Province can be found in Fyson & Helmstaedt (1987), Card & King (1992), Padgham & Fyson (1992), and Bleeker & Hall (2007), among others.

2.1.1 South-central Slave Province

The Archean Slave Province (Fig. 1.1) in the Northwest Territories and Nunavut consists of a variety of plutonic suites, greenstone belts, and sedimentary successions structurally and stratigraphically overlying >2.8 Ga basement gneisses and granitoid plutons of the Central Slave Basement Complex (Card & King, 1992; Bleeker *et al.,* 1999a). In contrast to most Archean cratons, which consist of granite-greenstone terranes, the Slave Province contains relatively few volcanic belts relative to sialic crust and sedimentary rocks (Card & King, 1992; Padgham & Fyson, 1992). The Acasta gneiss of the Central Slave Basement Complex, the oldest identified rock on Earth, yielded protolith ages up to 4.03 Ga and inherited zircons dates as old as 4.2 Ga (Stern & Bleeker, 1998; Bowring & Williams, 1999). The remainder of the basement has yielded ages ranging from 3325 ± 8 Ma to 2734 ± 2 Ma (Bleeker *et al.,* 1999a; Ketchum *et al.,* 2004). This basement is unconformably overlain by the Central Slave Cover Group that consists of ca. 2924-2820 Ma minor mafic to ultramafic volcanic rocks overlain by conglomerates, chromite-bearing fuchsitic quartzites, and banded iron formations (Bleeker *et al.,* 1999a; Sircombe *et al.,* 2001). The overlying ca. 2.73 - 2.58 Ga sedimentary and volcanic rocks are collectively called

the Yellowknife Supergroup (Henderson, 1970). This supergroup consists of the thin Central Slave Cover Group, two overlying greenstone sequences (Kam Group, ca. 2.70 Ga, and Banting Group, ca. 2.69 - 2.66 Ga), province-wide turbidites (Duncan Lake Group, ca. 2.66 - 2.61 Ga), and syn-orogenic conglomerates (ca. 2.60 Ga) (Bleeker & Hall, 2007). Correlation between lithological units of the Yellowknife Supergroup, particularly for the volcanic rocks, is largely based on geochronological data (Card & King, 1992). Pan-Slave plutonism includes ca. 2685-2670 Ma syn-volcanic intrusions as well as those emplaced syn- to post-turbidite deposition, e.g. Defeat Suite, ca. 2630-2620 Ma, and younger granitic bloom, ca. 2590-2580 Ma (Davis & Bleeker, 1999). The Slave Province underwent regional high temperature, low pressure metamorphism and the Neoarchean rocks underwent at least two stages of deformation: D_1 at ca. 2660-2630 Ma, and D_2 at ca. 2605-2580 Ma (Davis & Bleeker, 1999). Three main stages of VMS mineralization across the Slave Province coincided with major volcanic events ca. 2700, 2680 and 2670 Ma (Bleeker & Hall, 2007).

The Kam Group, the older of the greenstone sequences, consists of tholeiitic basalt flows, and lesser felsic volcaniclastic sequences (Helmstaedt & Padgham, 1986; Isachsen & Bowring, 1997; Cousens *et al.,* 2002). This ca. 2722-2701 Ma sequence ranges in thickness from several hundred meters to several kilometers and can be widely correlated across the Slave Province (Isachsen & Bowring, 1997; Cousens *et al.,* 2005; Bleeker & Hall, 2007).

The ca. 2680 Ma Raquette Lake Formation, and correlative Detour Lake Formation, of the Ross Lake Group comprises a wide variety of clastic and chemical sedimentary rocks, and volcaniclastic and volcanic rocks (Bleeker, 2001). The formation is defined by its basal conglomerate, which unconformably overlies the ca. 2.95 Ga composite basement and younger tonalite-trondhjemite-granodiorite (TTG) suites of the Sleepy Dragon Complex ~70 km northeast

of Yellowknife, and by its uppermost black mudstone, which underlies the Burwash Formation turbidites (Bleeker, 2001; Ketchum, *et al.,* 2004). The Raquette Lake Formation can be correlated with similar lithostratigraphic units across the Slave Province and may serve as a ~2690-2680 Ma marker horizon.

The volcanic belts and associated volcaniclastic rocks between 2.70 and 2.66 Ga are considered correlatives to the Banting Group, as defined at the type section in the Yellowknife greenstone belt (Helmstaedt & Padgham, 1986; Isachsen *et al.,* 1991; Bleeker & Hall, 2007). Their relationships and correlations across the province are shown in the schematic stratigraphic columns in Figure 2.1. Banting Group syn-volcanic plutonic suites were emplaced ca. 2.73-2.67 Ga along the margins of the Sleepy Dragon Complex and at Yellowknife (Ketchum *et al.,* 2004).

Regionally extensive ca. 2660 to 2610 Ma turbidite sequences of the Duncan Lake Group conformably to disconformably overlie the Banting Group volcanic rocks across the Slave Province (Henderson, 1970; Ferguson *et al.,* 2005; Bleeker & Hall, 2007; Ootes *et al.,* 2009). The turbidites consist of immature greywackes and mudstones locally up to 10 km thick, and are subdivided into a two packages based on detrital zircon geochronology (Henderson, 1970; Ootes *et al.,* 2009). The older package I has been dated at ca. 2660 Ma (Burwash Formation) and the younger, iron formation-bearing package II, has been less reliably dated at ~2640-2630 Ma (Ootes *et al.,* 2009, and references therein).

Collision of an unknown terrane with the eastern Slave Province between ca. 2660-2630 Ma closed the Burwash Basin and produced regional northeast-southwest-trending D_1 folds (Davis & Bleeker, 1999; Bleeker & Hall, 2007). Crustal thickening accompanying the D_1 deformation resulted in the uplift and erosion of Burwash turbidites, the partial unroofing of the ca. 2630 Ma Defeat Suite intrusions, and contemporaneous deposition of post-2630 Ma

turbidites (Ootes *et al.,* 2009). Craton-wide shortening (D_2) occurred between ca. 2605 and 2580 Ma and produced generally north-south to northwest-southeast trending folds and cleavage (Davis & Bleeker, 1999). This shortening was accompanied by regional high-temperature, low-pressure metamorphism resulting in the emplacement of pan-Slave ca. 2630-2605 Ma TTG suites and later ca. 2600-2580 Ma S- and I-type granites (Bleeker & Hall, 2007). This "granite bloom" was a key factor in craton stabilization (Kusky, 1990; Bleeker & Hall, 2007). Following ca. 70 Ma of cooling, and ca. 300 Ma of limited tectonic activity, attempted initial rifting in the Slave Province is evident from the ca. 2230 Ma Malley dyke swarms (Bleeker & Hall, 2007).

There have been a number of suggested tectonic settings for the Slave Province greenstone belts including island arcs (Condie & Baragar, 1974), sutured slivers of oceanic crust (Kusky, 1990), back-arc basins later overlain by arc-like volcanism (Helmstaedt & Padgham, 1986), and continental rifts (Henderson, 1985). The Kam Group is considered parautochthonous and to have formed on sialic crust of the Central Slave Basement Complex, which was thinned along the décollement at the margins of the Sleepy Dragon Complex (Bleeker *et al.,* 1999b). This low-angle detachment may be related to rifting of the basement complex and later development of structurally-controlled basins (Bleeker *et al.,* 1999b). At its type section in the Yellowknife greenstone belt, a continental margin rift setting has been proposed for the Kam Group (Cousens *et al.,* 2005). Neodymium isotopic characteristics of mafic to felsic volcanic rocks, and inherited zircons in tuffaceous units of the Kam Group, strongly imply that these volcanic rocks are autochthonous upon the basement, thereby further confining the proposed rift setting (Sircombe *et al.,* 2001; Cousens *et al.,* 2005).
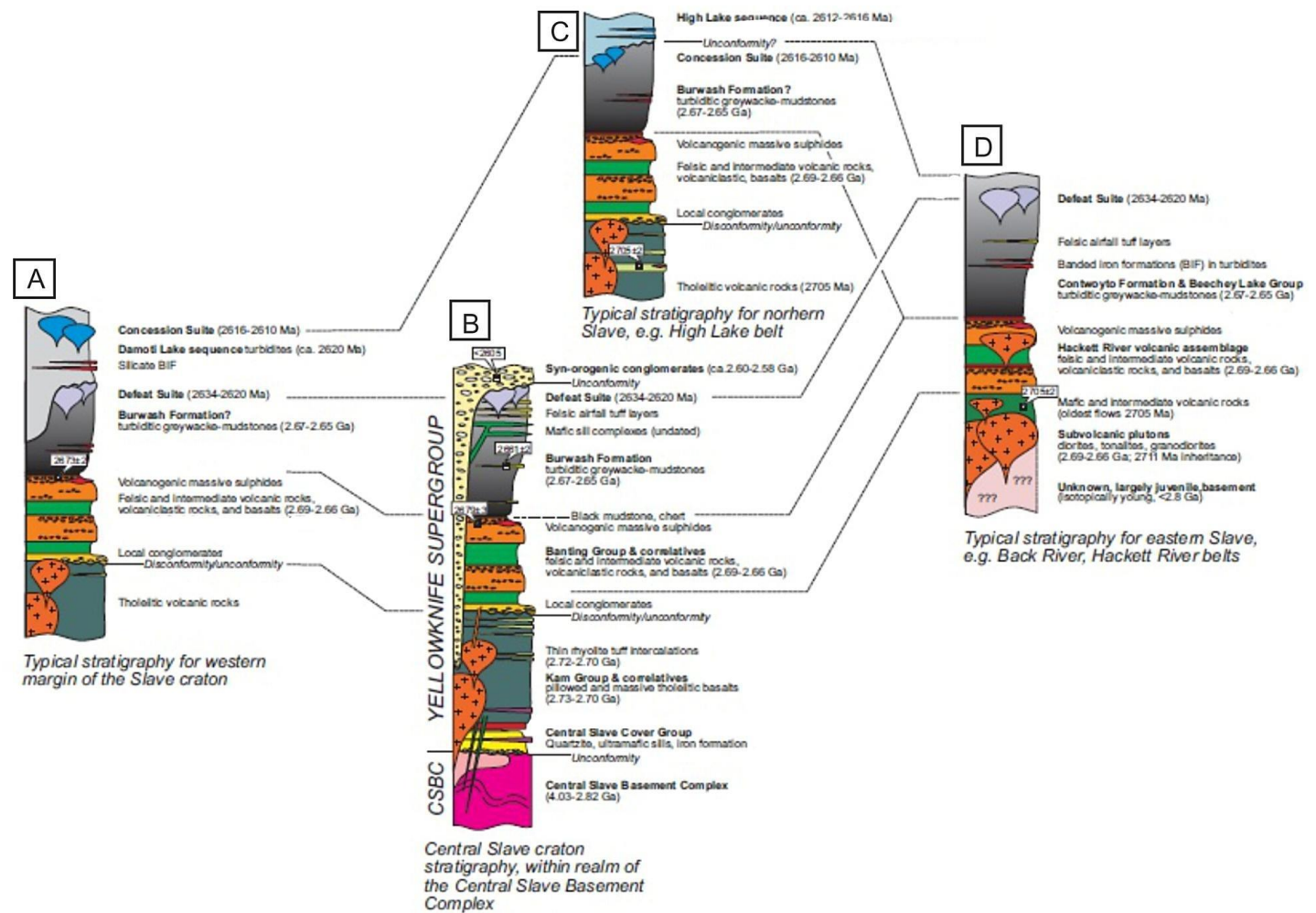
Figure 2.1: Schematic stratigraphic columns for (A) western Slave Province, (B) Central Slave Province, (C) northern Slave Province, and (D) eastern Slave Province correlating supracrustal sequences across the Slave Province. Modified after Bleeker & Hall, 2007.

Younger volcanic rocks and other supracrustal units of the Yellowknife Supergroup (including the Banting Group) are linked to the basement by dykes or unconformities and are therefore treated as essentially autochthonous (Henderson, 1985; Bleeker *et al.,* 1999b). The ca. 2680 Ma Raquette Lake Formation is proposed to represent the initiation of a sedimentary basin in a rifted arc environment (Bleeker, 2001). A convergent margin setting and melting of the subducted oceanic crust has been proposed to explain the geochemical signature of the felsic volcanic rocks of the Banting Group in the Yellowknife greenstone belt, whereas an extensional regime has been suggested for the Banting Group mafic volcanic rocks at this type section (Cousens *et al.,* 2002; Cousens *et al.,* 2005). An extensional tectonic regime has also been suggested for the Burwash Formation turbidites (Henderson, 1970; Ferguson *et al.,* 2005). The continental back-arc tectonic setting proposed for the turbidites is supported by intercalated volcanic rocks and felsic tuffs, and by abundant late mafic sills associated with the sediments (Ferguson *et al*., 2005; Ootes *et al.,* 2009). A schematic representation of the tectonic history in the Slave Province from ca. 2690-2660 Ma is shown in Figure 2.2.

2.1.2 Volcanic Rocks of the South-Central Slave Province

The ca. 2722-2701 Ma tholeiitic Kam Group and the ca. 2687-2660 Ma arc-like Banting Group are disposed in a number of greenstone belts in the south-central Slave Province including the Yellowknife greenstone belt and the Cameron River - Beaulieu River volcanic belt (CBVB) (Helmstaedt & Padgham, 1986; Isachsen *et al*., 1991; Isachsen & Bowring, 1997; Cousens *et al.,* 2005). The Kam Group is generally mafic-dominated, whereas the 2663 Ma Banting Group at its type section is commonly felsic-dominated (Cousens *et al.,* 2005). The structural relationship between the Kam and Banting groups is ambiguous. Other than at the Yellowknife type section

where the two formations are separated by a Proterozoic fault, they have not been seen in contact

(Cousens *et al.,* 2005).
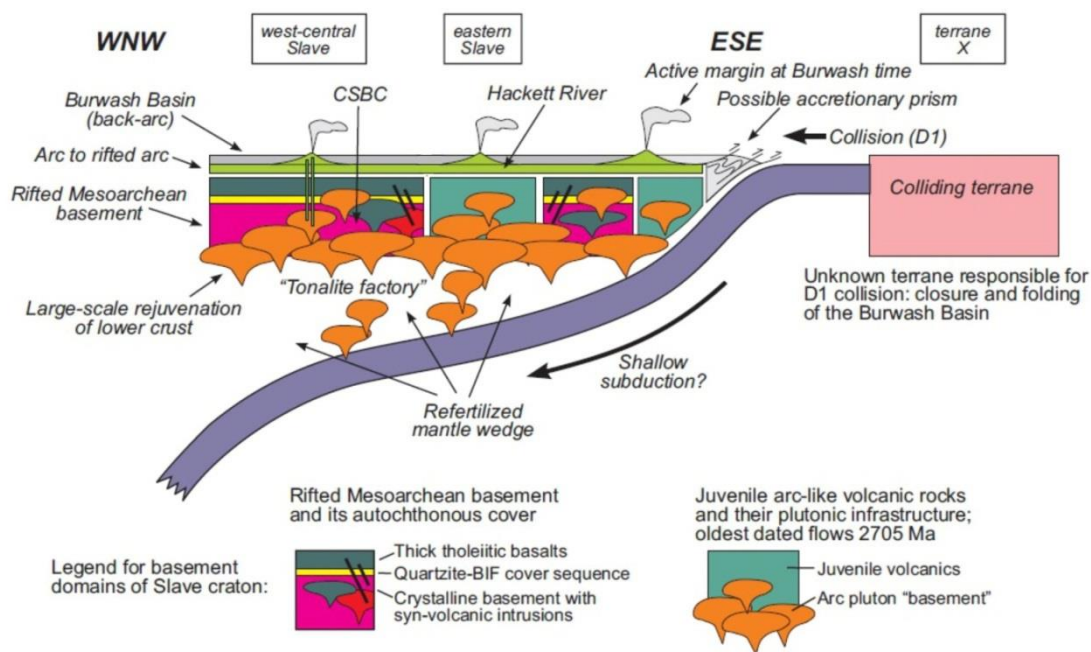
Figure 2.2: Generalized tectonic model for the Slave Province ca. 2690-2660 Ma showing widespread magmatism during the collision of unknown terrane (X) in the closure of the Burwash Basin (D_1). The autochthonous relationship between the supracrustal sequences and their crystalline basement in the western Slave craton, and the location of the postulated exotic eastern arc-like domain are also shown. Modified after Bleeker & Hall, 2007.

At its type section in the Yellowknife greenstone belt, the Kam Group consists of lower

subalkaline basalts and basaltic andesites, and upper evolved basalts, tuffaceous dacites, and

rhyolites (Cousens *et al.,* 2005). At the same locality, the overlying Banting Group comprises

calc-alkaline intermediate to felsic volcanic, volcaniclastic, and sedimentary rocks (Cousens *et al.,* 2002; Cousens *et al.,* 2005). Three tectonic models have been proposed for the Banting

Group: 1) a rift setting with a low rate of extension and underplating of the mafic magma, which

released significant heat to melt the lower crust, 2) an arc setting in which primary felsic magmas

were produced via direct melting of the subducting slab, and 3) partial melting generated by

delamination of the lowermost mafic crust (Cousens *et al.,* 2002; Cousens *et al.,* 2005). Despite

their 'arc-like' signature, the lack of distinct curvilinear greenstone belts, accretionary wedges,

and belts of subvolcanic plutons, and the scattered exposures of Banting-correlatives throughout

the Slave Province, imply that a modern arc model is not the best explanation for the

petrogenesis of the Banting Group (Cousens *et al.,* 2005).

2.2 Geology of the Sharrie Lake area

The Sharrie Lake field area is approximately 70 km east-northeast of Yellowknife, and

lies at the southern end of the sialic Sleepy Dragon basement Complex (Fig. 2.3). The

supracrustal rocks belong to the Yellowknife Supergroup (Henderson, 1970). Lambert (1988)

termed this area the Tumpline Lake subarea and distinguished it from the CBVB based on the

strongly bimodal character of its volcanic units (Fig. 2.3).

2.2.1 Lithological units

Based on 2012 and 2013 mapping at Sharrie Lake, the main lithological units include

mafic, intermediate, and felsic volcanic and volcaniclastic rocks, undifferentiated volcanic rocks

± volcaniclastic rocks, sedimentary rocks of the Burwash Formation, and granitic, mafic, and

ultramafic intrusions (V.A. Jackson, unpublished data). Geological field relationships are shown

in Figure 1.3.

A set of field criteria was established during the 2012 and 2013 mapping to differentiate

between mafic and intermediate pillows. These criteria are summarized in Table 2.1. Mafic

pillows are dark grey-green to black and are characterized by thin to non-existent selvages, a lack

of garnet, and cores that are moderately to strongly altered to pale grey-green or cream-white

(Fig. 2.4). Some of these altered pillow cores were previously interpreted as solid blocks of felsite trapped during the eruption of mafic magma (Lambert, 1988). The irregular shape of some felsite inclusions (Fig. 2.7 A and B) was attributed to rheological differences between the mafic and felsic material, causing the mafic material to mould around the felsite during deformation (Lambert, 1988).
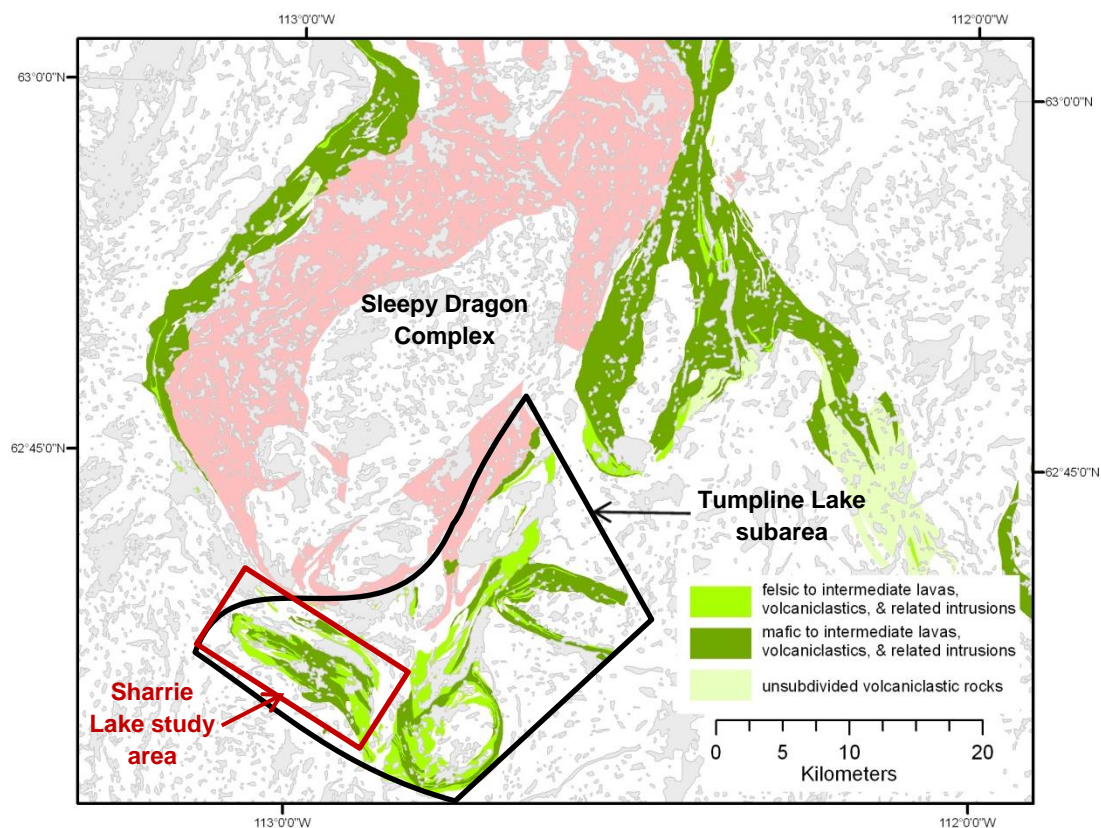
Figure 2.3: Simplified geological map of the Cameron River - Beaulieu River volcanic belt surrounding the basement complex (Sleepy Dragon Complex). The Tumpline Lake subarea (Lambert, 1988), and the Sharrie Lake study area are enclosed in black and red polygons, respectively. Pink areas represent granitoids of the Sleepy Dragon Complex. Modified after Stubley, 2005.

Table 2.1: Summary of the field criteria used to distinguish mafic from intermediate pillow lavas.

	Colour	Appearance of core	Appearance of selvage	Garnet	Amygdaloidal	See Fig.
Mafic	Dark grey-green to black	Moderately to strongly altered to pale grey-green or creamy white	Thin to non-existent	None to rare	Yes. Quartz and/or carbonate-filled voids.	2.6
Intermediate	~Uniformly pale grey-green	Pale grey-green	Thick, black biotite-amphibole±garnet-rich.	Common in selvage, sparse in core	Yes. Quartz and/or carbonate-filled voids.	2.7
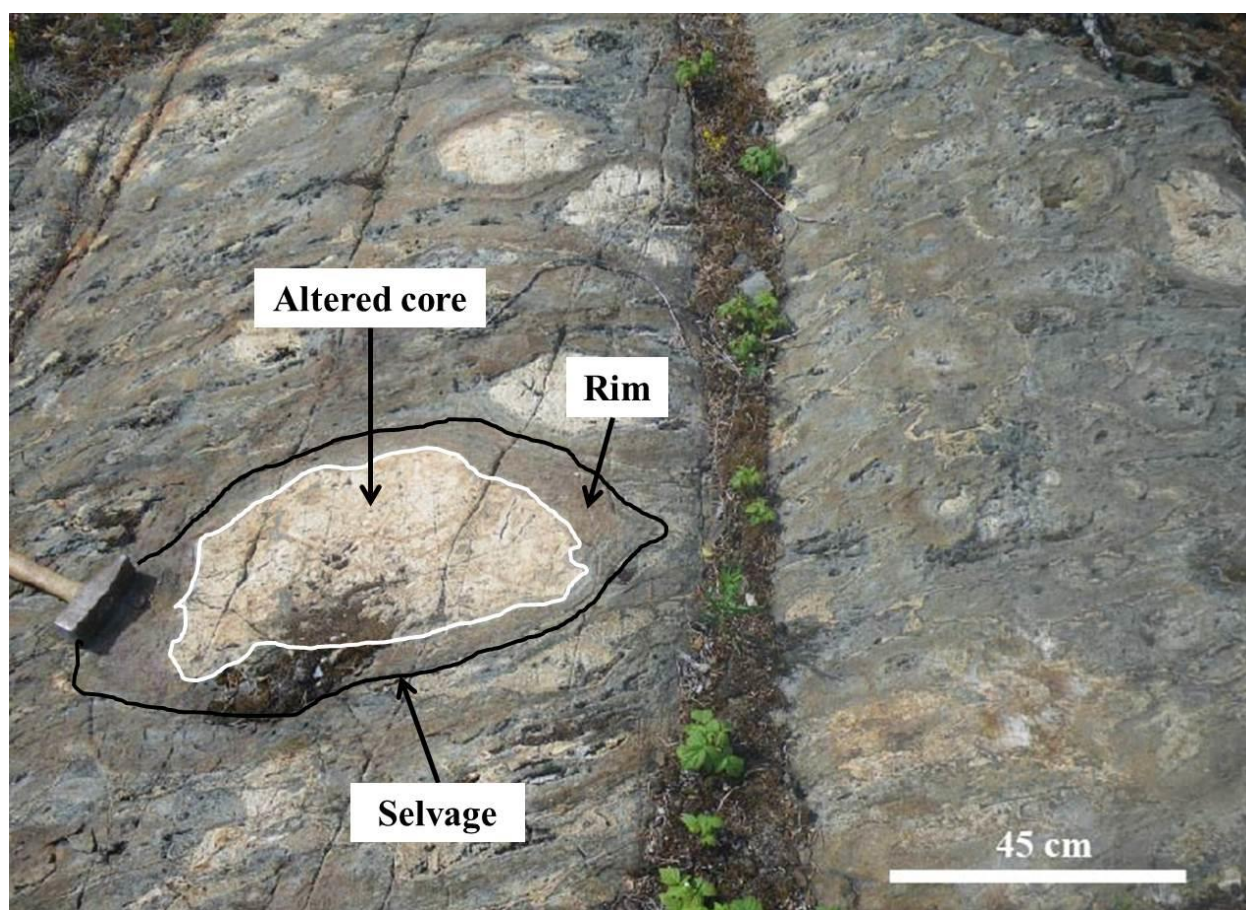
Figure 2.4: Mafic pillow lava flow with thin pillow selvages, grey rims, and cream altered cores. Note pillow colour and thin to absent selvage characteristic of mafic pillow lavas at Sharrie Lake.

In contrast, intermediate pillows have thicker biotite-amphibole±garnet-rich selvages around a pale grey-green core (Fig. 2.5). The exact nature of the material interpreted as the pillow selvage is ambiguous; it may be interstitial sedimentary or volcaniclastic material, or devitrified, altered, recrystallized and/or metamorphosed selvage material. Both mafic and intermediate pillows are commonly highly amygdaloidal, having quartz and/or carbonate ovoid aggregates interpreted in the field as variably deformed amygdules. Amygdule size ranges from <1 mm to 10 mm. Amygdule morphology in two-dimensions, perpendicular to the regional foliation and lineation, varies from near circular to elongate. Amygdules are most common in the core, but are found in both core and selvage material.
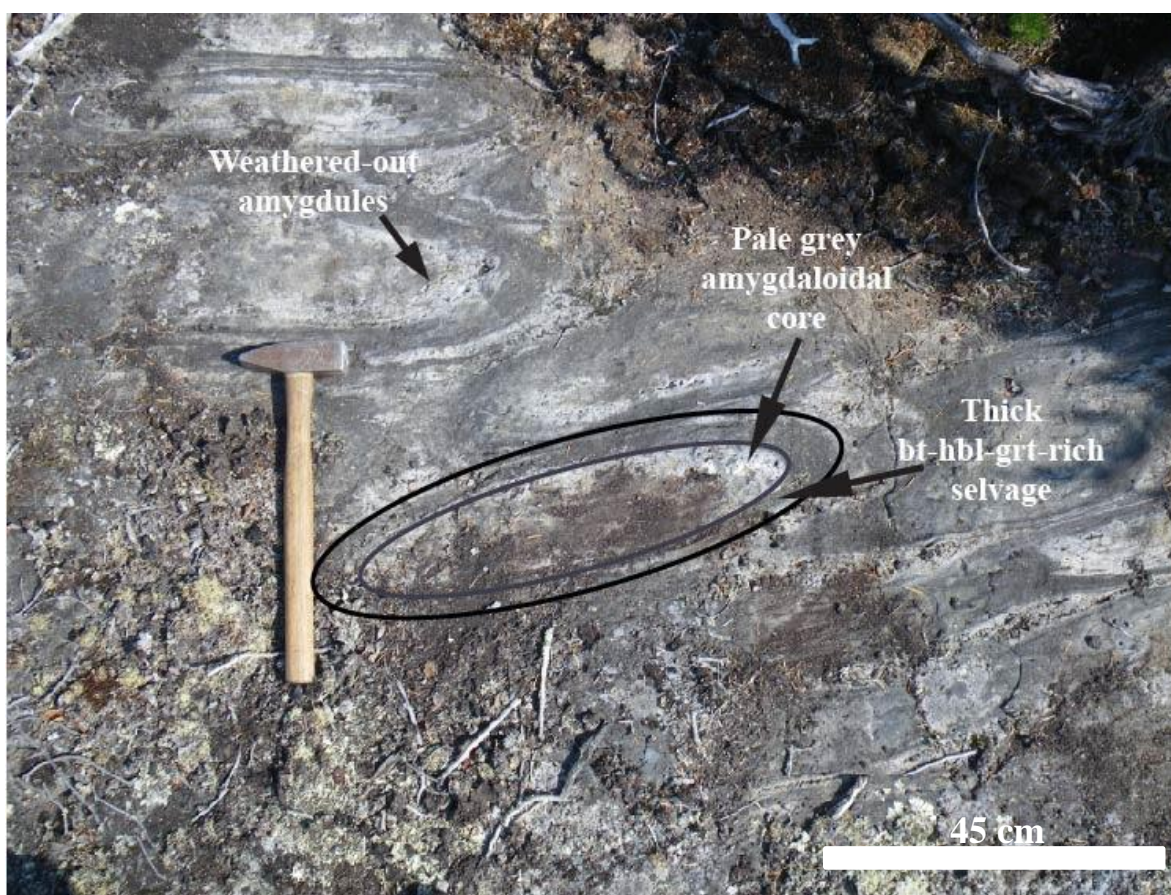
Figure 2.5: Intermediate pillow lava flow with paler colour and thicker amphibole- , biotite-, and garnet-rich pillow selvages typical of intermediate pillow lavas at Sharrie Lake. Pitted appearance of outcrop surface due to recessive weathering of amygdules.

2.2.2 Stratigraphic units and relations

As defined by Lambert (1988), the volcanic rocks of the Tumpline Lake subarea have been assigned to three units: (1) Tumpline basalt, (2) Turnback rhyolite and (3) Sharrie rhyolite. Stratigraphic relations and unit thicknesses are difficult to constrain due to heterogeneous strain within the Tumpline Lake subarea.

Tumpline basalt is composed mainly of pillow lava flows and layered volcaniclastic rocks of basaltic to intermediate composition. This unit includes basalt, andesite, and dacite members near Sharrie Lake, and is estimated to be roughly 1000 m thick. The Tumpline basalt overlies the Turnback rhyolite to the east, and over- and underlies the Sharrie rhyolite to the west of Sharrie Lake (Fig. 2.6). To the north and south of Sharrie Lake, the basalts are overlain by Burwash Formation sedimentary rocks.

The Turnback rhyolite is not well represented in the Sharrie Lake area. Where it is better exposed near Tumpline and Turnback lakes, it consists of five discrete units: massive porphyritic rhyolite, breccias, tuffs, cataclastic rhyolite, and altered rhyolite (Lambert, 1988). The estimated thickness of this unit ranges from <25 m to ca. 1000 m owing to the effects of tight to isoclinal folding. In a number of localities in the CBVB belt, the Turnback rhyolite and Tumpline basalt are interlayered at both large- and small-scale and their relationship is thought to be conformable. The overlying Burwash Formation is also conformable upon the Turnback rhyolite.

Whereas the Turnback rhyolite and Tumpline basalt units are found throughout the CBVB belt, the Sharrie rhyolite is essentially restricted to the anticlinorium at Sharrie Lake. It comprises quartz- and minor feldspar-phyric massive rhyolites, volcaniclastic rocks, and crystal tuffs. It is estimated to be 850 m thick in the nose of the anticlinorium but pinches out along the northern side of Sharrie Lake, and interfingers with the mafic to intermediate volcanic rocks

along the southern side of the lake (Fig. 2.6). Previous field observations placed the Sharrie

rhyolite conformably between the Tumpline basalt and the Burwash Formation (Lambert, 1988).

Ages of the volcanic rocks are currently being re-assessed and recent U-Pb geochronology

indicates that the Sharrie Lake rhyolite erupted at ca. 2680 Ma (M. Hamilton, personal

communication, November 2013).
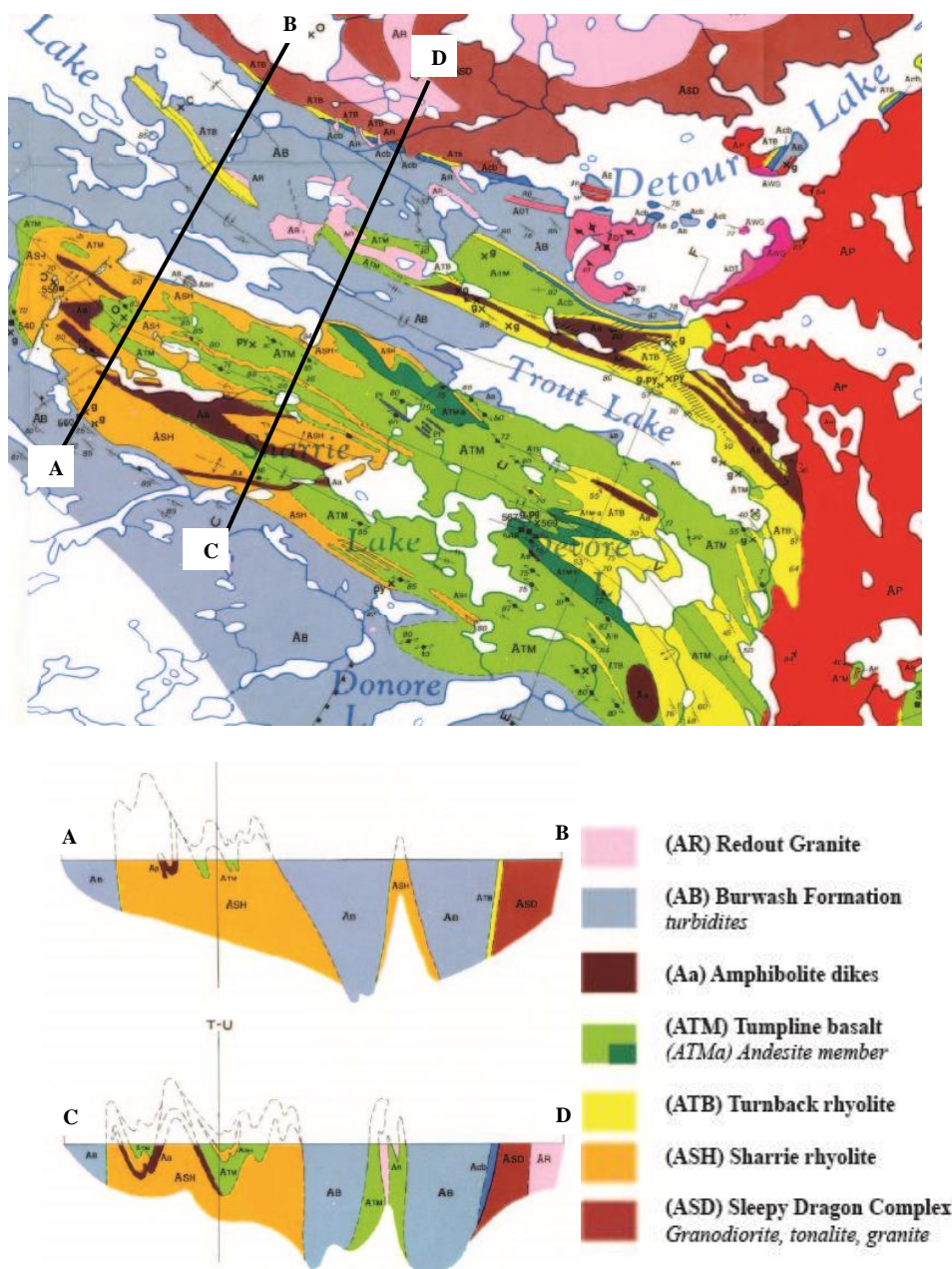
Figure 2.6: Sharrie Lake area map and two cross sections (A-B and C-D) as interpreted by Lambert (1988). Cross section lines shown in black on map. Legend abbreviated for cross sections only.

2.2.3 Alteration

Evidence for significant outcrop-scale alteration in the mafic to intermediate pillow lava flows at Sharrie Lake includes chalk-white weathered surfaces, bleached pillow cores, and abundant quartz- and/or carbonate-filled amygdules and veins. Zones enriched in silica, sericite, and carbonate can be found in felsic, intermediate, and mafic units. Many flows, mapped as mafic or intermediate (based on the criteria outlined in Table 2.1), are pale grey to creamy white in colour and have the weathered appearance of a dacite or rhyolite (Fig. 2.7), yet display distinct pillow shapes characteristic of mafic subaqueous volcanism. Other distinct textures at outcrop scale include spots formed by amphibole and plagioclase-quartz-carbonate aggregates in the pillow cores of one intermediate flow (Fig. 2.7). The timing of alteration is not everywhere straightforward, although some alteration is interpreted as syn-volcanic. The variably altered pillows within a single flow exposed in a continuous outcrop (Fig. 2.8), and the heterogeneous nature of the alteration in adjacent flows provide additional evidence for early alteration. Alteration associated with later deformation and metamorphism could be expected to be more homogeneous in nature.
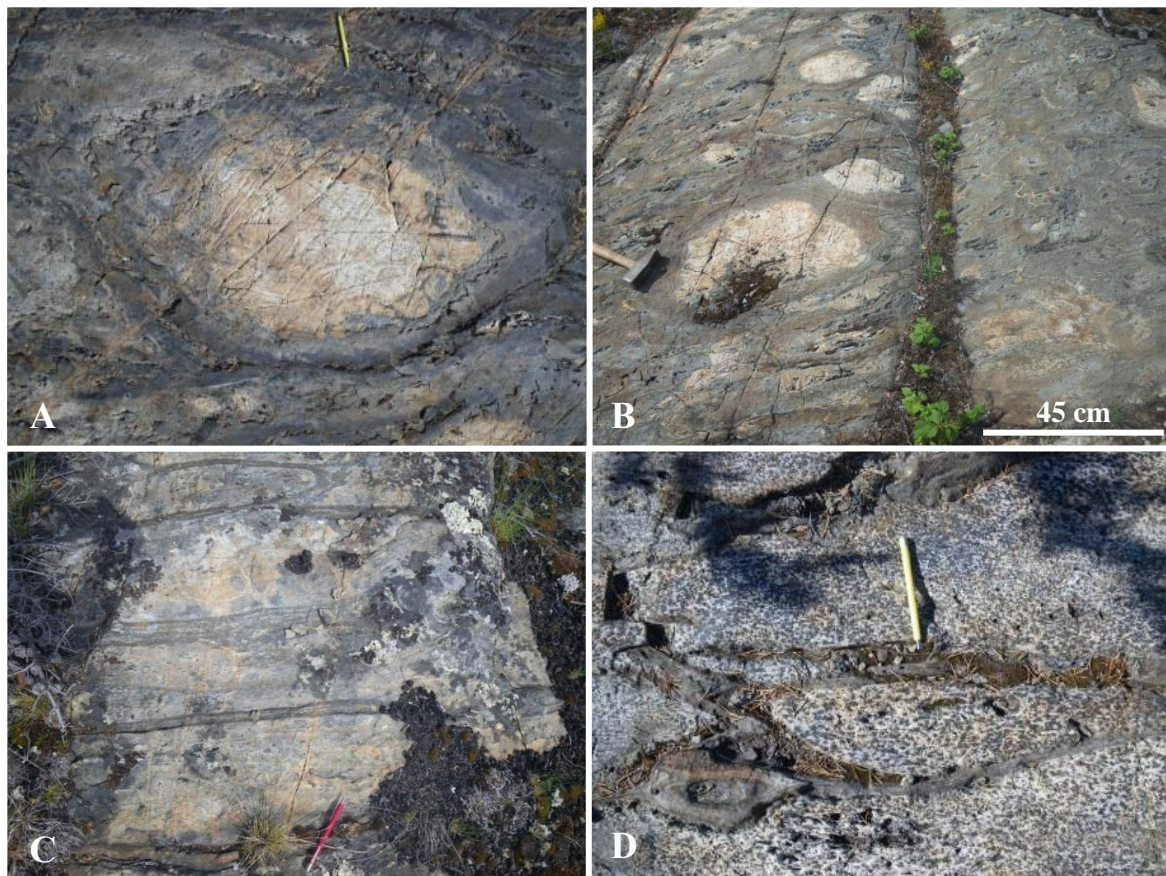
Figure 2.7: Pale mafic pillows can have the weathered appearance of a dacite or rhyolite. This can be restricted to the pillow core (A and B) or can affect the entire pillow (C). D) Spotted amphibole and plagioclase-quartz-carbonate aggregates in an intermediate pillow.
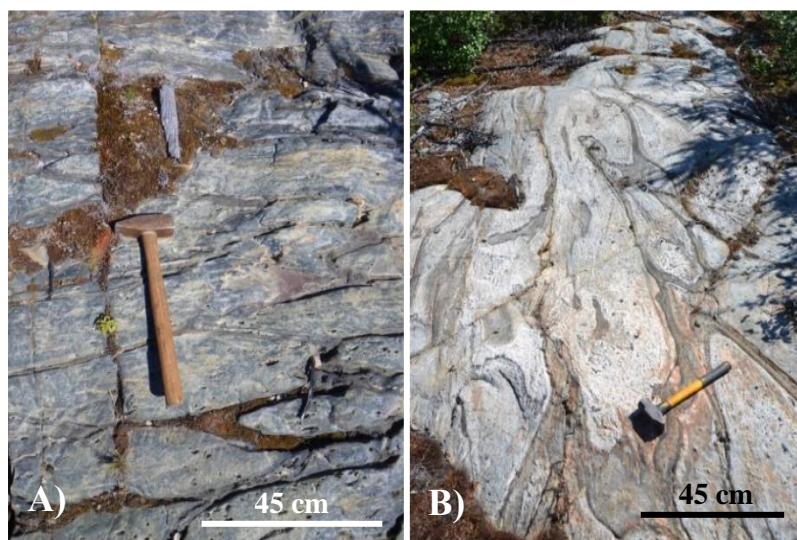
Figure 2.8: Variable alteration, based on weathered appearance, in two areas <40 m apart within the same flow indicates alteration was likely syn-volcanic.

2.2.4 Deformation and regional metamorphism

The dominant structure in the vicinity of the Sleepy Dragon Complex and the CBVB is a regional-scale mushroom fold interference pattern with northeast-southwest trending D_1 folds refolded by northwest-southeast trending D_2 folds (Fig. 2.9) (Bleeker, 1996). This interference pattern, identified in the southern part of the Sleepy Dragon Complex, was interpreted to affect both the basement and adjacent supracrustal sequences (Burwash Formation sedimentary rocks). The Tumpline Lake subarea at Sharrie Lake is underlain by a northwest-plunging anticlinorium approximately 3 km wide (Lambert, 1988; V. Jackson, unpublished data, 2012). This structure is typical of the CBVB belt, where isoclinal folds generally have steeply inclined axial planes and gently to steeply plunging fold axes. East of Sharrie Lake the anticlinorium is truncated by the ca. 2595 Ma Prosperous Granite (Lambert, 1988).
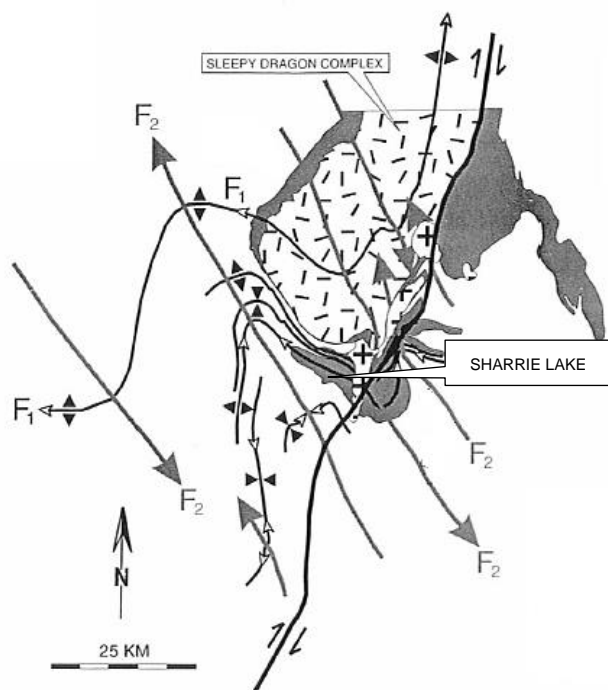
Figure 2.9: Mushroom-type fold interference patterns of northeast-southwest F_1 and northwest-southeast F_2 in the Sleepy Dragon Complex and adjacent supracrustal rocks. After Bleeker, 1996.

The volcanic rocks at Sharrie Lake display both a strong regional foliation and a sub-vertical lineation. The northwest-striking foliation, likely S_2, is defined at outcrop scale by flattening of pillows, or of clasts in volcaniclastic rocks, and by a cleavage or schistosity in rhyolites (Lambert, 1988). Elongated clasts, pillows, and quartz ±carbonate aggregates, interpreted as amygdules, define the steeply-plunging lineation. The lineation lies in the plane of S_1, and likely developed late in the D_1 deformation (Bleeker, 1996). The F_1 fold axes, now steeply plunging and sub-parallel to L_1, may have rotated into their current orientation during the development of the lineation.

The extent of pillow flattening, as measured by length-to-width aspect ratios of individual pillows, is variable (Fig. 2.10). Pillow morphology in two-dimensions, perpendicular to the S_2 foliation, varies from nearly equant to moderately elongated (4:1) to strongly elongated and ribbon-like (up to 50:1). The relationship of apparent pillow flattening in outcrop to true three-dimensional strain is not known.

Figure 2.10: Variable pillow flattening at Sharrie Lake as shown by A) an intermediate pillow (pits from weathered-out amygdules), and by B) mafic pillows with isolated felsite cores (pillow outlined in black).

The volcanic and volcaniclastic rocks, and overlying Burwash Formation sedimentary rocks, at Sharrie Lake have undergone greenschist to lower amphibolite facies regional metamorphism (Lambert, 1988; Jackson & Ootes, 2012). The transition from greenschist to amphibolite facies is indicated by the cordierite-in isograd in the Burwash Formation and the hornblende-in isograd in the volcanic rocks (Fig. 2.11) (Lambert, 1988). A discussion of metamorphic mineral assemblages and P-T estimates is presented in section 3.5.
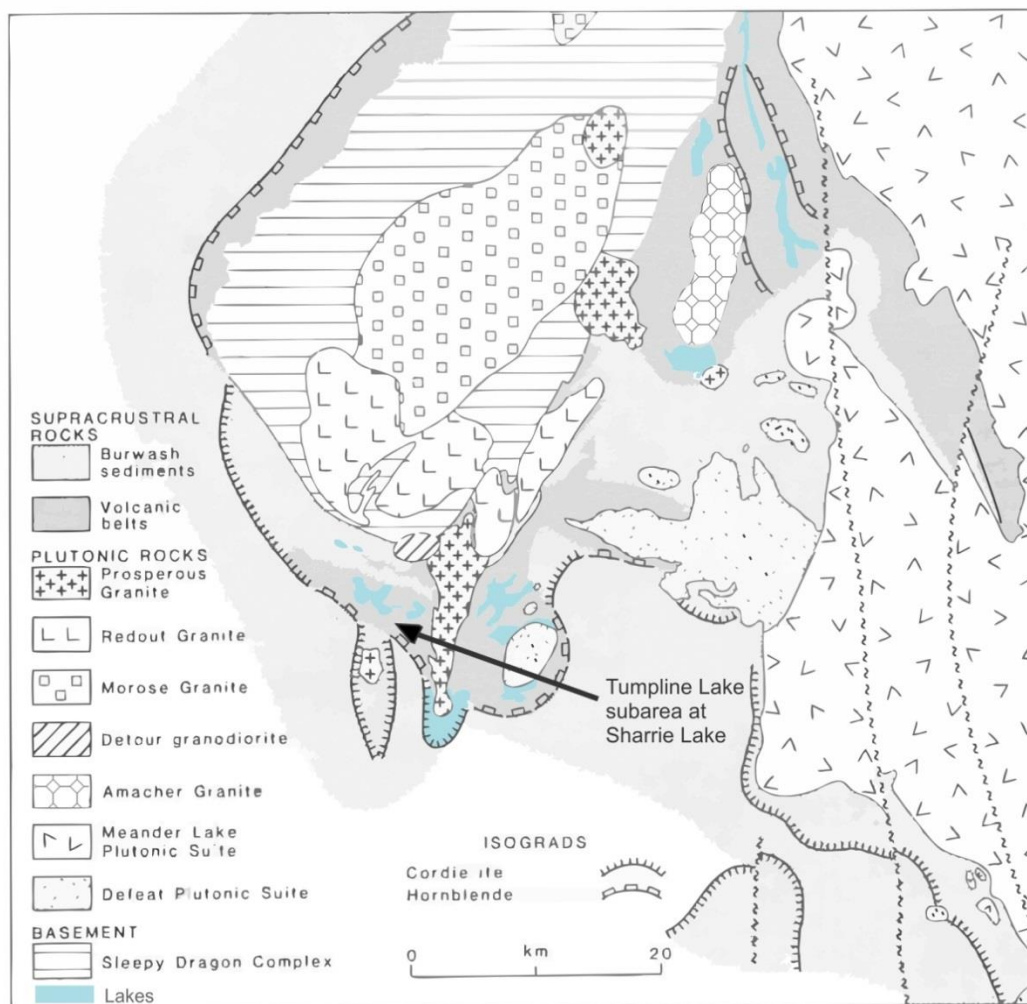
Figure 2.11: Distribution of basement, granitic plutons, supracrustal rocks, and cordierite-in (sedimentary rocks) and hornblende-in (volcanic rocks) isograds, defining the onset of amphibolite facies metamorphism near the CBVB. Symbols are on the high T side of the isograds. Modified after Lambert, 1988.

CHAPTER 3: Petrography, Mineral Chemistry and Metamorphic P-T Conditions

3.1 Methods

3.1.1 Sample collection and preparation

Sample collection was conducted with the support of the Northwest Territories Geoscience Office (NTGO) Banting-VMS project during bedrock mapping at Sharrie Lake in June 2013. For this study, samples of pillow lavas were collected from a variety of flows at Sharrie Lake (see Fig. 1.3 for map of sample locations and Appendix A for GPS coordinates). Pillow core material was the primary sampling target, although some selvage material was also collected for textural and mineralogical comparison. Sample locations were recorded along with outcrop data, structural measurements (where applicable), and photograph locations using GPS and ArcView Software on a Pocket PC.

Samples were slabbed for thin sections and geochemistry in Yellowknife at the NTGO. Samples Maf6a-A and Int2-A were slabbed in Halifax at Dalhousie University. Geochemical samples included only pillow core material; all selvage material was removed prior to crushing. Samples were crushed at the Crystal Isolation Laboratory at Dalhousie University and at Acme Analytical Laboratories in Vancouver, B.C (see Appendix A for details).

3.1.2 Petrography and electron microprobe analysis

Standard thin sections and polished sections were prepared by Gordon Brown at the Dalhousie University Thin-section laboratory. A petrographic analysis was completed to document primary and secondary micro-scale features, to constrain the timing of peak mineral assemblages, to compare the mineralogy and texture of mafic and intermediate pillows, to document mineralogical controls on geochemistry, and to identify mineral assemblages suitable

for P-T work. This was completed at Dalhousie University using a Nikon 50*i* transmitted light microscope. Photomicrographs were captured using a Nikon Eclipse camera (50*i* Pol, LV-UEP1). Petrographic data are organized based on mapped lithologies, and results are presented for both pillow cores and selvages (where applicable).

The JEOL 8200 Superprobe electron microprobe (EMP) in the Robert M. MacKay Electron Microprobe Laboratory at Dalhousie University was used to obtain mineral compositions for mineral identification and thermobarometry. Analyses were obtained from garnet, amphibole, carbonate, plagioclase, epidote and opaque minerals. Back-scattered electron images of analysis points, a description of the EMP analytical parameters, and a complete table of mineral analyses are presented in Appendix B.

3.2 Mineralogy and mineral chemistry

3.2.1 Mafic pillow lavas

The mineral assemblage present in mafic pillow lavas consists of plagioclase, quartz, amphibole, carbonate, ilmenite, titanite, epidote, biotite, chlorite, and sericite. Primary mafic minerals such as pyroxene have been entirely replaced and/or overprinted by the secondary and metamorphic assemblages. The matrix in the pillow core consists of a microcrystalline aggregate of near-granoblastic feldspar and quartz. Grain size ranges from <0.05 to 0.3 mm, most commonly ~0.1 mm. Irregular, typically elongate patches of coarser grained (0.1-0.3 mm) matrix quartz and feldspar are common. In some samples, matrix plagioclase is weakly to strongly sericitized. Sparse to common (5-15%) relict plagioclase phenocrysts average 1 mm in length, although the length can range from 0.5 - 2 mm. Laths are subhedral to anhedral, commonly embayed, and display sieve texture with common inclusions of fine-grained amphibole, biotite,

and matrix plagioclase and quartz. The plagioclase phenocrysts are weakly to strongly sericitized, and in rare cases are glomeroporphyric. Laths are typically randomly oriented. Plagioclase composition, based on Ca/[Ca+Na+K], ranges from An_{31-41} (andesine).

Amphibole is the most abundant porphyroblast in the mafic samples. Amphibole is anhedral to subhedral, embayed, poikiloblastic, and ranges from blocky to prismatic to acicular. Some blocky crystals have feathery edges and form patchy aggregates. Grain size ranges from 0.05 to 0.5 mm and rarely up to 1.5 mm. Amphibole porphyroblasts contain abundant fine-grained inclusions of matrix plagioclase, quartz, and oxides. Amphibole composition is variable among mafic samples and includes pale green actinolite, yellow-green to green actinolitic hornblende, and green to blue-green hornblende. Representative amphibole compositions from mafic sample Maf6a-A are shown in Table 3.1. Biotite forms anhedral grains, locally up to 0.4 mm long although most commonly 0.1 mm in length. In mafic pillow cores biotite is typically found in irregular patches, locally proximal to veins. No analyses of biotite in mafic samples were obtained. Both biotite and amphibole are partially replaced by chlorite in some samples.

Epidote forms fine-grained (~0.1 mm) anhedral, typically rounded grains and rarely forms fine-grained (<0.1 mm) acicular grains in the matrix of some mafic samples. Grain size ranges from 0.05-0.5 mm. In mafic samples, epidote is sparse and resides in the pillow core and matrix. Epidote Fe^{3+} /[Fe^{3+} + Al] ratios, range from 0.11 to 0.20.

Secondary quartz and carbonate are common in all samples. Both are matrix constituents, and form vein- and vesicle-filling phases. Quartz-filled vesicles typically contain anhedral grains ranging in size from 0.2 to 1 mm, and may be poly- or monocrystalline. Grain boundaries vary from near-granoblastic to irregular. Quartz veins are thin (<0.1 mm wide), filled with fine-grained (<0.05-0.1 mm) granoblastic quartz, and typically cross-cut any fabrics present.

Carbonate content and distribution are variable between samples. Carbonate forms sparse to abundant disseminated anhedral grains 0.1-0.3 mm in diameter and irregular elongated patches of anhedral grains, and fills well defined ovoid to elongate vesicles. Carbonate-filled vesicles may be poly-or monocrystalline, with grain size ranging from 0.1 mm to 7 mm. In the mafic sample analysed by EMP, calcite was the only carbonate mineral present.

Sericite is a sparse microcrystalline alteration product of relict plagioclase phenocrysts and the plagioclase-rich matrix. Sericite is also found in rare thin (<0.05 mm) veins cross-cutting fabrics and amygdules. Chlorite is rare to sparse in both mafic and intermediate samples, and commonly forms pseudomorphs partially replacing biotite and/or amphibole. Chlorite also forms rare coarse-grained crystals within carbonate-quartz amygdules and rare fine-grained crystals within the matrix. Chlorite is typically anhedral, fine-grained (~0.2-0.3 mm) and can display sieve texture with abundant matrix inclusions. Based on the few analyses completed, chlorite compositions in mafic samples have an average Mg/[Mg+Fe] ratio of ~0.48.

Titanite is a sparse to common accessory mineral in the mafic samples. It forms elongate aggregates of anhedral, very fine-grained (<<0.05 mm) crystals, and in some samples defines a weak foliation. Ilmenite is the most common oxide present and is commonly found as disseminated anhedral grains <0.1 mm in size. Grains can be rounded, elongated parallel to the foliation, or in elongate aggregates parallel to the foliation. Rare veins are lined with, or contain coarser grained, ilmenite. In some cases ilmenite is coarser in pillow selvages than in the pillow core, and coarsens near carbonate veins. Ilmenite is locally partially replaced by fine-grained aggregates of titanite.

Based on the current mineralogy characterized by variable proportions of relict plagioclase phenocrysts, quartz + feldspar matrix, amphibole, carbonate, ilmenite, titanite,

epidote, biotite, chlorite, and sericite, the primary igneous assemblage in the mafic pillows is interpreted to have included plagioclase phenocrysts, clinopyroxene, oxides, and volcanic glass.

3.2.2 Intermediate pillow lavas

Intermediate pillow lavas are characterised by the assemblage plagioclase, quartz, amphibole, biotite, carbonate, ilmenite, garnet, chlorite, titanite, epidote, sericite, and apatite. The mineralogy of intermediate pillow lavas is similar to that of the mafic pillow lavas, with variations in mineral composition and abundance. For example, plagioclase composition in intermediate samples is slightly more sodic than in mafic samples (An_{22-30} vs An_{31-41}). Carbonate composition also differs in the intermediate pillows, and includes calcite and minor ankerite based on EMP analyses. Epidote is less abundant (rare to sparse) in intermediate samples than in mafic samples, and is found in the matrix, near or within veins, and in the pillow selvage. Chlorite forms sparse partial pseudomorphs of amphibole and biotite in some intermediate pillow lavas. Chlorite is also common in pillow selvages (Fig. 3.4). Based on the few analyses completed, chlorite composition in intermediate samples is more Fe-rich than in mafic samples (Mg/(Mg+Fe) ratio ~0.24 vs ~0.48). Apatite is rare in intermediate samples, and forms fine-grained (<0.05 mm) inclusions in garnet and coarser grained (~0.2 mm) crystals near carbonate veins.

Biotite content in intermediate pillows is highly variable, but is generally higher than in mafic samples. Biotite is anhedral to subhedral, ranges in size from <0.1 to 0.3 mm, and is typically more abundant and larger in the pillow selvage than in the core. Biotite is Fe-rich and ranges from $Phl_{0.24-0.29}$. Amphibole content is variable among intermediate samples and ranges from sparse to abundant. In general, amphibole is less abundant than in mafic pillow lavas, and

where present, is often more abundant in and near the selvage than in the core. Amphibole forms anhedral to subhedral, blocky to acicular grains 0.5-1 mm in size. Amphibole is commonly embayed and poikiloblastic, and in some samples, feathery anhedral crystals form aggregates 1-6 mm in length. Amphibole composition in intermediate pillows is variable and includes rare pale green actinolite, yellow-green to green actinolitic hornblende, and most commonly green to blue-green hornblende. An analysis from an amphibole in intermediate sample Int1-E is compared to mafic amphiboles in Table 3.1.

Garnet is found exclusively in intermediate pillows. It is sparse to common in the pillow selvage and rare to sparse in the pillow core. Garnet is anhedral to subhedral and ranges in size from 0.2-6 mm. Average garnet size is ~1.5 mm. Smaller garnets (<0.3 mm) are closer to euhedral. Garnet is poikiloblastic and contains abundant fine-grained inclusions of apatite, ilmenite, titanite, and matrix plagioclase and quartz. Garnet composition is variable, although all garnets analysed in two intermediate samples are notably Mg-poor and Fe-rich. Garnets display growth zoning with Mn-rich cores and Ca-rich rims (Fig 3.1). A slight increase in Mn at the rim (Fig. 3.1), possibly indicating retrograde cation exchange with the matrix, was documented on one side of the garnet. Sample garnet analyses from the core and rim are given in Table 3.2.

Based on the current mineralogy characterized by variable proportions of relict plagioclase phenocrysts, quartz + feldspar matrix, amphibole, biotite, carbonate, ilmenite, garnet, chlorite, titanite, epidote, sericite, and apatite, the primary igneous assemblage in intermediate pillows is interpreted to have included plagioclase phenocrysts, clinopyroxene, oxides, possibly minor amphibole, and volcanic glass.

Table 3.1: Selected analyses of amphiboles in mafic pillow Maf6a-A (mafic rim and altered core) and intermediate pillow Int1-B. FeO is Fe_{total} (Fe^{3+} not calculated). Cations pfu = cations per formula unit, here calculated based on 23 oxygens.

Sample	Maf6a-A (mafic rim)	Maf6a-A (altered core)	Int1-B
Mineral	Hbl	Act	Hbl
Analysis #:	16	100	204
Wt % oxides			
SiO_2	44.18	54.38	42.88
Al_2O_3	12.26	4.96	12.20
Cr_2O_3	0.07	0.00	0.00
TiO_2	0.55	0.00	0.48
FeO	17.81	15.71	23.87
MnO	0.46	0.20	0.50
MgO	8.73	9.72	4.65
CaO	11.85	10.38	11.07
Na_2O	1.26	0.40	1.19
K_2O	0.36	0.12	0.41
TOTAL	97.51	95.88	97.25
Cations pfu	(based on 23 O)		
Si	6.626	7.970	6.636
Al_{IV}	1.374	0.031	1.365
Al_{VI}	0.793	0.827	0.860
Ti	0.062	0.000	0.055
Fe	2.233	1.925	3.089
Mn	0.058	0.025	0.064
Mg	1.950	2.125	1.074
Ca	1.904	1.631	1.835
Na	0.366	0.115	0.357
K	0.069	0.023	0.081
Cr	0.007	0.000	0.000
TOTAL	15.445	14.674	15.415
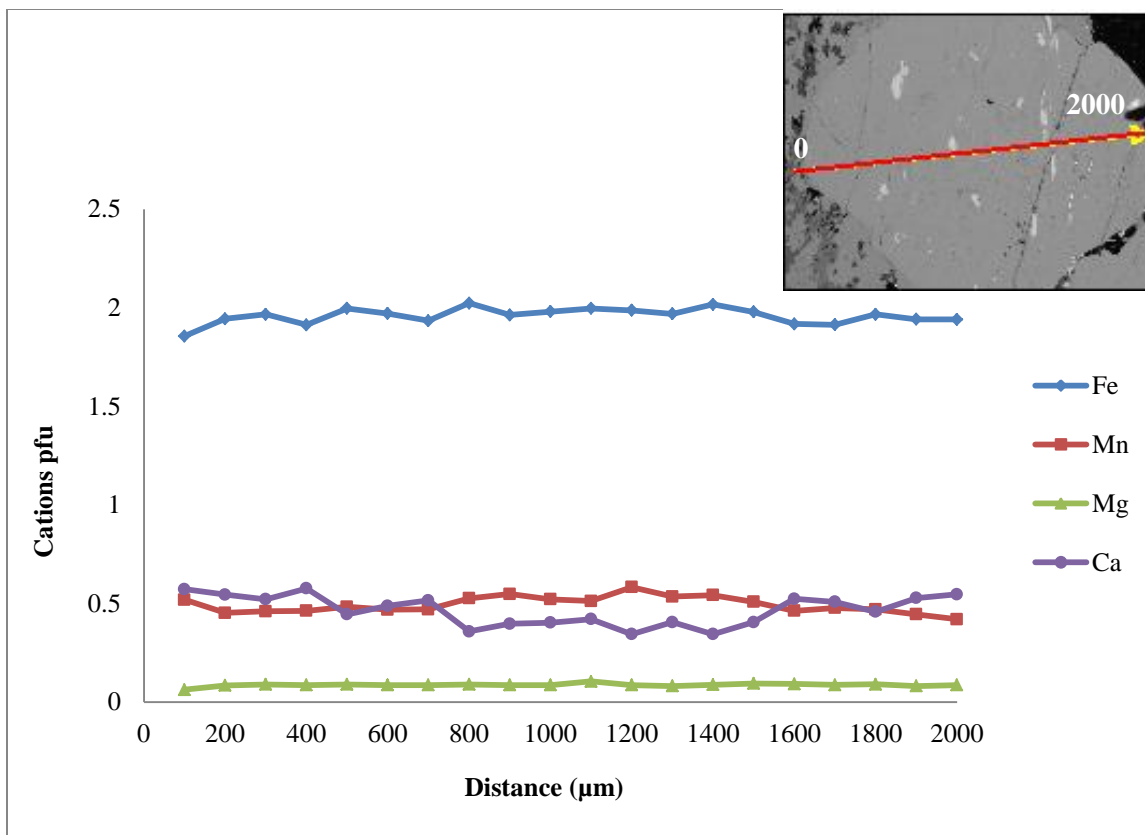
Figure 3.1: Garnet zoning profile (Fe, Mn, Mg, and Ca per formula unit, based on 12 oxygens, with $Fe^{2+} = Fe_{total}$) for the line traverse across Garnet 1 of sample Int1-B. Note the low Mg content, the reciprocal zoning in Ca and Mn, and the slight increase in Mn at the rim. Analyses taken ~100 μm along the line shown in the BSE image.

3.3 Deformation and distinct mineralogical domains

3.3.1 Evidence of heterogeneous strain

Heterogeneous strain is evident from a variably developed foliation defined by amphibole

and biotite, and locally by oxides and titanite. Amphibole and biotite in both mafic and

intermediate pillows can form porphyroblasts statically overgrowing the matrix or with a strong

preferred orientation (Fig. 3.2). Amygdules range from near circular in 2D to strongly elongate,

and locally display sigma-type morphologies (Fig. 3.3). This micro scale evidence of variable

strain is not surprising given the heterogeneous strain in pillows at outcrop scale (Fig. 2.10).
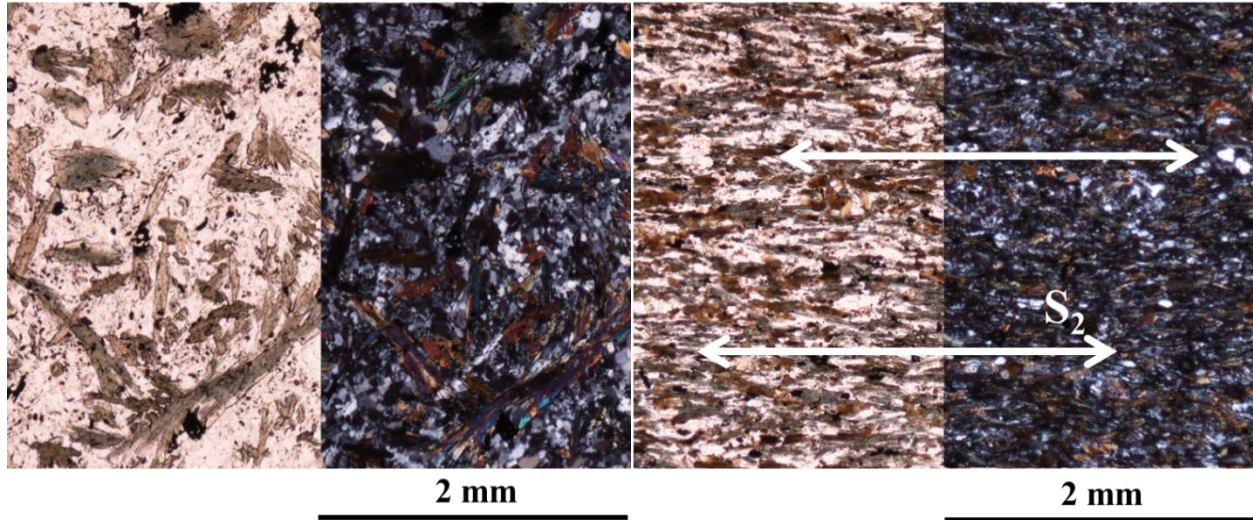
Figure 3.2: Heterogeneous strain illustrated by a variably developed foliation. Poikiloblastic randomly-oriented amphibole in Maf2a-A (left, PPL and XPL), and a well-developed foliation defined by amphibole and biotite in Maf3a-A (right, PPL and XPL). Both photomicrographs taken in mafic pillow cores. White arrows indicate orientation of foliation.
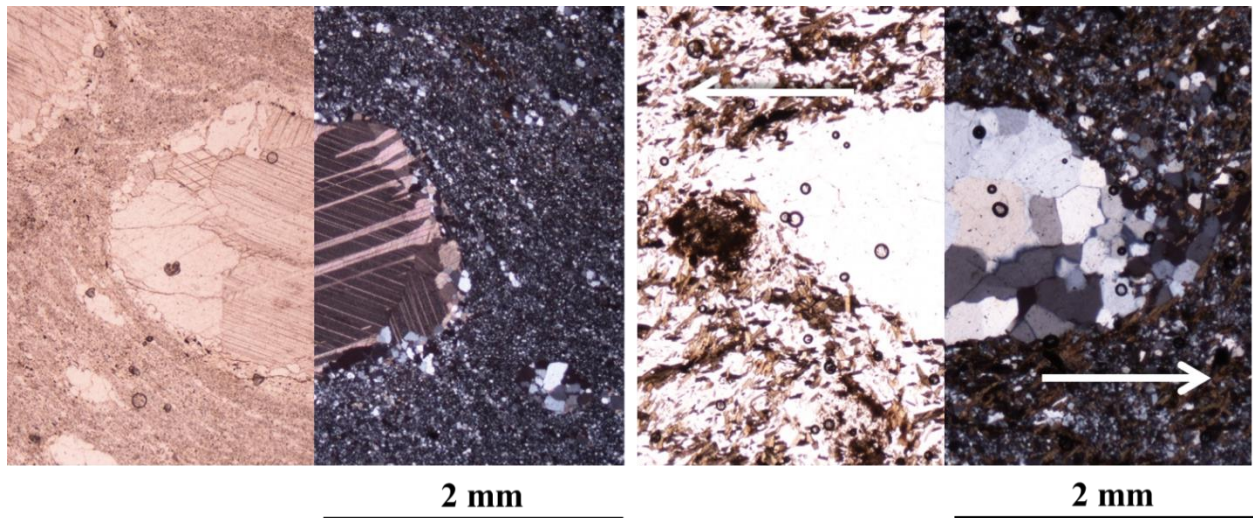
Figure 3.3: Heterogeneous strain illustrated by variable amygdule morphology. Rounded, equant calcite and quartz-filled amygdule in Int1-E (left, PPL and XPL). Sigma-type deformed quartz amygdule in Int1-A (right, PPL and XPL). Arrows indicate relative sense of shear. Unoriented samples.

3.3.2 Selvage vs core mineralogy

In intermediate pillows, pillow selvages are commonly biotite-amphibole±garnet-rich,

and cores consist primarily of matrix plagioclase and quartz, sparse amphibole and biotite, rare

garnet, and common amygdules (Fig. 3.4). The regional foliation, where present, is subtle in the

core and well developed in the selvage owing to the abundant biotite and amphibole in the latter.

Intermediate sample Int2-A (Fig. 3.4) contains a pillow selvage lined with pale green to green

actinolitic hornblende and serves as a prime example of selvage mineralogy. Within the selvage

is an aggregate of anhedral, randomly oriented biotite, chlorite, epidote, white mica, opaque

minerals, minor blue-green hornblende, and minor carbonate. Some chlorite is partially replacing

biotite, and both contain radiation-induced pleochroic halos surrounding microcrystalline

radioactive inclusions. Hornblende in the pillow selvage is weakly foliated. The selvage in

sample Int2-A completely lacks matrix plagioclase and quartz.

3.3.3 Altered pillow core mineralogy

Mafic pillow sample Maf6a-A was selected based on its bleached pillow core (Fig. 3.5)

to test a previous interpretation of this core material proposed by Lambert (1988). Lambert

suggested that some of the pale pillow cores were trapped blocks of felsic volcanic rock within

the mafic pillows. Two thin sections were made of the "primary" mafic pillow rim and the

altered pillow core to test this interpretation. The mafic rim comprises randomly oriented

hornblende, relict plagioclase phenocrysts (An_{31-41}), ilmenite, and rare chlorite. The altered core

displays a similar overall texture (Fig. 3.5). However, in the outer core, plagioclase phenocrysts

have been replaced by quartz aggregates, and any primary mafic phases have been replaced by

epidote-carbonate aggregates. The sparse amphibole present is actinolite rather than hornblende,
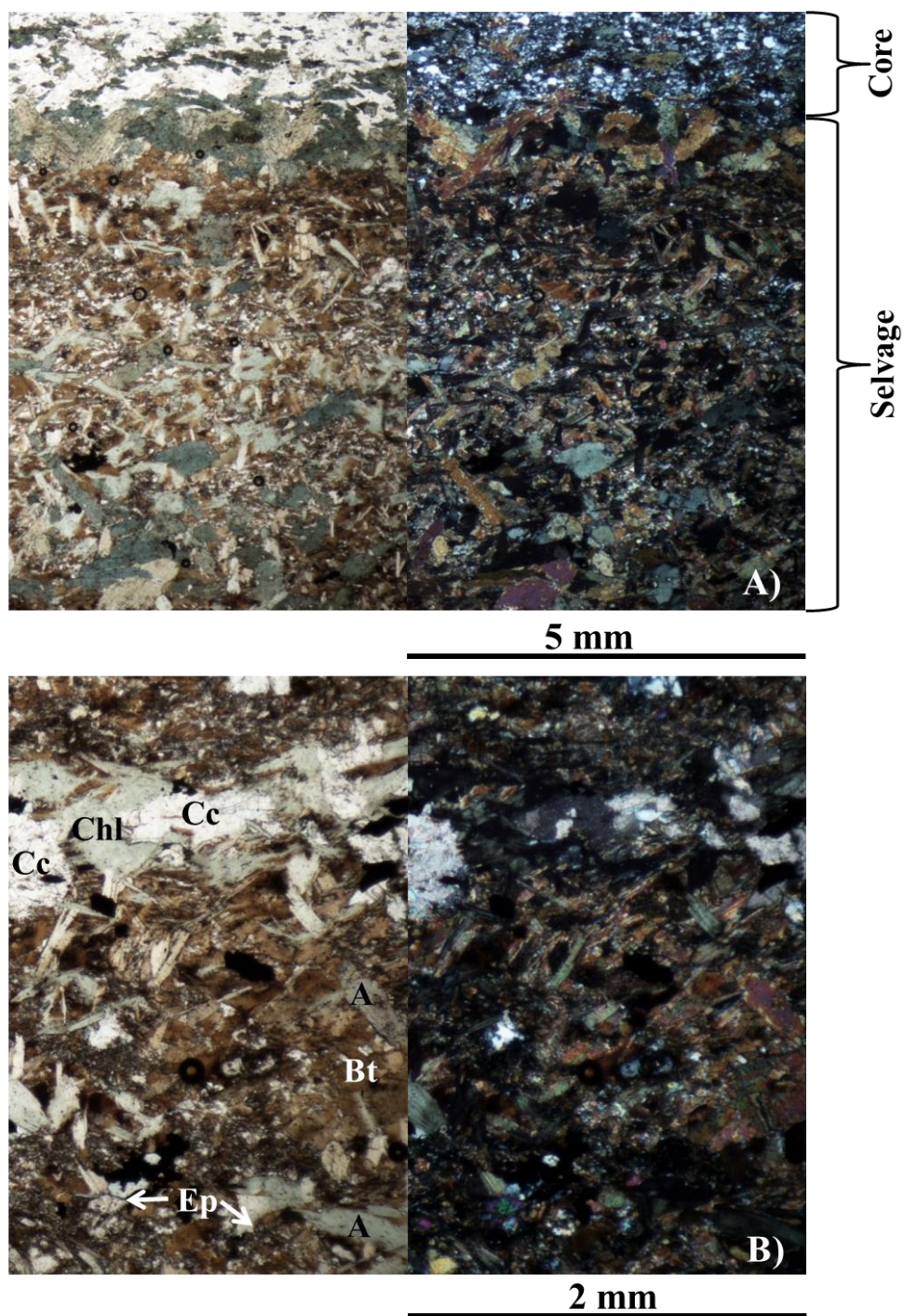
Figure 3.4: Pillow selvage and core (A) in sample Int2-A illustrating the mineralogical and textural differences between the two. A closer look at the selvage (B) shows the mineral assemblage of biotite (Bt), amphibole (A), chlorite (Chl), carbonate (Cc), and epidote (Ep). White mica and oxides are also present.
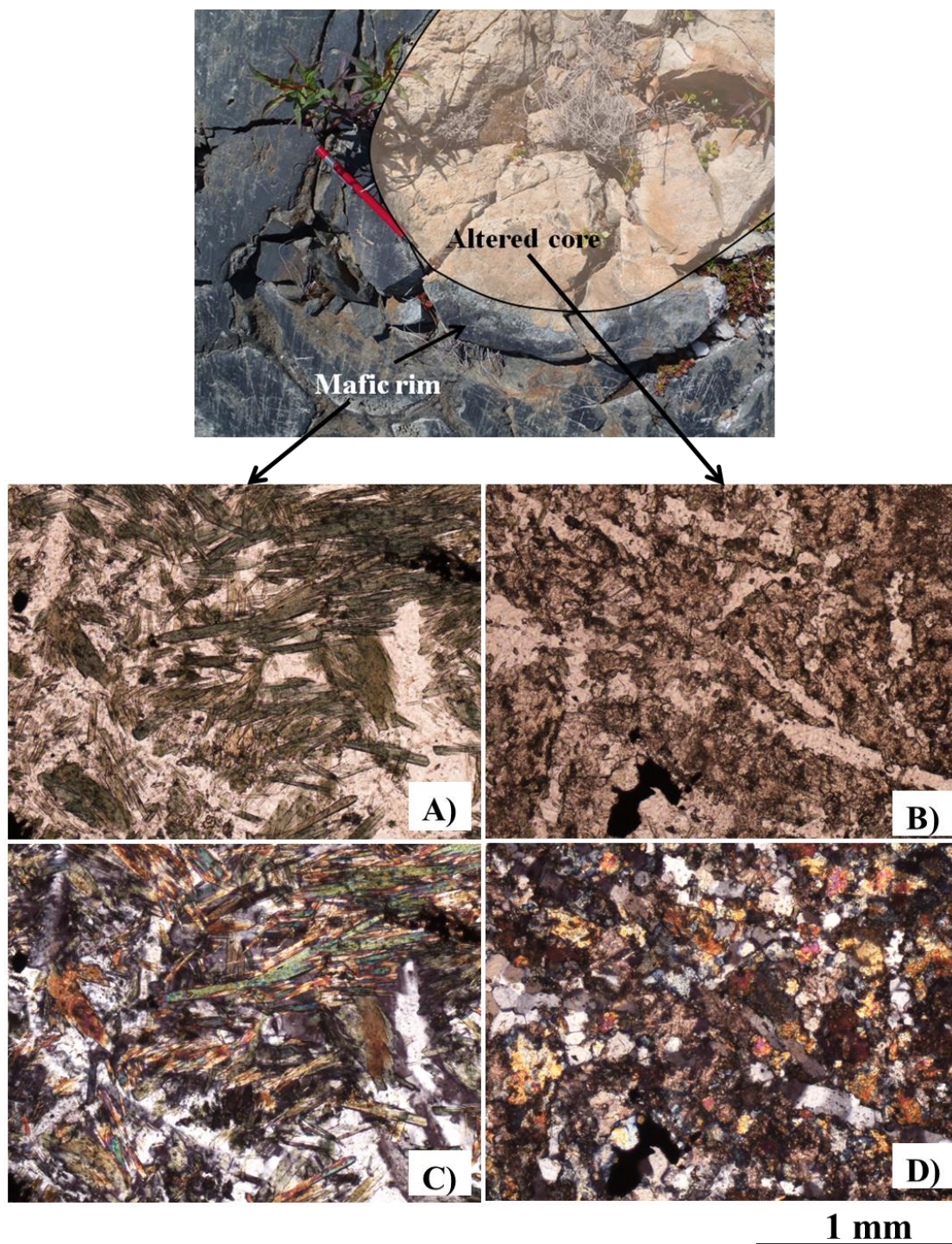
Figure 3.5: Pale core in a mafic pillow lava (sample Maf6a-A), previously interpreted as trapped felsic volcanic material (Lambert, 1988). Photomicrographs taken from the mafic rim (A) in PPL, and (C) in XPL, and altered core (B) in PPL, and (D) in XPL, display similar textures and significantly different mineralogy. Relict plagioclase phenocrysts and primary mafic minerals have been completely replaced by quartz and epidote-calcite aggregates in the pillow core (B and D).

indicating that actinolite is the stable amphibole in the Ca-rich altered core. Ilmenite is present throughout the sample. All primary mafic mineralogy has been replaced in the inner pillow core, which now consists of calcite, sponge-like epidote with abundant quartz inclusions, quartz aggregates, ilmenite, sparse chlorite, and rare pyrrhotite (Fig. 3.5). The core mineralogy and the textural similarities between the mafic rim and altered core demonstrate that the pale cores are likely secondary, alteration-related, features rather than felsic volcanic xenoliths.

3.4 Relative timing of mineral formation

The relative timing of mineral phases present in the mafic and intermediate pillow lavas can be grouped into four categories: relict primary, early secondary, metamorphic (see section 3.5.1), and "ambiguous". The relict primary minerals include plagioclase phenocrysts and the feldspar-quartz matrix. Although the crystal textures are primary, plagioclase composition likely reflects the metamorphic overprint, as the compositional range oligoclase to andesine is too sodic for primary plagioclase in mafic to intermediate volcanic rocks, and is more typical of upper greenschist to lower amphibolite facies metamorphism. Matrix fine- to medium-grained epidote is considered an early secondary phase, possibly a by-product of plagioclase alteration, although it may also be metamorphic in origin. If the epidote present was an early secondary phase, its composition was most likely modified during metamorphism. The presence of secondary quartz and carbonate mainly as void-filling phases indicates that they are probably early secondary phases. Furthermore, as the quartz and/or carbonate amygdules are deformed and deformation predated, or was roughly synchronous with, metamorphism, it is clear that the amygdules must also predate both deformation and metamorphism.

The relative timing of ilmenite, titanite, sericite, and chlorite is ambiguous. Ilmenite forms common inclusions in amphibole and garnet, in some cases defines a weak foliation, and is locally partially replaced by titanite. Ilmenite may therefore be a primary or early secondary phase, whereas titanite may be an early secondary phase replacing ilmenite. Rare pyrrhotite and pyrite is found in the altered core of a mafic pillow (Maf6a-A) and in an altered intermediate pillow (Int1-E). They form anhedral grains that range in size from 0.02 to 0.1 mm. Based on their apparent restriction to altered domains, pyrrhotite and pyrite may also be early secondary phases. Sericite and chlorite are also ambiguous in their timing of formation, but are likely late alteration phases replacing earlier minerals. Early sericite and chlorite were likely replaced by biotite and amphibole during lower amphibolite facies metamorphism. Some chlorite, however, may be related to early secondary processes, such as the rare chlorite found within quartz-carbonate amygdules and as a separate phase in the matrix.

3.5 Metamorphism

3.5.1 Metamorphic mineral assemblages and relative timing of metamorphism

The metamorphic mineral assemblage in mafic pillow lavas consists of sodic plagioclase, quartz, amphibole, carbonate, titanite, epidote, and minor biotite and chlorite. In intermediate pillow lavas, the peak metamorphic mineral assemblage is sodic plagioclase, quartz, amphibole, biotite, carbonate, garnet, titanite, and minor chlorite and epidote. These mineral assemblages correspond to a lower amphibolite facies metabasite. The peak thermal assemblage is syn- to post-kinematic with respect to the variably developed foliation. This is shown by syn- to post-kinematic amphibole in both mafic and intermediate samples (Fig. 3.2), and post-kinematic

garnet in intermediate samples. The latter is evident from inclusions in garnet that form an internal fabric (S_i) concordant and continuous with the matrix foliation (S_e) (Fig. 3.7).

3.5.2 Metamorphic P-T conditions

Intermediate pillow sample Int1-B was selected for use in thermobarometric calculations based on its peak metamorphic sodic plagioclase-quartz-amphibole-biotite-garnet mineral assemblage. Using mineral composition data collected by EMP, the garnet-biotite thermometer (Spear, 1993), two garnet-hornblende thermometers (Graham & Powell, 1984; Krogh Ravna, 2000), and the garnet-hornblende-plagioclase-quartz barometer (Kohn & Spear, 1990) were applied to calculate P-T conditions of metamorphism. Data points were selected in order to minimize the effects of late-stage cation exchange between garnet rims and adjacent matrix phases (See Figs. 3.6-3.9 for points used in P-T estimates. See Appendix B for all points analysed and for complete set of EMP data). Data points from mineral rims were also used for comparison with mineral core data.

Two analyses, one rim and one core, were selected for hornblende, biotite, plagioclase, garnet, and quartz in intermediate sample Int1-B to be used in thermobarometric calculations. The analyses are presented below in Table 3.2, and were all taken in Zone 1 (as shown in Figure 3.6), with the exception of the garnet (labeled as Grt 1 in Figure 3.6). The results of the garnet-biotite and both garnet-hornblende thermometers (Table 3.3) agree reasonably well and indicate a temperature of 500±25 ºC. Pressure estimates for the sample are more variable (Table 3.4). The range of pressures calculated is 2.5 to 6.7 kb, beyond the nominal analytical uncertainty of ± 1 kb. The pressures calculated for the Mg end-members are lower, ranging from 2.5 to 3.9 ±1 kb, compared those for the Fe end-members, which range from 4.8 to 6.7 ±1 kb. The first cordierite-

in isograd, within the andalusite stability field, in the Burwash Formation turbidites overlying the volcanic rocks limits the maximum pressure to ~4.0 kb and therefore the Fe end-member pressures are unreliable. The discrepancy between the pressures calculated for the Fe and the Mg end members may be attributed to the notably low Mg-content of the garnet in this sample, and an average pressure of ca. 4.0 ± 2 kb has been assumed for purposes of interpretation.

Figure 3.6: Scanned polished section of Int1-B showing the zones where analyses were conducted. Back-scattered electron images of the zones are shown in Figure 3.7 (Grt 1), Figure 3.8 (Zone 1), and Figure 3.9 (Bt 5). Analyses from Zone 2 were not used in P-T calculations. Note that the term "zone" as applied here refers to an area where points of analysis were selected and not to specific textural and/or mineralogical domains.
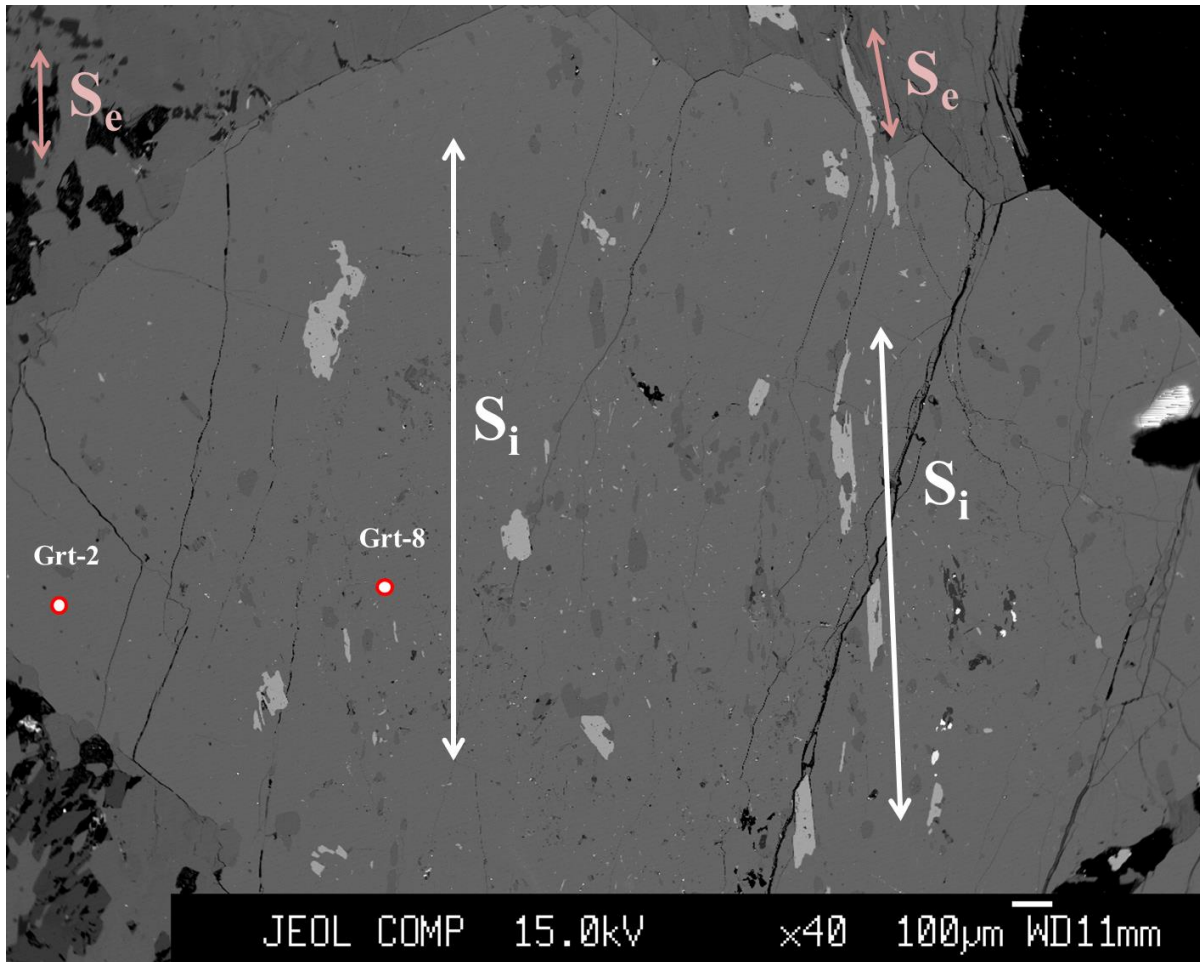
Figure 3.7: The BSE image shows abundant inclusions of apatite, ilmenite, and titanite in Grt 1 from sample Int1-B. Post-kinematic garnet growth shown by inclusion trails within Grt 1 (S_i) that are concordant with the external foliation (S_e). Also showing the point locations for garnet analyses Grt-2 (rim) and Grt-8 (core).
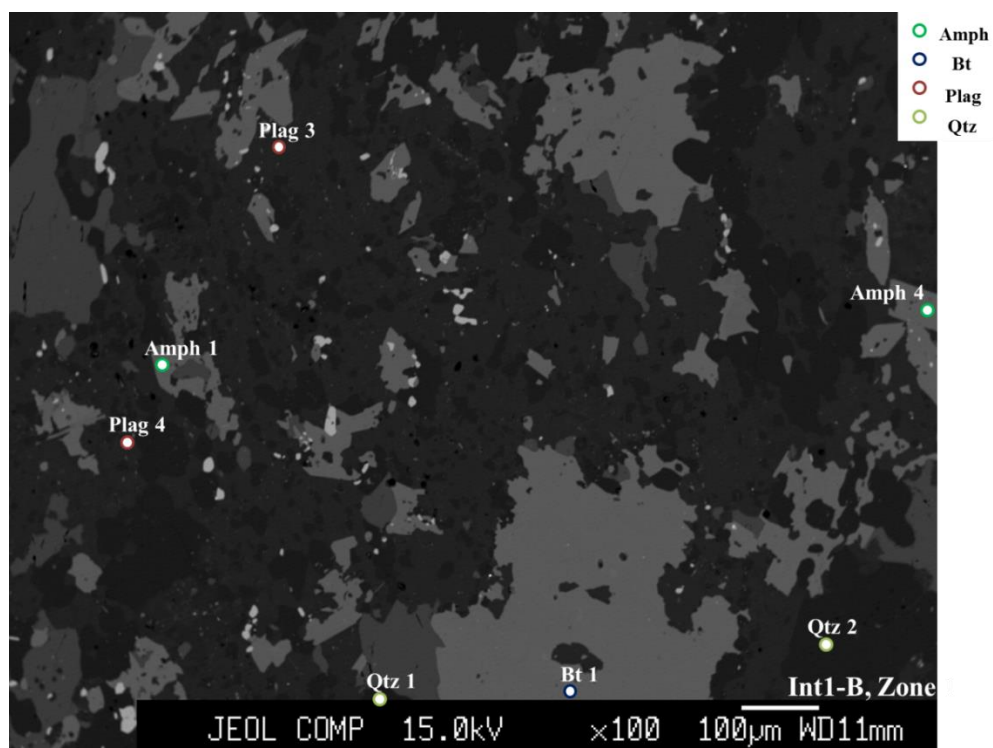
Figure 3.8: BSE image taken of Zone 1 (see Fig. 3.6) showing the point locations for analyses Amph 1 (rim) and Amph 4 (core), Bt 1 (core), Plag 3 (rim), Plag 4 (core), Qtz 1 (rim), and Qtz 2 (core).
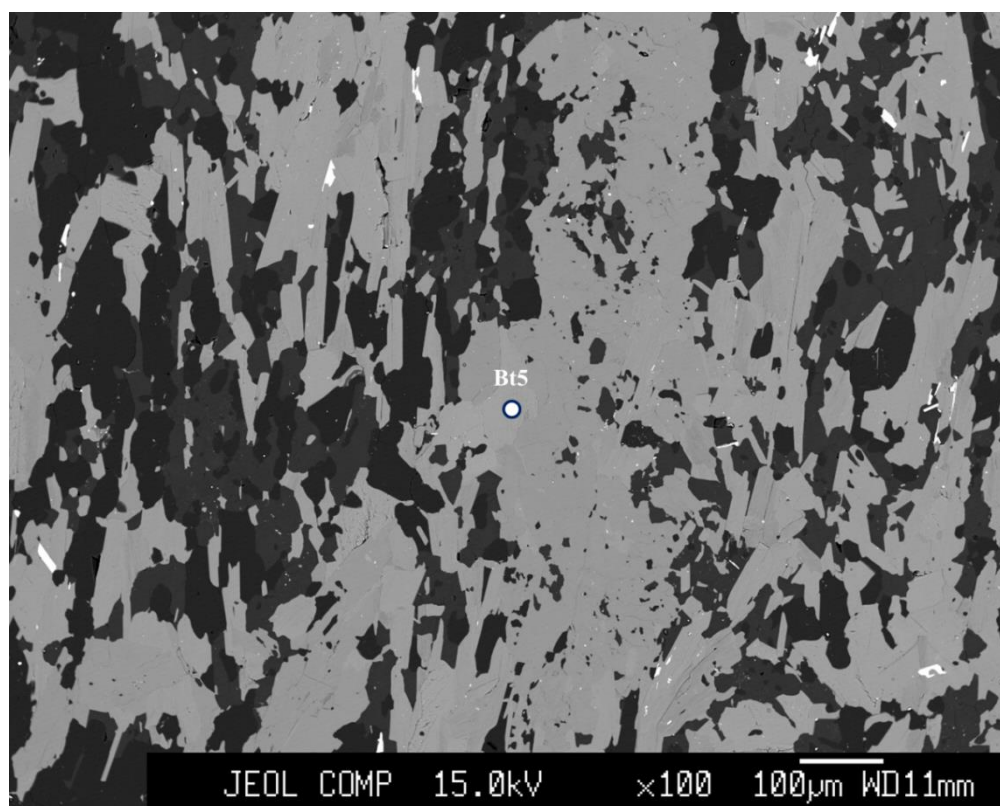
Figure 3.9: BSE image taken at Bt 5 (see Fig. 3.6) showing the point location for biotite analysis Bt 5 (rim).

Table 3.2: Analyses selected for thermobarometric calculations. (Bt = biotite, Grt = garnet, Amph = amphibole, Plag = plagioclase, and Qtz = quartz). Number of oxygens used to calculate cations per formula unit (pfu) are given in brackets for each mineral, e.g. 22 O = 22 oxygens used to calculate cations pfu in biotite. Core analyses indicated by *.

	Bt-1*	Bt-5	Grt-8*	Grt-2	Amph-4*	Amph-1	Plag-4*	Plag-3	Qtz-2*	Qtz-1
	146	174	121	115	157	154	167	166	161	160
Wt % oxides										
SiO_2	34.87	35.06	36.51	36.65	40.84	40.63	61.54	61.42	100.32	100.74
Al_2O_3	16.42	16.30	20.86	20.60	14.41	14.62	24.52	24.44	0.00	0.00
TiO_2	2.21	2.44	0.08	0.17	0.50	0.52	0.00	0.00	0.00	0.00
FeO	28.65	27.53	29.61	28.53	24.86	24.93	0.01	0.14	0.00	0.00
MnO	0.16	0.19	7.62	6.56	0.38	0.34	0.00	0.00	0.00	0.00
MgO	5.01	5.30	0.74	0.70	3.68	3.41	0.00	0.00	0.00	0.00
CaO	0.00	0.04	4.10	6.24	11.30	11.31	5.99	6.24	0.00	0.00
Na_2O	0.10	0.13	0.00	0.01	1.36	1.31	8.39	8.27	0.00	0.00
K_2O	9.38	9.40	0.05	0.04	0.66	0.88	0.04	0.07	0.00	0.00
Cr_2O_3	0.00	0.00	0.10	0.09	0.00	0.00	0.00	0.00	0.00	0.00
TOTAL	96.80	96.39	99.67	99.59	97.98	97.95	100.49	100.58	100.32	100.74
Cations pfu	(22 O)	(22 O)	(12 O)	(12 O)	(23 O)	(23 O)	(8 O)	(8 O)	(2 O)	(2 O)
Si	5.489	5.513	2.983	2.987	6.332	6.311	2.720	2.716	1.000	1.000
Al	3.047	3.023	2.009	1.979	2.634	2.677	1.278	1.274	0.000	0.000
Ti	0.262	0.288	0.005	0.010	0.058	0.062	0.000	0.000	0.000	0.000
Fe	3.771	3.621	2.023	1.944	3.225	3.238	0.000	0.005	0.000	0.000
Mn	0.022	0.026	0.527	0.452	0.051	0.046	0.000	0.000	0.000	0.000
Mg	1.175	1.243	0.090	0.085	0.849	0.789	0.000	0.000	0.000	0.000
Ca	0.000	0.007	0.359	0.545	1.877	1.881	0.284	0.296	0.000	0.000
Na	0.031	0.040	0.000	0.001	0.409	0.396	0.718	0.710	0.000	0.000
K	1.885	1.888	0.005	0.005	0.131	0.175	0.002	0.004	0.000	0.000
Cr	0.000	0.000	0.006	0.006	0.000	0.000	0.000	0.000	0.000	0.000
TOTAL	15.684	15.651	8.006	8.015	15.566	15.578	5.002	5.004	1.000	1.000

Table 3.3: Results of the garnet-biotite (Spear, 1993), garnet-hornblende (Krogh Ravna, 2000), and garnet-hornblende (Graham & Powell, 1984) thermometers in degrees Kelvin (as calculated) and Celsius. Analysis name shortened for convenience. Nominal errors for these calculations are ±25 °C.

Method	Sample	T (K)	T (°C)
Grt-Bt	core (Bt-1,Grt-8)	780	510
Grt-Bt	rim (Bt-5,Grt-2)	750	480
Grt-Hbl (KR)	core (Grt-8,Amph-4)	740	470
Grt-Hbl (KR)	rim (Grt-2,Amph1)	760	490
Grt-Hbl (GP)	core (Grt-8,Amph-4)	780	510
Grt-Hbl (GP)	rim (Grt-2,Amph-1)	840	560

Table 3.4: Results of the garnet-plagioclase-hornblende-quartz barometer (Kohn & Spear, 1990). Results given for the (A) Mg and (B) Fe end members, and (C) an average of both. For the sake of convention, results given in °C and kb. Results calculated using the temperature result of each of the three thermometers. Nominal errors for these calculations are ± 1.0 kb.

A) Mg end member			
Thermometer Used	**Sample**	**T(°C)**	**P (kb)**
Grt-Bt	core (Grt-8,Amph-4,Plag-4)	510	2.5
Grt-Bt	rim (Grt-2,Amph-1,Plag-3)	480	3.9
Grt-Hbl (KR)	core (Grt-8,Amph-4,Plag-4)	470	2.6
Grt-Hbl (KR)	rim (Grt-2,Amph-1,Plag-3)	490	3.9
Grt-Hbl (GP)	core (Grt-8,Amph-4,Plag-4)	510	2.5
Grt-Hbl (GP)	rim (Grt-2,Amph-1,Plag-3)	560	3.8

B) Fe end member			
Thermometer Used	**Sample**	**T(°C)**	**P (kb)**
Grt-Bt	core (Grt-8,Amph-4,Plag-4)	510	5.1
Grt-Bt	rim (Grt-2,Amph-1,Plag-3)	480	6.1
Grt-Hbl (KR)	core (Grt-8,Amph-4,Plag-4)	470	4.9
Grt-Hbl (KR)	rim (Grt-2,Amph-1,Plag-3)	490	6.1
Grt-Hbl (GP)	core (Grt-8,Amph-4,Plag-4)	510	5.1
Grt-Hbl (GP)	rim (Grt-2,Amph-1,Plag-3)	560	6.7

C) Average			
Thermometer Used	**Sample**	**T(°C)**	**P (kb)**
Grt-Bt	core (Grt-8,Amph-4,Plag-4)	510	3.8
Grt-Bt	rim (Grt-2,Amph-1,Plag-3)	480	5.0
Grt-Hbl (KR)	core (Grt-8,Amph-4,Plag-4)	470	3.7
Grt-Hbl (KR)	rim (Grt-2,Amph-1,Plag-3)	490	5.0
Grt-Hbl (GP)	core (Grt-8,Amph-4,Plag-4)	510	3.8
Grt-Hbl (GP)	rim (Grt-2,Amph-1,Plag-3)	560	5.2

CHAPTER 4: Whole-rock geochemistry

4.1 Methods

Twenty-two samples were selected to be analysed for major, trace and rare earth elements at Acme Analytical Laboratories in Vancouver, B.C. Powdered samples were analysed for major oxides and LOI using x-ray fluorescence (XRF). Trace and rare earth elements were analysed by inductively coupled plasma mass spectrometry (ICP-MS). Samples underwent borate fusion in preparation for both XRF analyses and ICP-MS analyses of rare earth and refractory elements. Samples were digested in aqua regia prior to analysis by ICP-MS for precious metals and base metals. Geochemical data were plotted and analysed using the Igpet software package produced by RockWare. Specific gravities, used in the mass change calculations after Gresens (1967), were calculated using a Jolly balance.

4.2 Geochemical variations between lava flows

4.2.1 Lithology and magmatic affinity by flow unit

To facilitate interpretation of the whole-rock geochemical data, samples were grouped into related units based on mapped lithology and map patterns. This provided a means to test within-flow correlations and between-flow differences in composition and magmatic affinity. Samples of like lithology located along strike without stratigraphic breaks (e.g., intervening flow of a different composition) were grouped as possible flow units. This first-order division of the samples yielded two mafic lava flow units and five intermediate lava flow units. The locations of the samples within each flow unit are shown in Figure 4.1. A table of sample names and corresponding flow unit names is given in Appendix A. Sample groups are treated as separate flows in the diagrams below.
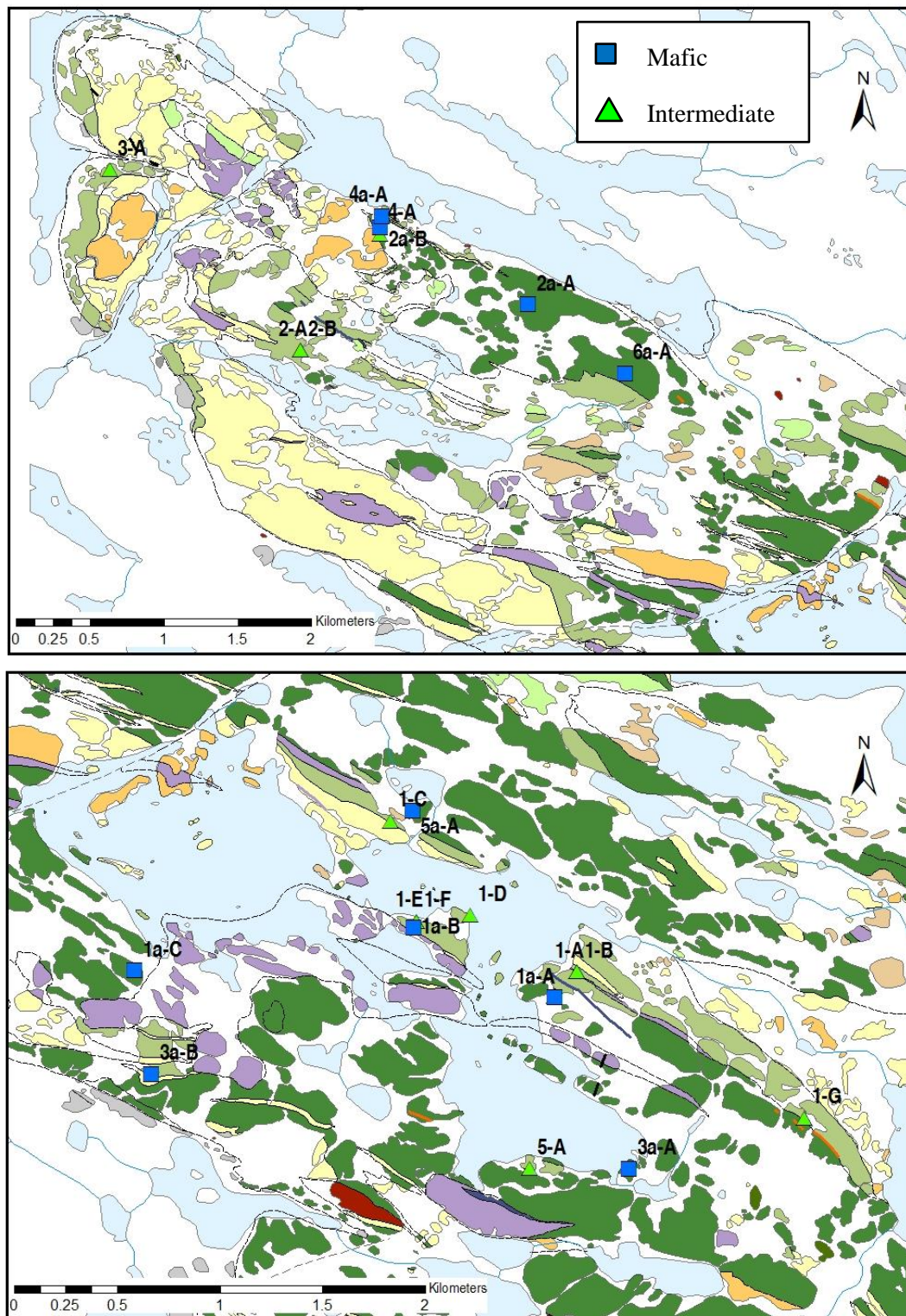
Figure 4.1: Sample locations labeled by flow unit. Sample point labels, shortened for convenience, refer to sub-divided flows (ie: 1, 2a) and sample number within the flow (ie: 1-A, 2a-B). After Jackson, 2013 (unpublished data). Full map with all sample locations shown in Figure 1.3.

Data from each flow unit were plotted on a variety of discrimination diagrams to test interpreted lithological affinity and similarity within flow units. Many of the standard geochemical discriminants are designed for the classification of pristine igneous rocks and rely on parameters such as SiO_2, Mg-number, alkalis, and differentiation indices. In hydrothermally altered systems, however, many elements used in these diagrams are mobilized by water-rock interaction (MacLean & Barrett, 1993), which renders these well established discrimination techniques unsuitable for identifying magmatic affinity and precursor lithology. Given field observations of suspected alteration, specifically silicification, diagrams and classification schemes based on major and/or mobile elements were avoided as indicators of primary magmatic affinity. However, SiO_2 variation (Fig. 4.2) was used to illustrate the interpreted mobility of silica.

Interpretations of geochemical signatures, magmatic affinity, and lithological classification in this study rely on immobile elements such as Al, Ti, Nb, Zr, and in some cases Y, and rare earth elements (REE), which have been shown to be immobile under hydrothermal alteration and greenschist facies metamorphic conditions (MacLean & Kranidiotis, 1987; MacLean, 1990; Barrett & MacLean, 1991). Within each flow unit, element immobility was tested following the methodology proposed by MacLean and Kranidiotis (1987). Using bivariate plots (Appendix D), immobile element pairs were identified as those forming a highly correlated linear trend (ideally r>0.85), which in an ideal, homogeneous, single-precursor system passes through the origin. This trend is the result of mass gains and losses in mobile components within the system.
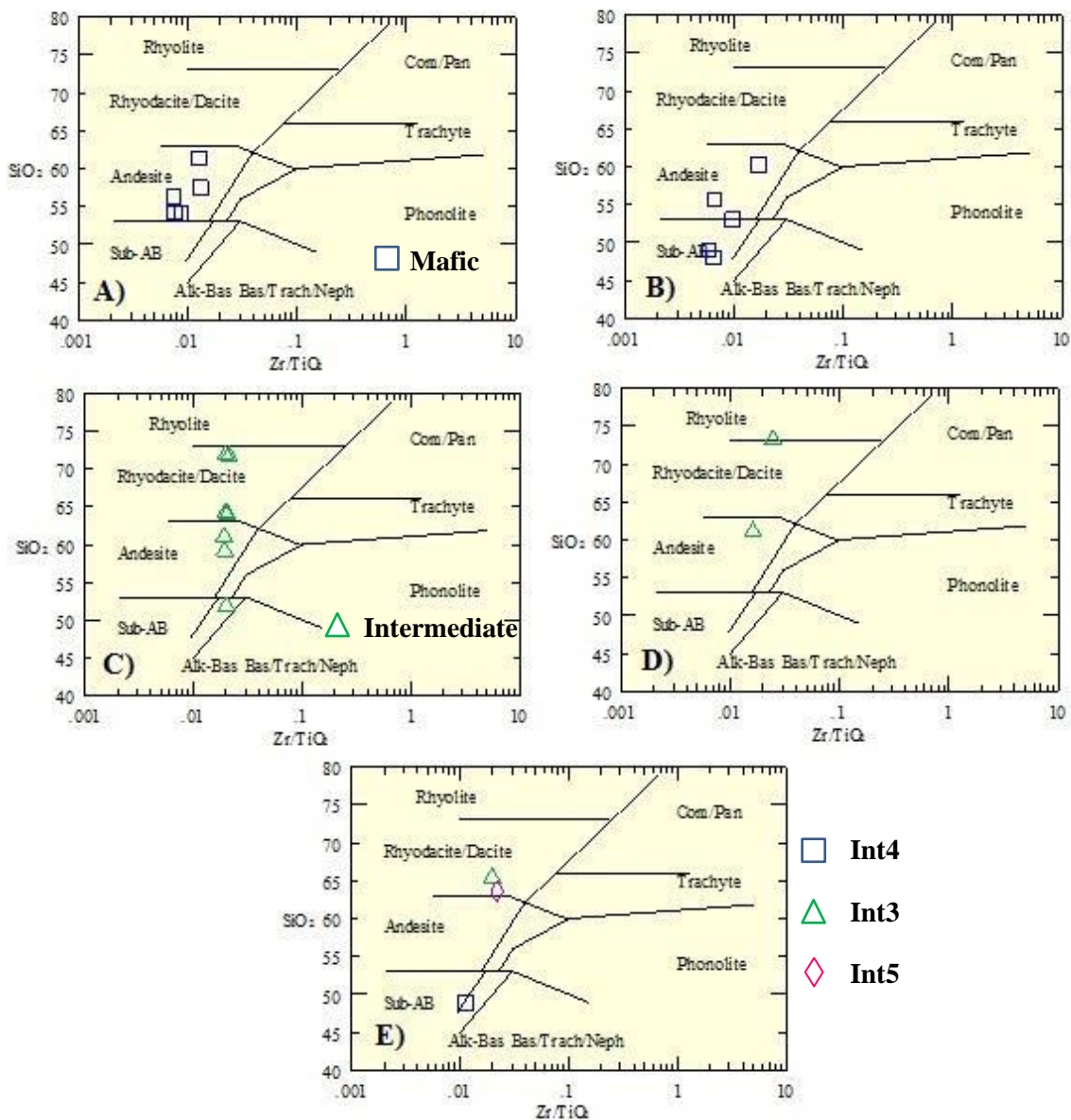
Figure 4.2: SiO_2-Zr/TiO_2 discrimination diagrams (after Winchester & Floyd, 1977) for the sample suites. The diagrams illustrate the highly variable SiO_2 content reflecting silica mobility during alteration. (A) Mafic 1, (B) Mafic 2, (C) Intermediate 1, (D) Intermediate 2, and (E) Intermediate flows 3, 4 and 5, plotted together for convenience.

This technique confirmed the relative immobility of Y, Zr and many REE in all the mafic samples from the Sharrie Lake sample set. Some REE (e.g., Sm, Dy) as well as Al, Ti, Nb, and Ta yielded a weaker correlation that may indicate slight mobility or primary igneous variation.

Immobile element testing for one intermediate sample suite (Intermediate 1, see Appendix A for sample groupings) revealed very poor correlations of Zr with Ce, Eu, La, Nb, Nd, Ta, and Th. Even a plot of Hf against Zr, a pair of elements with high chemical affinity, yielded a low r value of 0.71. Although other REE (e.g. Dy, Lu, Sm, Y, and Yb) had higher correlation coefficients (r=0.77-0.88) when plotted against Zr, these correlations are still not ideal. Bearing this in mind, the results of discrimination diagrams based on Y, La, and Th values for flow unit Intermediate 1 should be treated with caution. Element mobility testing could not be applied to Intermediate flow units 2, 3, 4 and 5, as they contain too few samples to yield statistically meaningful results. In these flows, Al, Ti, Zr, Nb, Y, and REE immobility must be assumed.

The discrimination diagrams employed here to delineate fields for common volcanic rocks are SiO_2-Zr/TiO_2 (Winchester & Floyd, 1977), Zr/TiO_2-Nb/Y (Winchester & Floyd, 1977), and Zr/Ti-Nb/Y (Pearce, 1996). The significant variations in SiO_2 both within and between flow units are shown in Figure 4.2. Many intermediate samples fall in the rhyodacite/dacite field due to their high SiO_2 content; the abnormally high SiO_2 values in these samples are attributed to alteration. For example, sample Int2-B plots as a rhyolite despite meeting the field criteria for an intermediate pillow lava (Table 2.1). There are a number of problems with the apparently "evolved" composition of these samples, which plot as dacite, rhyodacite, or rhyolite. Lavas of this composition rarely form pillow structures because of their high viscosity. Instead, submarine eruptions of evolved magmas tend to form domes or tabular structures or pyroclastic deposits. As the SiO_2-Zr/TiO_2 diagrams fail to identify plausible precursor lithologies for the sample sets, each flow unit was plotted on alternative diagrams based on immobile element ratios.

The Zr/TiO_2-Nb/Y discrimination diagrams use two immobile element ratios, both indices of alkalinity, with Zr/TiO_2 serving also as a differentiation index (Winchester & Floyd,

1977). Plotting all the data together reveals a steep trend of increasing Zr/TiO_2 ratios with near-constant Nb/Y ratios (Fig. 4.3). In contrast to the diagrams based on SiO_2 (Fig. 4.2), here all samples plot within a plausible range of lithologies for pillow lavas. Using separate diagrams for each flow unit, it is possible to subdivide the samples further (Fig. 4.4). In Mafic 1, for example, two distinct clusters of samples can be separated into different flows, one basaltic and another slightly more evolved andesite/basalt. Likewise Mafic 2 can be divided into three flows: sub-alkaline basalt, andesite/basalt and andesite. Intermediate 1 is andesitic and shows very little compositional variation in terms of immobile elements. The two samples of intermediate 2 appear to have distinct geochemical signatures despite being sampled only ~40 m apart along a continuous outcrop within what appeared to be a single flow (Fig. 1.3). Sample Int2-A plots on the low Zr/TiO_2 end of the andesite field whereas Int2-B lies on the rhyodacite/dacite-andesite border. Intermediate flows 3, 4 and 5 plot as andesitic, andesitic/basaltic and andesitic, respectively. These newly subdivided flows can also be distinguished on a plot of Zr/Al_2O_3 against Zr/TiO_2 (Fig. 4.5) as clusters of samples, or as single isolated samples.
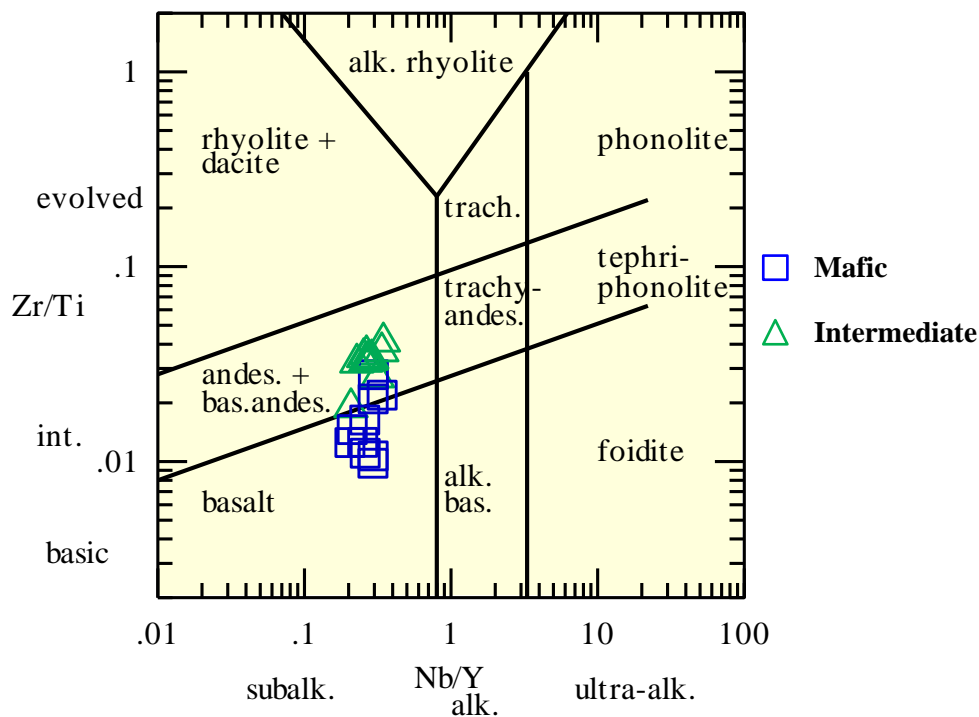
Figure 4.3: Zr/TiO_2-Nb/Y discrimination diagram (after Pearce, 1996) for all samples illustrating the narrow range of Nb/Y ratios in comparison to the Zr/TiO_2 ratios.

From these discrimination diagrams, one sample (Maf4a-A), mapped as mafic, is shown to be intermediate (andesite) and conversely, sample Int4-A, mapped as intermediate, is in fact slightly less evolved (andesite/basalt). However, for the remaining samples the lithologies according to these diagrams match their field classifications.

Immobile elements and incompatible major elements can also be used as discriminants of magmatic affinity. Of particular value in differentiating between suites with tholeiitic, "transitional", and calc-alkaline affinities are bivariate plots of Zr-Y, La-Yb, and Th-Yb (MacLean & Barrett, 1993; Ross & Bédard, 2009). The boundary values defining the fields in all three diagrams are given in Table 4.1. Rocks of transitional affinity are those that would plot at the boundary of the tholeiitic and calc-alkaline fields on an AFM diagram (Ross & Bédard, 2009).
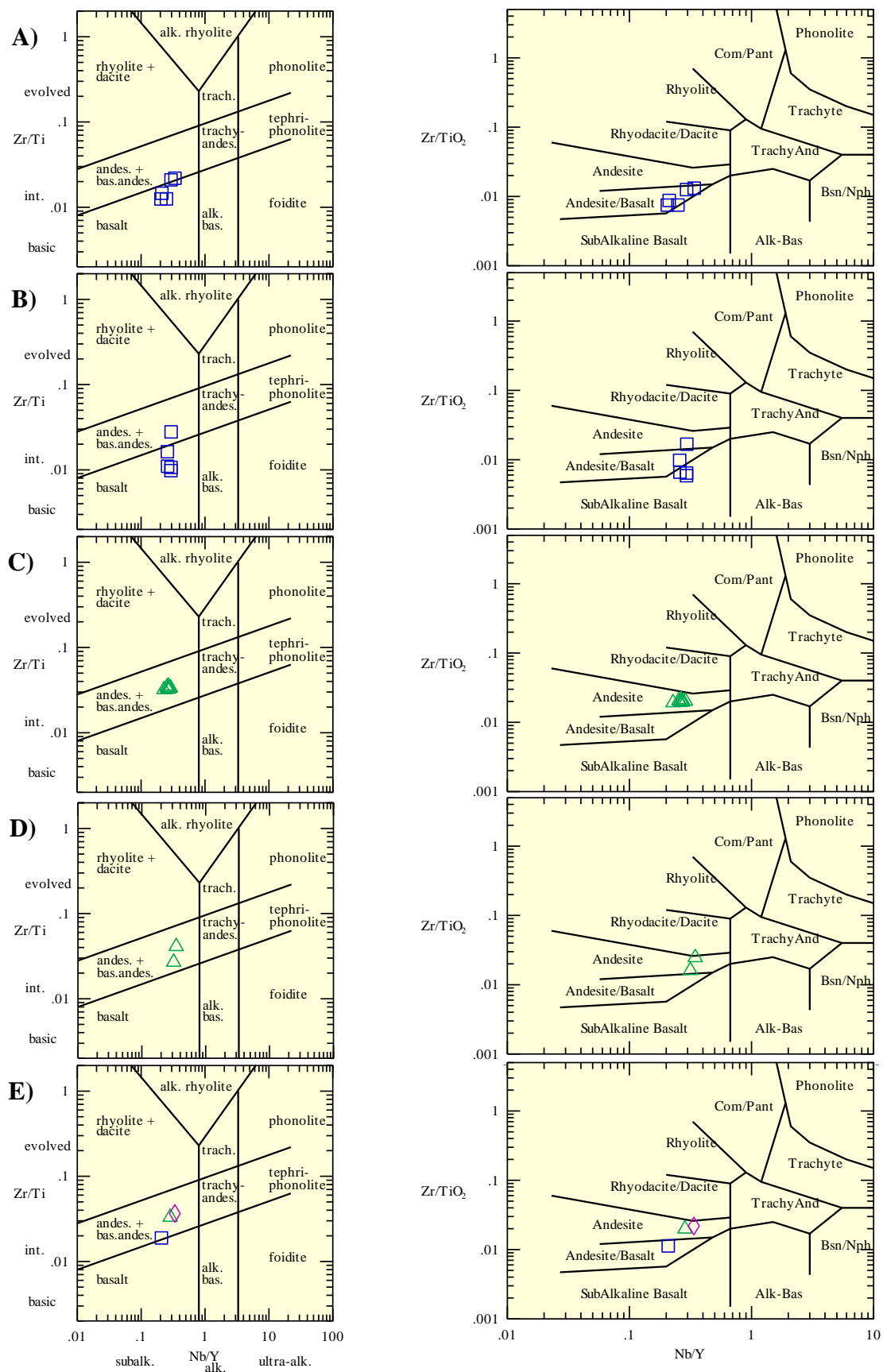
Figure 4.4: Zr/TiO$_2$-Nb/Y discrimination diagram for Mafic 1 (A), Mafic 2 (B), Intermediate 1 (C), Intermediate 2 (D) and Intermediate 3, 4 and 5 (E). Diagrams in the left-hand column after Pearce, 1996. Diagrams in the right-hand column after Winchester & Floyd, 1977.
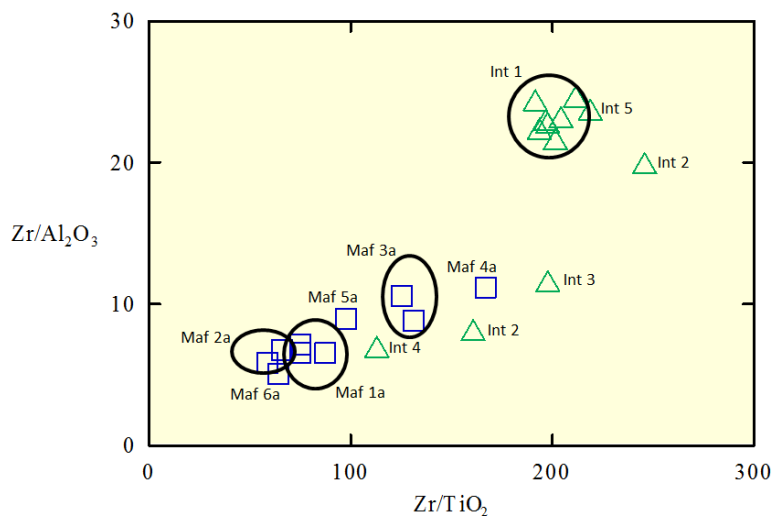
Figure 4.5: Flow units, sub-divided into six mafic flows and five intermediate flows based on distinct chemical differences revealed in the Zr/TiO_2-Nb/Y discrimination diagrams. Flow unit names abbreviated for convenience.

Table 4.1: Boundary values for tholeiitic, transitional and calc-alkaline fields on Zr/Y, La/Yb and Th/Yb diagrams. After Ross & Bédard, 2009.

Diagram	Tholeiitic	Transitional	Calc-alkaline
Zr/Y	<2.8	2.8-4.5	>4.5
La/Yb	<2.6	2.6-5.3	>5.3
Th/Yb	<0.35	0.35-0.8	>0.8

Most flow units are of calc-alkaline affinity based on immobile element ratios in all three diagrams (Fig. 4.6). Intermediate flows 1 and 5 are strongly calc-alkaline and have high values of La, Th, Y, Yb and Zr relative to the other flows. Mafic flows 1, 2 and 6, as well as intermediate flow 4, are distinguished by their transitional to mildly calc-alkaline affinities.
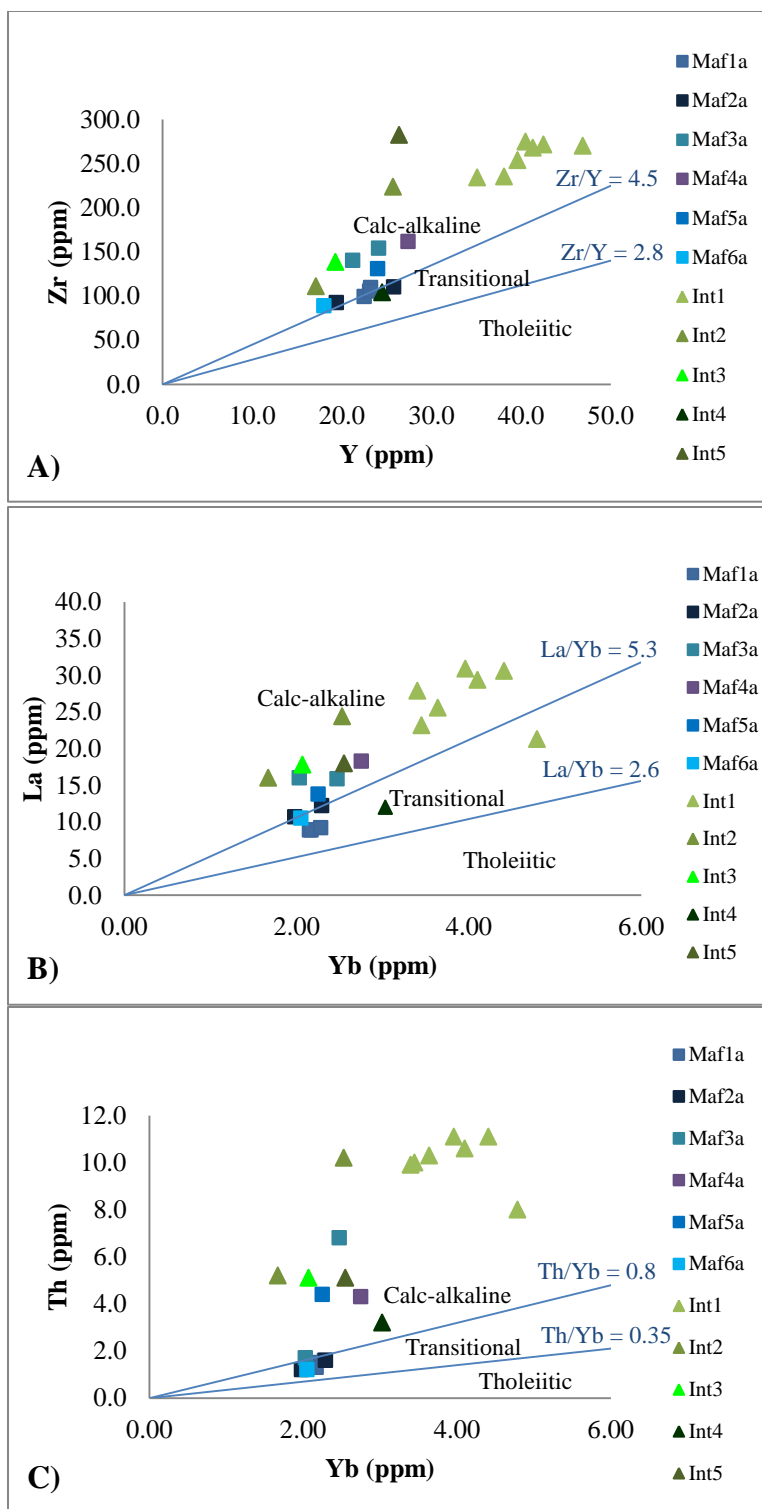
Figure 4.6: Zr/Y (A), La/Yb (B) and Th/Yb (C) diagrams (after Ross & Bédard, 2009) for the sample suite, allowing discrimination between samples of tholeiitic, transitional and calc-alkaline magmatic affinities. Flow unit names abbreviated for convenience.

4.2.2 Geochemical signatures by flow unit

Normalized multi-element diagrams of trace element data can provide insight into mineral/melt fractionation processes and serve as petrogenetic indicators (Winter, 2010). In these diagrams, trace element data are normalized to their assumed abundances in a given uniform reservoir (e.g., chondrite, primitive mantle). Ideally, samples within a homogeneous flow unit should have similar patterns illustrating that they share a common source, process, or type of contamination. The diagrams for each flow unit are shown below, first normalized to chondrite values (Fig. 4.7), and then to primitive mantle (Appendix D). In the chondrite-normalized diagrams, all the flow units display LREE enrichment over HREE and relatively flat HREE. In the primitive mantle-normalized diagram, the variable concentrations of Rb, Ba, K, and U indicate heterogeneous mobilization of these components. The variability of these elements obscures the patterns and hinders interpretation of the diagram. In an effort to reduce this effect, the primitive mantle-normalized diagram was modified (Fig. 4.8) to remove these mobile elements.

The modified diagrams are much clearer and flow units can be subdivided according to their trace element patterns. All the subdivisions discussed in this section match those described in section 4.2.1. Flow unit Mafic 1 (Fig. 4.8A) displays two different trace element patterns, suggesting it should be subdivided into two separate flows. Both flows have negative Nb, P and Ti anomalies, generally considered a subduction zone signature (Kerrich & Wyman, 1996). The first of these two newly defined flow units, Mafic 1a, is characterized by lower Th values, and slight negative Eu and slight positive Zr anomalies. Mafic 3a, in contrast, has higher La and Ce values, and a more pronounced negative P anomaly.
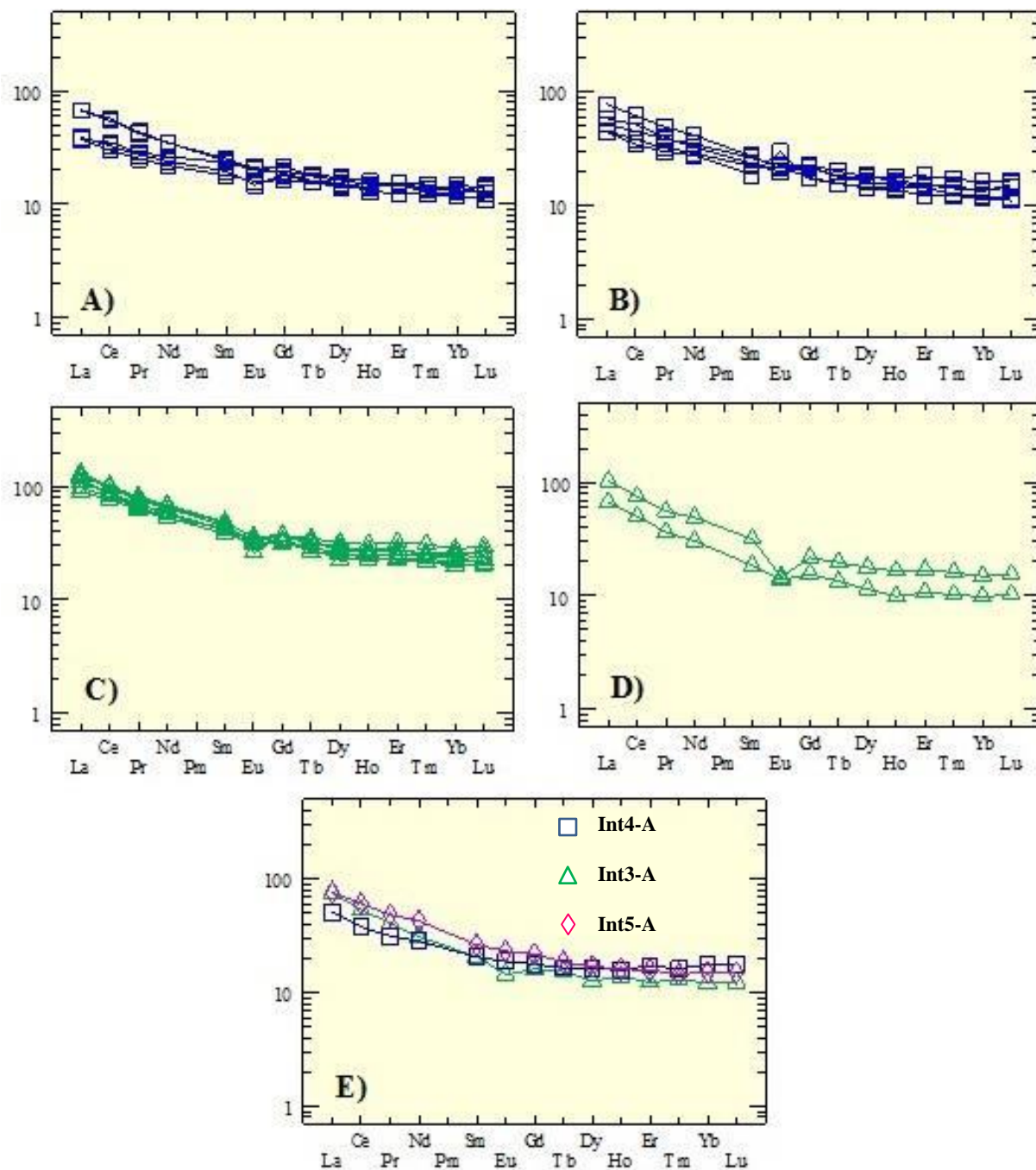
Figure 4.7: Chondrite-normalized REE diagrams (after Sun & McDonough, 1989) for Mafic 1 (A), Mafic 2 (B), Intermediate 1 (C), Intermediate 2 (D) and Intermediate 3, 4 and 5 (E), showing arc-like characteristics of LREE enrichment and relatively flat HREE.
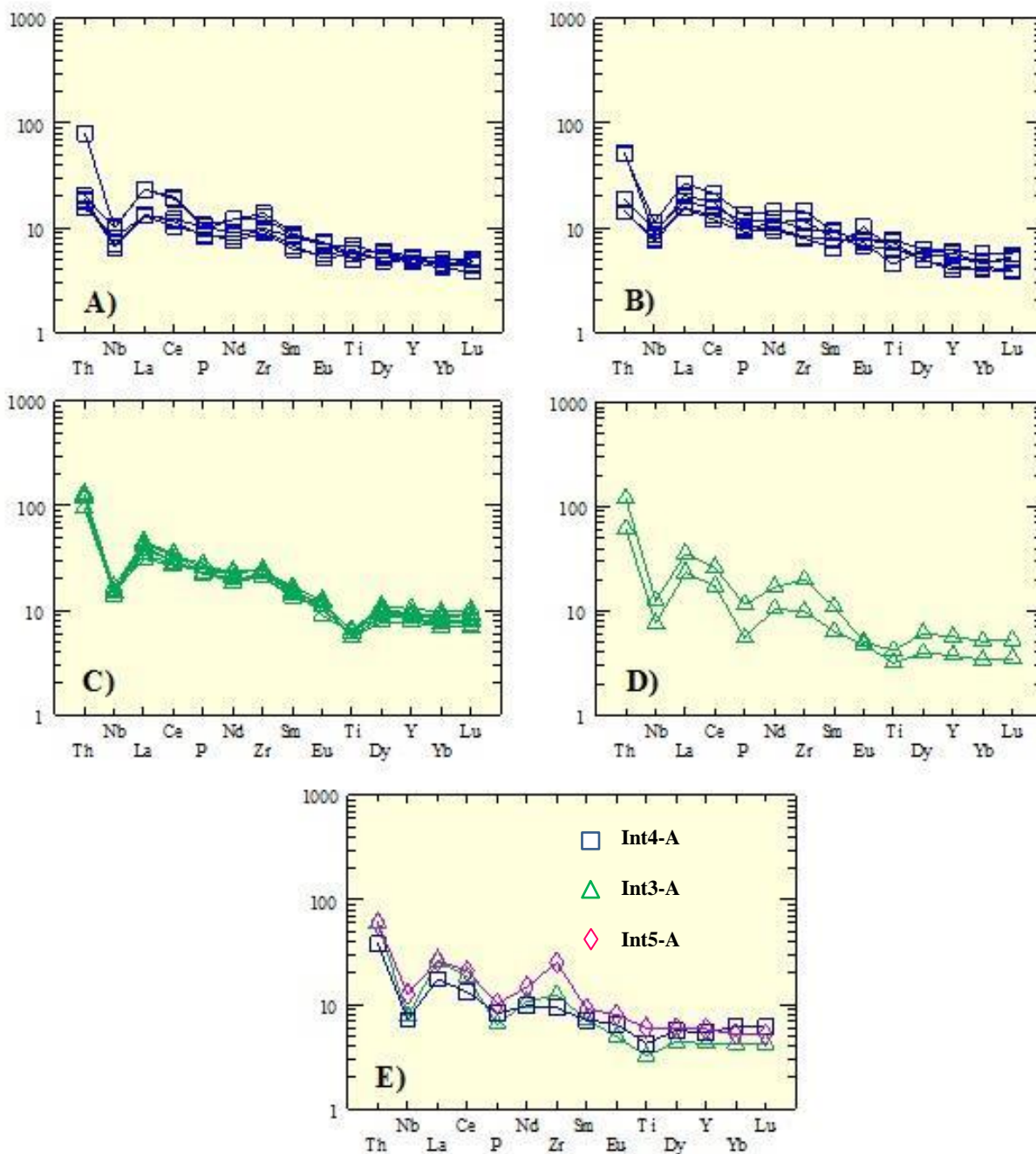
Figure 4.8: Modified primitive mantle-normalized trace element diagrams (after Sun & McDonough, 1989) for Mafic 1 (A), Mafic 2 (B), Intermediate 1 (C), Intermediate 2 (D), and Intermediate 3, 4 and 5 (E). Modified to exclude mobile elements Rb, Ba, U, K, and Sr.

In the Mafic 2 diagram (Fig. 4.8B), four separate flows can be distinguished, here termed Mafic 2a, 4a, 5a, and 6a. Mafic 2a is characterized by low Th values, slight HREE depletion, and a lack of negative P and Ti anomalies. Mafic 4a has higher Th, a slight positive Zr anomaly, and

a negative Eu-Ti anomaly. Flow Mafic 5a has a similar signature to Mafic 4a but lacks the negative Eu-Ti anomaly and has a slight negative Yb anomaly. Finally, Mafic 6a has a similar signature to Mafic 2a, with a slight negative Sm anomaly, a distinct positive Eu anomaly, and slightly depleted HREE.

No further subdivisions are necessary for flow unit Intermediate 1 (Fig. 4.8C), as the trace element patterns are consistent within the sample suite. This flow unit is distinguished by high Th and La values, resulting in a negative Nb anomaly, enrichment in LREE to Zr, a negative Ti anomaly, and flat HREE. The intermediate 2 (Fig. 4.8D) samples share similar signatures defined by negative Nb, P, Eu and Ti anomalies, although sample Int2-B is enriched in nearly all components relative to Int2-A. Flow units Intermediate 3, 4, and 5 are plotted together for convenience (Fig. 4.8E). Intermediate 3 is characterized by a strong negative Eu anomaly. Flow unit Intermediate 4 has higher HREE. Finally, flow unit Intermediate 5 has negative Nb and P anomalies, a positive Zr anomaly, and lacks any Eu or Ti anomalies. A discussion of the petrogenetic significance of these trace element patterns is presented in section 5.1.

4.3 Alteration

4.3.1 Selection method and criteria for least altered samples

In the study of altered volcanic rocks, the identification of a least altered, or preferably unaltered, sample is paramount in understanding the alteration history. At Sharrie Lake no outcrops of unaltered mafic or intermediate rocks were identified. In lieu of an unaltered sample, a set of criteria was created to identify the least altered and most altered sample for the mafic and intermediate pillow lava flows. These criteria are summarized in Table 4.2. Least and most

altered sample pairs from within a single flow unit were selected for comparison in mass change

calculations.

Table 4.2: Criteria for least altered mafic and intermediate samples. Silica values after LeMaître (1989) and specific gravity values from EduMine (2014). Zr/TiO_2-Nb/Y refers to the discrimination diagram of Winchester & Floyd (1977).

	Mapped Lithology	Outcrop	Hand Sample	Specific Gravity	Mineralogy	SiO$_2$ (wt %)	Zr/TiO$_2$-Nb/Y	Total alkalis (wt %)	LOI (wt %)
Least altered mafic	Mafic	Minimal veins, amygdules, and altered pillow cores.	Minimal veins and amygdules.	2.8-3.0	Minimal sericite, chlorite, epidote, carbonate, or secondary quartz.	45-57	Basalt-basaltic andesite	2-6	<1
Least altered intermediate	Intermediate	Minimal veins and amygdules.	Minimal veins and amygdules.	2.5-2.8	Minimal sericite, chlorite, epidote, carbonate, or secondary quartz.	57-63	Andesite	2-6	<1

Based on an evaluation of all the samples against these criteria, two least altered and two

most altered mafic samples, and one least altered and one most altered intermediate sample, were

selected to investigate alteration at Sharrie Lake. Table 4.3 displays the least altered criteria as

applied to these samples.

Table 4.3: Criteria for the least altered mafic and intermediate pillow lavas applied to two least altered mafic samples (Maf1a-A and Maf2a-A), and one least altered intermediate sample (Int1-A). Specific gravities determined using a Jolly balance. See Appendix F for a full set of specific gravity calculations.

	Mapped Lithology	Outcrop	Hand Sample	Specific Gravity	Mineralogy	SiO$_2$ (wt %)	Zr/TiO$_2$-Nb/Y	Total alkalis	LOI (wt %)
Maf1a-A	Mafic	Rare altered cores to cream white. No amygdules. Sample taken in dark grey-green pillow.	Sparse fractures with <1 mm alteration halos.	2.82	Minor ser on plag phenocrysts, minor chl+ep. Qtz+plag±bt vein lined with oxides.	56.23	Basalt	4.79	0.37
Maf2a-A	Mafic	Some altered cores to light grey-green. Sample taken in dark grey-green pillow.	Rare <1 cm long, <1 mm wide fractures.	2.8	Minor ser on plag phenocrysts, minor chl+ep. Rare veins lined with oxides.	55.63	Basalt	4.58	0.06
Int1-A	Intermediate	~5% qtz±cc amygdules in selvages, 1-5% in cores. <0.4-10 mm.	2-5% qtz amygdules, ~1 mm diameter.	2.83	Minor ser on plag phenocrysts, minor chl and cc. Rare sigmoidal qtz amygdules.	64.03	Andesite	4.94	0.25

Samples Maf6a-A and Maf1a-C were selected as the most altered mafic samples. Sample
Maf6a-A has a strongly altered pale core that consists primarily of a carbonate-epidote-quartz
alteration assemblage, and a mafic rim composed of amphibole, relict plagioclase phenocrysts,
ilmenite, and a microcrystalline quartz-feldspar matrix. As the boundary between the mafic rim
and altered core in this sample was difficult to define, the slabs crushed for geochemical analysis
contained material from both domains. The analysis for this sample is therefore treated with
caution as it represents a mixture of strongly altered and "primary" mafic materials. For the
intermediate flows, sample Int1-E was deemed the most altered sample. Whole-rock major
element analyses for the least altered and most altered samples are shown in Table 4.4. A full set
of geochemical analyses is presented in Appendix C.

Table 4.4: Major oxide data (wt %) and specific gravities (g) for the three least altered-most altered pairs used in the Gresens calculations. (*) Least altered samples.

Sample #	Maf2a-A*	Maf6a-A	Maf1a-A*	Maf1a-C	Int1-A*	Int1-E
g	2.80	3.00	2.82	2.81	2.83	2.60
SiO_2	55.63	47.99	56.23	54.04	64.03	71.84
TiO_2	1.67	1.39	1.33	1.21	1.33	1.19
Al_2O_3	16.37	17.64	15.25	16.22	11.84	10.43
Fe_2O_3	9.85	7.90	9.12	8.61	12.17	4.60
MnO	0.22	0.11	0.15	0.19	0.15	0.13
MgO	3.83	1.73	6.14	5.48	1.41	0.13
CaO	6.87	17.64	7.89	8.52	2.79	4.92
Na_2O	4.43	0.40	4.51	4.28	2.62	4.08
K_2O	0.15	0.33	0.28	0.28	2.32	0.14
P_2O_5	0.25	0.20	0.19	0.18	0.55	0.50
LOI	0.06	4.14	0.37	0.63	0.25	1.21
Total	99.33	99.47	101.46	100	99.46	99.17

4.3.2 Geochemical evidence of alteration

A number of geochemical characteristics may indicate alteration. In this study, where
only pillow lava flows of mafic to intermediate composition were sampled, the broad range of

SiO_2 values is the first indication that there has been significant alteration-related element mobility. Likewise, variations in other major elements (CaO, Fe_2O_3, MgO, and Na_2O) can be attributed to alteration processes. The spread of values for Rb, Ba, U, and K in the primitive mantle-normalized diagrams (Appendix D) indicates that these elements may have been variably mobilized during alteration or variably diluted/enriched due to mass gain/loss. The variable degree of mobility of REE between different flow units may also be evidence of heterogeneous alteration. In all the mafic samples, many incompatible trace elements and REE are interpreted to be immobile based on good to excellent correlations with Zr. In contrast, for the samples in Intermediate 1, few supposedly immobile elements display such correlations; many have very poor correlations with Zr (r = 0.00-0.33). This may indicate that many high field strength elements (HFSE) and REE in this flow have been mobilized or variably diluted/enriched as a result of mass change during alteration.

Similarly, variations in elements presumed to be immobile, such as Al_2O_3, TiO_2, and Zr, within the mafic and intermediate sample sets are likely due to dilution or concentration from mass gain or loss during alteration. For example, samples in Intermediate 1 that display evidence of immobile element mobility also have significantly higher Zr values than mafic samples or some other intermediate samples. These Zr values may indicate that this flow experienced mass loss. Strongly altered mafic samples Maf2a-B and Maf6a-A have the two lowest Zr values in the entire sample set, which may indicate that the samples experienced mass gain during alteration. Evidence of this mass gain includes abundant carbonate-filled vesicles and a carbonate-rich matrix in sample Maf2a-B, and a carbonate-rich altered core in Maf6a-A.

4.3.3 Qualitative characterization of alteration

Qualitative interpretations of the type(s) of alteration occurring at Sharrie Lake can be made using ratios of alteration indices, such as the Ishikawa alteration index and chlorite-carbonate-pyrite index. The Ishikawa alteration index (AI) deals primarily with the effects of chlorite and sericite replacing albite and volcanic glass (Ishikawa *et al.,* 1976; Large *et al.,* 2001). These reactions include:

$$3NaAlSi_3O_8 + K^+ + 2H^+ = KAl_3Si_3O_{10}(OH)_2 + SiO_2 + 3Na^+, \qquad [1]$$
$$\text{(albite)} \qquad\qquad \text{(sericite)} \qquad \text{(quartz)}$$

and,

$$KAl_3Si_3O_{10}(OH)_2 + 3H_4SiO_4 + 9Fe^{2+} + 6Mg^{2+} + 18H_2O = \qquad [2]$$
$$\text{(sericite)} \qquad\qquad 3Mg_2Fe_3Al_2Si_3O_{10}(OH)_8 + 2K^+ + 28H^+.$$
$$\text{(chlorite)}$$

Mass changes associated with these reactions include loss of Na_2O and CaO, and gain of K_2O in reaction 1, and loss of K_2O and gain of FeO and MgO in reaction 2 (Large *et al.,* 2001). These changes are based on assumed constant Al_2O_3. The Ishikawa index is calculated using the following formula (components in wt %):

$$AI = \frac{100(K_2O + MgO)}{(K_2O + MgO + Na_2O + CaO)} \qquad [3]$$

Unaltered rocks have AI values ranging from 20 to 60 whereas values in hydrothermally altered rocks vary between 50 and 100. Application of the Ishikawa index to Sharrie Lake samples has a significant limitation as it does not incorporate carbonate alteration. As a result, in samples with carbonate alteration and high CaO, the AI will appear lower, even where high-intensity alteration has occurred. Combining the AI with the chlorite-carbonate-pyrite index (CCPI) reduces this limitation.

The CCPI measures increasing MgO and FeO_T ($FeO + Fe_2O_3$), and decreasing Na_2O and K_2O associated with chlorite, carbonate (dolomite, ankerite, siderite), pyrite, magnetite or hematite formation (Large *et al.,* 2001). The CCPI is calculated using the formula:

$$CCPI = \frac{100\ (MgO + FeO_T)}{(MgO + FeO_T + Na_2O + K_2O)} \qquad [4]$$

This alteration index is strongly affected by variations in primary composition. Values ranging from 50 to 90 are typical of andesites and basalts. Plotting CCPI against AI yields a "least altered" box plot (Fig. 4.9). Altered samples plot near the principal end-member alteration mineral and least altered samples plot near the centre of the diagram. The relative intensity of alteration increases with distance from the box of least altered samples. End-member alteration minerals and mineral assemblages are plotted along the perimeter of the diagram. Altered rocks affected by diagenetic (seafloor alteration) processes tend to have alteration trends towards the lower left corner of the diagram, whereas hydrothermally altered rocks will trend towards the upper right corner. This lithogeochemical technique has two limitations relevant to this study. The first is its inability to quantify silicification and the second is that it is better suited for rocks of felsic to intermediate composition because the least altered field for intermediate to mafic volcanic rocks overlaps the hydrothermal alteration field (upper right corner).

For this study, the "least altered" box (Fig. 4.9) was defined by the AI range of values for unaltered rocks (AI = 20-60) and by the composition-based range of CCPI values for intermediate to mafic rocks (CCPI = 50-90). In Figure 4.9, samples plotting outside the least altered box indicate that the principal alteration assemblage varies between epidote-carbonate, epidote-carbonate-albite, and albite-chlorite. The two mafic samples plotting outside the box (Maf6a-A and Maf2a-B) trend towards the epidote-carbonate and epidote-carbonate-albite alteration assemblages, respectively. Petrographic analysis of these samples confirmed the

presence of these assemblages. Although they typically contain rare to sparse epidote, the altered intermediate samples do contain the carbonate-albite ± chlorite alteration mineral assemblages suggested by the diagram. Some samples plotting within the least altered box may follow the carbonate-sericite alteration trend. This alteration trend is obscured by the overlap of the least altered box for andesites and basalts and the hydrothermal alteration field.
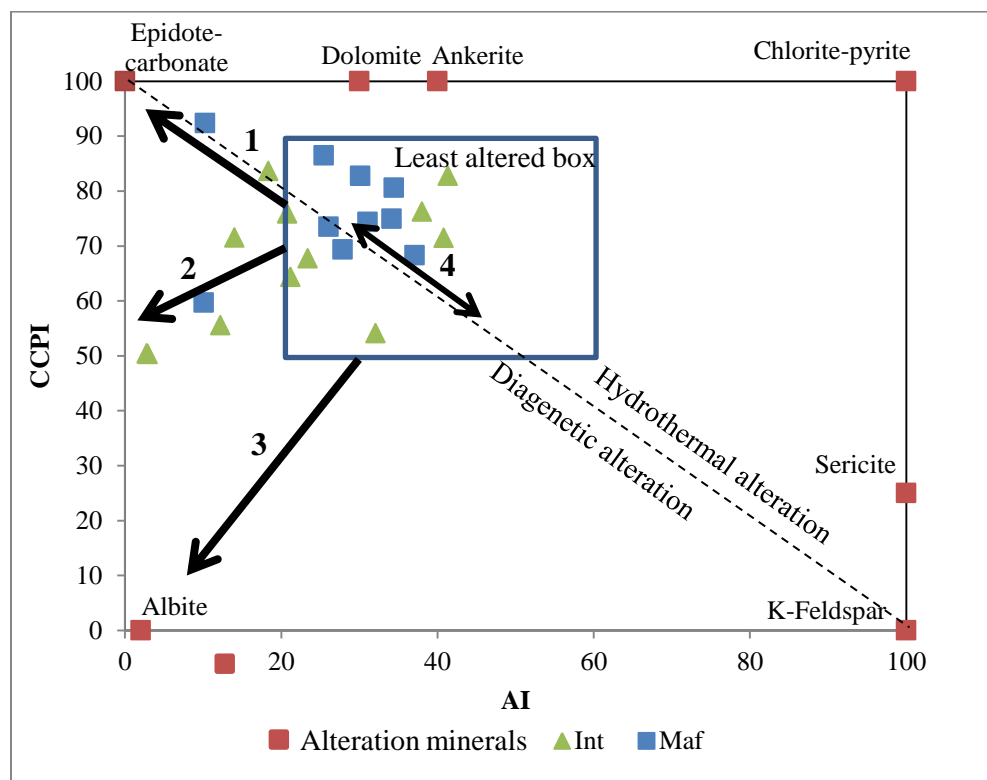
Figure 4.9: Alteration box plot (after Large *et al.*, 2001) of chlorite-carbonate-pyrite index (CCPI) versus the Ishikawa alteration index (AI) (indices defined in text). End-member alteration minerals and mineral assemblages are shown by red squares outlining the boundaries of the diagram. The blue box denotes the field assumed to contain least altered samples of andesites and basalts. Dashed line separates the diagenetic alteration field (lower left) from the hydrothermal alteration field (upper right). Trends in samples outside the box of least altered samples (black arrows) indicate diagenetic alteration to principal alteration assemblages of epidote-carbonate (1) and epidote-carbonate-albite (2). Weaker trends also indicate albite-chlorite (3) and carbonate-sericite (4) alteration.

4.3.4 Methods of quantifying alteration

Geochemical, mineralogical, and field evidence indicates that rocks at Sharrie Lake have experienced variable degrees of alteration, and quantifying which components have been gained or lost from the samples is vital to characterizing the type of alteration. Two main methods were applied in this study to quantify alteration: mass change calculations outlined by Gresens (1967), and mass change calculations using immobile elements Al, Ti, and Zr as correction factors.

The Gresens approach for rocks that have undergone metasomatic alteration is based on evaluating chemical components in terms of composition-volume relationships (Gresens, 1967). A set of equations is derived to relate the specific gravities, volumes, and concentration of a chemical component between two samples in order to assess the change in that chemical component and/or volume. The equation, modified after Gresens (1967), is as follows:

$$\Delta x_n = a \, [(f_v \bullet x_n^B \, g^B/g^A) - x_n^A] \qquad\qquad [5]$$

where Δx_n is the change from parent rock A to product rock B in chemical component n (g), a is the mass of parent rock A (here for convenience, let a = 100, so Δx_n = g/100 g or wt %), f_v is the volume factor (the ratio of the final to initial volume of the rock, V^B/V^A), x_n^A and x_n^B are the weight fractions of chemical component n in parent rock A and product rock B, and g^A and g^B are the specific gravities of A and B. These calculations were applied to the parent (least altered) and product (most altered) sample pairs listed in Table 4.5.

Table 4.5: Least altered (A) - most altered (B) sample pairs selected to quantify metasomatic reactions using the Gresens method.

	Mafic	**Mafic**	**Intermediate**
Parent (A)	Maf2a-A	Maf1a-A	Int1-A
Product (B)	Maf6a-A	Maf1a-C	Int1-E

In each comparison, data were treated using four different assumptions:

1) that the change from rock A to B was isochemical ($\Delta x_n = 0$),

2) that the change from rock A to B was isovolumetric ($f_v = 1$),

3) that Al_2O_3 remained constant during the change from rock A to B ($x_{Al}^A = x_{Al}^B$), and

4) that TiO_2 remained constant during the change from rock A to B ($x_{Ti}^A = x_{Ti}^B$).

Each treatment of the data is presented here as a graph showing relative mass gain and loss for each component. Tables of major and trace element calculations are presented in Appendix E. A composition-volume diagram was made for each comparison by calculating the change in each component for volume factors of 0.6, 0.8, 1.0 and 1.2. The y-intercepts of these diagrams were then plotted along a horizontal line to identify a value for f_v indicated by a clustering of points near a single f_v value. Points that plot at either end of the line indicate components that have likely been gained or lost during the metasomatic alteration.

Mass change calculations for the least altered - most altered sample pairs were also completed using three different mass correction factors. The correction factors applied were calculated by the ratios of Al, Ti, and Zr in the least altered sample to that of the most altered sample. These correction factors were then applied to the major oxide data for each least altered - most altered sample pair (Appendix E).

4.4 Comparison of least and most altered mafic pillow lava flows

4.4.1 Gresens Calculations

Applying the Gresens method to the alteration of Maf2a-A to Maf6a-A under the assumption that the alteration was isochemical yields the results in Appendix E. If the alteration was truly isochemical, the resulting volume factors should be near 1. The scatter of values,

particularly the high values of f_v for MnO, MgO, and Na$_2$O, indicate this is not the case for this alteration reaction. Results of data treatment using two different volume factors are shown in Figures 4.10A (f_v =1) and 4.10B (f_v =1.12). The value of f_v in Figure 4.10B was estimated by the clustering of y-intercept values from the composition-volume diagram (Fig. 4.13). Figures 4.10C and 4.10D present data treated under the assumption that Al$_2$O$_3$ and TiO$_2$ concentrations remained constant during the metasomatic alteration. The volume factors (f_v=0.87 and 1.12) in these calculations are those from the isochemical reaction for the appropriate component (Appendix E). Results from the isovolumetric (Fig. 4.10A) and constant Al$_2$O$_3$ (Fig. 4.10C) calculations agree, and indicate gains in Al$_2$O$_3$, CaO, and LOI, and losses in SiO$_2$, Fe$_2$O$_3$, MgO, and Na$_2$O. For the data treated with f_v =1.12 (Fig. 4.10B) and constant TiO$_2$ (Fig. 4.10D), the results demonstrate gains in SiO$_2$, Al$_2$O$_3$, CaO, and LOI, and losses in Fe$_2$O$_3$, MgO, and Na$_2$O. The composition-volume diagram for this alteration (Fig. 4.11) and the y-intercept (f_v) values (Fig. 4.12) support the results of the isovolumetric and constant Al$_2$O$_3$ calculations. Significant mass changes (>1 ppm) in trace elements are summarized in Figure 4.14. Trace element data were treated under two assumptions: constant volume and a 12% increase in volume (Fig. 4.14A-B).

Based on the spread of volume factors, some components were gained and lost during alteration of Maf1a-A to Maf1a-C (Appendix E). The calculations assuming constant volume and Al$_2$O$_3$ (Figs. 4.14A, C) both indicate significant gain of CaO, LOI, MnO, and Al$_2$O$_3$, and loss of SiO$_2$, Fe$_2$O$_3$, MgO, and Na$_2$O. The data treated with a volume factor of 1.05 (as estimated by the clustering of y-intercept values in Fig. 4.17) differ only in the change in SiO$_2$, which shows an apparent mass gain (Fig. 4.15B). In contrast to the other calculations, data treated assuming constant TiO$_2$ (Fig. 4.15D) show significant mass gains of SiO$_2$, Al$_2$O$_3$, and CaO, a loss of MgO,

and lesser gains in all other components. The mass gains and losses shown in the composition-volume diagram (Fig. 4.16) and the y-intercept values (Fig. 4.17) support the results of the isovolumetric and constant Al_2O_3 calculations. The likely value of f_v derived from Figure 4.17 is 1.05, implying the altered sample experienced a 5% volume increase. Significant mass gains and losses in trace elements are summarized in Figure 4.18. Trace element data were treated under two assumptions: constant volume and a 5% increase in volume (Fig. 4.18A-B).
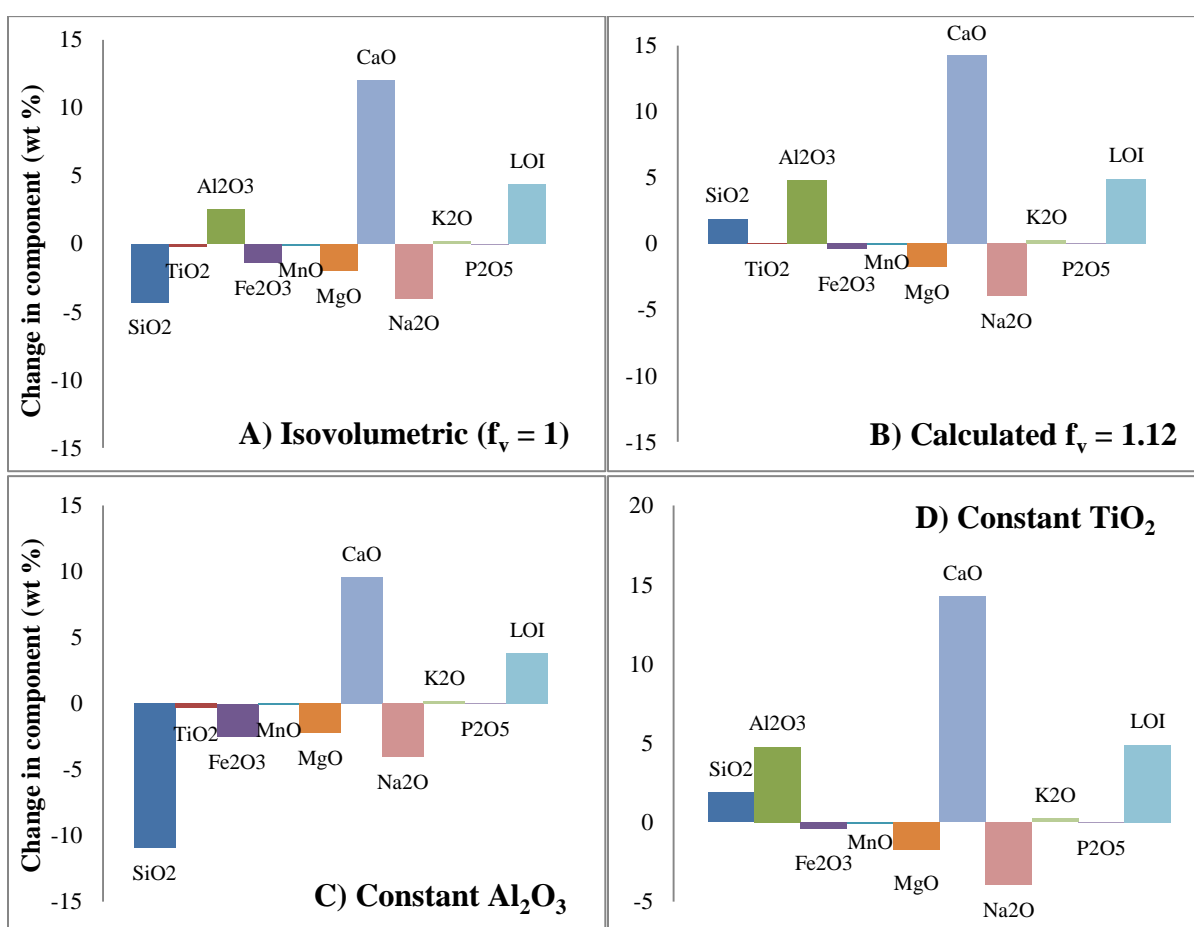
Figure 4.10: Graphical representation of mass change (in wt %) for the alteration of Maf2a-A to Maf6a-A as calculated after Gresens (1967). (A) Reaction treated as isovolumetric (f_v =1), (B) reaction treated with f_v =1.12 (estimated volume factor from Fig. 4.13), (C) assuming constant Al_2O_3, and (D) assuming constant TiO_2.
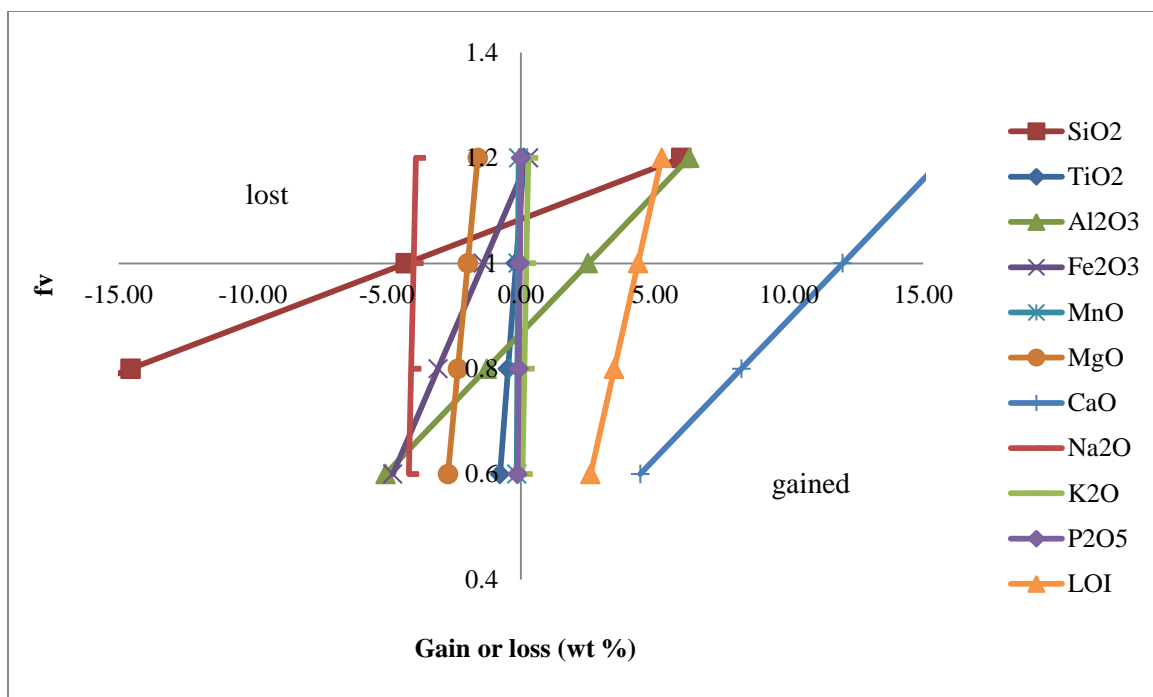
Figure 4.11: Composition-volume diagram (after Gresens, 1976) for the alteration of Maf2a-A to Maf6a-A.
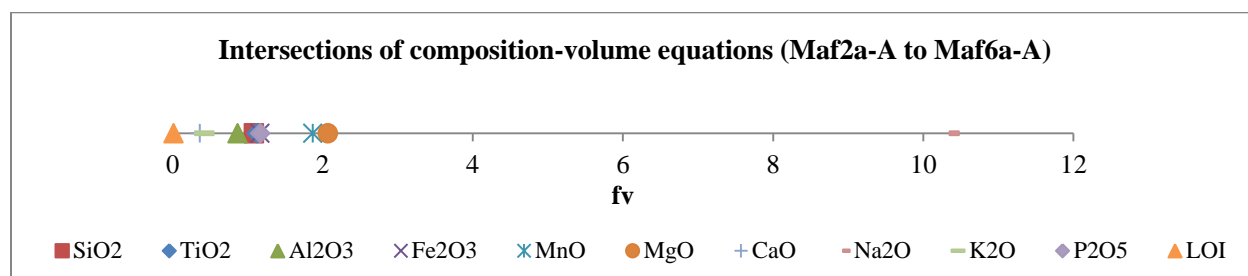
Figure 4.12: Y-intercept values for the composition-volume diagram shown in Fig. 4.11. Extreme values, such as those for Na_2O, MgO, LOI and CaO indicate significant mass change of these components. After Gresens, 1967.
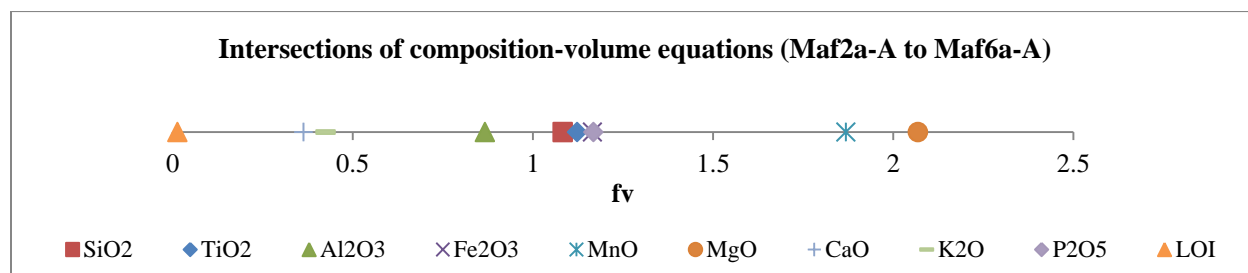
Figure 4.13: Y-intercept values for the composition-volume diagram shown in Fig. 4.11, modified to exclude Na_2O. The clustering of points around $f_v = 1.12$ indicates the reaction likely resulted in a volume gain of ~12%. After Gresens, 1967.
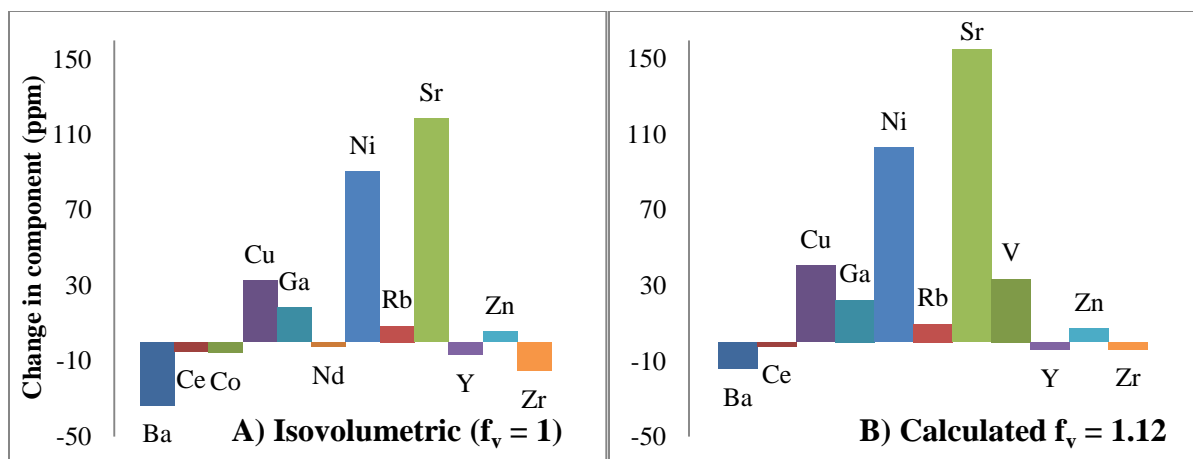
Figure 4.14: Trace element data for the alteration of Maf2a-A to Maf6a-A treated assuming that (A) volume remained constant, and (B) that a 12% increase in volume accompanied the alteration reactions.
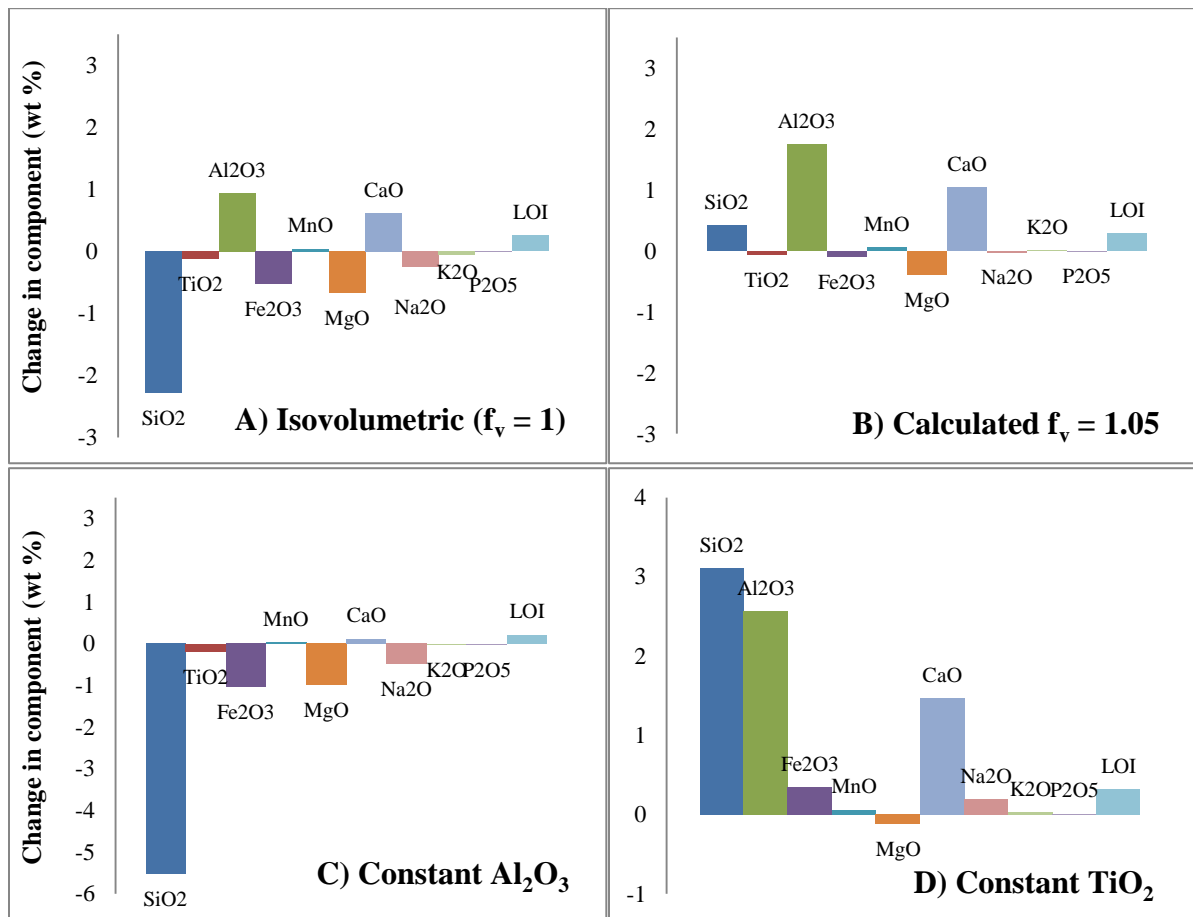
Figure 4.15: Graphical representation of mass change (in wt %) for the alteration of Maf1a-A to Maf1a-C as calculated after Gresens (1967). (A) Reaction treated as isovolumetric ($f_v = 1$), (B) reaction treated with $f_v = 1.05$ (estimated volume factor from Fig. 4.16), (C) assuming constant Al_2O_3, and (D) assuming constant TiO_2.
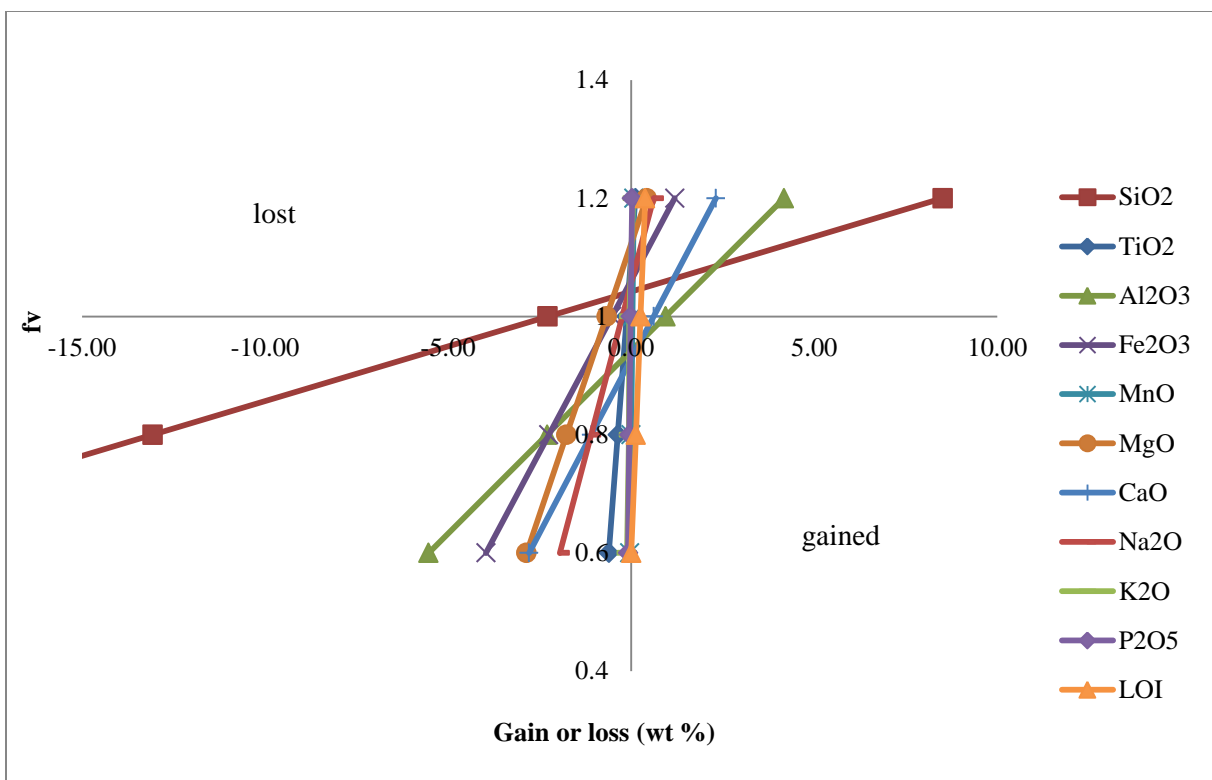
Figure 4.16: Composition-volume diagram after Gresens (1967) for the alteration of Maf1a-A to Maf1a-C.
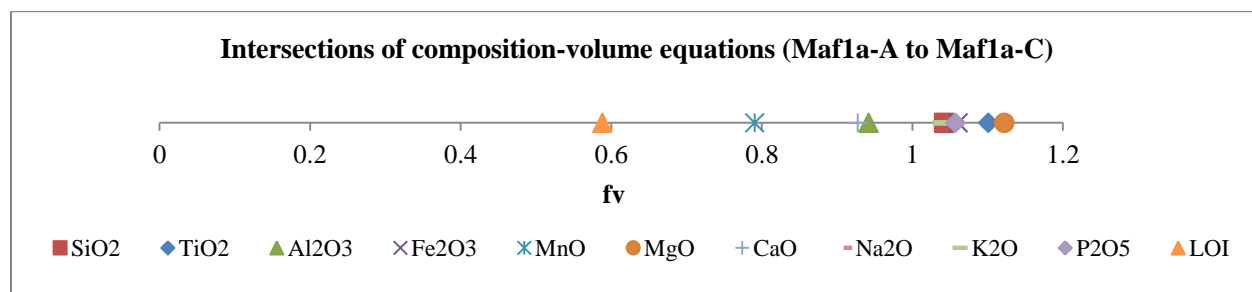
Figure 4.17: Y-intercept values for the composition-volume diagram shown in Fig. 4.16. Values for LOI, MnO, CaO, and MgO plotting at the ends of the line indicate these components experienced mass change during alteration. The interpreted volume factor is 1.05. After Gresens, 1967.
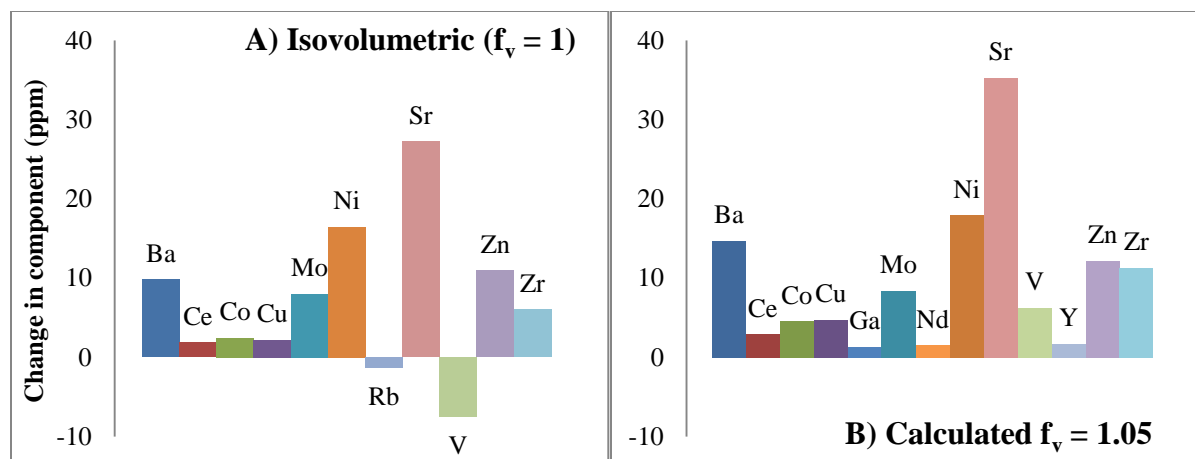
Figure 4.18: Trace element data for the alteration of Maf1a-A to Maf1a-C treated assuming that (A) volume remained constant, and (B) that a 5% increase in volume accompanied the alteration reactions.

4.4.2 Mass change calculations

The results of the mass change calculations based on correction factors of ratios of Al, Ti, and Zr in the least and most altered samples show variable gains and losses depending on the correction factor applied. For the alteration of Maf2a-A to Maf6a-A, the data corrected by the factor of $Al_2O_{3LeastAlt}/Al_2O_{3Alt}$ show slight gains in all components whereas data corrected by Ti and Zr show loss of all components, with significant loss of SiO_2, Al_2O_3, Fe_2O_3, and CaO (Fig. 4.19A). In the alteration of Maf1a-A to Maf1a-C, calculations using Al_2O_3 and Zr as correction factors indicate mass gain in all components, most notably in SiO_2 (Fig. 4.19B). In contrast, there appears to be mass loss in all components for the data corrected using the Ti correction factor.
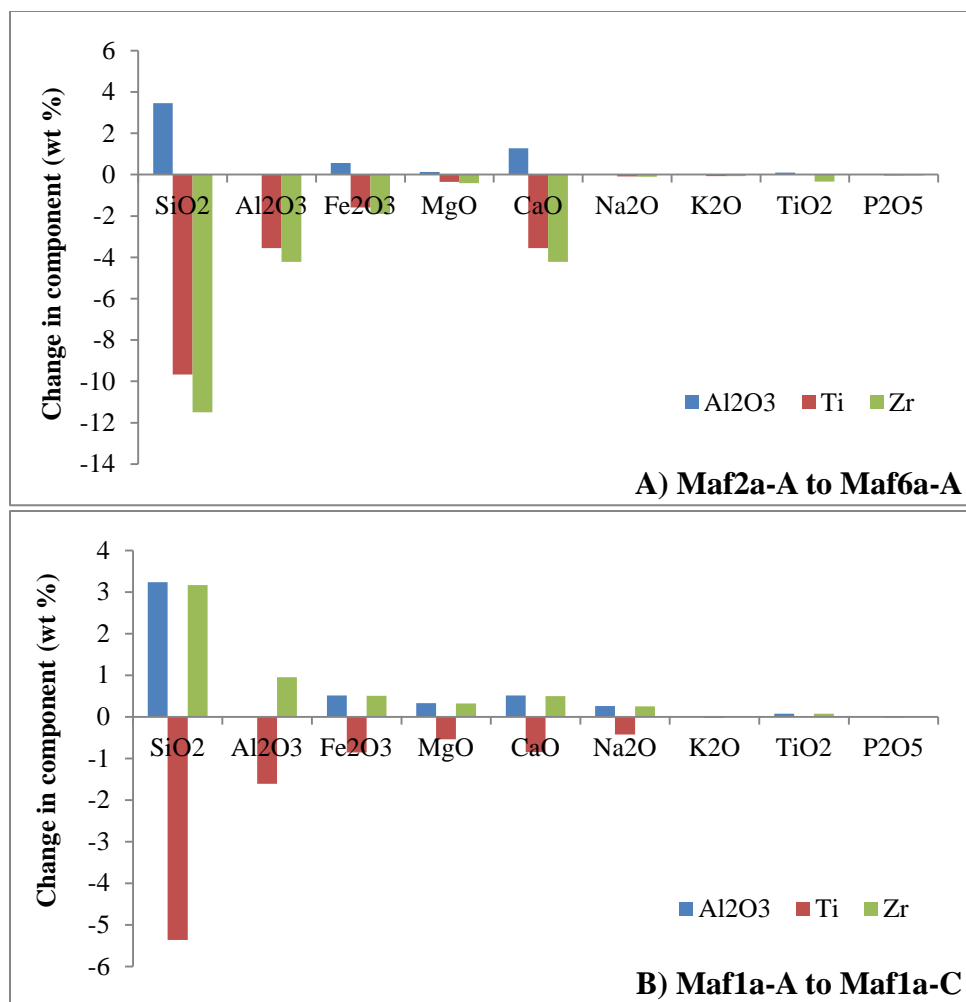
Figure 4.19: Mass change in major oxides for the alteration of Maf2a-A to Maf6a-A (A) and Maf1a-A to Maf1a-C (B) using correction factors based on the ratios of Al_2O_3, Ti, and Zr in the least altered rock to those of the most altered rock.

4.5 Comparison of least and most altered intermediate pillow lava flows

4.5.1 Gresens calculations

Similar to the alteration of Maf2a-A to Maf6a-A, the alteration reaction Int1-A to Int1-E was not isochemical, as shown by the wide range of calculated volume factors (Appendix E). In contrast with the mafic samples, results for data treated under the assumptions that there has been no change in volume , a 25% increase in volume, no change in Al_2O_3, and no change in TiO_2 (Fig. 4.20A-D) were consistent. In all four cases, there has been significant loss of Fe_2O_3, K_2O,

and MgO, and gain of SiO_2, CaO, Na_2O, and LOI. These results are also shown in Figures 4.21 and 4.22. The clustering of y-intercept points around $f_v=1.25$ in Figure 4.23 indicates that the alteration reaction resulted in a 25% volume increase. Significant mass changes in trace elements are summarized in Figure 4.24. Trace element data were treated under two assumptions: constant volume and a 25% increase in volume (Fig. 4.24A-B).
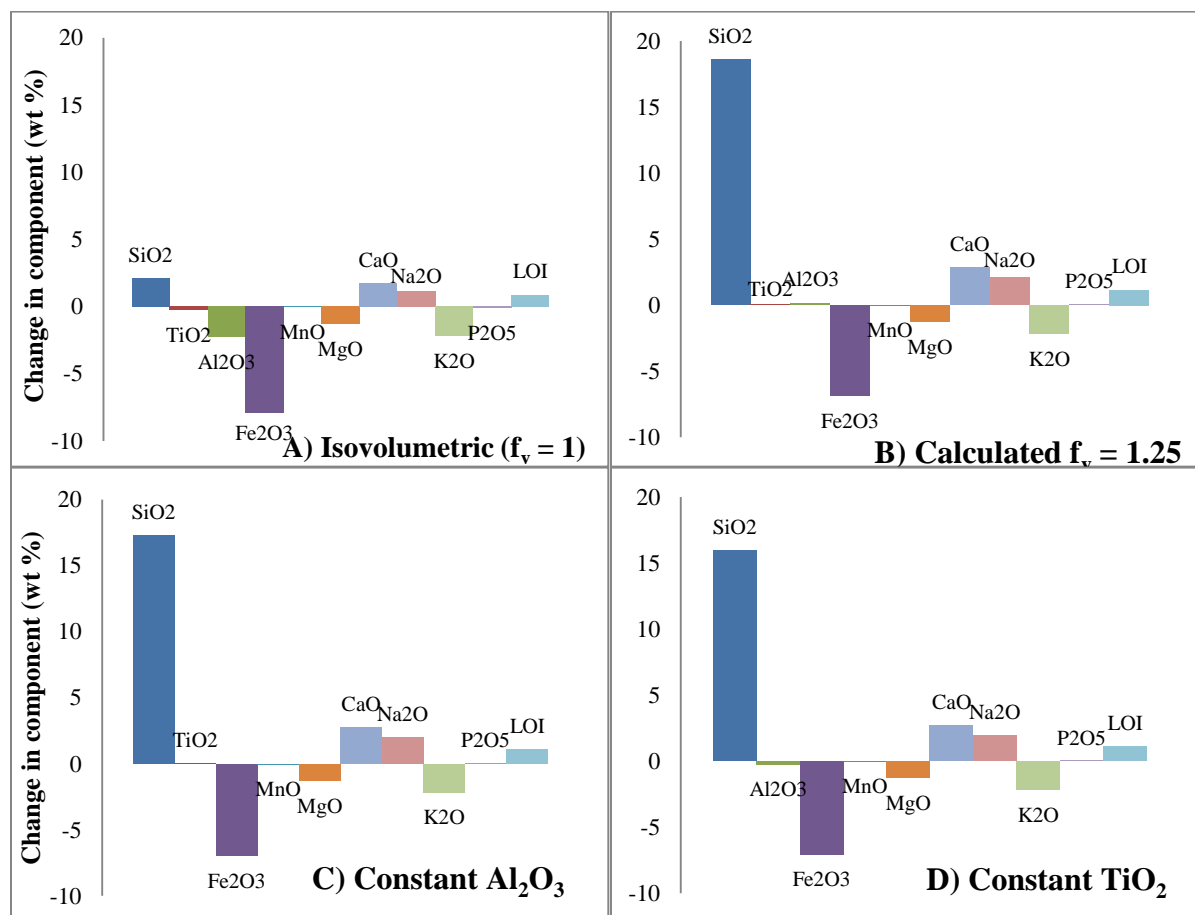
Figure 4.20: Graphical representation of mass change (in wt %) for the alteration of Int1-A to Int-E as calculated after Gresens (1967). (A) Reaction treated as isovolumetric (f_v =1), (B) reaction treated with f_v =1.25 (estimated volume factor from Fig. 4.23), (C) assuming constant Al_2O_3, and (D) assuming constant TiO_2.
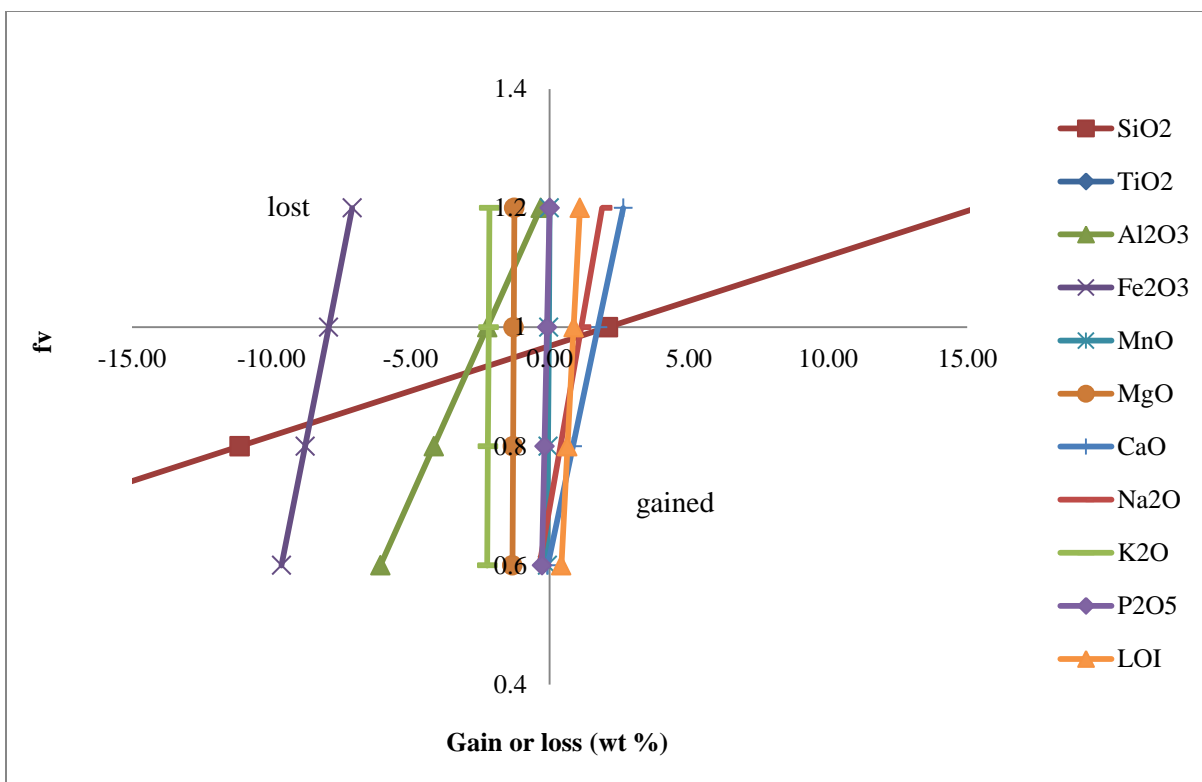
Figure 4.21: Composition-volume diagram (after Gresens, 1967) for the alteration of Int1-A to Int1-E.
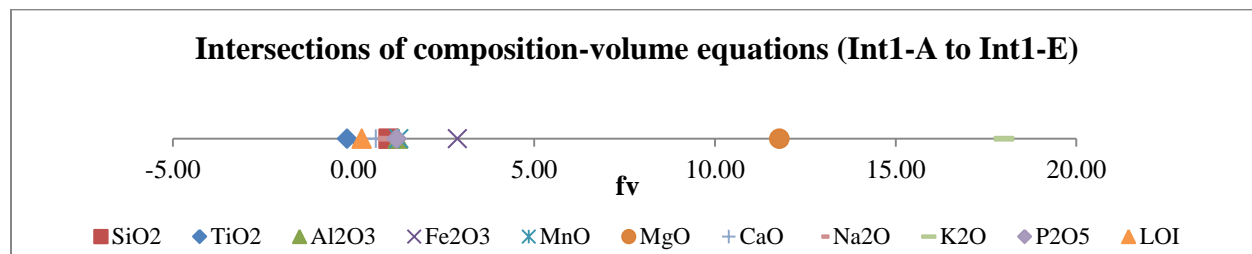
Figure 4.22: Y-intercept values for the composition-volume diagram shown in Fig. 4.21. This indicates mass loss of MgO and Fe_2O_3, and mass gain of LOI, SiO_2 and Na_2O. The interpreted volume factor is 1.25. After Gresens, 1967.
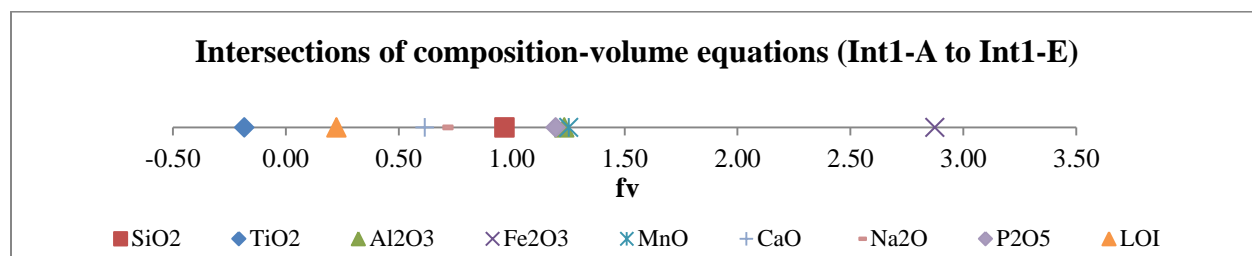
Figure 4.23: Y-intercept values for the composition-volume diagram shown in Fig. 4.21 modified to exclude Na_2O and MgO. The clustering of points around $f_v = 1.25$ indicates the reaction likely resulted in a volume gain of ~25%. After Gresens, 1967.
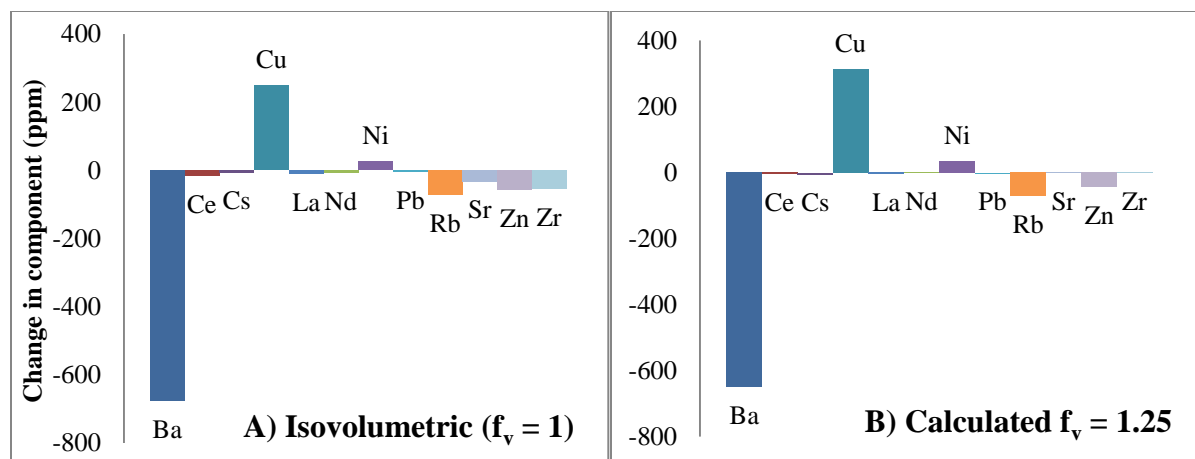
Figure 4.24: Trace element data for the alteration of Int1-A to Int1-E treated assuming that (A) volume remained constant, and (B) that a 25% increase in volume accompanied the alteration reactions.

4.5.2 Mass change calculations

In contrast with the mafic samples, the results of the mass change calculations based on correction factors of Al, Ti, and Zr in the intermediate samples are consistent for all the correction factors applied. For the alteration of Int1-A to Int1-E there appears to be loss of all components, most notably of SiO_2 (Fig. 4.25).
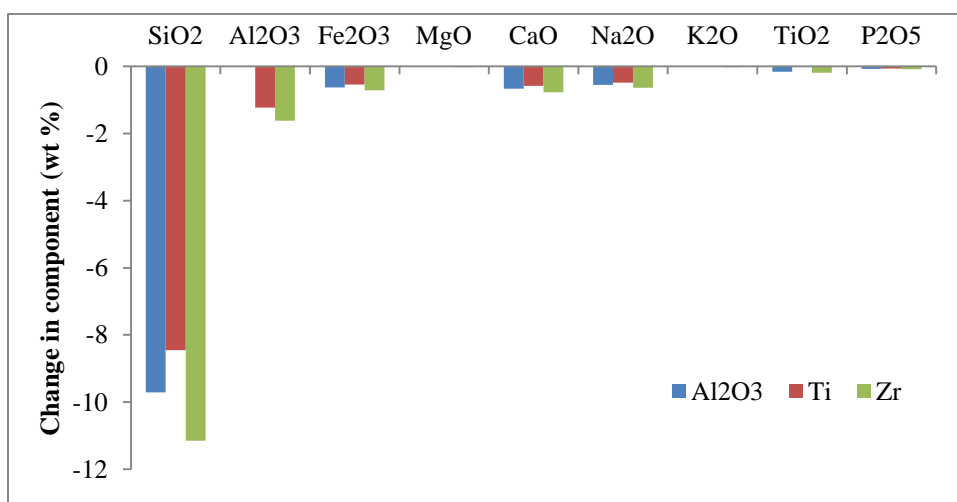
Figure 4.25: Mass change in major oxides for the alteration of Int1-A to Int1-E using correction factors based on the ratios of Al_2O_3, Ti, and Zr in the least altered rock to those of the most altered rock.

4.6 Summary of mass changes

Based on the results of the Gresens calculations, TiO_2 appears to be less mobile than Al_2O_3 (Figs. 4.10, 4.15, and 4.20). The calculations using the most likely volume factor for each reaction (Figs. 4.10B, 4.15B, and 4.20B) appear to be more reliable than those assuming constant volume (Figs. 4.10A, 4.15A, and 4.20A). The apparent mass loss of SiO_2 assuming constant Al_2O_3 and constant volume in the mafic samples requires the corrected SiO_2 value for the most altered sample to be equal to or greater than the amount of SiO_2 in the corresponding least altered sample. As the most altered samples typically contain more evidence of secondary quartz than the least altered samples, this seems unlikely. The assumptions that the alteration reactions proceeded with constant TiO_2, and with a 12% (Maf2a-A to Maf6a-A), 5% (Maf1a-A to Maf1a-C), and 25% (Int1-A to Int1-E) increase in volume therefore appear to be the most reasonable. Corrections of the data from the most altered samples using the mass change results from the Gresens calculations under these assumptions are summarized and compared to the original data for the least and most altered samples in Table 4.6.

Table 4.6: Summary of original and corrected data for major oxides and select trace elements. Data corrected according the mass change results of the Gresens calculations using the calculated volume factor for that reaction (e.g. Maf6a-A'), and assumed constant TiO_2 (e.g. Maf6a-A"). (*) Least altered sample.

	SiO$_2$ wt %	Al$_2$O$_3$ wt %	TiO$_2$ wt %	Fe$_2$O$_3$ wt %	MgO wt %	MnO wt %	CaO wt %	K$_2$O wt %	Na$_2$O wt %	P$_2$O$_5$ wt %	LOI wt %	Nb ppm	Y ppm	Zr Ppm
Maf2a-A*	55.63	16.37	1.67	9.85	3.83	0.22	6.87	0.15	4.43	0.25	0.06	6.70	25.80	110.20
Maf6a-A	47.99	17.64	1.39	7.90	1.73	0.11	17.64	0.33	0.40	0.20	4.14	5.30	18.00	88.90
Maf6a-A'	46.11	12.87	1.39	8.28	3.49	0.20	3.37	0.08	4.35	0.21	-0.76	5.65	22.23	92.57
Maf6a-A''	46.11	12.87	-	8.28	3.49	0.20	3.37	0.08	4.35	0.21	-0.76	-	-	-
Maf1a-A*	56.23	15.25	1.33	9.12	6.14	0.15	7.89	0.28	4.51	0.19	0.37	4.60	22.50	99.50
Maf1a-C	54.04	16.22	1.21	8.61	5.48	0.19	8.52	0.28	4.28	0.18	0.63	4.90	23.10	105.70
Maf1a-C'	53.62	14.47	1.27	8.70	5.88	0.14	7.48	0.27	4.30	0.18	0.34	-3.38	13.25	97.80
Maf1a-C''	50.93	13.66	-	8.27	5.60	0.13	7.05	0.25	4.09	0.17	0.31	-	-	-
Int1-A*	64.03	11.84	1.33	12.17	1.41	0.15	2.79	2.32	2.62	0.55	0.25	10.80	42.50	271.10
Int1-E	71.84	10.43	1.19	4.60	0.13	0.13	4.92	0.14	4.08	0.50	1.21	10.30	38.10	235.20
Int1-E'	53.22	10.27	1.15	11.48	1.39	0.13	2.05	2.30	2.01	0.47	0.07	10.10	37.88	235.09
Int1-E''	54.54	10.41	-	11.56	1.39	0.13	2.14	2.30	2.08	0.48	0.09	-	-	-

Plotting these corrected data along with the original data for the least and most altered samples on discrimination diagrams yields the results shown in Figure 4.26. With the corrected data, the SiO_2 content is much more reasonable for pillow lavas. The small changes in the corrected values of Nb, Y, and Zr indicate that these elements were relatively immobile (Fig. 4.26).
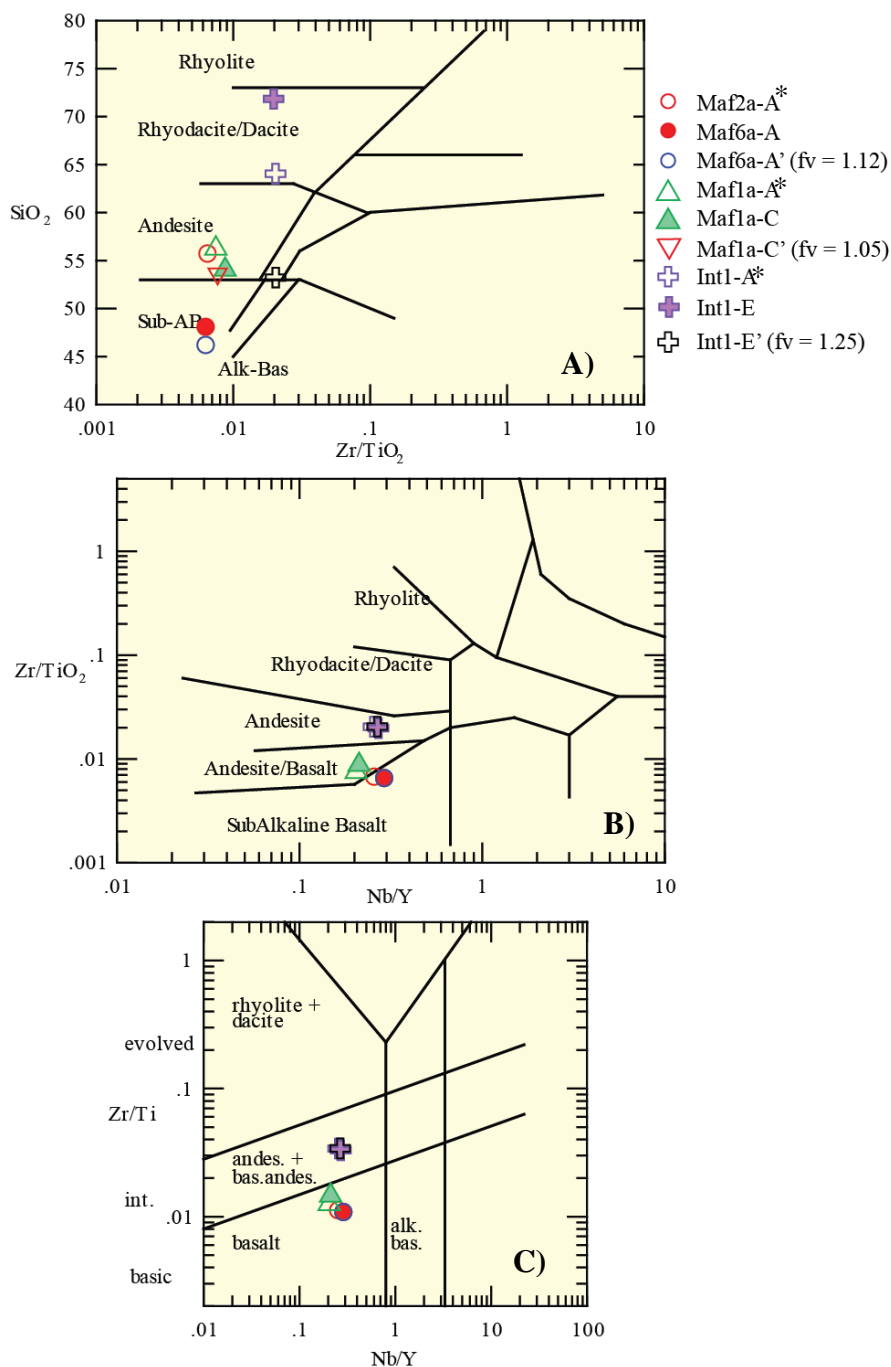
Figure 4.26: Discrimination diagrams showing the least altered samples (Maf2a-A*, Maf1a-A*, and Int1-A*), most altered samples (Maf6a-A, Maf1a-C, and Int1-E), and the most altered samples with data corrected using the most likely volume factor for each reaction in the Gresens calculations (Maf6a-A', Maf1a-C', and Int1-E'). Panel A illustrates the effect of silica mobility on the interpreted primary lithology. The corrected data for the most altered samples all plot within reasonable fields for a mafic or intermediate volcanic rock, whereas one of the most altered samples did not (Int1-E). Panels B and C illustrate the immobility of Zr, Ti, Nb, and Y, as there is little to no change in the interpreted lithologies based on the original and corrected data. Diagrams after Winchester & Floyd, (1977), and Pearce, (1996).

CHAPTER 5: Discussion

5.1 Petrogenetic significance of Eu anomalies

Several flows with negative Eu anomalies indicate that plagioclase fractionation was an important petrogenetic process. There are plagioclase phenocrysts in both mafic and intermediate samples, from ~5-15%. It is possible that, as a result of fractional crystallization, most of the plagioclase phenocrysts remained in the chamber as these melts were extruded, thereby producing the negative Eu anomalies. Alternatively, Eu may have been depleted in some samples that resided in oxidizing domains of a hydrothermal system (Kerrich & Wyman, 1996). Sample Maf6a-A has a pronounced positive Eu anomaly and plagioclase phenocrysts are common in its mafic rim. This sample may have formed in a reducing domain of a submarine hydrothermal alteration system, where Eu can be enriched (Kerrich & Wyman, 1996). The pale cream-green colour of the altered pillow core in Maf6a-A could reflect the reduction of iron in this sample, although the colour is more likely attributed to the presence of abundant epidote, quartz, and carbonate. Mafic flows 2a and 6a have opposing Eu anomalies, yet have similar geochemical signatures overall. It is possible that this reflects variable oxidizing/reducing conditions within the same lava flow, or between adjacent related flows. Alternatively, the variable Eu anomalies may reflect variable plagioclase fractionation and/or accumulation.

5.2 Tectonomagmatic environment

A summary of the interpreted magmatic affinities and defining trace element characteristics for each flow unit is given in Table 5.1. Data from all the flows indicate calc-alkaline affinity. Four flows are characterized by a transitional to mildly calc-alkaline affinity. The trace element patterns, which show LREE enrichment and relatively flat HREE, along with

the negative Nb, P, and Ti anomalies found in many flows, are typically attributed to volcanism in a suprasubduction zone magmatic arc environment (Kerrich & Wyman, 1996; Winter, 2010). This subduction-zone signature is present in all the samples, though it is less pronounced and/or lacks certain anomalies in flows of transitional to mildly calc-alkaline affinity.

If the geochemical signatures do reflect an arc setting, then the calc-alkaline pillow lava flows may be the product of submarine eruptions of basaltic to andesitic lava in an evolving volcanic arc or perhaps in a back-arc spreading centre (Fig. 5.1). The vesicle size and abundance in the pillows may indicate eruption in a shallow marine environment. Lambert (1988) interpreted the volcanic sequence in the Tumpline Lake subarea as the explosive, possibly shallow marine, eruption of voluminous felsic magmas from two or three volcanic centres, followed by the eruption of basaltic magma through the pile of overlying felsic volcanic rocks. According to Lambert, the pillow lavas may have filled the submarine topographic lows between and on the flanks of the felsic centres. This interpretation is based on the interpreted subaerial or shallow marine eruption of some felsic lava flows indicating the felsic centres were likely topographic highs; original topography is no longer discernible from field relations owing to variable strain. In terms of a possible magma source, the flat HREE pattern in the Sharrie Lake samples may indicate melting of a spinel peridotite at depths of 40-60 km (Corcoran & Dostal, 2001).

A suprasubduction zone setting is not, however, the only explanation for the geochemical signatures observed. Certain anomalies, such as Nb depletion, are also common where there has been crustal contamination by granitic material (Cousens, 2000). In a greenstone belt of similar age, the ca. 2.70-2.67 Ga Point Lake volcanic belt in the Slave Province, Corcoran (2001) found that εNd values indicated that some samples appear to have interacted with older sialic crust, but

this did not fully account for the calc-alkaline affinity and 'arc-like' characteristics of some units within the belt. Based on physical volcanology and geochemical studies, Corcoran interpreted that this volcanic sequence formed in a back-arc environment. Further work, particularly Nd isotope work, is needed to confirm whether the geochemical signatures in the Sharrie Lake samples indicate a subduction zone setting or crustal contamination.

Table 5.1: Summary of magmatic affinities and trace element pattern characteristics by flow unit, as described in section 4.2. Note that negative Nb, P, and Ti anomalies ("subduction zone signature" below) are commonly, but not necessarily, indicative of a subduction zone setting.

Flow unit	Magmatic Affinity	Trace Element Characteristics
Maf1a	Transitional to mildly calc-alkaline	Slight LREE enrichment. Subduction zone signature. Small negative Eu anomaly and small positive Zr anomaly.
Maf2a	Transitional to mildly calc-alkaline	Slight LREE enrichment and HREE depletion. Weak subduction zone signature. Lacks negative P and Ti anomalies.
Maf3a	Calc-alkaline	Moderate to strong LREE enrichment. Subduction zone signature. Enriched La and Ce, more pronounced negative P anomaly.
Maf4a	Calc-alkaline	Moderate to strong LREE enrichment. Strong subduction zone signature. Small negative Eu anomaly and small positive Zr anomaly.
Maf5a	Calc-alkaline	Moderate to strong LREE enrichment. Weak subduction zone signature. Lacks negative Eu and Ti anomalies.
Maf6a	Transitional to mildly calc-alkaline	Slight LREE enrichment and HREE depletion. Weak subduction zone signature. Positive Eu anomaly, negative Sm anomaly.
Int1	Strongly calc-alkaline	Strong LREE enrichment. Moderate subduction zone signature. Lacks negative P anomaly. Enriched in all components relative to other flows.
Int2	Calc-alkaline	Strong LREE enrichment. Strong subduction zone signature. Negative Eu anomaly.
Int3	Calc-alkaline	Strong LREE enrichment. Strong subduction zone signature. Pronounced negative Eu-Ti anomaly.
Int4	Transitional to mildly calc-alkaline	Moderate to strong LREE enrichment. Weak to moderate subduction zone signature. Small negative Nb, P and Ti anomalies.
Int5	Strongly calc-alkaline	Moderate to strong LREE enrichment. Moderate subduction zone signature. Lacks negative Eu-Ti anomaly. Pronounced positive Zr anomaly.

A) Extrusion of pillow lavas at seamounts in arc and back-arc environments

B) Pillow lavas erupting and flowing down the flanks of a seamount in A
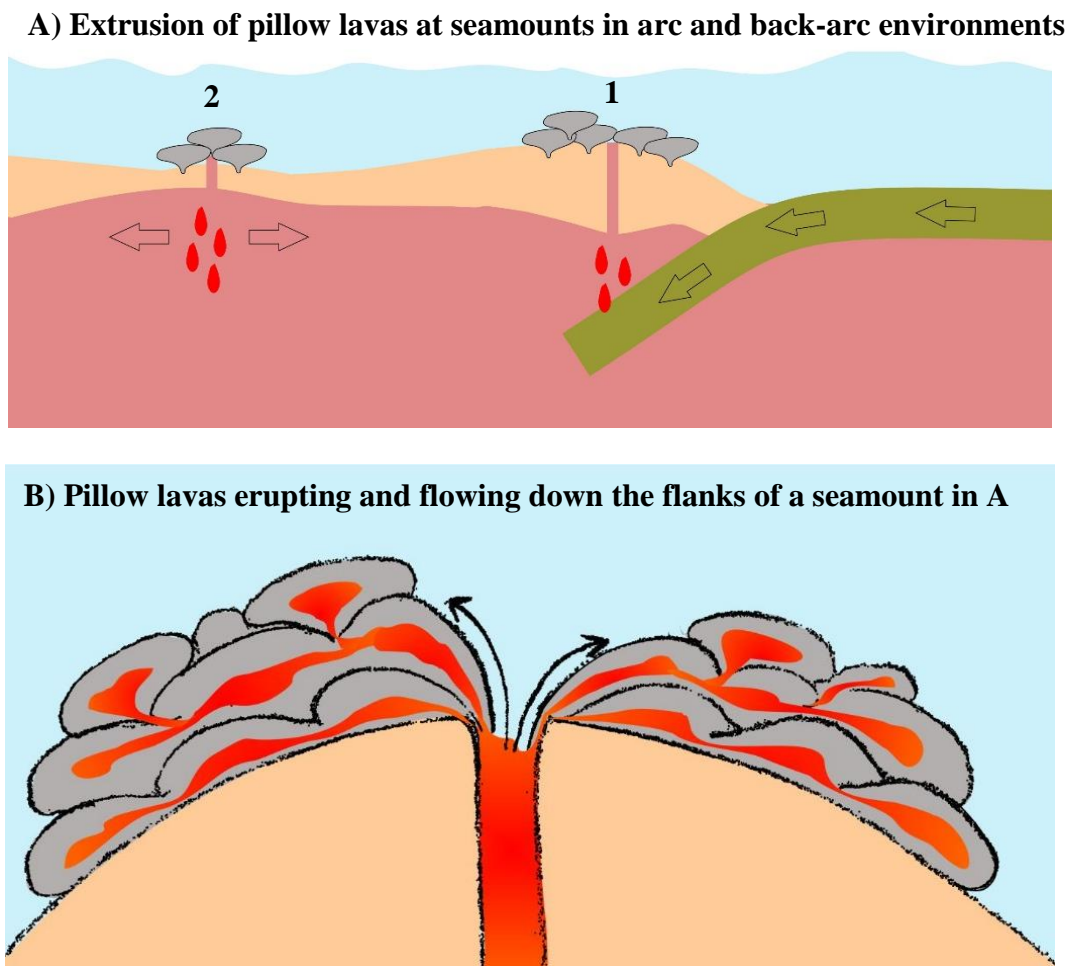
Figure 5.1: Schematic tectonic environment (A) for the mafic to intermediate pillow lava flows at Sharrie Lake based on the interpretation of their geochemical characteristics (trace element signatures and magmatic affinity) as 'arc-like'. If these geochemical signatures are the result of an arc origin, the pillow lavas may have been extruded at seamounts formed in the suprasubduction zone (1), or in the back-arc spreading centre (2). Relative plate motions (indicated by arrows) illustrate the convergent margin and divergent back-arc. A closer view of a seamount (B) illustrates the extrusion of the pillow lavas from a fissure, and pillow growth as the lava flows down the seamount flank.

5.3 Testing of the felsic volcanic inclusion hypothesis

The previous interpretation of the pale pillow cores (Fig. 1.2) in some mafic lava flows as trapped blocks of felsic volcanic rock (Lambert, 1988) is inconsistent with the results of this study. The textural similarity between the mafic rim and the altered core in sample Maf6a-A, and the secondary mineral assemblage in the pillow core, indicate that the pale core is altered

primary mafic material rather than a felsic volcanic xenolith. Alteration may have been

concentrated in the pillow core because of porosity and permeability differences between the rim

and core created by quenching of the pillow selvage and/or rim soon after eruption (Fig. 5.2).

Once the pillow selvage and/or rim became rigid and glassy it would have been protected from

further interaction with seawater; however, the core may have remained partially molten and

may have had greater porosity and permeability owing to the vesicles present (Fig. 5.3). Vesicles

are most common in the pillow core, although can be present in both the core and selvage. The

fluids circulating through the volcanic pile would likely access the route with the greatest

porosity and permeability, in this the case the pillow core. In doing so, the fluids would

preferentially alter the pillow core material.
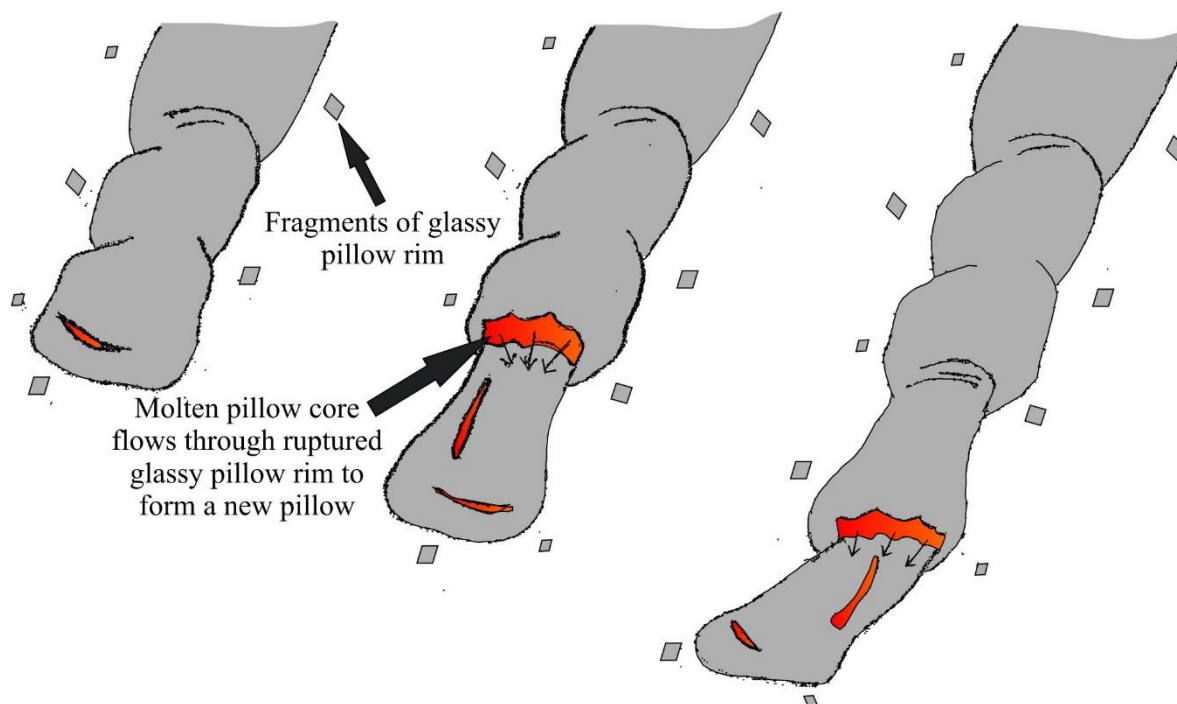
Figure 5.2: Growth of a pillow lobe as it travels down the flank of a seamount (side view of the seamount illustrated in Fig. 5.1B). The pillow selvage is quenched upon extrusion, forming a glassy crust on the pillow, which may break into fragments. Rupturing of the rigid pillow selvage allows the molten core material to continue flowing and form a new pillow. The growth of one pillow from another can be identified in the field, although it is obscured by strain.

A) t_0 (eruption)

Fluids access the pillow core via fractures in the rigid, glassy pillow selvage

Pillow core remains slightly molten

Glassy pillow selvage, quenched upon pillow extrusion and contact with seawater

Vesicles in the pillow core

Possible interstitial sediments between pillows

Fluid path with greatest porosity and permeability is through the pillow core
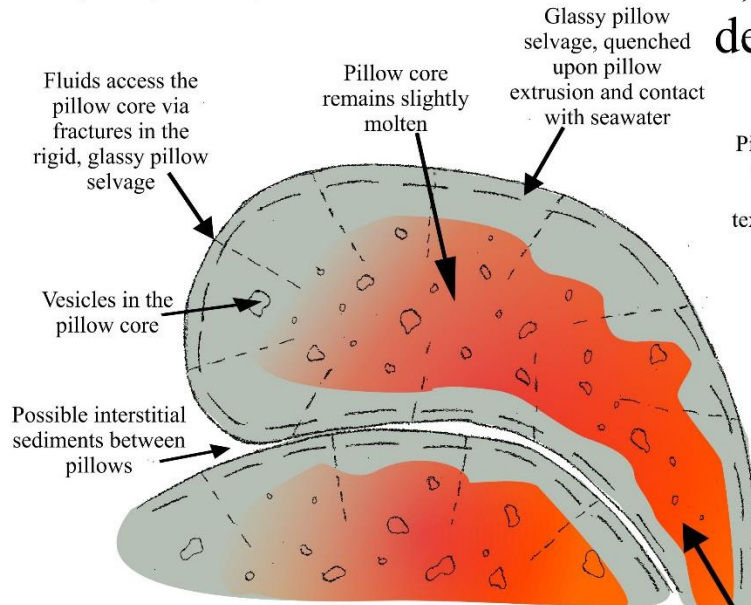
B) t_1 (post-seafloor alteration, pre-deformation, pre-metamorphism)

Selvage devitrified. Selvage and/or interstitial sediments altered to clay minerals and chlorite

Pillow rim retains some primary mineralogy ± textures (e.g. relict plagioclase phenocrysts)

Vesicles filled by secondary quartz and carbonate

Some pillow cores preferentially altered to ep+cc+qtz

C) t_2 (present geometry)

Selvage and/or interstitial sediments metamorphosed to biotite and amphibole ± garnet

Pillows flattened and elongated during regional deformation

Preferntially altered pillow cores appear pale or 'bleached' compared to pillow rim and selvage

Figure 5.3: Cross section through a pillow extruded along the flank of a seamount in Fig. 5.1 and 5.2. At t_0, immediately after eruption, the pillow selvage is quenched to form volcanic glass. Fractures in the rigid selvage may allow seawater-rock interaction by providing a fluid pathway to the core. Fluids also access the pillow through the slightly molten vesicular pillow core, where there is greater porosity and permeability. At t_1, early, possibly syn-volcanic, seafloor alteration processes begin to alter the pillow lava. The selvage is devitrified and altered to clay minerals and chlorite. Vesicles, fractures, and other pore space is filled with secondary quartz, carbonate, and rarely oxides and chlorite. In some mafic pillows, the inner core primary igneous mineralogy is completely altered to assemblages of quartz-carbonate-epidote and oxides. The pillow rim maintains some primary mineralogy and textures (e.g. relict plagioclase phenocrysts), as alteration is concentrated in the pillow core by fluid flow. Seafloor alteration is accompanied by loss of Fe_2O_3, MgO, Na_2O, and K_2O, and gain of SiO_2, CaO, and LOI. At t_2 (present), pillow appearance reflects seafloor alteration, regional deformation (D_1 and D_2), regional lower amphibolite facies metamorphism, and surface weathering processes. Pillow flattening defines the regional foliation (S_2), and elongated pillows also define the steeply-plunging lineation (L_1). Pillow selvages, previously clay- and chlorite-rich, have been metamorphosed to biotite, amphibole, and occasionally garnet. Secondary quartz and carbonate-filled amygdules have been deformed and recrystallized. Mineral compositions (e.g. plagioclase and epidote) have been modified during metamorphism. Metamorphic mineral compositions (e.g. notably Mg-poor garnet) reflect changes in bulk rock geochemistry as a result of alteration.

5.4 Characterizing alteration

The variable element mobility, particularly of the high field strength and rare earth elements, in some flows may indicate that fluids involved in alteration processes varied between flows. In flow Intermediate 1, for example, the LREE, Eu, Ho, Tm, Ta, Nb, and Th all appear to have been mobilized. The mobility of LREE, particularly in conditions of intense fluid-rock interaction, has been well documented (Hellman *et al.,* 1979; Ludden & Thompson, 1978). Under high water/rock ratios or in cases of significant carbonate alteration, LREE are thought to be more susceptible to secondary processes than the MREE or HREE (Kerrich & Wyman, 1996). For instance, Ludden and Thompson (1978) suggested that low-temperature seafloor alteration of mid-ocean ridge basalts can result in flat or enriched LREE/HREE and can lead to false interpretations of the REE pattern. The apparent mobility of specific LREE in the Sharrie Lake sample set may therefore be attributed to seafloor alteration, particularly carbonate alteration.

The moderate to poor correlations ($r = 0.74-0.86$) of several HREE with Zr in the mafic flows demonstrates that these elements may have been mobilized. Although the HREE are generally thought to be immobile during seafloor hydrothermal alteration and up to greenschist facies metamorphism (Kerrich & Wyman, 1996), fluids rich in phosphate, fluorine, and chlorine ions can mobilize the REE by forming complexes (Pan & Fleet, 1996; Wood, 1990). Carbonate complexes may also play a role in this process, though with increasing temperature fluoride complexes dominate. Trivalent REE are also known to form strong complexes with phosphate at low temperatures, a process that may be indicated by the presence of phosphate-bearing phases (e.g., apatite). The rare apatite present in the matrix and as inclusions in garnet in at least two samples of the Intermediate 1 flow unit is likely primary igneous in origin, however an apatite crystal within a quartz and carbonate vein indicates apatite may also be a secondary phase. If fluorine-rich fluids were the cause of REE mobility, varying amounts of fluorine may have been incorporated into apatite, amphibole (generally calcic amphibole), and biotite in the altered samples (Deer *et al.,* 1997). This cannot be confirmed as no analyses of fluorine were obtained in this study. Apparent mobility of other HFSE (V and Ta), as well as in Cs and Pb, may be due to the values of these elements approaching their respective detection limits (see Appendix D for complete set of analyses). Alternatively, the moderate to poor correlations in question may reflect primary igneous compositional variations.

Field evidence of alteration indicates local zones of silica, sericite, and carbonate enrichment. A petrographic analysis revealed that the secondary mineral assemblage consists of carbonate, quartz, epidote, chlorite and sericite (Ch. 3). Mineral compositions indicate that plagioclase is Na-rich in both mafic and intermediate samples. Secondary carbonate and quartz

filling vesicles, disseminated carbonate throughout the matrix, and fine- to medium-grained epidote constitute the dominant alteration minerals.

In the Gresens calculations, the gain in CaO and LOI in each of the three altered samples is likely due to carbonate formation. All the altered samples (Maf6a-A, Maf1a-C and Int1-E) contain carbonate amygdules and/or significant matrix carbonate. Other Ca-rich phases present in these samples include epidote, titanite, and apatite. The loss of Na_2O and slight gain of K_2O in the alteration of Maf2a-A to Maf6a-A may be due to sericitization as shown in reaction 2 (section 4.3.3). The mass gain in SiO_2 in the alteration from Int1-A to Int1-E is likely due to the abundant quartz-filled vesicles in Int1-E.

The volume factors calculated for the three sets of samples demonstrate that alteration resulted in the following volume increases: 12% (Maf2a-A to Maf6a-A), 5% (Maf1a-A to Maf1a-C), and 25% (Int1-A to Int1-E). These interpreted changes in volume are too high relative to the volume of amygdules or veins in each sample. In the first comparison, the volume increase of 12% may have been accommodated by abundant veins present in Maf6a-A, filled predominantly with quartz, and by carbonate filling void spaces in the rock. Similarly, the more reasonable 5% volume increase in Maf1a-C is consistent with field observations, which recorded 5-10% quartz and carbonate amygdules by volume at this location. Although sample Int1-E is highly amygdaloidal, the proposed 25% increase in volume is significantly greater that the ~10% amygdules by volume recorded in the field.

The alteration box plot of CCPI versus AI suggests that the samples have undergone epidote-carbonate ± albite alteration, with minor albite-chlorite and carbonate-sericite alteration. This alteration was likely associated with diagenetic (seafloor alteration) processes, with a weak hydrothermal signature indicated by the carbonate-sericite alteration (Large *et al.,* 2001).

Seafloor diagenetic processes are typified by devitrification of volcanic glass to form clays, feldspars, zeolites, carbonates, quartz, and oxides (Munha & Kerrich, 1980; Gifkins *et al.*, 2005). Under greenschist facies metamorphic conditions, these minerals are altered to albite, K-feldspar, carbonate, chlorite, and epidote (Large *et al.,* 2001; Bonnet & Corriveau, 2007). If the secondary mineral assemblage (carbonate-quartz-epidote-chlorite-sericite) present in the Sharrie Lake samples represents the original alteration assemblage, the dominant alteration type was likely carbonate propylitic (Bonnet & Corriveau, 2007; Gifkins *et al.*, 2005). In this case, mafic minerals (probably clinopyroxene) would have been replaced by chlorite, epidote and carbonate, and plagioclase by epidote, carbonate and sericite (Wilshire, 1957; Gifkins *et al.*, 2005).

The effects of the ~500 °C peak metamorphism on this assemblage, however, cannot be ignored. The secondary mineral assemblage likely reflects the combined effects of the early alteration and the lower amphibolite facies metamorphism. For this reason the exact timing of epidote formation is ambiguous; it was likely a by-product of early plagioclase alteration, but could also have formed, and was likely modified, during metamorphism. The sodic plagioclase composition (An_{22-41}) likely reflects the combined effects of alteration and the metamorphic overprint rather than a primary composition. Similarly, the variable composition of some metamorphic minerals reflects local changes in bulk composition as a result of heterogeneous mass change in some components during early alteration. Garnet compositions in Int1-A and Int1-E are notably Mg-poor ($X_{pyr} = 0.02$-0.03), probably reflecting the effect of Mg-loss during alteration.

5.5 Relative timing of alteration, deformation, and metamorphism

The presence of the most abundant secondary minerals, quartz and carbonate, as vesicle- and vein-filling phases indicates that they are early secondary phases. Epidote is also interpreted as an early secondary phase, although it may also have formed, or have been modified, during later metamorphism. The geochemical characterization of this alteration assemblage (see Fig. 4.9) also suggests early diagenetic (seafloor) alteration processes. These minerals likely formed soon after emplacement of the pillow lavas in a shallow marine environment. The alteration was most certainly pre-kinematic and pre-metamorphic as shown by the heterogeneous nature of the alteration, the recrystallized quartz and carbonate, and the deformed amygdules. The timing of chlorite and sericite formation is more ambiguous. Chlorite may have experienced two stages of growth: first as an early secondary mineral in pillow selvages and rare amygdules, and later as a retrograde phase replacing biotite and amphibole. Peak greenschist to lower amphibolite facies metamorphism was syn- to post-kinematic with respect to the dominant S_2 foliation, based on syn- to post-foliation hornblende growth and post- foliation garnet growth. The alteration, deformation, and metamorphic history of the Sharrie Lake pillow lavas is illustrated in Figure 5.3.A summary of the crystallization sequence of primary, early secondary (seafloor alteration), metamorphic, and late (retrograde) minerals is presented in Figure 5.4.

Interpreted timing of crystallization

Possible timing of crystallization (timing obscured or ambiguous)

Textural or compositional change, or alteration of an existing mineral

S_1 L_1 S_2

Eruption of pillow lavas (ca. 2680 Ma)

D_1 (ca. 2660-2630 Ma)

D_2 (ca. 2605-2580 Ma)
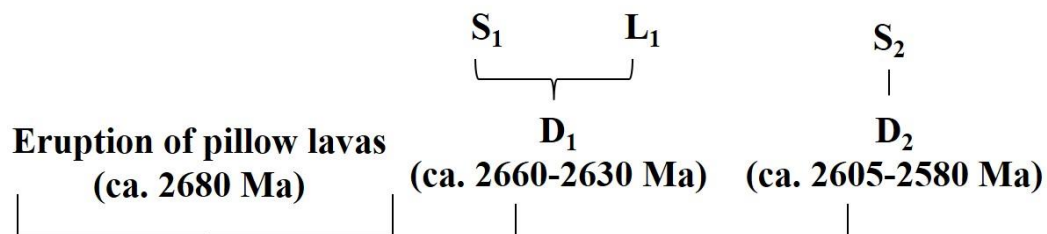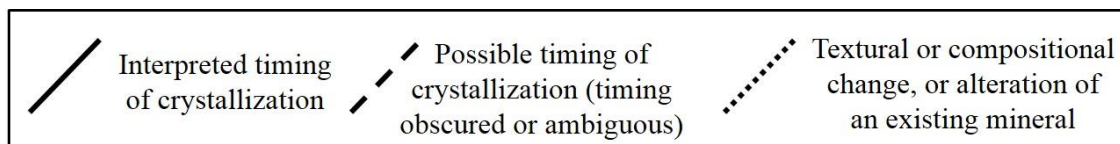
Mineral	Primary	Early Secondary	Metamorphic	Late
Plagioclase phenocrysts		Alteration to albite	Modified X to An $_{22-41}$	
Matrix (qtz+fspar)			Recrystallized	
Ilmenite		Replaced by Ttn		
Epidote			Modified X	
Quartz*			Recrystallized	
Carbonate				
Sericite				
Chlorite				
Titanite				
Apatite				
Pyrrhotite				
Biotite				Replaced by Chl
Amphibole				
Garnet				

Figure 5.4: Sequence of crystallization of primary, early secondary (seafloor alteration products), metamorphic, and late (retrograde) minerals in the mafic and intermediate pillow lavas sampled around Sharrie Lake. Timing of regional deformation (D_1 and D_2) and metamorphism shown to place the timing of local foliation (S_1 and S_2) and lineation (L_1) development in a regional context. (Modified X = original mineral composition modified during metamorphism, Replaced by = partially replaced by another mineral, and * = secondary).

5.6 VMS potential

Some of the necessary components for a VMS system may be present at Sharrie Lake in the form of intrusions that may have been subvolcanic, and faults and fractures that may have acted as pathways for hydrothermal fluids to circulate within the volcanic pile. The secondary mineral assemblage and geochemistry of the mafic to intermediate pillow lavas at Sharrie Lake indicate that alteration was likely early and possibly syn-volcanic. This alteration likely involved heterogeneous hydrothermal fluid-rock interaction, as shown by selective alteration of pillow cores. There are sparse visible sulphides in some of the mafic to intermediate samples, typically pyrrhotite and pyrite, and gossanous zones are common at sediment-volcanic and mafic-felsic volcanic interfaces around Sharrie Lake. Mass changes in trace elements indicate that, for the three least altered - most altered sample pairs analysed, there is an increase net change in Cu (up to 311 ppm), Ni (up to 103 ppm), and Zn (up to 33 ppm).

Although these concentrations are far from minimum commodity grades, there are nearby VMS-style mineral showings reported in the Northern Minerals Database (NORMIN.db) (Jackson *et al.,* 2013). One such showing, approximately 3.5 km east of the Sharrie Lake field area, yielded >5000 ppm Pb, 36500 ppm Zn, 199 ppb Au, 294 ppm Ag, and 442 ppm Cu (Jackson *et al.,* 2013). Other known VMS-type deposits within the CBVB include the Sunrise Zn-Pb-Ag-Au deposit and the Turnback/XL Zn-Ag-Cu-Pb deposit (Roscoe & Wallis, 2003; NTGO Showing Report, 2011). Preliminary geochemical results from Sharrie Lake felsic

volcanic rocks indicate that they are FII rhyolites according to the Superior classification and yield similar REE patterns to those from felsic volcanic rocks of the Sunrise deposit (Lesher *et al.,* 1986; Barrie *et al.,* 1993; Berger *et al.,* 2013). Owing to the sampling strategy used in this study, it was not possible to delineate zones of alteration typically diagnostic of VMS-style mineralization. Nonetheless, there are indications that the volcanic belt at Sharrie Lake may warrant further exploration.

CHAPTER 6: Conclusions and recommendations

6.1 Conclusions

1) Primary compositional heterogeneities between flow units exist in the pillow lava flows
   at Sharrie Lake, with interpreted primary lithologies including subalkaline basalt, basaltic
   andesite, and andesite. Furthermore, there was good consistency between mapped
   lithology and true primary lithology.

2) The pillow lavas are predominantly of calc-alkaline magmatic affinity and have trace
   element patterns indicating a possible subduction zone signature. These pillows may have
   formed in a submarine or shallow marine environment within an evolving arc or back-arc
   system.

3) Pillow lavas mapped as mafic and intermediate contain broadly similar mineral
   assemblages, with key differences being in metamorphic assemblages, plagioclase
   composition, and abundance of epidote.

4) In contrast to Lambert's interpretation, the pale mafic pillow cores are not inclusions of
   felsic volcanic rock but are rather altered primary mafic material.

5) The secondary mineral assemblage present in both mafic and intermediate pillow lavas
   consists of carbonate, quartz, epidote, chlorite, and sericite. Alteration was early, possibly
   syn-volcanic, and likely related to seafloor alteration processes. Alteration was certainly
   pre-kinematic and pre-metamorphic with respect to the variably developed foliation and

lower amphibolite facies metamorphism (~500 ± 25 ˚C and ~4 ± 2 kbar), and probably influenced the subsequent metamorphic mineral assemblage.

6) The alteration may be characterized as carbonate propylitic-type alteration if the secondary mineral assemblage represents the alteration assemblage. However, it is more likely that the present assemblage and mineral compositions represent a combination of the seafloor alteration mineralogy and later metamorphic overprint.

7) Due to the nature of this study, no distinct alteration zones could be identified to evaluate the prospectivity of the volcanic rocks at Sharrie Lake as a potential VMS-environment. There are, however, several indications (visible sulphides, gossanous zones, evidence of significant fluid-rock interaction, and similarity of felsic REE patterns to nearby known VMS-type deposits) that Sharrie Lake may warrant further study.

6.2 Recommendations for further study

To verify the interpretation that the pale mafic pillow cores are an alteration feature, more samples of such pillows should be collected for petrographic analysis. Furthermore, the mafic rim on such pillows should be removed and documented separately from the pillow core prior to geochemical analysis to better constrain the whole-rock geochemistry of these highly dissimilar domains. As fluid-rock interaction appears played a significant role in the alteration of the pillow lavas, further studies could focus on constraining the fluid composition. If there are suitable fluid inclusions within the samples, a fluid inclusions study supplemented by more data on the fluid content of the dominant minerals (e.g. F in amphibole and biotite) could constrain the fluid

composition(s). Isotope studies, particularly of Nd isotopes, would be of great value in delineating whether the subduction zone geochemical signature in the mafic to intermediate pillow lavas can be attributed to a subduction zone setting or to crustal contamination. Forthcoming studies related to the NTGO Banting-VMS project on the geochemistry, geochronology, and isotope characteristics of the Sharrie Lake volcanic rocks will augment the geochemical characterization presented in this study.

REFERENCES

Barrie, C.T., Ludden, J.N., and Green, T.H. 1993. Geochemistry of volcanic rocks associated with Cu-Zn and Ni-Cu deposits in the Abitibi subprovince. Economic Geology, **88:** 1341-1358.

Barrett, T.J. and MacLean, W.H. 1991. Chemical, mass, and oxygen-isotopic changes during extreme hydrothermal alteration of an Archean rhyolite, Noranda. Economic Geology, **86:** 406-414.

Barrett, T.J., Cattalani, S., and MacLean, W.H. 1993. Volcanic lithogeochemistry and alteration at the Delbridge massive sulfide deposit, Noranda, Quebec. Journal of Geochemical Exploration, **48:** 135-173.

Berger, A., Cousens, B., Williams, B., Ootes, L., and Jackson, V.A. 2013. Geochemistry of the Archean volcanic rocks around the Sleepy Dragon Complex, Northwest Territories. *In* 41st Annual Yellowknife Geoscience Forum Abstracts. *Compiled by* D. Irwin; Northwest Territories Geoscience Office, Yellowknife, NT. YKGSF Abstracts Volume 2013.

Bleeker, W. 1996. Thematic structural studies in the Slave Province Northwest Territories: the Sleepy Dragon Complex. *In* Current Research 1996-C. Geological Survey of Canada: 37-48.

Bleeker, W., Ketchum, J.W.F., Jackson, V.A., and Villeneuve, M.E. 1999a. The Central Slave Basement Complex, Part I: its structural topology and autochthonous cover. Canadian Journal of Earth Sciences, **36**: 1083-1109.

Bleeker, W. Ketchum, J.W.F., and Davis, W.J. 1999b. The Central Slave Basement Complex, Part II: age and tectonic significance of high-strain zones along the basement-cover contact. Canadian Journal of Earth Sciences, **36**: 1111-1130.

Bleeker, W. 2001. The ca. 2680 Ma Raquette Lake Formation and correlative units across the Slave Province, Northwest Territories: evidence for a craton-scale overlap sequence. Geological Survey of Canada, Current Research 2001-C7.

Bleeker, W., and Hall, B. 2007. The Slave Craton: Geology and metallogenic evolution. *In* Mineral Deposits of Canada: A Synthesis of Major Deposit-Types, District Metallogeny, the Evolution of Geological Provinces, and Exploration Methods. *Edited by* W.D. Goodfellow. Geological Association of Canada, Mineral Deposits Division, Special Publication No. 5, p. 849-879.

Bonnet, A.-L., and Corriveau, L. 2007. Alteration vectors to metamorphosed hydrothermal systems in gneissic terranes. *In* Mineral deposits of Canada - A synthesis of major deposit types, district metallogeny, the evolution of geological provinces, and exploration methods. *Edited by* W.D. Goodfellow. Geological Association of Canada, Mineral Deposits Division, Special Publication, **5:** 1035-1049.

Bowring, S.A., and Williams, I.S. 1999. Priscoan (4.00-4.03 Ga) orthogneisses from northwestern Canada. Contributions to Mineralogy and Petrology, **134:** 3-16.

Card, K.D. and King, J.E. 1992. The tectonic evolution of the Superior and Slave provinces of the Canadian Shield: introduction. Canadian Journal of Earth Sciences, **29**: 2059-2065.

Condie, K.C., and Baragar, W.R.A. 1974. Rare-earth element distributions in volcanic rocks from Archean greenstone belts. Contributions to Mineralogy and Petrology, **45**: 237-348.

Corcoran, P.L. 2001. Physical volcanology, geochemistry, and tectonic evolution of three selected areas in the Point Lake and Beaulieu River volcanic belts, Slave Province, Northwest Territories, Canada. Ph.D. Thesis, Department of Earth Sciences, Dalhousie University, Halifax, N.S.

Corcoran, P. L., and Dostal, J. 2001. Development of an ancient back-arc basin overlying continental crust: the Archean Peltier Formation, Northwest Territories, Canada. Journal of Geology, **109:** 3, 329-348.

Cousens, B. L. 2000. Geochemistry of the Archean Kam Group, Yellowknife Greenstone Belt, Slave Province, Canada. Journal of Geology, **108:** 181–197.

Cousens, B., Facey, K., and Falck, H. 2002. Geochemistry of the late Archean Banting Group, Yellowknife greenstone belt, Slave Province, Canada: simultaneous melting of upper mantle and juvenile mafic crust. Canadian Journal of Earth Sciences, **39**: 1635-1656.

Cousens, B., Falck, H., Ootes, L., Jackson, V., Mueller, W., Corcoran, P., Finnigan, C., van Hees, E., Facey, C., and Alcazar, A. 2005. Regional correlations, tectonic settings, and stratigraphic solutions in the Yellowknife greenstone belt and adjacent areas from geochemical and Sm-Nd isotopic analyses of volcanic and plutonic rocks; Chapter 9. *In* Gold in the Yellowknife Greenstone Belt, Northwest Territories: Results of the EXTECH III Multidisciplinary Research Project. *Edited by* C.D. Anglin, H. Falck, D.F. Wright and E.J. Ambrose; Geological Association of Canada, Mineral Deposits Division, Special Paper No. 3.

Davis, W.J., and Bleeker, W. 1999. Timing of plutonism, deformation, and metamorphism in the Yellowknife Domain, Slave Province, Canada. Canadian Journal of Earth Sciences, **36:** 7, 1169-1187.

Deer, W. A., Howie, R. A., Zussman, J., and Geological society of London. 1997. *Rock-forming minerals: Vol. 2B, Double-chain silicates.* London: Geological Society.

EduMine. Professional development and training for mining and the geosciences: Average specific gravity of various rock types [online]. Available from http://www.edumine.com/xtoolkit/tables/sgtables.htm [cited January 7, 2014].

Ferguson, M.E., Waldron, J.W.F., and Bleeker, W. 2005. The Archean deep-marine environment: turbidite architecture of the Burwash Formation, Slave Province, Northwest Territories. Canadian Journal of Earth Sciences, **42**: 935-954.

Franklin, J.M., Gibson, H.L., Jonasson, I.R., and Galley, A.G. 2005. Volcanogenic Massive Sulphide Deposits. Economic Geology 100th Anniversary Volume. Society of Economic Geologists, Inc. pp. 523-560.

Galley, A.G., Hannington, M.D., and Jonasson, I.R., 2007. Volcanogenic massive sulphide deposits. *In* Mineral Deposits of Canada: A Synthesis of Major Deposit-Types, District Metallogeny, the Evolution of Geological Provinces, and Exploration Methods. *Edited by* W.D. Goodfellow. Geological Association of Canada, Mineral Deposits Division, Special Publication No. 5, p. 141-161.

Gifkins, C., Herrmann, W., and Large, R. 2005. *Altered volcanic rocks: A guide to description and interpretation*. Tasmania, Australia: Centre for Ore Deposit Research, University of Tasmania, Australia.

Gresens, R.L. 1967. Composition-volume relationships of metasomatism. Chemical Geology, **2:** 47-65.

Goodwin, A.M., Lambert, M.B., and Ujike, O. 2006. Geochemical and metallogenic relations in volcanic rocks of the southern Slave Province: implications for late Neoarchean tectonics. Canadian Journal of Earth Sciences, **43**: 1835-1857.

Graham, C.M., and Powell, R. 1984. A garnet-hornblende geothermometer: calibration, testing, and application to the Pelona Schist, Southern California. Journal of Metamorphic Geology, **2:** 1, 13-31.

Hellman, P.L., Smith, R.E., and Henderson, P. 1979. The mobility of the rare earth elements: evidence and implications from selected terrains affected burial metamorphism. Contributions to mineralogy and petrology, **71:** 23-44.

Helmstaedt, H., and Padgham, W.A. 1986. A new look at the stratigraphy of the Yellowknife Supergroup at Yellowknife, NWT. - Implications for the age of gold-bearing shear zones and Archean basin evolution. Canadian Journal of Earth Sciences, **23**: 454-475.

Henderson, J. B. 1970. Stratigraphy of the Archean Yellowknife Supergroup, Yellowknife Bay - Prosperous Lake area, District of Mackenzie. Geological Survey of Canada, Paper 70-26.

Henderson, J.B. 1985a. Geology of the Yellowknife – Hearne Lake area, District of Mackenzie: a segment across an Archean basin. Geological Survey of Canada, Memoir 414.

Henderson, J.B., 1985b. Geology, Yellowknife – Hearne Lake, District of Mackenzie, NWT; Geological Survey of Canada, Map 1601A, scale 1:250 000.

Isachsen, C. E., Bowring, S. A., and Padgham, W. A. 1991. U-Pb Zircon Geochronology of the Yellowknife Volcanic Belt, NWT, Canada: New Constraints on the Timing and Duration of Greenstone Belt Magmatism. The Journal of Geology, **99:** 1, 55-67.

Isachsen, C.E., and Bowring, S.A. 1997. The Bell Lake Group and Anton Complex. A basement-cover sequence beneath the Archean Yellowknife greenstone belt revealed and implicated in greenstone belt formation. Canadian Journal of Earth Sciences, **34**:169-189.

Ishikawa, Y., Sawaguchi, T., Iwaya, S., and Horiuchi, M. 1976. Delineation of prospecting targets for Kuroko deposits based on modes of volcanism of underlying dacite and alteration halos: Mining Geology, **26:**105–117 (in Japanese with English abs.).

Jackson, V.A., and Ootes, L. 2012. The Banting Group VMS Project: results and speculations from 2012 (Sharrie Lake, NTS 85I). *In* 40th Annual Yellowknife Geoscience Forum Abstracts. *Compiled by* D. M. Watson; Northwest Territories Geoscience Office, Yellowknife, NT. YKGSF Abstracts Volume 2012.

Jackson, V.A., Ootes, L., Hamilton, M., Berger, A., Williams, B., and McGoldrick, S. 2013. The Banting Group VMS Project: results from bedrock mapping in 2013. *In* 41st Annual Yellowknife Geoscience Forum Abstracts. *Compiled by* D. Irwin; Northwest Territories Geoscience Office, Yellowknife, NT. YKGSF Abstracts Volume 2013.

Kerrich, R., and Wyman, D.A. 1996. The trace element systematics of igneous rocks in mineral exploration: an overview. *In* Trace element geochemistry of volcanic rocks: applications for massive sulphide exploration. *Edited by* D.A., Wyman. Geological Association of Canada, Short Course Notes, **12:** 1-50.

Ketchum, J.W.F., Bleeker, W., and Stern, R.A. 2004. Evolution of an Archean basement complex and its autochthonous cover, southern Slave Province, Canada. Precambrian Research, **135:** 149-176.

Kohn, M.J., and Spear, F.S. 1990. Two new barometers for garnet amphibolites, with applications to southeastern Vermont. American Mineralogist, **75:** 89-96.

Krogh Ravna, E. 2000. Distribution of Fe^{2+} and Mg between coexisting garnet and hornblende in synthetic and natural systems: an empirical calibration of the garnet-hornblende Fe-Mg geothermometer. Lithos, **53:** 265-277.

Kusky, T.M. 1990. Evidence for Archean ocean opening and closing in the southern Slave Province. Tectonics, **9**: 1533-1563.

Lambert, M.B. 1988. Cameron River and Beaulieu River volcanic belts of the Archean Yellowknife Supergroup, District of Mackenzie, Northwest Territories. Geological Survey of Canada, Bulletin 382, 145 p.

Large, R.R., Gemmell, J.B., and Paulick, H. 2001. The alteration box plot: a simple approach to understanding the relationship between alteration mineralogy and lithogeochemistry associated with volcanic-hosted massive sulfide deposits. Economic Geology, **96:** 957-971.

LeMaitre, R. W. 1989. *A Classification of igneous rocks and glossary of terms*. Blackwell Scientific.

Lesher, C.M., Goodwin, A.M., Campbell, I.H., and Gorton, M.P. 1986. Trace-element geochemistry of ore-associated and barren, felsic metavolcanic rocks in the Superior Province, Canada. Canadian Journal of Earth Sciences, **23:** 2, 222-237.

Ludden, J.N., and Thompson, G. 1978. Behaviour of rare earth elements during submarine weathering of tholeiitic basalt. Nature, **274**: 147-149.

MacLean, W.H. 1990. Mass change calculations in altered rock series. Mineralia Deposita, **25:** 44-49.

MacLean, W.H, and Barrett, T.J. 1993. Lithogeochemical techniques using immobile elements. Journal of Geochemical Exploration, **48:** 109-133.

MacLean, W.H., and Kranidiotis, P. 1987. Immobile elements as monitors of mass transfer in hydrothermal; alteration: Phelps Dogde massive sulfide deposit, Matagami, Quebec. Economic Geology, **82:** 951-962.

Munha, J., and Kerrich, R. 1980. Sea water basalt interaction in spilites from Iberian Pyrite Belt. Contributions to Mineralogy and Petrology, **73:** 191-200.

Ootes, L., Davis, W.J., Bleeker, W., and Jackson, V.A. 2009. Two distinct ages of Neoarchean turbidites in the western Slave Craton: further evidence and implications for a possible back-arc model. The Journal of Geology, **117:** 15-36.

Padgham, W.A, and Fyson, W.K. 1992. The Slave Province: a distinct Archean craton. Canadian Journal of Earth Sciences, **29:** 2072-2086.

Pan, Y., and Fleet, M.E. 1996. Rare earth element mobility during prograde granulite facies metamorphism: significance of fluorine. Contributions to Mineralogy and Petrology, **123:** 251-262.

Pearce, J.A. 1996. A user's guide to basalt discrimination diagrams. *In* Trace element geochemistry of volcanic rocks: applications for massive sulphide exploration. *Edited by* D.A., Wyman. Geological Association of Canada, Short Course Notes, **12:** 79-113.

Roscoe, W.E., and Wallis, S.C. 2003. Report on the Sunrise Property, NWT. Report for Silver Standards Resources Inc. [online]. Available from http://www.silverstandard.com/assets/pdfs/SunriseLake.pdf [cited 14 February 2014].

Ross, P-S., and Bédard, J.H. 2009. Magmatic affinity of modern and ancient subalkaline volcanic rocks determined from trace-element discriminant diagrams. Canadian Journal of Earth Science, **46:** 823-839.

Sircombe, K.N., Bleeker, W., and Stern, R.A. 2001. Detrital zircon geochronology and grain size analysis of a ~2800 Ma Mesoarchean proto-cratonic cover succession, Slave Province, Canada. Earth and Planetary Science Letters, **189:** 207-220.

Spear, F. S. 1993. *Metamorphic phase equilibria and pressure-temperature-time paths*. Washington, D.C: Mineralogical Society of America.

Stern, R.A., and Bleeker, W. 1998. Age of the world's oldest rocks redefined using Canada's SHRIMP: the Acasta Gneiss Complex, Northwest Territories, Canada. Geoscience Canada, **25:** 1, 27-31.

Stubley, M.P. 2005. Slave Craton: Interpretive bedrock compilation. Northwest Territories Geoscience Office, NWT-NU Open File 2005-01. Digital files and 2 maps.

Sun, S., and McDonough, W. F. 1989. Chemical and isotopic systematics of oceanic basalts: implications for mantle composition and processes. Geological Society, London, Special Publications, **42:** 1, 313-345.

Thompson, P. H. 1978. Archean regional metamorphism in the Slave Structural Province - a new perspective on some old rocks, *in* Metamorphism in the Canadian Shield. *Edited by* J. A. Fraser and W. W. Heywood. Geological Survey of Canada, Paper 78-10, pp. 85- 105.

Unknown author. 2011. NTGO Detailed Showing Report [online]. Available from http://ntgomap.nwtgeoscience.ca/showing_detail.jsp?showingID=085PSE0114 [cited 27 September 2013].

Unknown author. 2011. NTGO Detailed Showing Report [online]. Available from http://ntgomap.nwtgeoscience.ca/showing_detail.jsp?showingID=085PSE0016 [cited 27 September 2013].

Unknown author. 2011. NTGO Detailed Showing Report [online]. Available from http://ntgomap.nwtgeoscience.ca/showing_detail.jsp?showingID=085INE0023 [cited 14 February 2014].

Wilshire, H. G. 1957. *Propylitization of Tertiary volcanic rocks near Ebbetts Pass, Alpine County, California*. Berkeley: University of California Press.

Winchester, JA., and Floyd, P.A. 1977. Geochemical discrimination of different magma series and their differentiation products using immobile elements. Chemical Geology, **20:** 325-343.

Winter, J.D. 2010. *Principles of igneous and metamorphic petrology*. New York: Prentice Hall.

Wood, D. A. 1980. The application of a Th-Hf-Ta diagram to problems of tectonomagmatic classification and to establishing the nature of crustal contamination of basaltic lavas of the British Tertiary volcanic province. Earth and Planetary Science Letters, **50:** 1, 11-30

Wood, S.A. 1990. The aqueous geochemistry of the rare-earth elements and yttrium. 2. Theoretical predictions of speciation in hydrothermal solutions to 350 C at saturation water vapor pressure. Chemical Geology, **88:** 99-125.

APPENDIX A

Table A: Sample information by field ID, flow unit ID, mapped lithology, sample location, and location of sample preparation Field sample ID numbers represent the year (13), mapping geologist's initials (AB), station number (2019), and sample number if multiple samples taken at a single station (2019A). Flow unit ID numbers refer to sample groupings based on map relations and geochemical similarities (see Chp 4). Samples were prepared at the Dalhousie University Crystal Isolation Laboratory (Dal), or at Acme Analytical Laboratories (Acme).

Field Sample ID	Flow Unit ID	Mapped lithology	Easting	Northing	Sample preparation
13AB2029C1	Int1-A	Intermediate	400161.3	6942796.12	Acme
13AB2029C4	Int1-B	Intermediate	400161.3	6942796.12	Dal
13AB2032B	Int1-C	Intermediate	399252.37	6943531.75	Acme
13AB2038A	Int1-D	Intermediate	399641.26	6943073.27	Acme
13BW1010A	Int1-E	Intermediate	399378.54	6943042.81	Dal
13SM1102A	Int1-F	Intermediate	399378.54	6943042.81	Dal
13VJ68A	Int1-G	Intermediate	401269.91	6942085.04	Acme
13AB2019A	Int2-A	Intermediate	394746.99	6945414.9	Acme
13AB2019B	Int2-B	Intermediate	394746.99	6945414.9	Acme
13VJ78A	Int3-A	Intermediate	393456.85	6946639.11	Acme
13AB2023A	Int4-A	Intermediate	395288.93	6946202.39	Acme
13AB2039A	Int5-A	Intermediate	399933.38	6941838.74	Dal
13AB2030B	Maf1a-A	Mafic	400052.16	6942675.27	Acme
13BW1011A	Maf1a-B	Mafic	399363.81	6943013.68	Dal
13VJ94A	Maf1a-C	Mafic	398004.76	6942805.61	Dal
13VJ60A	Maf2a-A	Mafic	396291.57	6945728.24	Dal
13AB2025B	Maf2a-B	Mafic	395288.56	6946252.88	Acme
13VJ63A	Maf3a-A	Mafic	400416.66	6941841.02	Dal
13VJ92A	Maf3a-B	Mafic	398084.91	6942301.69	Dal
13AB2027B	Maf4a-A	Mafic	395301.66	6946328.29	Acme
13AB2031B	Maf5a-A	Mafic	399359.48	6943583.44	Dal
13VJ38A	Maf6a-A	Mafic	396948.44	6945261.51	Acme

APPENDIX B

Figure A: BSE images for Int1-A. Points labeled by mineral type and analysis number.

Int1-B, Zone 1

JEOL COMP 15.0kV ×250 100µm WD11mm

Int1-B, Bt 5

174

JEOL COMP 15.0kV ×100 100µm WD11mm
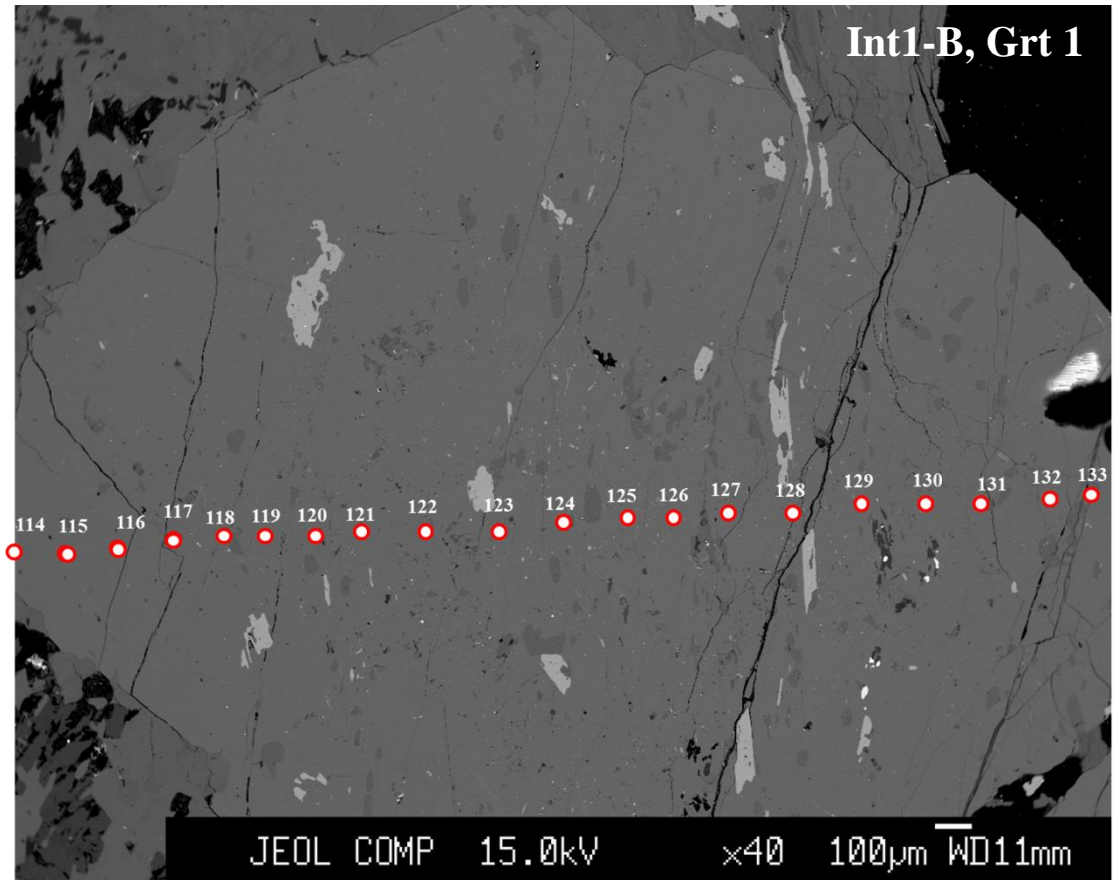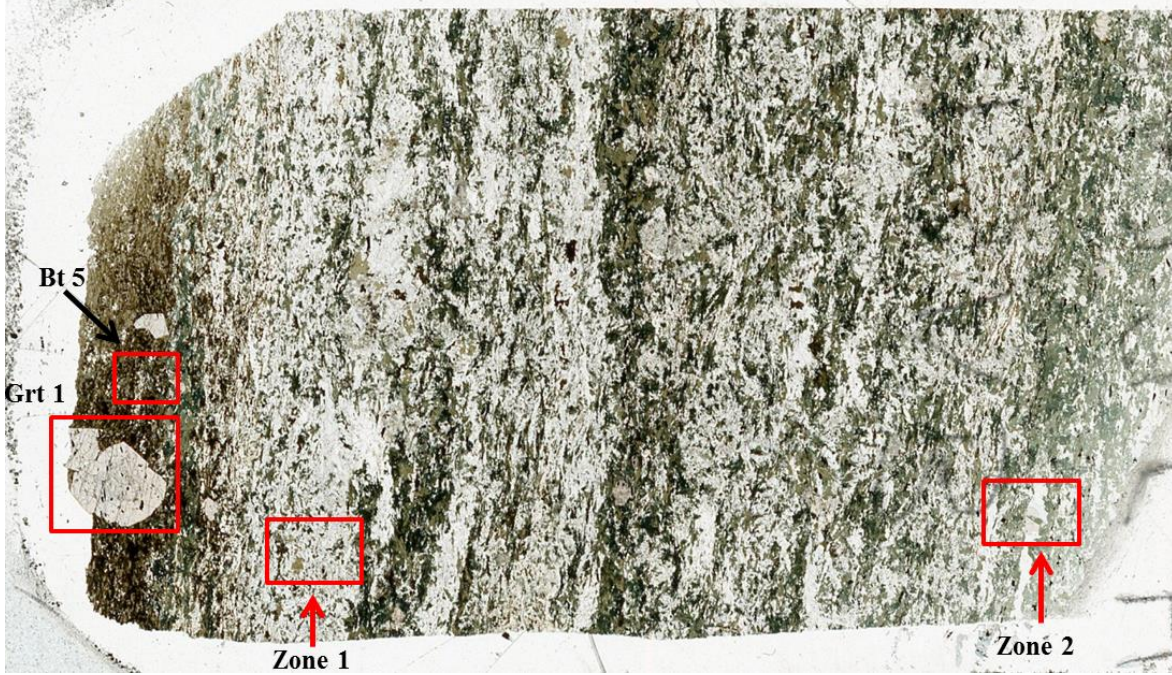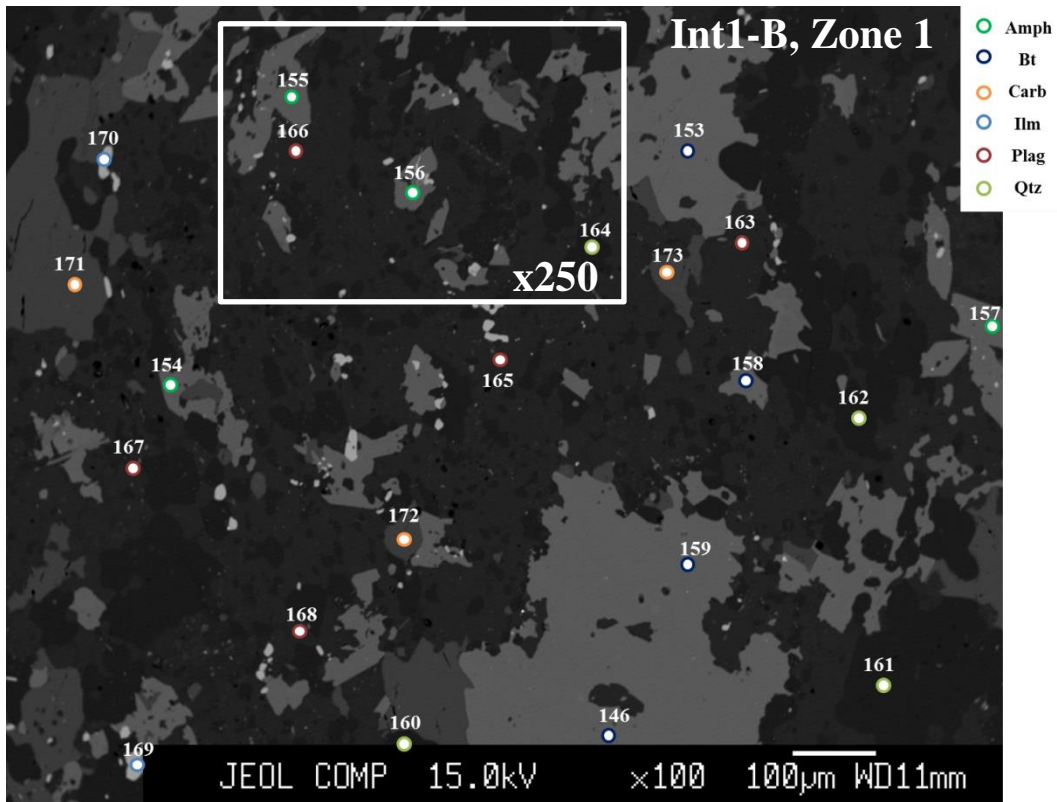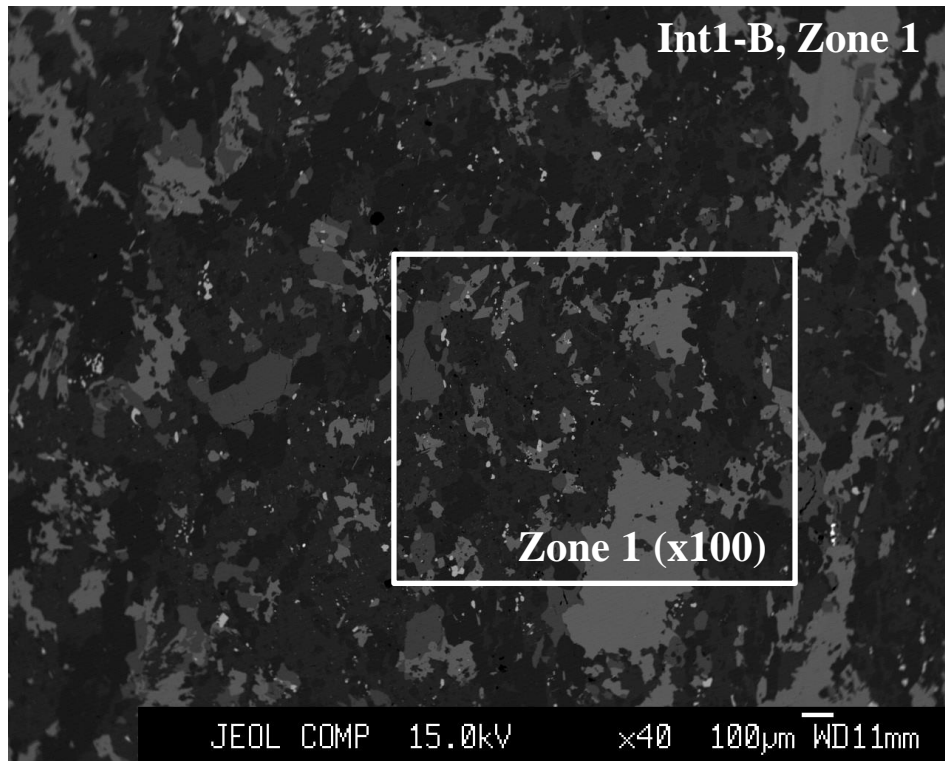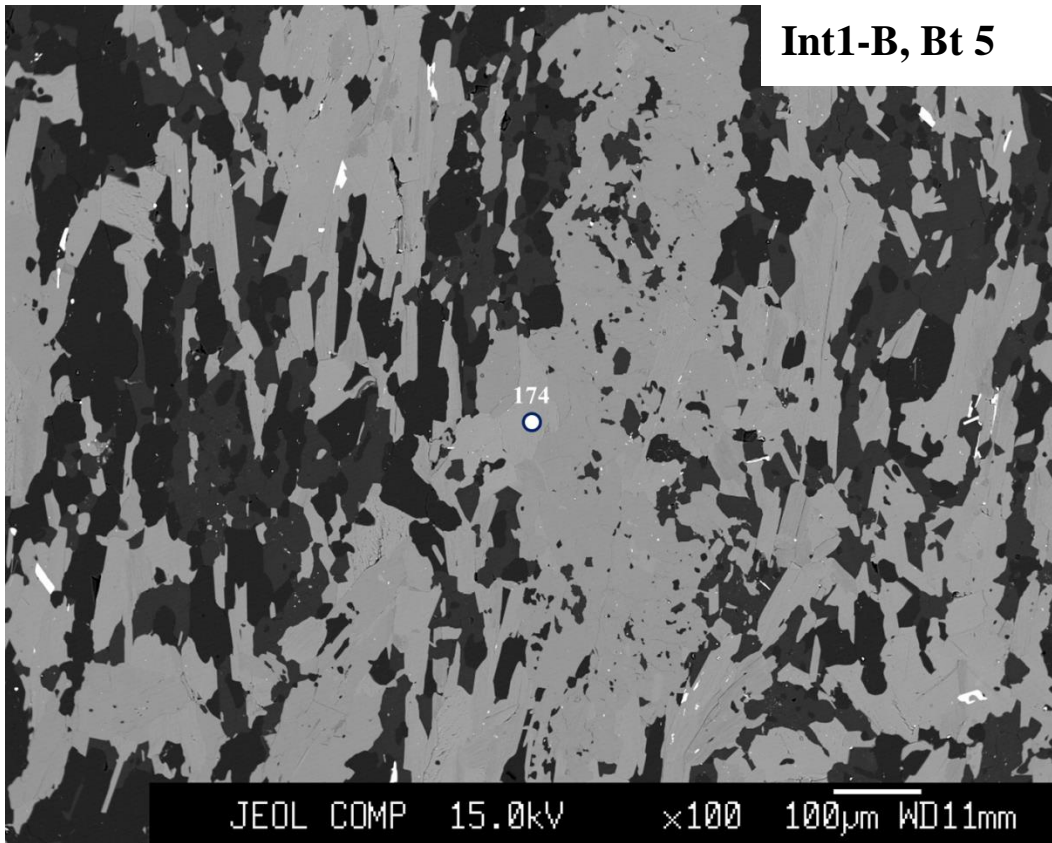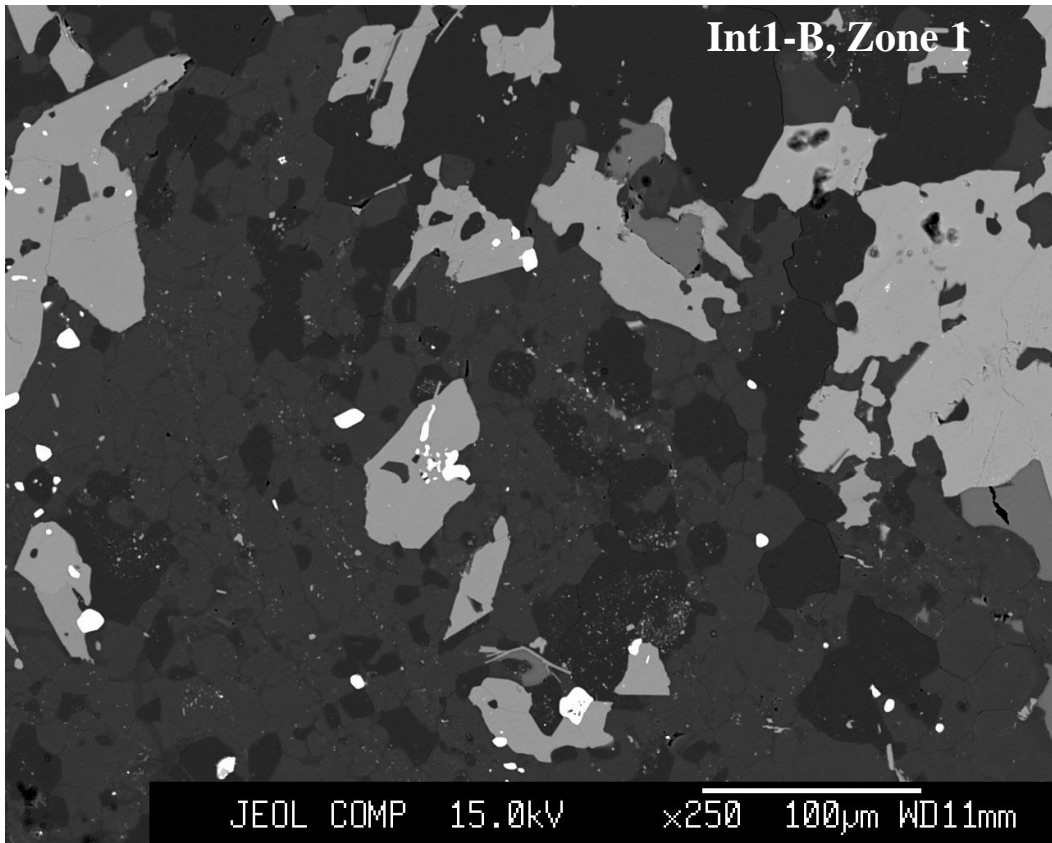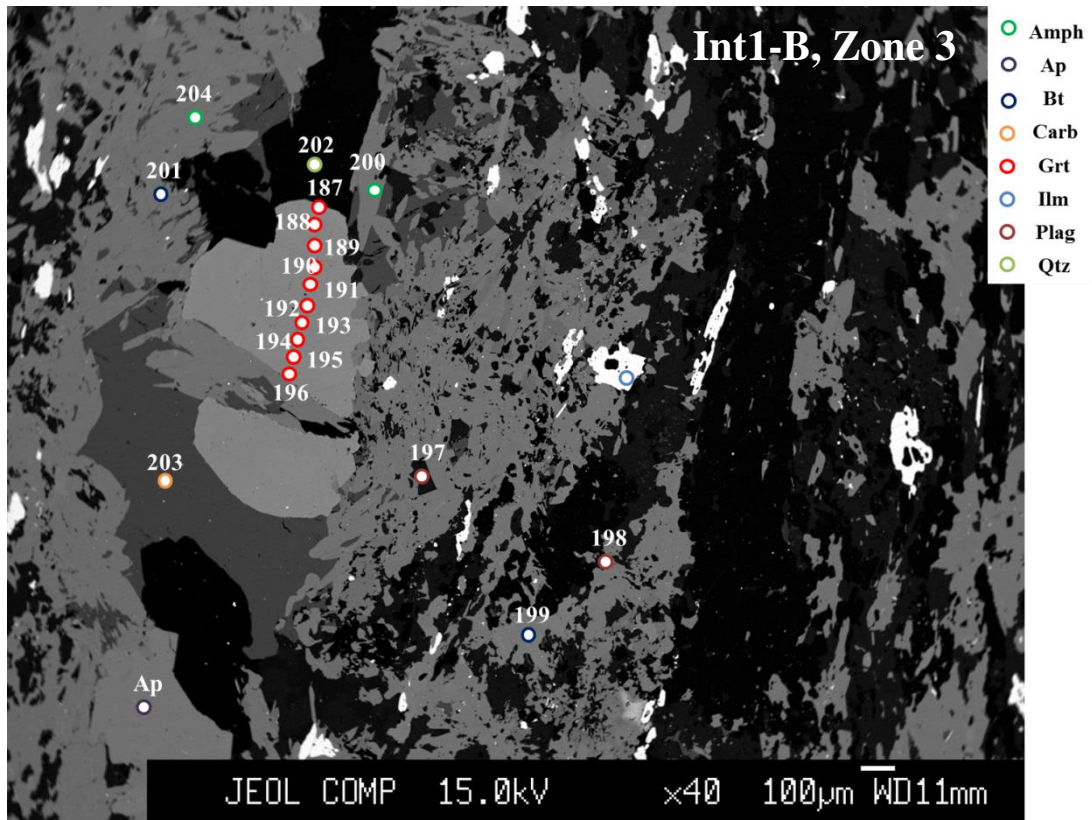
Figure B: BSE images for Int1-E. Points labeled by mineral type and analysis number.

Int1-E, Zone 1

Carb
Ilm
Qtz
Fe-S

JEOL COMP   15.0kV   ×40   100μm WD11mm

Chl
Bt
Carb
Grt
Fe-S

Int1-E, Zone 1

JEOL COMP   15.0kV   ×120   100μm WD11mm

Int1-E, Grt 1

○ Carb
○ Plag
○ Qtz
○ Grt
○ Fe-S

233

232

JEOL COMP   15.0kV   ×200   100µm WD11mm

Int1-E, Zone 2

○ Chl
○ Bt
○ Carb
○ Fe-S

Calcite

JEOL COMP   15.0kV   ×70   100µm WD11mm
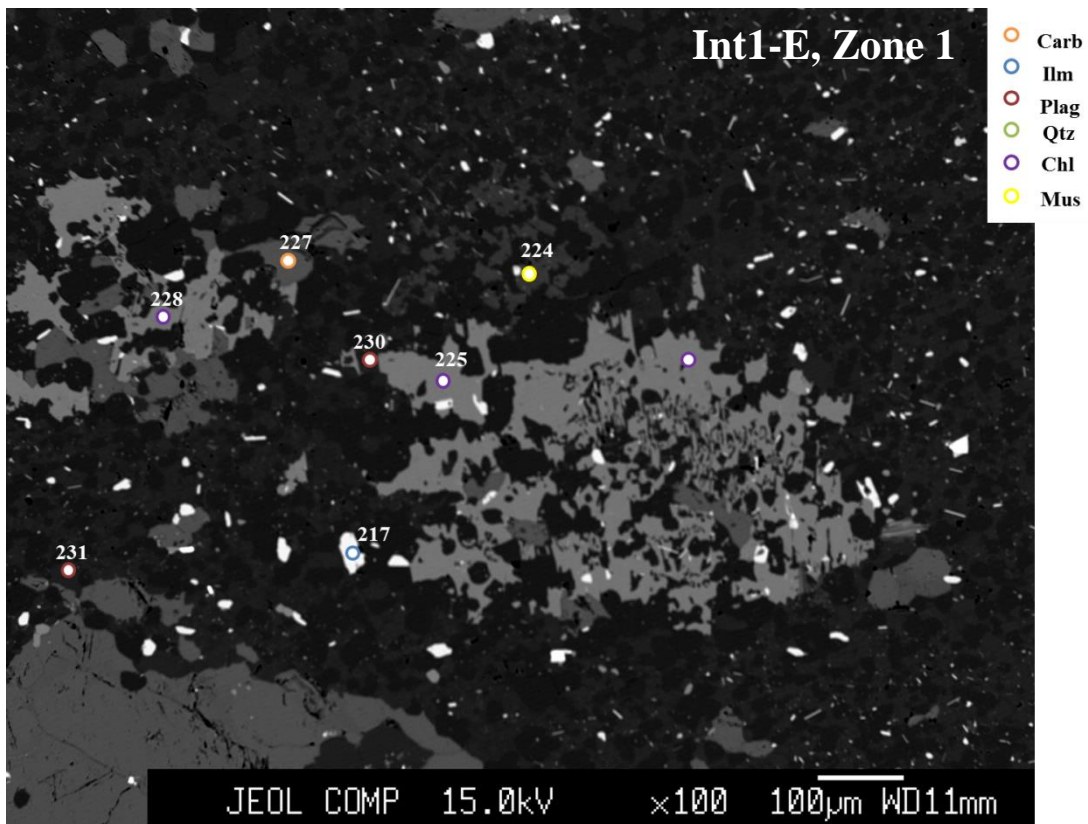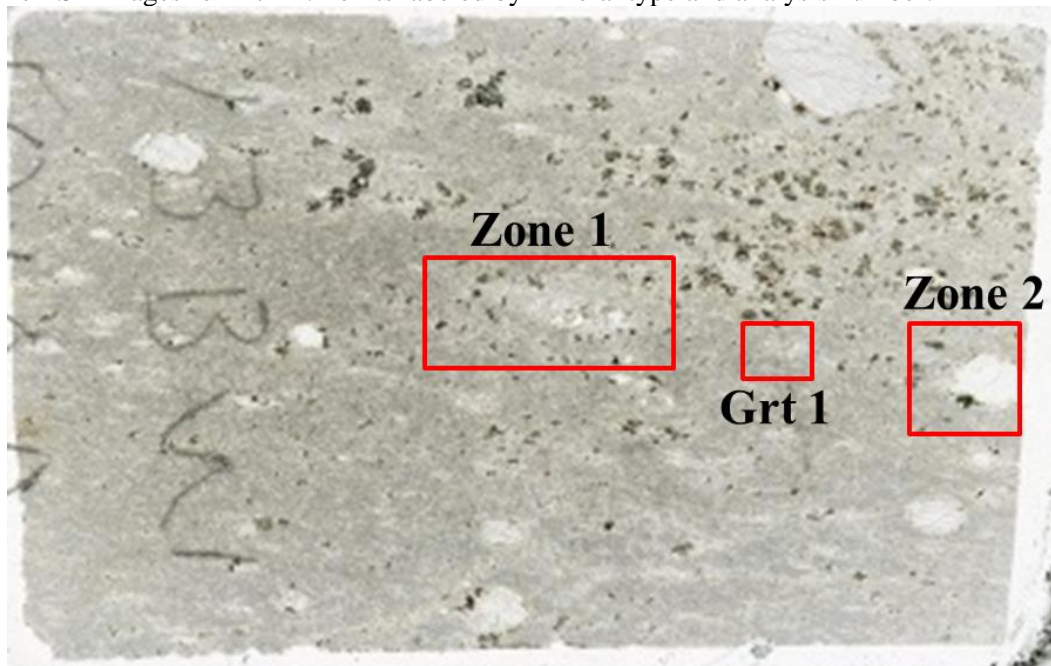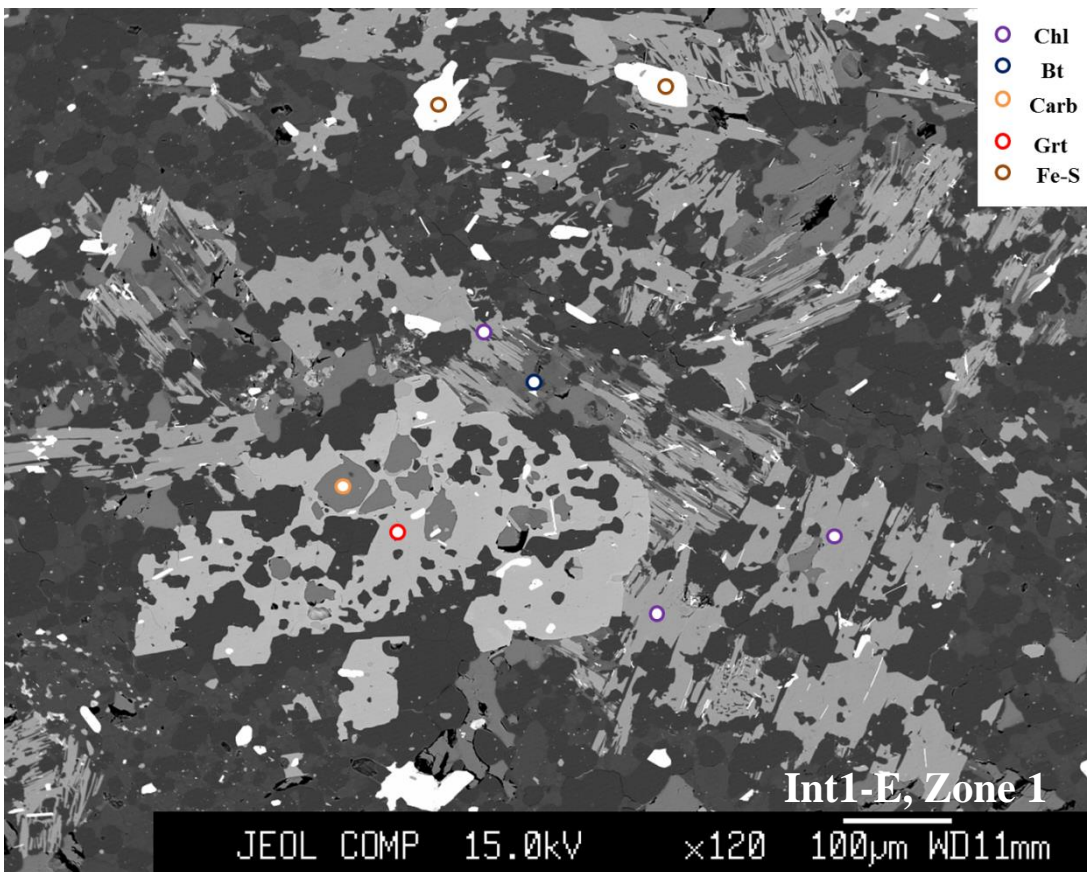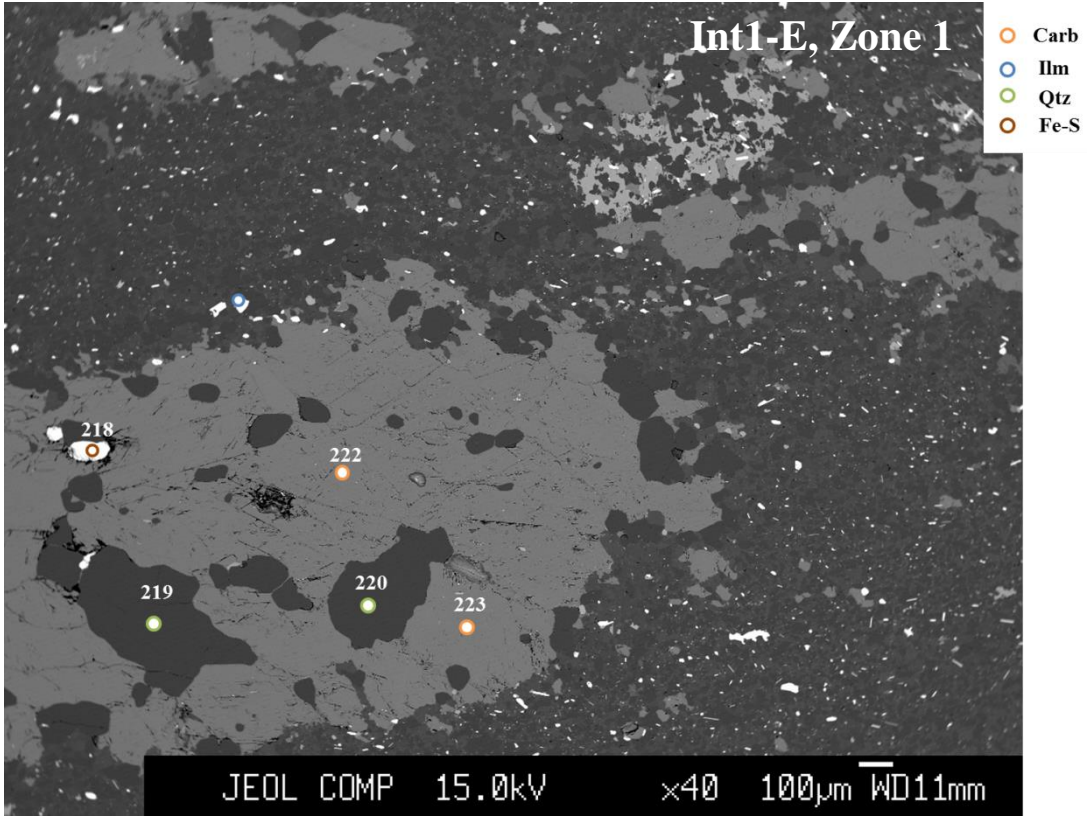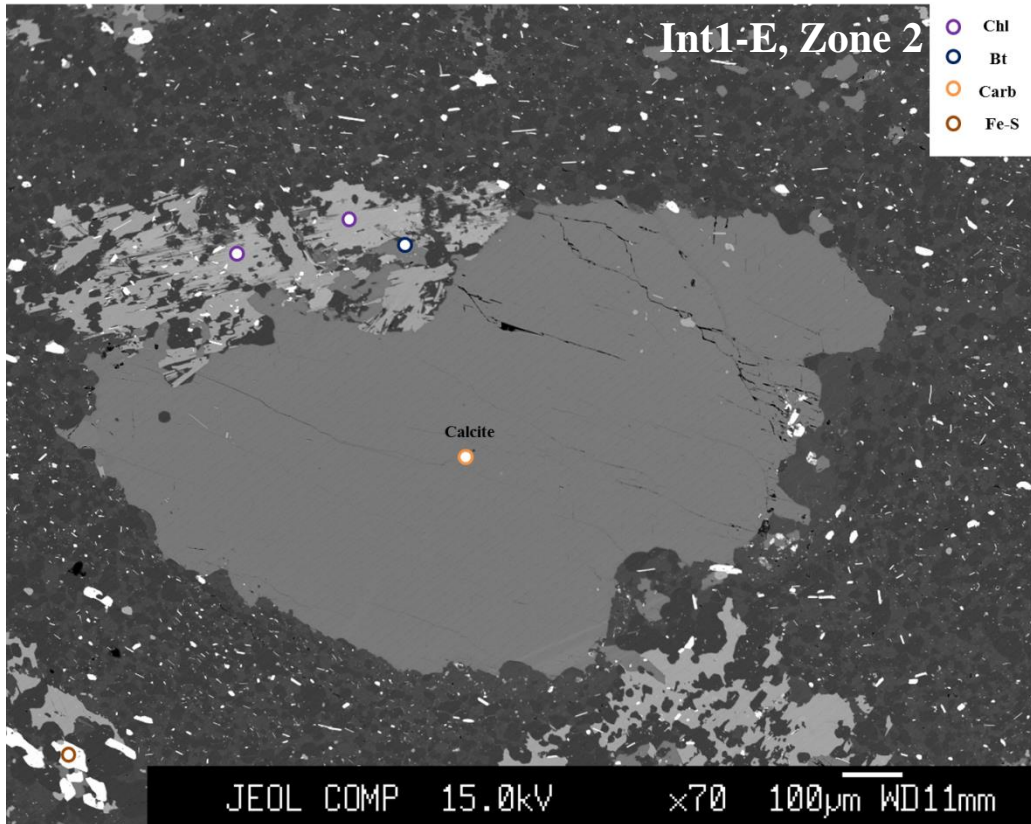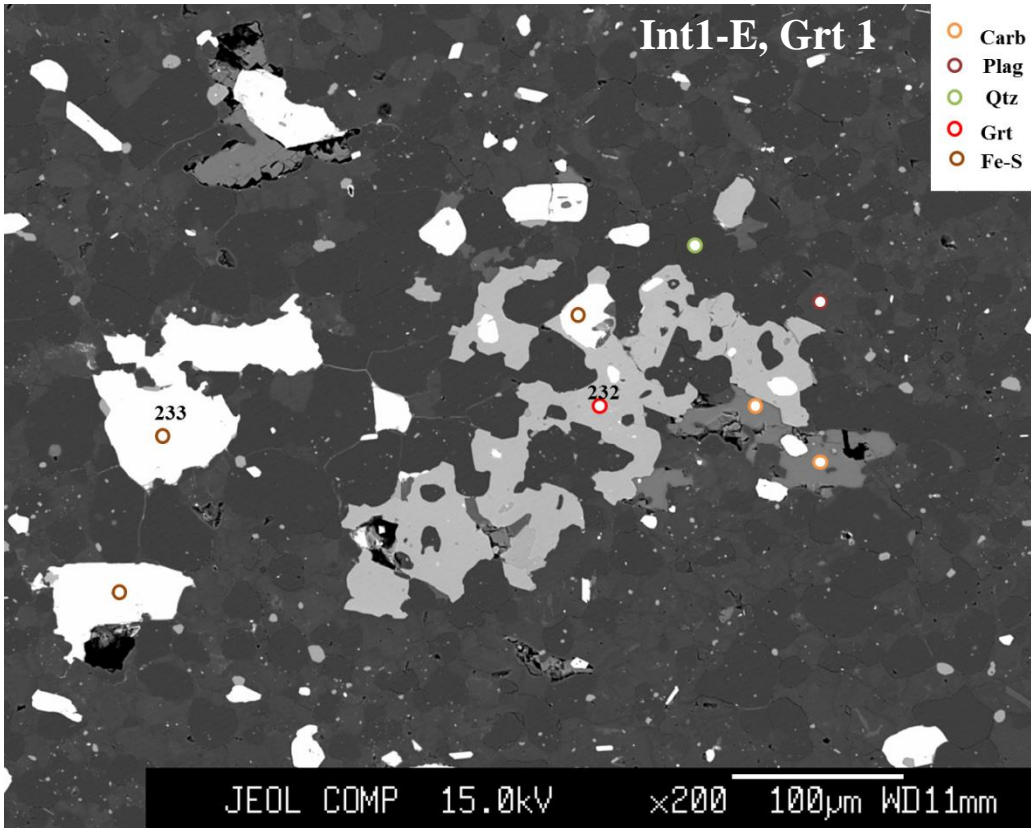
Figure C: BSE images for Maf6a-A (mafic rim). Points labeled by mineral type and analysis number.

Maf6a-A (mafic rim), Zone 1

Legend:
- ○ Amph
- ○ Carb
- ○ Ilm
- ○ Plag
- ○ Qtz
- ○ Chl
- ○ Ilm
- ○ Tit

JEOL COMP   15.0kV   ×100   100µm WD11mm

Z2 (x100)

Maf6a-A (mafic rim), Zone 2

JEOL COMP   15.0kV   ×40   100µm WD11mm

Maf6a-A (mafic rim), Zone 2

JEOL COMP   15.0kV   ×100   100μm WD11mm

Legend:
- Amph
- Ap
- Ilm
- Plag
- Qtz
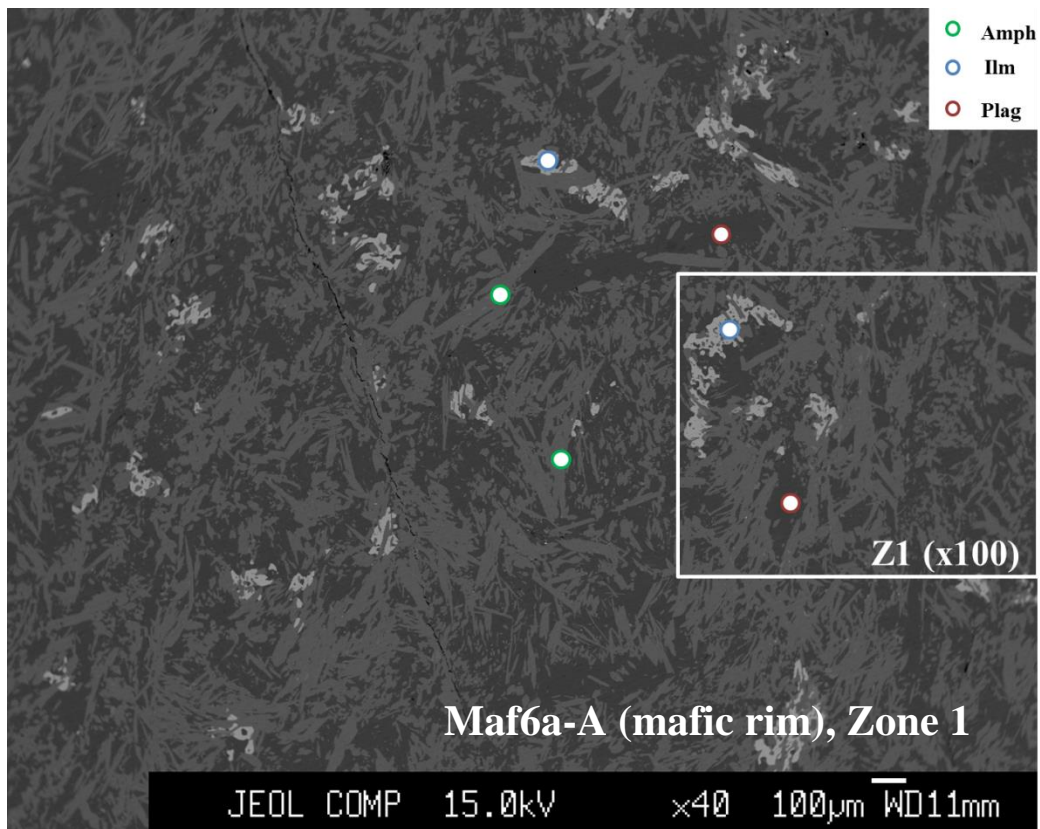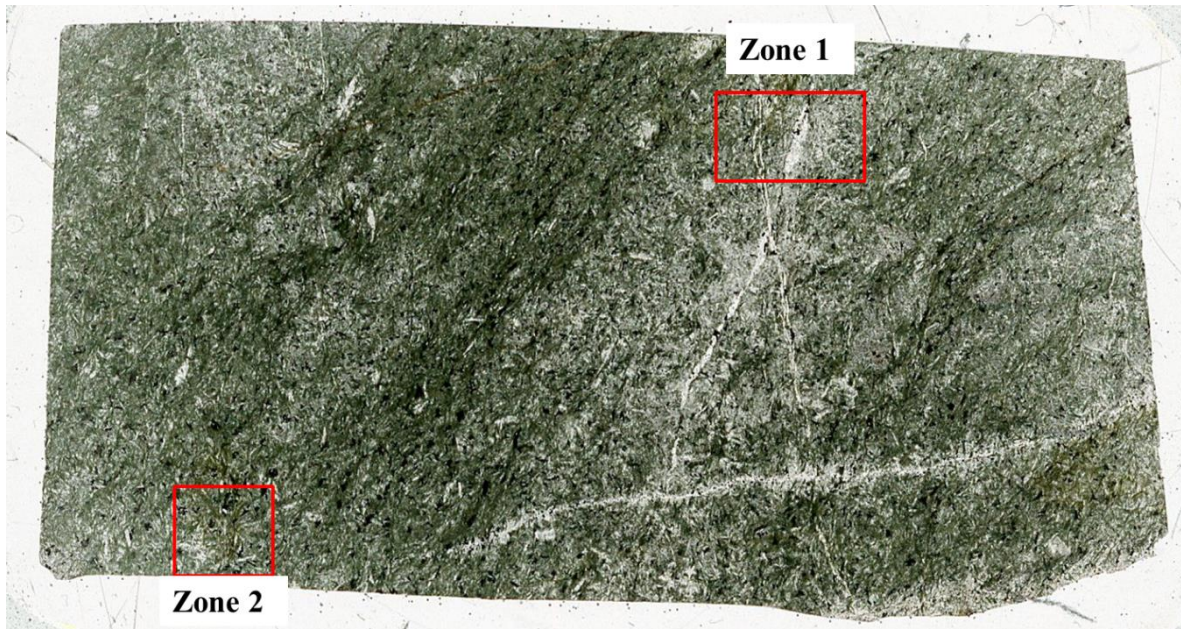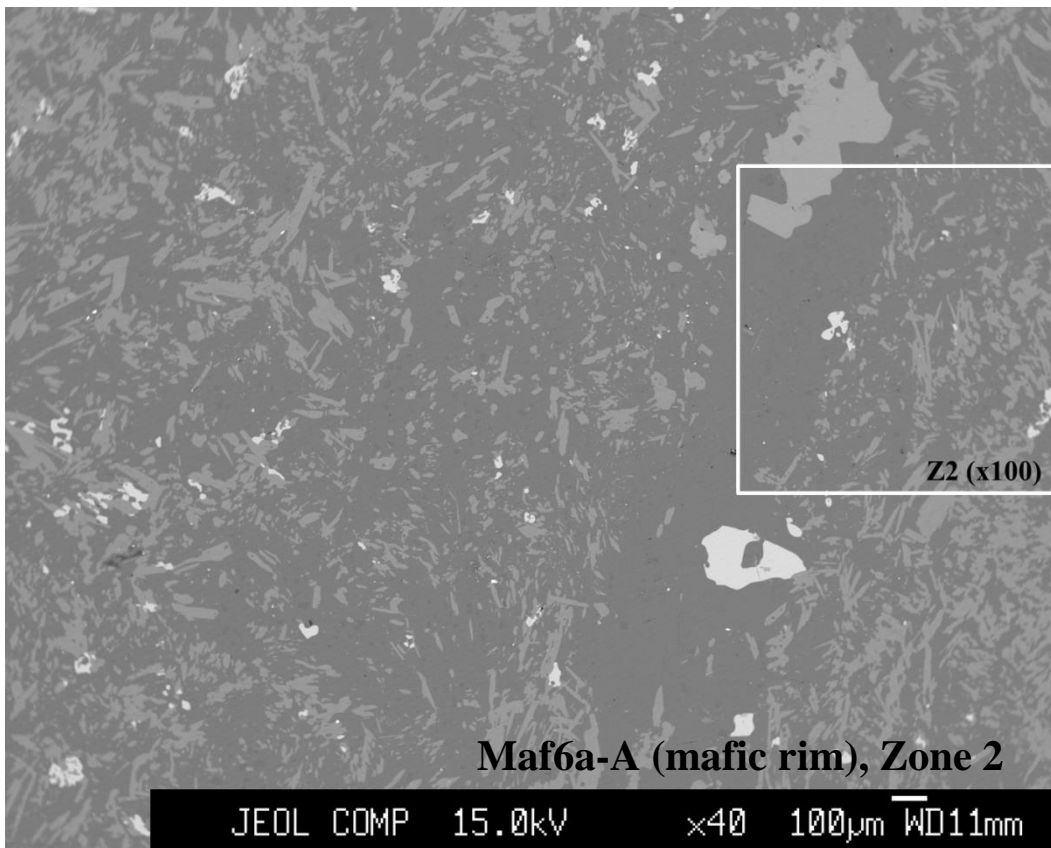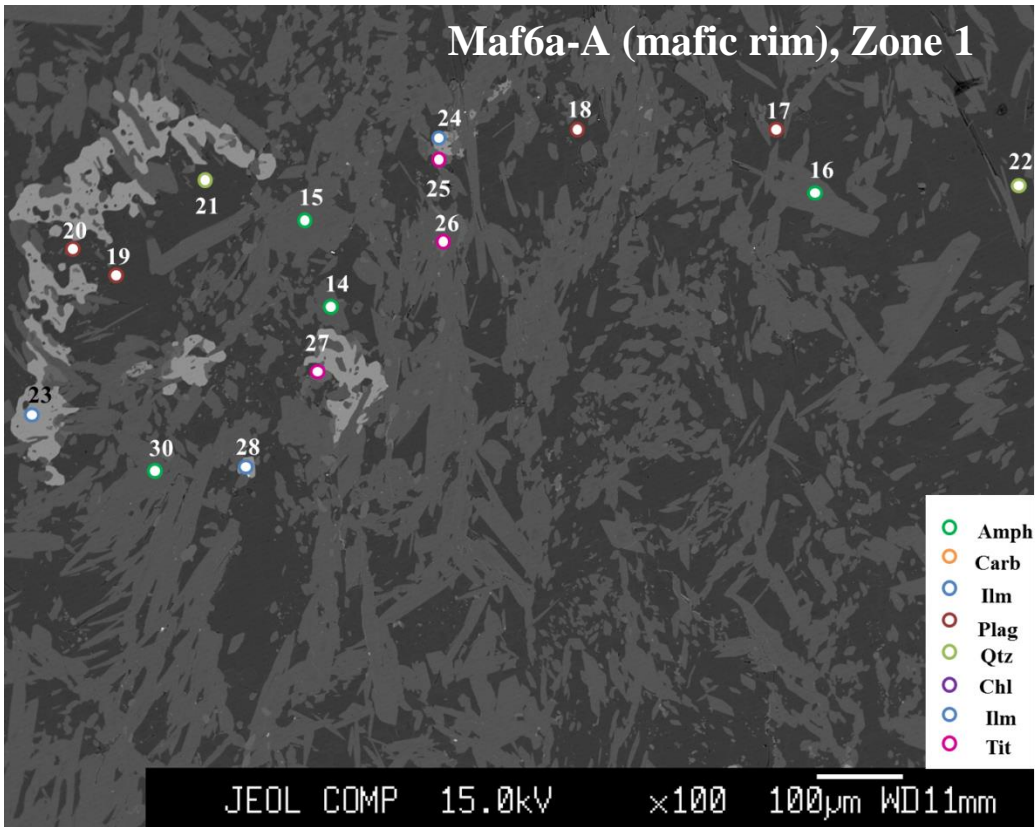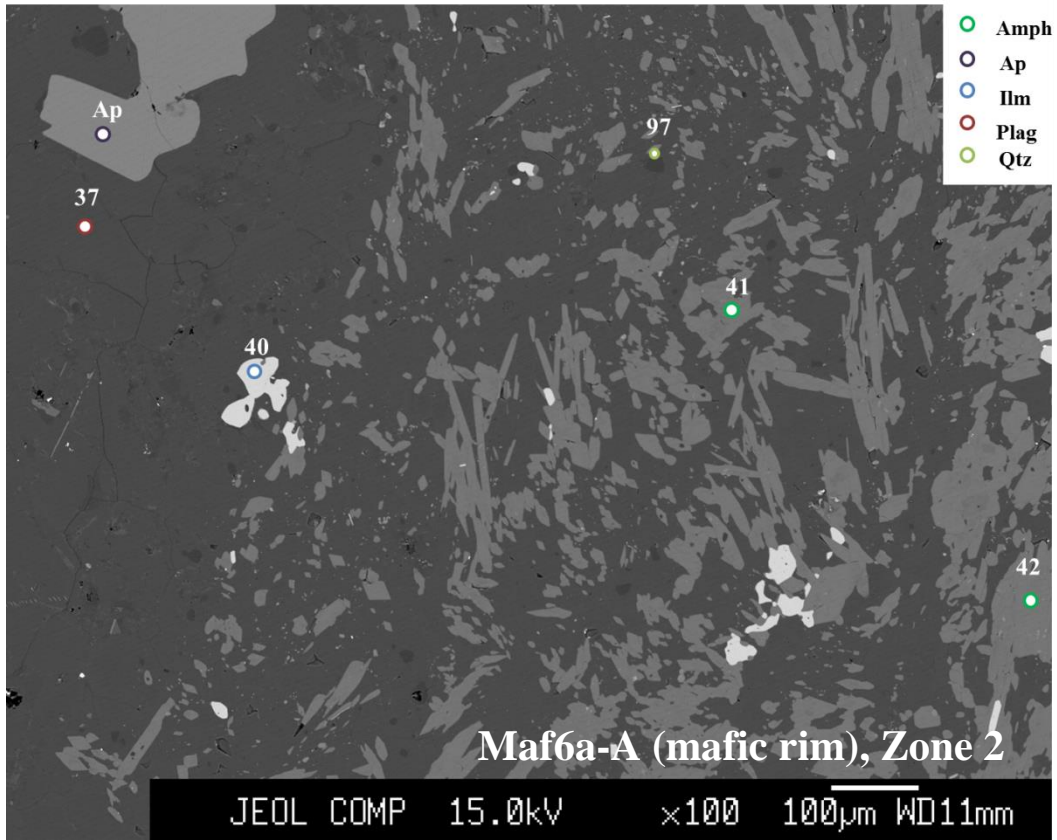
Figure D: BSE images for Maf6a-A (altered core). Points labeled by mineral type and analysis number.

Maf6a-A (altered core), Zone 1

○	Fe-S
○	Carb
○	Ap
○	Qtz
○	Ep
○	Tit

JEOL COMP 15.0kV ×100 100µm WD11mm

Maf6a-A (altered core), Zone 1

○	Carb
○	Qtz
○	Ep
○	Tit

JEOL COMP 15.0kV ×270 100µm WD11mm

Maf6a-A (altered core), Zone 2

Zone 2 (x100)

JEOL COMP 15.0kV ×40 100µm WD11mm

Maf6a-A (altered core), Zone 2

x400

JEOL COMP 15.0kV ×100 100µm WD11mm

- ○ Amph
- ○ Fe-S
- ○ Carb
- ○ Chl
- ○ Qtz
- ○ Ep
- ○ Tit

Maf6a-A (altered core), Zone 2

JEOL COMP 15.0kV ×400 10µm WD11mm

Legend:
- Amph
- Kspar
- Carb
- Qtz
- Ep
- Tit
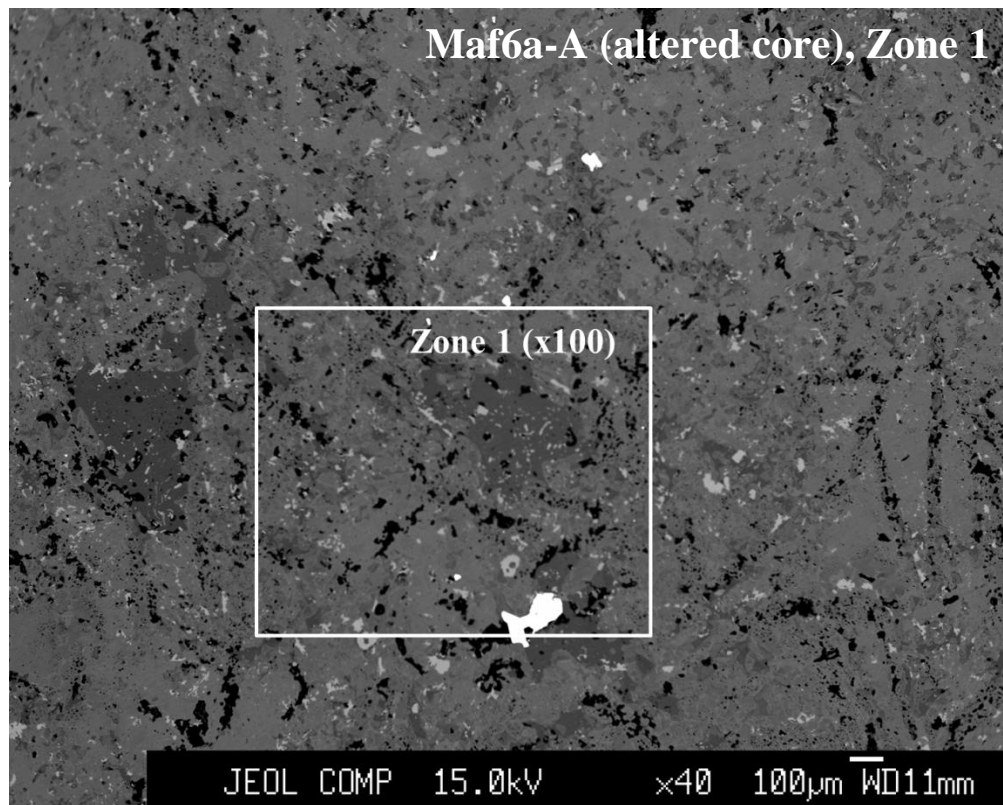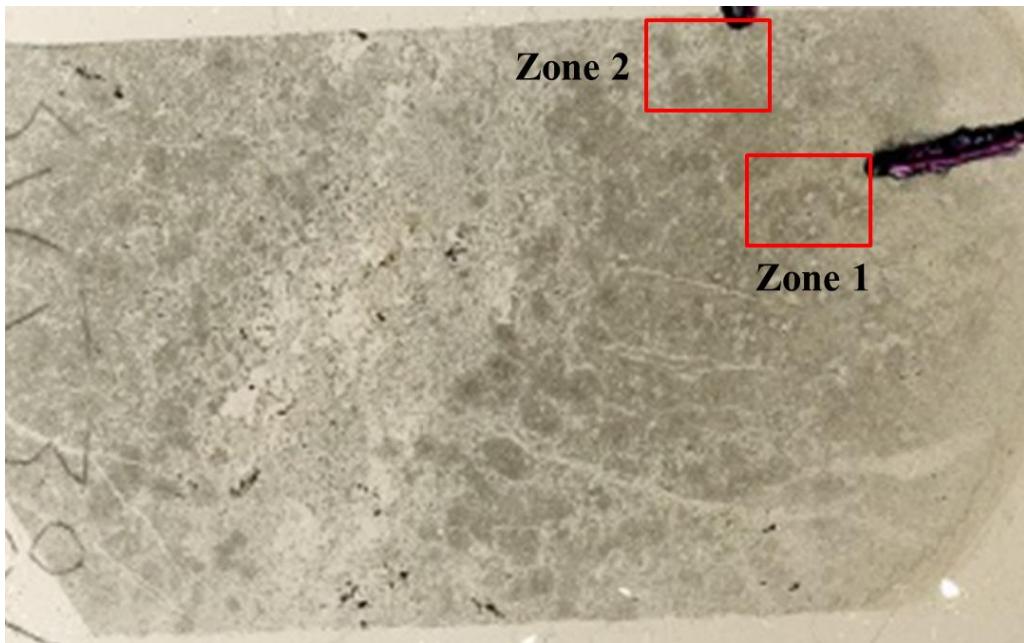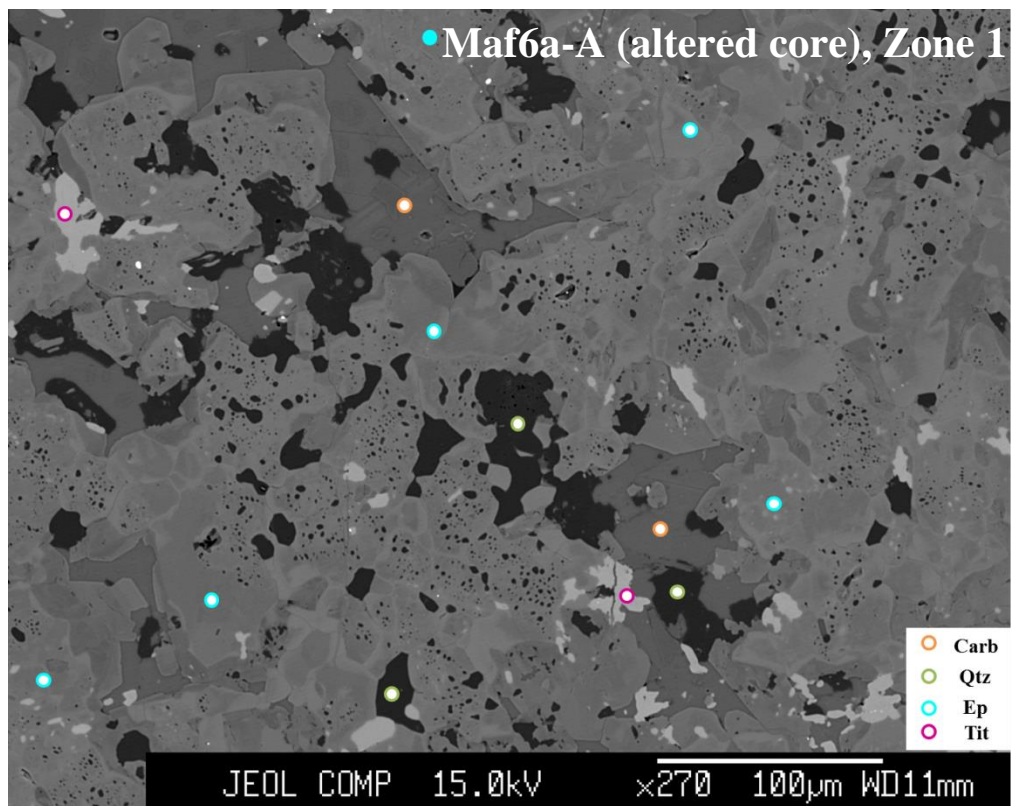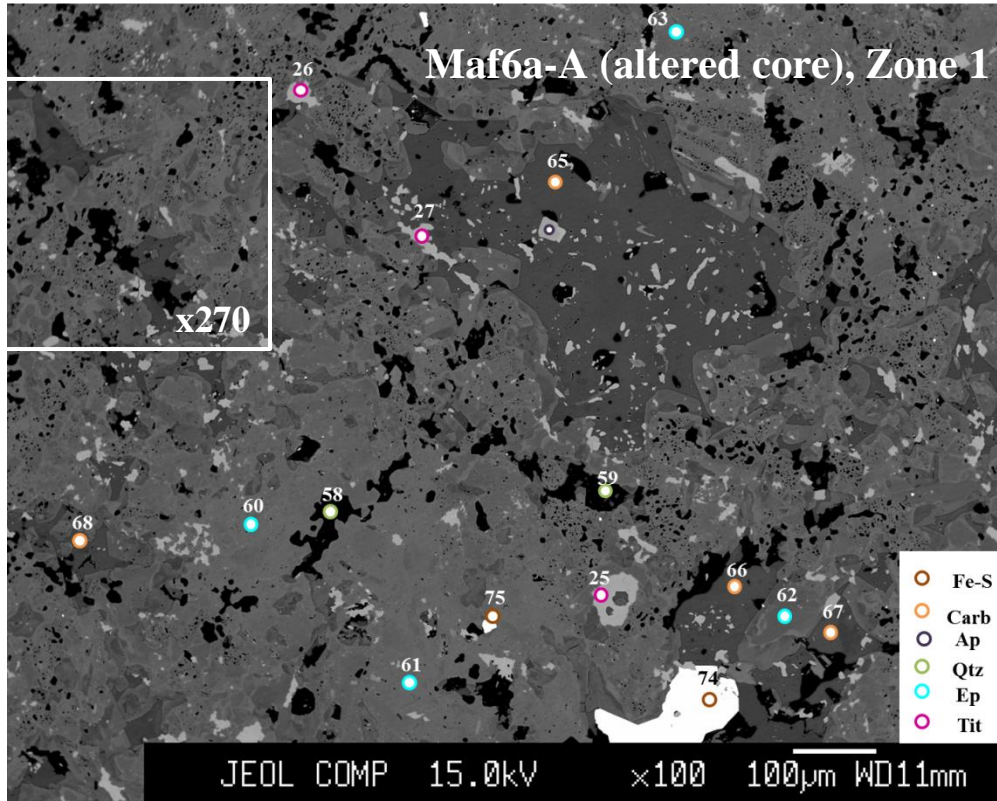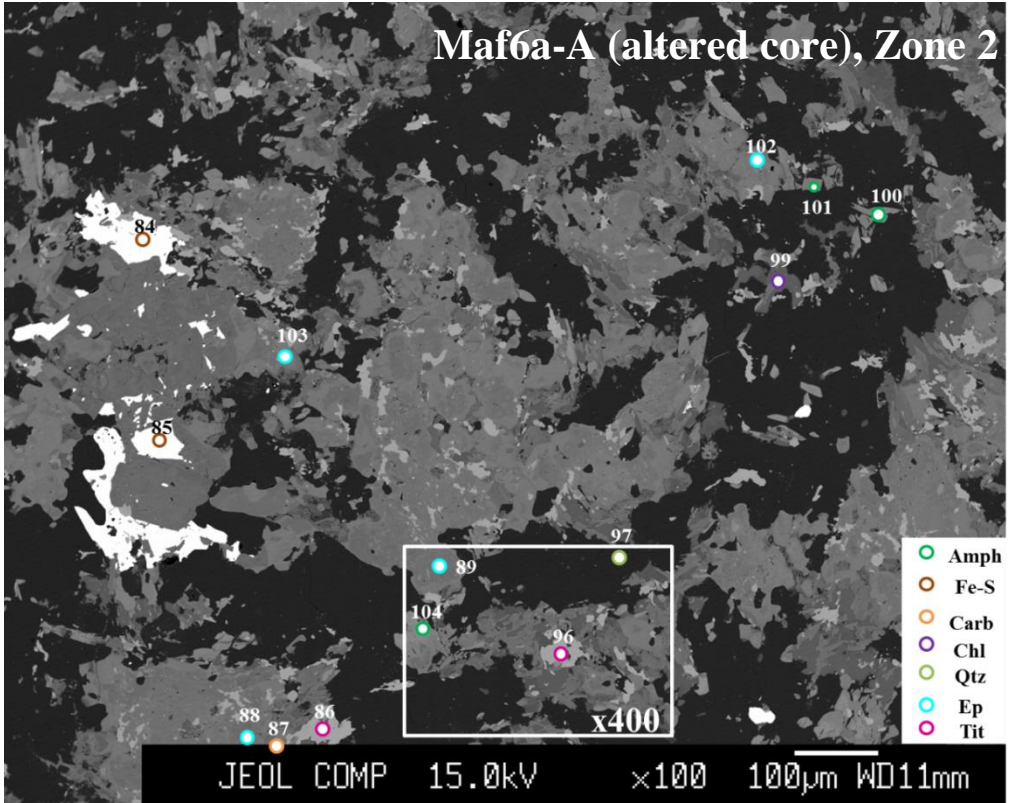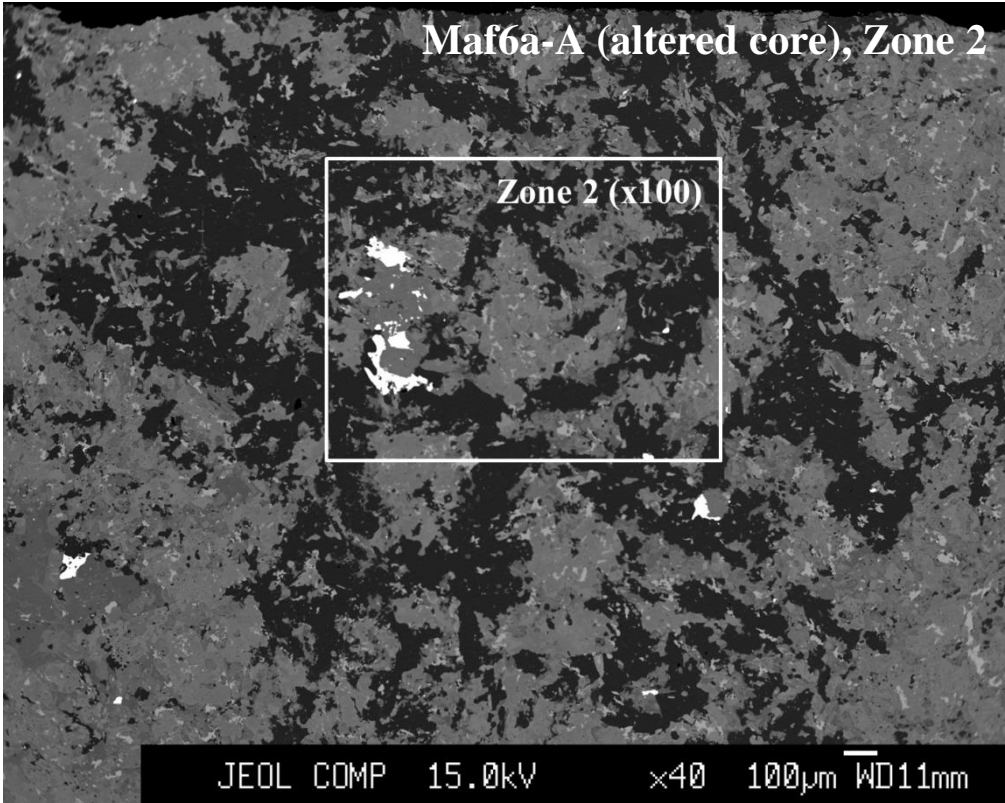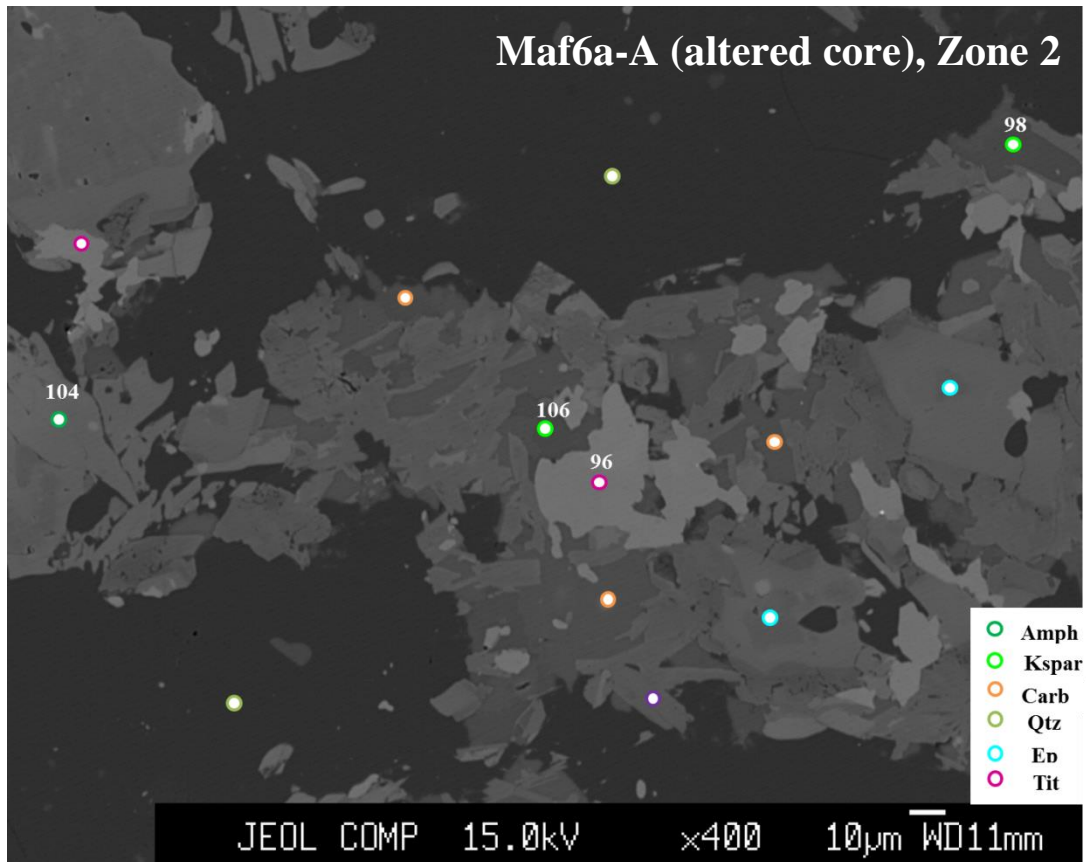
Analytical Parameters for the JEOL 8200 Superprobe electron microprobe

Beam diameter: 1 µm
Accelerating voltage: 15 kV
Beam current: 20 nA
Counting times: 20 s
Background counting times: 10 s

Correction method : ZAF
Standards for :

  K, Al, Si: Sanidine (Hohenfels)
  Cr : Cr metal
  Na : Jadeite
  Mn : Pyrolusite
  Ca, Ti, Mg : Kanganui Kaersutite
  Fe : Garnet 12442

Garnet recalculation completed using Garnet12442 for Fe, Al, and Si. Oxygen was assumed to be present in stoichiometric amounts relative to the total number of cations.

Mineral:
Amphibole

Sample:	Maf6a-A (mafic rim)							Maf6a-A (altered core)			Int1-B					
Analysis #:	14	15	16	30	41	42	44	100	101	104	154	155	156	157	200	204
Wt % oxides																
SiO_2	43.06	44.90	44.18	43.99	42.96	44.47	45.92	54.38	51.27	51.33	40.63	42.46	41.09	40.84	42.53	42.88
Al_2O_3	13.17	11.54	12.26	11.08	12.48	11.23	9.56	4.96	3.28	2.57	14.62	12.44	14.09	14.41	12.48	12.20
TiO_2	0.65	0.46	0.55	0.49	0.60	0.53	0.45	0.00	0.00	0.00	0.52	0.40	0.68	0.50	0.50	0.48
FeO	18.03	17.13	17.81	17.54	18.14	17.31	16.29	15.71	15.75	16.52	24.93	24.28	24.73	24.86	24.10	23.87
MnO	0.44	0.40	0.46	0.42	0.42	0.39	0.32	0.20	0.21	0.25	0.34	0.41	0.31	0.38	0.59	0.50
MgO	8.10	9.23	8.73	9.31	8.43	9.32	10.02	9.72	11.67	12.10	3.41	4.41	3.75	3.68	4.50	4.65
CaO	11.86	11.91	11.85	11.88	11.85	11.82	12.22	10.38	11.66	11.93	11.31	11.49	11.43	11.30	11.20	11.07
Na_2O	1.30	1.03	1.26	1.18	1.20	1.03	0.91	0.40	0.20	0.12	1.31	1.17	1.28	1.36	1.27	1.19
K_2O	0.42	0.31	0.36	0.30	0.41	0.39	0.28	0.12	0.05	0.03	0.88	0.60	0.86	0.66	0.41	0.41
Cr_2O_3	0.08	0.09	0.07	0.11	0.13	0.16	0.08	0.00	0.00	0.00	0.00	0.00	0.00	0.00	0.03	0.00
TOTAL	97.10	96.98	97.51	96.28	96.60	96.65	96.05	95.88	94.09	94.84	97.95	97.68	98.22	97.98	97.58	97.25

# of oxygens
used: 23

Cations pfu																
Si	6.507	6.734	6.626	6.684	6.534	6.711	6.925	7.970	7.767	7.758	6.311	6.571	6.357	6.332	6.576	6.636
Al	2.346	2.040	2.167	1.985	2.236	1.999	1.700	0.858	0.587	0.458	2.677	2.270	2.569	2.634	2.275	2.224
Ti	0.074	0.051	0.062	0.055	0.069	0.060	0.051	0.000	0.000	0.000	0.062	0.046	0.081	0.058	0.058	0.055
Fe	2.277	2.148	2.233	2.229	2.307	2.185	2.054	1.925	1.996	2.088	3.238	3.144	3.199	3.225	3.117	3.089
Mn	0.055	0.051	0.058	0.053	0.053	0.051	0.041	0.025	0.028	0.032	0.046	0.055	0.039	0.051	0.076	0.064
Mg	1.824	2.063	1.950	2.109	1.911	2.098	2.252	2.125	2.636	2.728	0.789	1.019	0.865	0.849	1.037	1.074
Ca	1.921	1.914	1.904	1.934	1.932	1.911	1.976	1.631	1.893	1.932	1.881	1.904	1.895	1.877	1.856	1.835
Na	0.380	0.299	0.366	0.347	0.352	0.299	0.267	0.115	0.060	0.035	0.396	0.352	0.382	0.409	0.380	0.357
K	0.081	0.060	0.069	0.058	0.081	0.074	0.053	0.023	0.009	0.005	0.175	0.120	0.170	0.131	0.081	0.081
Cr	0.009	0.012	0.007	0.014	0.016	0.018	0.009	0.000	0.000	0.000	0.000	0.000	0.000	0.000	0.005	0.000
TOTAL	15.472	15.373	15.445	15.470	15.491	15.408	15.327	14.674	14.975	15.037	15.578	15.484	15.560	15.566	15.461	15.415

Mineral: Apatite

Sample #	Maf6a-A (mafic rim)	Maf6a-A (altered core)
Analysis #:	38	64

Wt % oxides		
SiO$_2$	0.08	0.09
Al$_2$O$_3$	0.00	0.01
TiO$_2$	0.03	0.02
FeO	0.07	0.08
MnO	0.08	0.05
MgO	0.02	0.00
CaO	53.69	52.26
Na$_2$O	0.03	0.00
K$_2$O	0.03	0.02
Cr$_2$O$_3$	0.10	0.02
TOTAL	54.14	52.55

 # oxygens used: 12

Cations pfu		
Si	0.018	0.019
Al	0.000	0.004
Ti	0.005	0.004
Fe	0.012	0.013
Mn	0.014	0.010
Mg	0.005	0.000
Ca	11.890	11.920
Na	0.013	0.000
K	0.008	0.005
Cr	0.016	0.004
TOTAL	11.982	11.977

Mineral:
Biotite

Sample #:	Int1-B							Int1-E
Analysis #:	146	153	158	159	174	199	201	226

Wt % oxides								
SiO_2	34.87	35.12	35.03	35.07	35.06	35.35	35.10	47.81
Al_2O_3	16.42	16.56	16.61	16.23	16.30	16.30	16.43	33.90
TiO_2	2.21	1.89	1.90	2.13	2.44	2.11	1.83	0.21
FeO	28.65	27.82	27.85	28.20	27.53	26.94	26.68	2.68
MnO	0.16	0.16	0.16	0.17	0.19	0.20	0.21	0.00
MgO	5.01	5.13	5.18	5.15	5.30	5.71	6.02	1.01
CaO	0.00	0.00	0.02	0.00	0.04	0.02	0.02	0.05
Na_2O	0.10	0.12	0.10	0.09	0.13	0.09	0.11	0.23
K_2O	9.38	9.49	9.45	9.62	9.40	9.34	9.37	10.21
Cr_2O_3	0.00	0.00	0.00	0.00	0.00	0.04	0.03	0.00
TOTAL	96.80	96.31	96.30	96.64	96.39	96.08	95.78	96.09

Analysis #	XPhl	XAnn
146	0.238	0.762
153	0.247	0.753
158	0.249	0.751
159	0.245	0.755
174	0.256	0.744
199	0.274	0.726
201	0.287	0.713
226	0.400	0.600

# of oxygens
used: 22

Cations pfu								
Si	5.489	5.535	5.522	5.524	5.513	5.555	5.533	6.321
Al	3.047	3.078	3.087	3.014	3.023	3.018	3.051	5.282
Ti	0.262	0.224	0.224	0.251	0.288	0.249	0.218	0.020
Fe	3.771	3.667	3.672	3.716	3.621	3.540	3.516	0.297
Mn	0.022	0.022	0.020	0.022	0.026	0.026	0.026	0.000
Mg	1.175	1.203	1.217	1.208	1.243	1.338	1.415	0.198
Ca	0.000	0.000	0.004	0.000	0.007	0.004	0.002	0.009
Na	0.031	0.037	0.031	0.029	0.040	0.029	0.033	0.059
K	1.885	1.907	1.901	1.934	1.888	1.872	1.885	1.720
Cr	0.000	0.000	0.000	0.000	0.000	0.004	0.004	0.000
TOTAL	15.684	15.675	15.677	15.699	15.651	15.635	15.684	13.906

Mineral: Carbonate

Sample #	Maf6a-A (altered core)					Int1-B				Int1-E			
Analysis #:	65	66	67	68	87	171	172	173	203	222	223	227	234
Wt %													
SiO$_2$	0.00	0.01	0.03	4.42	0.02	0.00	0.01	0.00	0.00	0.00	0.02	0.01	0.00
Al$_2$O$_3$	0.00	0.00	0.00	5.53	0.00	0.00	0.00	0.00	0.00	0.00	0.00	0.00	0.00
TiO$_2$	0.00	0.00	0.00	0.00	0.00	0.00	0.00	0.00	0.00	0.00	0.00	0.00	0.00
FeO	0.02	0.05	0.10	1.38	0.07	2.89	3.19	2.67	3.89	2.90	2.48	2.90	2.06
MnO	0.12	0.04	0.16	0.12	0.00	1.40	1.31	1.33	1.85	1.62	1.46	1.73	1.44
MgO	0.07	0.00	0.09	0.00	0.00	0.37	0.39	0.33	0.55	0.09	0.26	0.31	0.24
CaO	55.79	55.86	54.69	51.14	56.98	55.73	55.51	57.17	55.73	53.18	57.19	57.26	59.90
Na$_2$O	0.00	0.00	0.00	0.00	0.00	0.00	0.00	0.00	0.00	0.00	0.00	0.00	0.00
K$_2$O	0.01	0.00	0.02	0.02	0.00	0.01	0.01	0.01	0.01	0.01	0.02	0.02	0.01
Cr$_2$O$_3$	0.00	0.02	0.00	0.00	0.00	0.00	0.00	0.00	0.00	0.00	0.00	0.00	0.00
TOTAL	56.01	55.98	55.08	62.61	57.07	60.39	60.41	61.52	62.03	57.79	61.43	62.22	63.65

# of oxygens used: 6

Cation pfu													
Si	0.000	0.001	0.003	0.355	0.002	0.000	0.001	0.000	0.000	0.000	0.002	0.001	0.000
Al	0.000	0.000	0.000	0.523	0.000	0.000	0.000	0.000	0.000	0.000	0.000	0.000	0.000
Ti	0.000	0.000	0.000	0.000	0.000	0.000	0.000	0.000	0.000	0.000	0.000	0.000	0.000
Fe	0.002	0.004	0.008	0.093	0.006	0.227	0.250	0.206	0.299	0.239	0.191	0.221	0.153
Mn	0.010	0.004	0.013	0.008	0.000	0.111	0.104	0.104	0.143	0.135	0.114	0.134	0.109
Mg	0.011	0.000	0.013	0.000	0.000	0.052	0.055	0.045	0.076	0.013	0.037	0.042	0.032
Ca	5.977	5.988	5.957	4.403	5.991	5.610	5.588	5.644	5.481	5.613	5.654	5.600	5.706
Na	0.000	0.000	0.000	0.000	0.000	0.000	0.000	0.000	0.000	0.000	0.000	0.000	0.000
K	0.001	0.001	0.003	0.001	0.000	0.002	0.001	0.001	0.001	0.001	0.002	0.002	0.001
Cr	0.000	0.001	0.000	0.000	0.000	0.000	0.000	0.000	0.000	0.000	0.000	0.000	0.000
TOTAL	6.001	5.999	5.998	5.384	5.999	6.001	6.000	6.001	6.000	6.000	6.000	6.000	6.000

Mineral: Chlorite

Sample #	Maf6a-A (mafic rim)	Maf6a-A (altered core)	Int1-E	
Analysis #:	29	99	225	228

Wt % oxides				
SiO_2	26.45	24.20	23.51	23.81
Al_2O_3	19.67	18.67	21.09	21.03
TiO_2	0.05	0.00	0.17	0.15
FeO	26.96	23.31	36.23	35.38
MnO	0.43	0.20	0.39	0.41
MgO	13.44	13.31	6.21	6.77
CaO	0.39	3.70	0.04	0.06
Na_2O	0.02	0.00	0.00	0.01
K_2O	0.02	0.00	0.02	0.02
Cr_2O_3	0.11	0.00	0.10	0.06
TOTAL	87.55	83.39	87.75	87.69

# of oxygens used: 18

Cations pfu				
Si	3.627	3.488	3.397	3.424
Al	3.179	3.172	3.591	3.564
Ti	0.005	0.000	0.018	0.016
Fe	3.091	2.810	4.378	4.255
Mn	0.050	0.025	0.047	0.050
Mg	2.747	2.860	1.337	1.451
Ca	0.056	0.571	0.005	0.009
Na	0.004	0.000	0.000	0.002
K	0.004	0.000	0.004	0.004
Cr	0.013	0.000	0.011	0.007
TOTAL	12.775	12.928	12.787	12.784

Mineral: Epidote

Sample #	Maf6a-A (altered core)						
Analysis #:	60	61	62	63	89	102	103

Wt % oxides							
SiO_2	35.09	34.72	35.13	34.84	36.17	37.50	37.25
Al_2O_3	26.30	25.77	28.61	26.33	26.40	24.71	24.62
TiO_2	0.04	0.04	0.22	0.16	0.00	0.00	0.00
FeO	8.07	8.49	5.16	7.71	7.14	9.68	9.56
Fe_2O_3	8.97	9.44	5.73	8.56	7.93	10.75	10.63
MnO	0.13	0.09	0.01	0.05	0.00	0.00	0.00
MgO	0.00	0.00	0.01	0.02	0.00	0.00	0.00
CaO	22.55	22.75	23.41	22.99	23.82	23.07	23.28
Na_2O	0.00	0.00	0.00	0.00	0.00	0.00	0.00
K_2O	0.02	0.02	0.03	0.02	0.00	0.00	0.00
Cr_2O_3	0.06	0.02	0.02	0.04	0.00	0.00	0.00
TOTAL	92.26	91.91	92.58	92.16	93.53	94.95	94.70

Analysis #	$Fe^{3+}/[Fe^{3+}+Al]$
60	0.169
61	0.179
62	0.109
63	0.163
89	0.153
102	0.205
103	0.203

# of oxygens used: 12.5

Cations pfu							
Si	2.966	2.959	2.915	2.949	3.004	3.094	3.085
Al	2.621	2.589	2.799	2.626	2.585	2.403	2.403
Ti	0.003	0.003	0.014	0.010	0.000	0.000	0.000
Fe	0.570	0.605	0.358	0.545	0.496	0.668	0.663
Mn	0.010	0.006	0.000	0.004	0.000	0.000	0.000
Mg	0.000	0.000	0.001	0.003	0.000	0.000	0.000
Ca	2.044	2.078	2.081	2.085	2.120	2.040	2.065
Na	0.000	0.000	0.000	0.000	0.000	0.000	0.000
K	0.003	0.003	0.003	0.003	0.000	0.000	0.000
Cr	0.004	0.001	0.001	0.003	0.000	0.000	0.000
TOTAL	8.220	8.243	8.173	8.228	8.205	8.205	8.215

Mineral:
Garnet

Sample #	Int1-B (Z1)																			
Analysis #:	114	115	116	117	118	119	120	121	122	123	124	125	126	127	128	129	130	131	132	133
Wt %																				
SiO$_2$	36.47	36.65	36.55	36.60	36.69	36.53	36.93	36.51	36.77	36.64	36.39	36.74	37.03	36.71	36.91	36.97	37.36	37.10	37.14	37.26
Al$_2$O$_3$	20.69	20.60	20.48	20.62	20.66	20.61	20.64	20.86	20.79	20.74	20.49	20.91	20.62	20.85	20.73	20.54	20.51	20.58	20.59	20.70
TiO$_2$	0.14	0.17	0.15	0.17	0.13	0.19	0.22	0.08	0.14	0.22	0.19	0.12	0.15	0.14	0.13	0.13	0.19	0.13	0.17	0.09
FeO	27.15	28.53	28.78	28.09	29.30	28.81	28.50	29.61	28.84	29.03	29.16	29.25	28.99	29.62	29.09	28.17	28.29	28.92	28.63	28.70
MnO	7.51	6.56	6.67	6.72	7.01	6.77	6.85	7.62	7.95	7.55	7.39	8.48	7.78	7.86	7.38	6.72	6.97	6.83	6.48	6.14
MgO	0.52	0.70	0.74	0.71	0.74	0.71	0.71	0.74	0.71	0.71	0.87	0.71	0.67	0.73	0.78	0.76	0.73	0.75	0.68	0.71
CaO	6.53	6.24	5.97	6.61	5.09	5.57	5.94	4.10	4.56	4.62	4.80	3.96	4.65	3.95	4.66	6.02	5.86	5.26	6.08	6.32
Na$_2$O	0.02	0.01	0.00	0.00	0.01	0.00	0.00	0.00	0.00	0.01	0.02	0.00	0.00	0.00	0.02	0.00	0.00	0.00	0.01	0.00
K$_2$O	0.09	0.04	0.04	0.04	0.03	0.05	0.05	0.05	0.04	0.04	0.05	0.05	0.04	0.04	0.02	0.04	0.05	0.04	0.04	0.03
Cr$_2$O$_3$	0.11	0.09	0.10	0.06	0.09	0.07	0.09	0.10	0.09	0.13	0.10	0.10	0.10	0.10	0.10	0.09	0.09	0.07	0.09	0.10
TOTAL	99.22	99.59	99.46	99.62	99.74	99.29	99.93	99.67	99.88	99.70	99.46	100.32	100.03	100.00	99.82	99.44	100.03	99.67	99.89	100.07

 # oxygens used: 12

Cations pfu																				
Si	2.982	2.987	2.987	2.981	2.990	2.987	2.996	2.983	2.993	2.988	2.980	2.984	3.008	2.989	3.002	3.010	3.023	3.016	3.011	3.012
Al	1.993	1.979	1.972	1.980	1.985	1.987	1.974	2.009	1.994	1.993	1.978	2.002	1.975	2.000	1.987	1.970	1.956	1.972	1.968	1.973
Ti	0.008	0.010	0.010	0.011	0.008	0.012	0.013	0.005	0.008	0.013	0.012	0.007	0.010	0.008	0.008	0.008	0.012	0.008	0.010	0.006
Fe	1.856	1.944	1.967	1.913	1.997	1.970	1.934	2.023	1.963	1.980	1.997	1.987	1.969	2.017	1.979	1.918	1.914	1.967	1.942	1.940
Mn	0.520	0.452	0.461	0.463	0.484	0.469	0.470	0.527	0.548	0.522	0.512	0.583	0.535	0.542	0.509	0.463	0.478	0.470	0.445	0.420
Mg	0.064	0.085	0.090	0.086	0.090	0.086	0.086	0.090	0.086	0.086	0.106	0.086	0.082	0.089	0.095	0.092	0.088	0.091	0.082	0.086
Ca	0.572	0.545	0.522	0.577	0.445	0.488	0.516	0.359	0.397	0.403	0.421	0.344	0.406	0.344	0.406	0.524	0.509	0.458	0.528	0.547
Na	0.002	0.001	0.000	0.000	0.002	0.000	0.000	0.000	0.000	0.002	0.002	0.000	0.000	0.000	0.002	0.000	0.000	0.000	0.002	0.000
K	0.010	0.005	0.004	0.004	0.002	0.005	0.005	0.005	0.005	0.004	0.006	0.005	0.004	0.004	0.002	0.005	0.005	0.005	0.004	0.004
Cr	0.007	0.006	0.006	0.004	0.006	0.005	0.006	0.006	0.006	0.008	0.006	0.006	0.006	0.006	0.006	0.006	0.006	0.005	0.006	0.006
TOTAL	8.015	8.015	8.018	8.020	8.010	8.010	8.002	8.006	8.003	8.002	8.021	8.006	7.996	8.002	7.998	7.998	7.990	7.993	7.997	7.994

Mineral: Garnet

Sample #	Int1-B (Z3)										Int1-E
Analysis #:	187	188	189	190	191	192	193	194	195	196	232

Wt % oxides											
SiO_2	36.86	37.08	37.25	37.16	37.03	37.02	37.19	36.82	36.99	36.83	36.75
Al_2O_3	20.21	20.21	20.16	20.31	20.27	20.22	20.12	19.97	20.19	20.21	20.38
TiO_2	0.17	0.19	0.20	0.21	0.24	0.23	0.24	0.27	0.24	0.22	0.07
FeO	24.65	23.81	23.60	23.64	23.33	23.59	23.11	23.00	24.09	23.57	24.05
MnO	7.86	7.22	7.17	7.09	7.11	7.20	7.08	6.98	7.28	7.02	11.11
MgO	0.57	0.55	0.54	0.54	0.57	0.57	0.52	0.51	0.58	0.53	0.51
CaO	7.45	9.21	9.41	9.50	9.96	9.46	10.33	10.04	8.90	9.79	5.92
Na_2O	0.00	0.00	0.00	0.00	0.00	0.00	0.00	0.00	0.01	0.00	0.02
K_2O	0.04	0.02	0.04	0.03	0.03	0.03	0.03	0.04	0.03	0.03	0.02
Cr_2O_3	0.06	0.02	0.03	0.01	0.04	0.06	0.03	0.03	0.03	0.05	0.07
TOTAL	97.86	98.30	98.39	98.47	98.57	98.38	98.65	97.66	98.34	98.25	98.90

 # oxygens used: 12

Cations pfu											
Si	3.031	3.029	3.037	3.026	3.016	3.022	3.025	3.025	3.024	3.012	3.013
Al	1.958	1.945	1.937	1.950	1.945	1.945	1.928	1.934	1.945	1.949	1.969
Ti	0.011	0.012	0.012	0.013	0.014	0.014	0.014	0.017	0.014	0.013	0.004
Fe	1.696	1.626	1.609	1.610	1.589	1.610	1.572	1.580	1.646	1.613	1.649
Mn	0.547	0.499	0.496	0.490	0.490	0.498	0.487	0.486	0.504	0.486	0.772
Mg	0.071	0.066	0.065	0.066	0.068	0.070	0.064	0.062	0.071	0.065	0.062
Ca	0.656	0.805	0.822	0.829	0.869	0.828	0.900	0.883	0.779	0.858	0.521
Na	0.000	0.000	0.000	0.000	0.000	0.000	0.000	0.000	0.001	0.000	0.004
K	0.004	0.002	0.004	0.002	0.002	0.002	0.004	0.004	0.004	0.002	0.002
Cr	0.004	0.001	0.002	0.001	0.002	0.004	0.002	0.002	0.002	0.004	0.005
TOTAL	7.979	7.986	7.985	7.988	7.997	7.994	7.997	7.994	7.992	8.003	8.002

Mineral: Garnet (continued)

Analysis #	Mg/Fe ratio
114	0.034
115	0.044
116	0.046
117	0.045
118	0.045
119	0.044
120	0.045
121	0.044
122	0.044
123	0.044
124	0.053
125	0.043
126	0.041
127	0.044
128	0.048
129	0.048
130	0.046
131	0.046
132	0.042
133	0.045
187	0.042
188	0.041
189	0.040
190	0.041
191	0.043
192	0.043
193	0.040
194	0.039
195	0.043
196	0.040
232	0.038

Analysis #	XPyr	XAlm	XGrs	XSpe
114	0.021	0.616	0.190	0.173
115	0.028	0.642	0.180	0.149
116	0.030	0.647	0.172	0.152
117	0.028	0.629	0.190	0.152
118	0.030	0.662	0.148	0.160
119	0.029	0.654	0.162	0.156
120	0.029	0.643	0.172	0.156
121	0.030	0.675	0.120	0.176
122	0.029	0.655	0.133	0.183
123	0.029	0.662	0.135	0.174
124	0.035	0.658	0.139	0.169
125	0.029	0.662	0.115	0.194
126	0.027	0.658	0.136	0.179
127	0.030	0.674	0.115	0.181
128	0.032	0.662	0.136	0.170
129	0.031	0.640	0.175	0.155
130	0.029	0.641	0.170	0.160
131	0.031	0.658	0.153	0.157
132	0.027	0.648	0.176	0.149
133	0.029	0.648	0.183	0.140
187	0.024	0.571	0.221	0.184
188	0.022	0.543	0.269	0.167
189	0.022	0.538	0.275	0.166
190	0.022	0.538	0.277	0.163
191	0.023	0.527	0.288	0.162
192	0.023	0.536	0.275	0.166
193	0.021	0.520	0.298	0.161
194	0.021	0.525	0.293	0.161
195	0.024	0.549	0.260	0.168
196	0.021	0.534	0.284	0.161
232	0.021	0.549	0.173	0.257

Mineral: Ilmenite

Sample #	Maf6a-A (mafic rim)				Int1-B		Int1-E	
Analysis #:	23	24	28	40	169	170	217	229

Wt % oxides								
SiO_2	0.11	0.11	0.13	0.12	0.41	0.17	0.14	0.20
Al_2O_3	0.00	0.02	0.00	0.00	0.17	0.04	0.01	0.01
TiO_2	52.09	52.14	51.83	51.59	50.79	51.47	51.72	51.53
FeO	42.10	41.90	41.50	42.99	44.52	44.22	44.19	43.23
MnO	3.83	4.16	4.06	3.12	1.74	2.19	2.08	2.65
MgO	0.07	0.03	0.07	0.10	0.07	0.02	0.03	0.03
CaO	0.18	0.29	0.43	0.14	0.15	0.56	0.09	0.12
Na_2O	0.02	0.00	0.03	0.00	0.00	0.02	0.02	0.03
K_2O	0.04	0.06	0.05	0.06	0.11	0.07	0.05	0.05
Cr_2O_3	0.21	0.17	0.21	0.28	0.11	0.11	0.20	0.19
TOTAL	98.65	98.88	98.30	98.40	98.06	98.86	98.54	98.02

# of oxygens used: 3

Cations pfu								
Si	0.003	0.003	0.003	0.003	0.011	0.004	0.004	0.005
Al	0.000	0.001	0.000	0.000	0.005	0.001	0.000	0.000
Ti	0.999	0.998	0.998	0.994	0.982	0.989	0.995	0.996
Fe	0.898	0.892	0.888	0.921	0.957	0.944	0.946	0.929
Mn	0.083	0.090	0.088	0.068	0.038	0.047	0.045	0.058
Mg	0.002	0.001	0.003	0.004	0.003	0.001	0.001	0.001
Ca	0.005	0.008	0.012	0.004	0.004	0.015	0.002	0.003
Na	0.001	0.000	0.001	0.000	0.000	0.001	0.001	0.001
K	0.002	0.002	0.002	0.002	0.004	0.002	0.002	0.002
Cr	0.004	0.003	0.004	0.006	0.002	0.002	0.004	0.004
TOTAL	1.997	1.999	1.999	2.002	2.006	2.007	2.000	1.999

Mineral: Plagioclase

Sample #	Maf6a-A (mafic rim)					Int1-B						Int1-E	
Analysis #:	17	18	19	20	37	163	166	167	168	197	198	230	231
Wt % oxides													
SiO_2	59.28	60.84	58.72	56.56	58.74	61.50	61.42	61.54	61.71	61.00	61.23	62.22	63.25
Al_2O_3	25.92	25.29	24.96	26.80	25.57	24.71	24.44	24.52	24.37	24.69	24.51	24.04	23.21
TiO_2	0.00	0.00	0.00	0.08	0.00	0.00	0.00	0.00	0.00	0.00	0.00	0.00	0.00
FeO	0.26	0.21	0.12	0.32	0.10	0.05	0.14	0.01	0.01	0.23	0.27	0.20	0.05
MnO	0.00	0.00	0.00	0.02	0.00	0.00	0.00	0.00	0.00	0.00	0.00	0.00	0.00
MgO	0.00	0.00	0.00	0.00	0.10	0.00	0.00	0.00	0.00	0.00	0.00	0.00	0.00
CaO	7.45	6.50	6.63	8.78	7.58	6.18	6.24	5.99	5.89	6.31	6.10	5.43	4.69
Na_2O	7.41	7.12	7.90	6.71	7.15	8.30	8.27	8.39	8.46	8.10	8.29	8.54	9.07
K_2O	0.05	0.05	0.06	0.05	0.10	0.06	0.07	0.04	0.07	0.04	0.08	0.07	0.08
Cr_2O_3	0.00	0.00	0.00	0.00	0.00	0.00	0.00	0.00	0.00	0.00	0.00	0.00	0.00
TOTAL	100.37	100.00	98.38	99.30	99.34	100.80	100.58	100.49	100.51	100.37	100.47	100.51	100.35

 # oxygens used: 8

Cations pfu													
Si	2.638	2.697	2.662	2.558	2.640	2.712	2.716	2.720	2.726	2.704	2.712	2.746	2.789
Al	1.359	1.322	1.334	1.429	1.354	1.284	1.274	1.278	1.270	1.290	1.279	1.250	1.206
Ti	0.000	0.000	0.000	0.002	0.000	0.000	0.000	0.000	0.000	0.000	0.000	0.000	0.000
Fe	0.010	0.008	0.005	0.012	0.004	0.002	0.005	0.000	0.001	0.009	0.010	0.007	0.002
Mn	0.000	0.000	0.000	0.001	0.000	0.000	0.000	0.000	0.000	0.000	0.000	0.000	0.000
Mg	0.000	0.000	0.000	0.000	0.006	0.000	0.000	0.000	0.000	0.000	0.000	0.000	0.000
Ca	0.355	0.309	0.322	0.426	0.365	0.292	0.296	0.284	0.278	0.300	0.290	0.257	0.222
Na	0.640	0.612	0.694	0.589	0.622	0.710	0.710	0.718	0.724	0.696	0.711	0.731	0.775
K	0.002	0.003	0.003	0.002	0.006	0.003	0.004	0.002	0.004	0.002	0.004	0.004	0.005
Cr	0.000	0.000	0.000	0.000	0.000	0.000	0.000	0.000	0.000	0.000	0.000	0.000	0.000
TOTAL	5.005	4.950	5.019	5.019	4.998	5.002	5.004	5.002	5.004	5.002	5.006	4.996	4.998

| %An | 0.356 | 0.334 | 0.316 | 0.419 | 0.367 | 0.291 | 0.293 | 0.283 | 0.277 | 0.300 | 0.288 | 0.259 | 0.221 |

Mineral: Quartz

Sample #	Maf6a-A (mafic rim)			Maf6a-A (altered core)	Int1-B					Int1-E		
Analysis #:	21	22	43	97	160	161	162	164	202	219	220	221
Wt % oxides												
SiO_2	96.25	98.94	97.93	97.02	100.74	100.32	100.23	100.22	99.61	99.73	99.82	99.71
Al_2O_3	0.18	0.22	0.04	0.00	0.00	0.00	0.00	0.01	0.01	0.02	0.02	0.02
TiO_2	0.00	0.00	0.00	0.00	0.00	0.00	0.00	0.00	0.00	0.00	0.00	0.00
FeO	0.13	0.16	0.12	0.00	0.00	0.00	0.00	0.08	0.00	0.00	0.00	0.01
MnO	0.00	0.00	0.00	0.00	0.00	0.00	0.00	0.00	0.00	0.00	0.00	0.00
MgO	0.00	0.00	0.01	0.00	0.00	0.00	0.00	0.00	0.00	0.00	0.00	0.00
CaO	0.09	0.07	0.06	0.00	0.00	0.00	0.00	0.08	0.00	0.00	0.00	0.00
Na_2O	0.01	0.02	0.00	0.00	0.00	0.00	0.00	0.00	0.00	0.00	0.00	0.00
K_2O	0.00	0.00	0.04	0.00	0.00	0.00	0.00	0.00	0.00	0.00	0.00	0.01
Cr_2O_3	0.00	0.00	0.00	0.00	0.00	0.00	0.00	0.00	0.00	0.00	0.00	0.00
TOTAL	96.65	99.40	98.20	97.02	100.74	100.32	100.23	100.38	99.62	99.75	99.84	99.76

 # oxygens used: 2

Cations pfu												
Si	0.997	0.997	0.999	1.000	1.000	1.000	1.000	0.999	1.000	1.000	1.000	1.000
Al	0.002	0.003	0.000	0.000	0.000	0.000	0.000	0.000	0.000	0.000	0.000	0.000
Ti	0.000	0.000	0.000	0.000	0.000	0.000	0.000	0.000	0.000	0.000	0.000	0.000
Fe	0.001	0.001	0.001	0.000	0.000	0.000	0.000	0.001	0.000	0.000	0.000	0.000
Mn	0.000	0.000	0.000	0.000	0.000	0.000	0.000	0.000	0.000	0.000	0.000	0.000
Mg	0.000	0.000	0.000	0.000	0.000	0.000	0.000	0.000	0.000	0.000	0.000	0.000
Ca	0.001	0.001	0.001	0.000	0.000	0.000	0.000	0.001	0.000	0.000	0.000	0.000
Na	0.000	0.000	0.000	0.000	0.000	0.000	0.000	0.000	0.000	0.000	0.000	0.000
K	0.000	0.000	0.000	0.000	0.000	0.000	0.000	0.000	0.000	0.000	0.000	0.000
Cr	0.000	0.000	0.000	0.000	0.000	0.000	0.000	0.000	0.000	0.000	0.000	0.000
TOTAL	1.002	1.002	1.001	1.000	1.000	1.000	1.000	1.001	1.000	1.000	1.000	1.000

Mineral: Titanite

Sample #	Maf6a-A (mafic rim)			Maf6a-A (altered core)				
Analysis #:	25	26	27	69	70	71	86	96
Wt % oxides								
SiO_2	31.07	30.51	30.86	28.84	29.18	36.54	29.18	29.88
Al_2O_3	1.46	1.45	1.12	1.25	1.38	26.79	1.54	1.35
TiO_2	37.02	36.69	37.35	36.98	37.01	0.26	36.36	36.93
FeO	1.03	0.99	0.65	0.52	0.47	6.98	0.12	0.27
MnO	0.13	0.12	0.11	0.05	0.07	0.08	0.00	0.00
MgO	0.00	0.00	0.00	0.00	0.00	0.02	0.00	0.00
CaO	27.97	28.63	28.25	27.28	27.55	22.90	28.47	28.35
Na_2O	0.01	0.02	0.00	0.00	0.00	0.00	0.00	0.00
K_2O	0.03	0.03	0.02	0.02	0.03	0.02	0.00	0.00
Cr_2O_3	0.07	0.09	0.06	0.08	0.07	0.03	0.00	0.00
TOTAL	98.79	98.52	98.43	95.01	95.75	93.62	95.66	96.78

 # oxygens used: 5

Cations pfu								
Si	1.026	1.014	1.023	0.993	0.996	1.207	0.997	1.008
Al	0.057	0.057	0.044	0.051	0.056	1.044	0.062	0.054
Ti	0.919	0.917	0.931	0.957	0.950	0.007	0.934	0.937
Fe	0.029	0.028	0.018	0.015	0.014	0.193	0.004	0.008
Mn	0.004	0.004	0.003	0.002	0.002	0.003	0.000	0.000
Mg	0.000	0.000	0.000	0.000	0.000	0.001	0.000	0.000
Ca	0.990	1.019	1.003	1.006	1.008	0.811	1.042	1.024
Na	0.001	0.001	0.000	0.000	0.000	0.000	0.000	0.000
K	0.001	0.002	0.001	0.001	0.001	0.001	0.000	0.000
Cr	0.002	0.003	0.002	0.002	0.002	0.001	0.000	0.000
TOTAL	3.027	3.042	3.024	3.026	3.027	3.267	3.039	3.030

Appendix C

Table A: Major oxide data for mafic pillow lavas. All data in wt % oxides. * = least altered, and ** = most altered mafic samples used in Gresens calculations.

Sample	13AB2030B	13BW1011A	13VJ94A	13VJ60A	13AB2025B	13VJ63A	13VJ92A	13AB2027B	13AB2031B	13VJ38A
ID	Maf1a-A*	Maf1a-B	Maf1a-C**	Maf2a-A*	Maf2a-B	Maf3a-A	Maf3a-B	Maf4a-A	Maf5a-A	Maf6a-A**
Oxide										
SiO_2	56.23	54.18	54.04	55.63	49.00	61.37	57.50	60.26	53.03	47.99
TiO_2	1.33	1.46	1.21	1.67	1.58	1.23	1.07	0.97	1.34	1.39
Al_2O_3	15.25	15.36	16.22	16.37	15.85	14.60	15.92	14.50	14.61	17.64
Fe_2O_3	9.12	9.88	8.61	9.85	5.04	8.76	7.57	6.50	12.89	7.90
FeO	8.21	8.89	7.75	8.86	4.53	7.88	6.81	5.85	11.60	7.11
MnO	0.15	0.19	0.19	0.22	0.19	0.14	0.14	0.12	0.16	0.11
MgO	6.14	6.13	5.48	3.83	2.06	3.46	4.94	4.29	3.42	1.73
CaO	7.89	8.53	8.52	6.87	15.08	4.44	9.97	7.45	10.20	17.64
Na_2O	4.51	3.45	4.28	4.43	4.33	3.84	2.16	4.25	1.70	0.40
K_2O	0.28	0.16	0.28	0.15	0.12	1.42	0.29	0.23	0.64	0.33
P_2O_5	0.19	0.22	0.18	0.25	0.22	0.23	0.21	0.29	0.21	0.20
Cr_2O_3	0.031	0.031	0.028	0.029	0.021	0.004	0.033	0.013	0.016	0.014
LOI	0.37	0.22	0.63	0.06	6.37	0.25	0.26	0.69	1.60	4.14
Total	101.49	99.81	99.67	99.36	99.86	99.74	100.06	99.56	99.82	99.48

Table B: Trace element data for mafic pillow lavas. All data in ppm. * = least altered, and ** = most altered mafic samples used in Gresens calculations.

ID	Maf1a-A*	Maf1a-B	Maf1a-C**	Maf2a-A*	Maf2a-B	Maf3a-A	Maf3a-B	Maf4a-A	Maf5a-A	Maf6a-A**
Element										
As	<0.5	<0.5	<0.5	25.0	5.4	1.0	<0.5	1.3	<0.5	1.2
Au	<0.5	2.9	<0.5	1.3	<0.5	2.4	<0.5	<0.5	<0.5	<0.5
Ba	88	35	98	195	37	438	80	150	229	151
Ce	18.3	21.5	20.2	27.4	23.2	34.8	33.4	37.6	31.4	21.1
Co	40.3	48.1	42.8	53.7	46.6	28.9	32.2	24.6	35.2	44.9
Cs	0.3	<0.1	0.2	<0.1	<0.1	0.9	0.1	0.6	0.7	0.2
Cu	48.7	109.5	51.0	35.7	55.0	59.0	157.5	47.3	229.9	63.8
Dy	3.54	4.14	3.75	4.57	3.60	4.42	3.90	4.58	4.07	3.67
Er	2.51	2.58	2.49	2.52	2.01	2.52	2.08	2.99	2.47	2.36
Eu	0.93	1.16	0.86	1.31	1.27	1.19	1.23	1.23	1.14	1.70
Ga	15.1	18.2	15.7	15.8	17.8	15.9	20.2	17.3	18.3	31.9
Gd	3.36	4.01	3.69	4.47	3.60	4.39	3.87	4.70	4.53	3.55
Hf	2.6	2.4	2.6	3.0	2.3	4.1	3.5	3.7	3.3	2.0
Ho	0.81	0.84	0.80	0.94	0.78	0.89	0.73	1.01	0.88	0.80
La	8.9	8.9	9.2	12.2	10.7	15.9	16.0	18.3	13.8	10.5
Lu	0.34	0.37	0.32	0.37	0.28	0.36	0.28	0.41	0.39	0.30
Mo	0.2	4.1	8.2	0.6	<0.1	7.6	7.4	0.3	2.5	0.5
Nb	4.6	5.8	4.9	6.7	5.7	7.1	7.2	8.1	6.2	5.3
Nd	10.2	12.3	11.2	16.2	13.5	16.2	16.4	19.4	15.2	12.9
Ni	12.6	10.0	29.1	18.1	75.4	24.3	15.5	33.0	45.9	101.4
Pb	0.4	0.3	0.5	0.3	1.2	1.9	1.0	1.6	1.7	0.6
Pr	2.39	2.71	2.58	3.64	3.04	3.98	4.13	4.63	3.79	2.82
Rb	7.9	1.0	6.6	0.6	0.5	42.9	4.8	7.3	17.5	8.7
Sm	2.75	3.59	3.00	4.00	3.38	3.87	3.69	4.15	3.57	2.84
Sr	134.1	184.9	161.6	183.8	219.6	83.1	217.5	88.4	204.8	282.8
Ta	0.4	0.4	0.3	0.5	0.3	0.5	0.3	0.4	0.4	0.2
Tb	0.59	0.66	0.59	0.67	0.59	0.67	0.60	0.74	0.67	0.58
Th	1.5	1.3	1.6	1.6	1.2	6.8	1.7	4.3	4.4	1.2

Tm	0.32	0.38	0.34	0.36	0.31	0.35	0.31	0.43	0.38	0.32
U	0.5	0.3	0.5	0.5	0.3	1.8	0.9	1.0	1.3	0.2
V	282	298	275	284	257	215	231	161	242	265
W	0.8	0.5	0.7	0.8	0.6	1.0	0.6	1.4	<0.5	0.7
Y	22.5	23.2	23.1	25.8	19.4	24.1	21.2	27.4	24.0	18.0
Yb	2.15	2.17	2.28	2.29	1.98	2.47	2.03	2.75	2.25	2.05
Zn	14	8	25	6	12	64	6	13	23	11
Zr	99.5	109.6	105.7	110.2	92.6	154.2	140.4	161.8	131.0	88.9

Table C: Major oxide data for intermediate pillow lavas. All data in wt % oxides. * = least altered, and ** = most altered intermediate samples used in Gresens calculations.

Sample	13AB 2029C1	13AB 2029C4	13AB 2032B	13AB 2038A	13BW 1010A	13SM 1102A	13VJ 68A	13AB 2019A	13AB 2019B	13VJ 78A	13AB 2023A	13AB 2039A
ID	Int1-A*	Int1-B	Int1-C	Int1-D	Int1-E**	Int1-F	Int1-G	Int2-A	Int2-B	Int3-A	Int4-A	Int5-A
Oxide												
SiO_2	64.03	51.82	60.98	64.12	71.84	71.71	59.12	61.07	73.20	65.37	48.85	63.60
TiO_2	1.33	1.33	1.41	1.19	1.19	1.20	1.42	0.69	0.91	0.70	0.92	1.29
Al_2O_3	11.84	12.53	11.19	10.29	10.43	10.40	12.42	14.05	11.36	12.19	15.47	12.03
Fe_2O_3	12.17	17.43	15.82	7.20	4.60	4.63	14.06	5.72	4.40	3.78	7.72	8.68
FeO	10.95	15.68	14.23	6.48	4.14	4.17	12.65	5.15	3.96	3.40	6.95	7.81
MnO	0.15	0.39	0.26	0.24	0.13	0.13	0.20	0.11	0.09	0.11	0.33	0.20
MgO	1.41	1.72	2.31	1.13	0.13	0.13	2.12	2.90	1.52	1.46	4.53	2.60
CaO	2.79	8.50	3.26	8.05	4.92	4.94	4.47	7.98	2.53	8.07	11.34	6.98
Na_2O	2.62	2.63	2.03	2.45	4.08	4.09	2.47	4.11	3.38	3.71	5.01	3.23
K_2O	2.32	0.78	1.42	0.58	0.14	0.13	2.14	0.35	1.27	0.18	0.46	0.08
P_2O_5	0.55	0.48	0.55	0.49	0.50	0.50	0.60	0.12	0.25	0.14	0.18	0.22
Cr_2O_3	<0.001	0.043	0.003	<0.001	0.009	0.011	<0.001	0.016	0.007	0.002	0.014	0.009
LOI	0.25	1.80	0.01	4.01	1.21	1.24	0.55	2.39	0.47	3.71	5.06	0.71
Total	99.46	99.45	99.24	99.75	99.18	99.11	99.57	99.51	99.39	99.42	99.88	99.63

Table D: Trace element data for intermediate pillow lavas. All data in ppm. * = least altered, and ** = most altered intermediate samples used in Gresens calculations.

Sample	13 AB 2029C1	13 AB 2029C4	13 AB 2032B	13 AB 2038A	13 BW 1010A	13 SM 1102A	13 VJ 68A	13 AB 2019A	13 AB 2019B	13 VJ 78A	13 AB 2023A	13 AB 2039A
ID	Int1-A*	Int1-B	Int1-C	Int1-D	Int1-E**	Int1-F	Int1-G	Int2-A	Int2-B	Int3-A	Int4-A	Int5-A
Element												
Au	<0.5	0.8	<0.5	<0.5	<0.5	1.4	0.9	<0.5	<0.5	0.7	1.3	3.0
Ba	777	150	135	426	110	109	493	279	94	91	205	155
Ce	61.9	62.3	47.2	52.8	49.7	53.8	59.5	30.7	46.2	32.6	23.2	36.9
Co	15.7	16.9	20.2	9.4	18.7	18.4	18.1	20.2	12.2	17.4	30.9	25.9
Cs	6.1	1.5	4.7	0.6	0.1	0.1	3.6	0.8	1.4	<0.1	1.3	<0.1
Cu	2.0	171.7	18.3	0.9	272.6	264.2	18.1	56.1	10.3	39.7	36.7	227.0
Dy	6.92	7.73	8.09	5.69	6.43	6.68	7.17	2.92	4.50	3.22	2.86	4.31
Er	4.61	4.18	5.34	3.77	3.70	3.83	4.57	1.77	2.80	2.03	1.09	2.60
Eu	1.51	2.09	1.99	1.80	1.83	2.00	1.86	0.80	0.85	0.83	18.1	1.34
Ga	17.8	17.9	19.1	15.6	13.9	14.7	19.3	12.0	10.8	14.1	3.63	12.4
Gd	7.58	7.61	7.63	6.41	6.86	6.80	7.57	3.20	4.45	3.30	<0.01	4.47
Hf	6.7	6.4	5.6	5.1	5.8	6.3	6.6	2.7	5.0	3.2	0.89	5.9
Ho	1.55	1.42	1.75	1.29	1.36	1.29	1.54	0.56	0.94	0.78	12.0	0.91
La	30.6	30.9	21.3	27.9	23.2	25.6	29.4	16.0	24.4	17.8	0.45	18.0
Lu	0.66	0.60	0.75	0.52	0.51	0.57	0.68	0.26	0.39	0.31	<0.1	0.38
Mo	0.8	3.7	1.4	0.9	5.3	5.7	1.4	0.2	0.2	0.1	5.1	3.1
Nb	10.8	11.9	10.7	9.7	10.3	10.5	10.6	5.4	8.9	5.5	3.2	8.9
Nd	31.0	32.1	24.4	27.6	25.0	26.3	30.4	14.2	23.0	14.4	13.7	19.9
Ni	0.8	17.6	9.3	0.7	30.0	28.7	0.4	40.4	12.5	20.3	<0.1	28.2
Pb	8.1	4.6	3.4	4.6	4.4	4.5	3.7	1.9	3.4	2.2	<0.5	1.6
Pr	7.46	7.69	5.89	6.48	6.19	6.69	7.13	3.48	5.31	3.88	3.14	4.56
Rb	74.4	16.2	56.0	13.2	1.9	2.0	67.2	28.4	24.1	2.5	197.1	0.9
Sm	7.28	7.45	6.61	6.25	5.87	6.38	6.89	2.84	4.86	3.16	3.2	4.01
Sr	153.5	202.6	81.3	168.2	131.6	140.2	111.5	227.4	85.1	131.9	0.41	181.4
Ta	1.0	0.8	0.7	0.8	0.9	0.8	0.9	0.4	0.7	0.4	1.1	0.6
Tb	1.23	1.16	1.30	1.06	1.00	1.07	1.23	0.50	0.74	0.57	222	0.69

Th	11.1	11.1	8.0	9.9	10.0	10.3	10.6	5.2	10.2	5.1	3.2	5.1
Tm	0.65	0.63	0.79	0.55	0.55	0.59	0.64	0.26	0.41	0.33	0.41	0.37
U	4.3	4.9	3.5	3.5	4.0	3.9	4.8	2.1	2.6	1.2	1.1	1.7
V	19	20	48	16	17	15	20	147	67	117	222	224
W	0.7	1.1	0.8	0.9	0.7	2.2	0.8	<0.5	1.0	0.5	0.7	1.2
Y	42.5	41.3	46.9	35.1	38.1	39.6	40.5	17.1	25.7	19.3	24.5	26.4
Yb	4.41	3.96	4.79	3.40	3.45	3.64	4.10	1.67	2.53	2.07	3.03	2.55
Zn	118	49	79	40	65	57	78	18	51	26	45	10
Zr	271.7	268.0	270.0	234.1	235.2	253.8	274.9	110.9	223.6	138.4	103.9	282.3

APPENDIX D

Figure A: Primitive mantle-normalized spider diagrams for Mafic 1 (A), Mafic 2 (B), Intermediate 1 (C), Intermediate 2 (D), and Intermediate 3, 4 and 5 (E). Element mobility of Rb, Ba, Th and U is illustrated by the highly variable concentration of these elements. After Sun & McDonough, 1989.
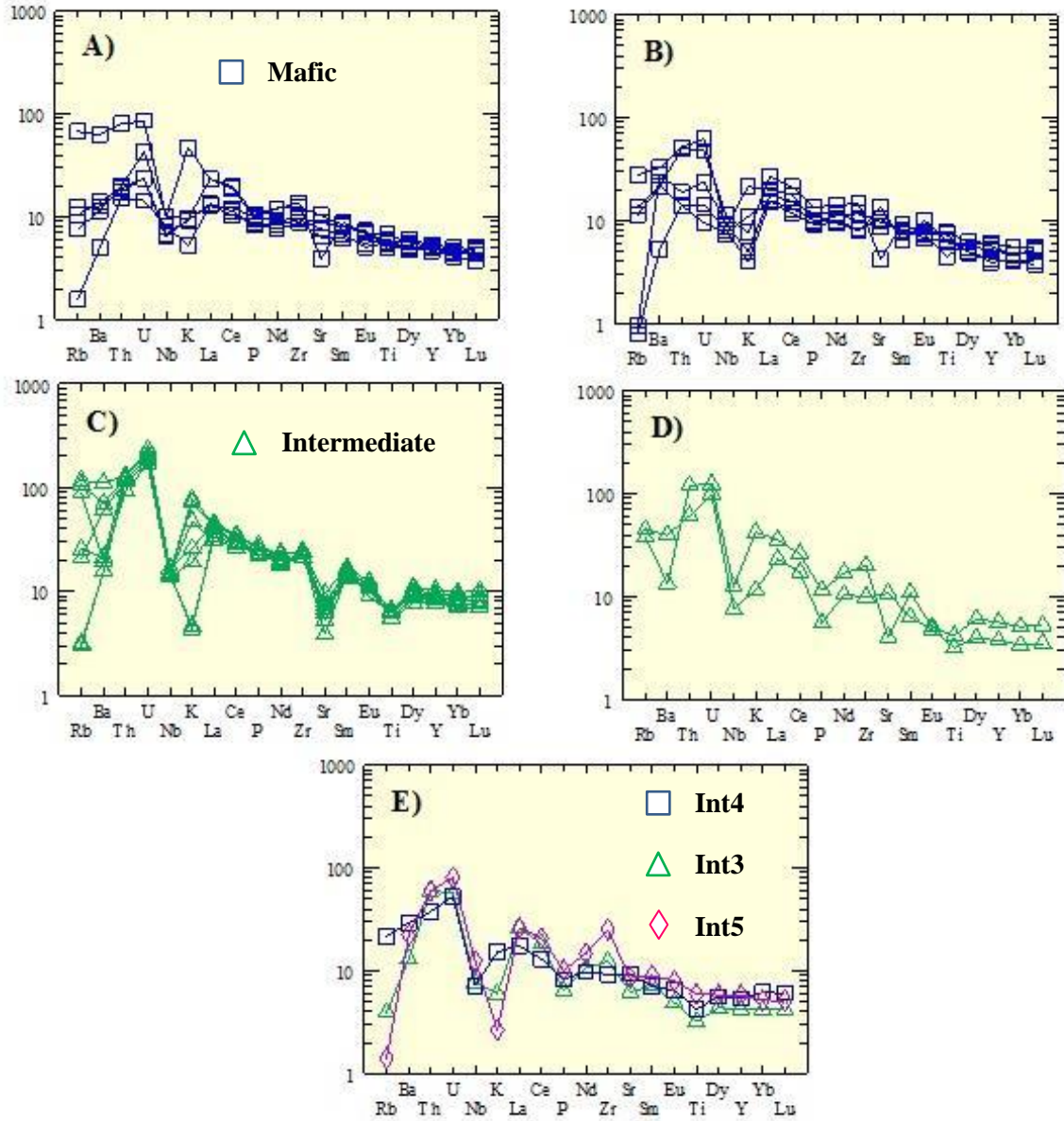
Figure B: Pearce element ratios for all samples illustrated using diagrams of X/TiO_2 against CaO/TiO_2 (left side) and X/TiO_2 against SiO_2/TiO_2 (right side). The Pearce element ratios use a conserved component as a common denominator for both axes (here TiO_2).
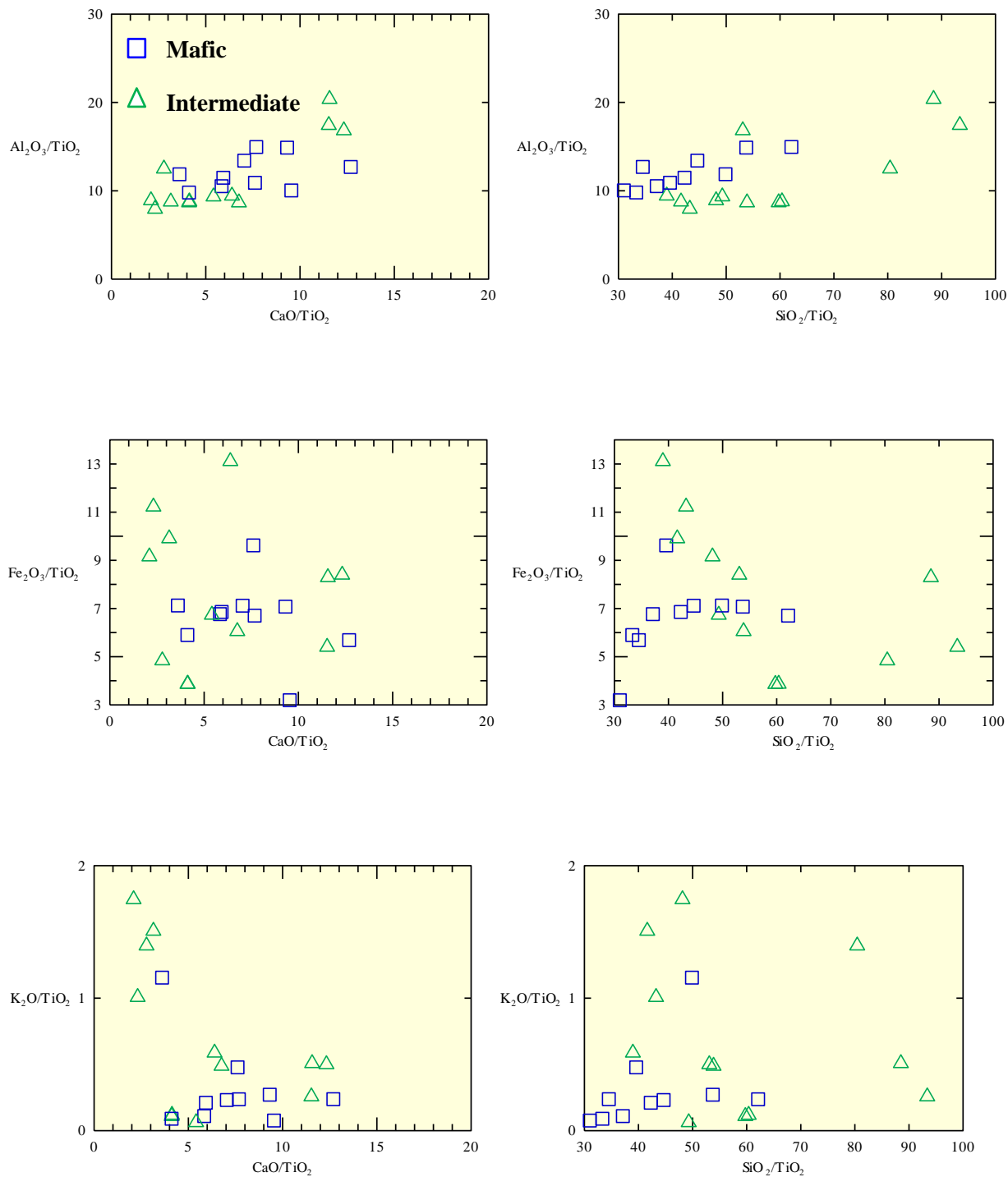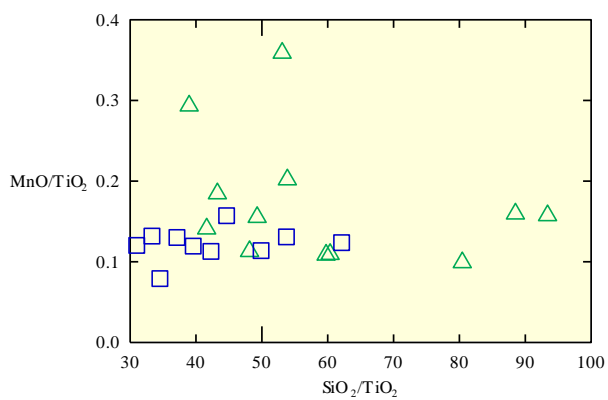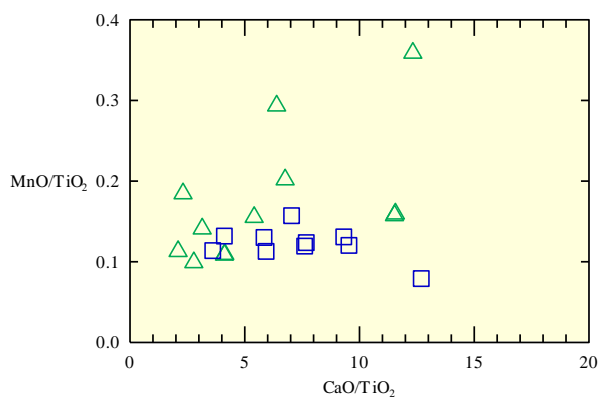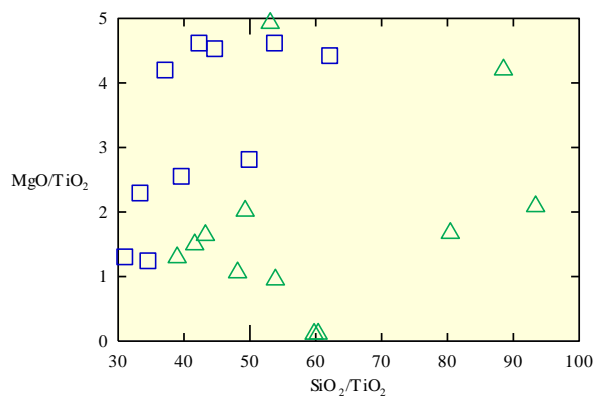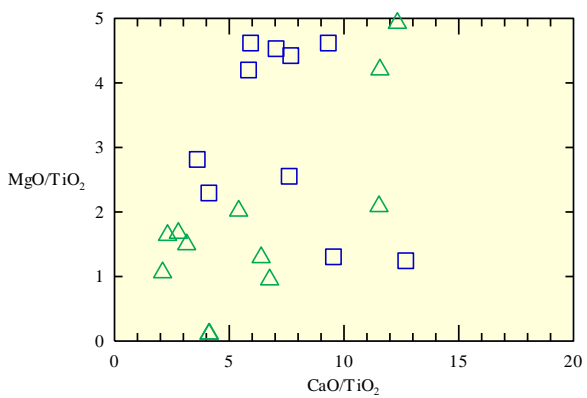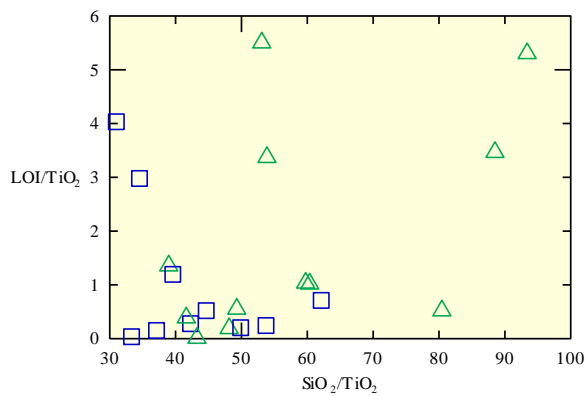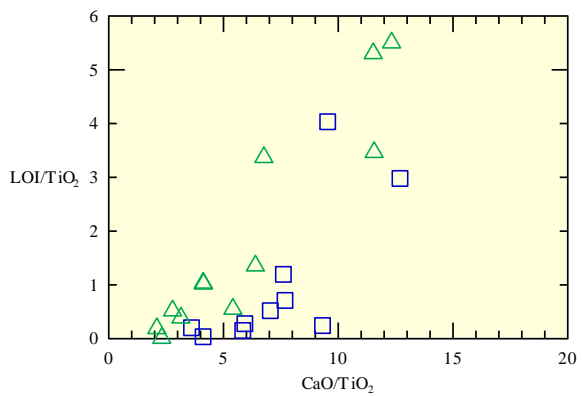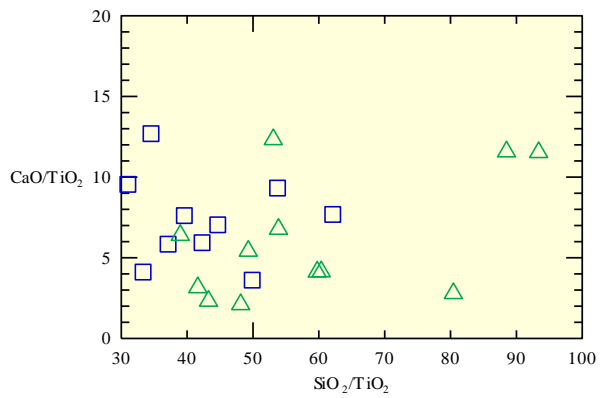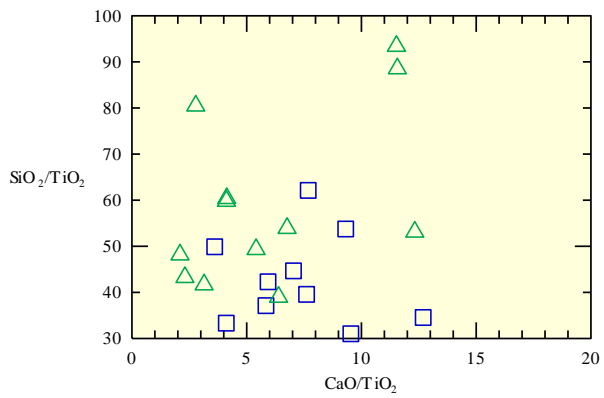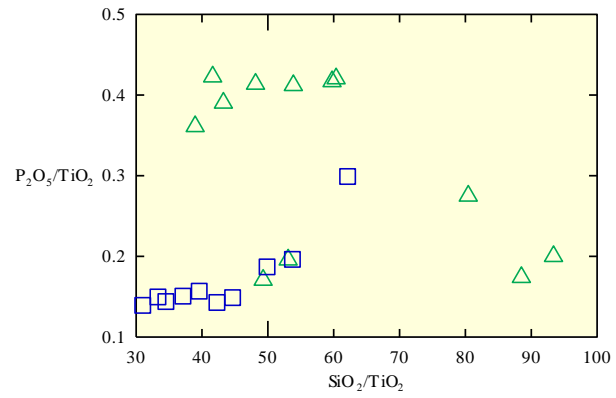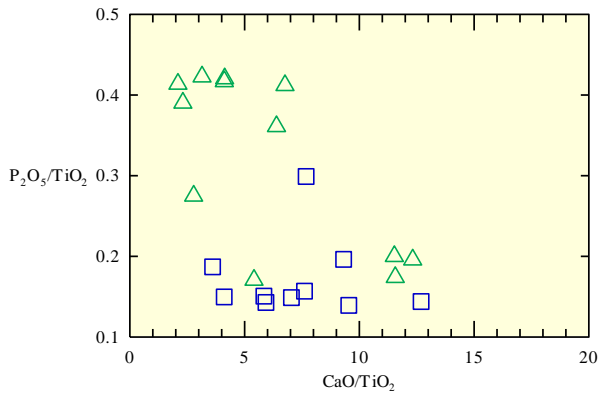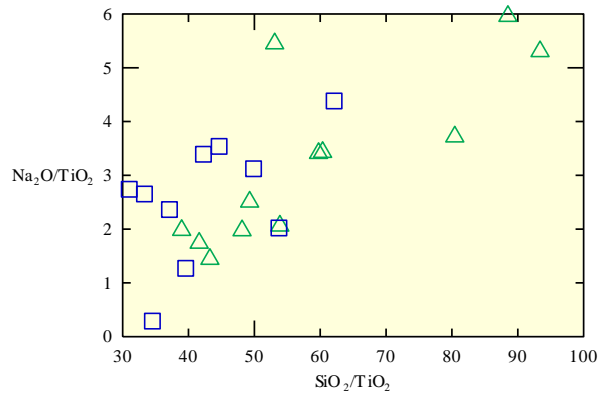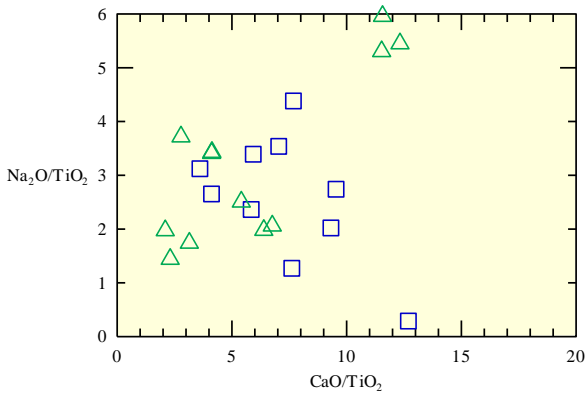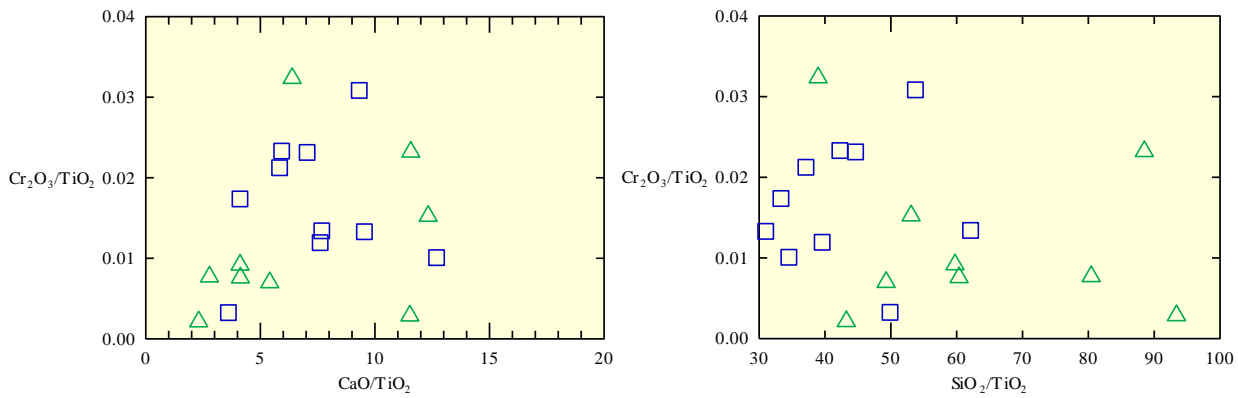
Figure C: Discrimination diagrams of tectonomagmatic environment showing the apparent arc-signature of the Sharrie Lake basalts, basaltic andesites, and andesites. After Wood, 1980.
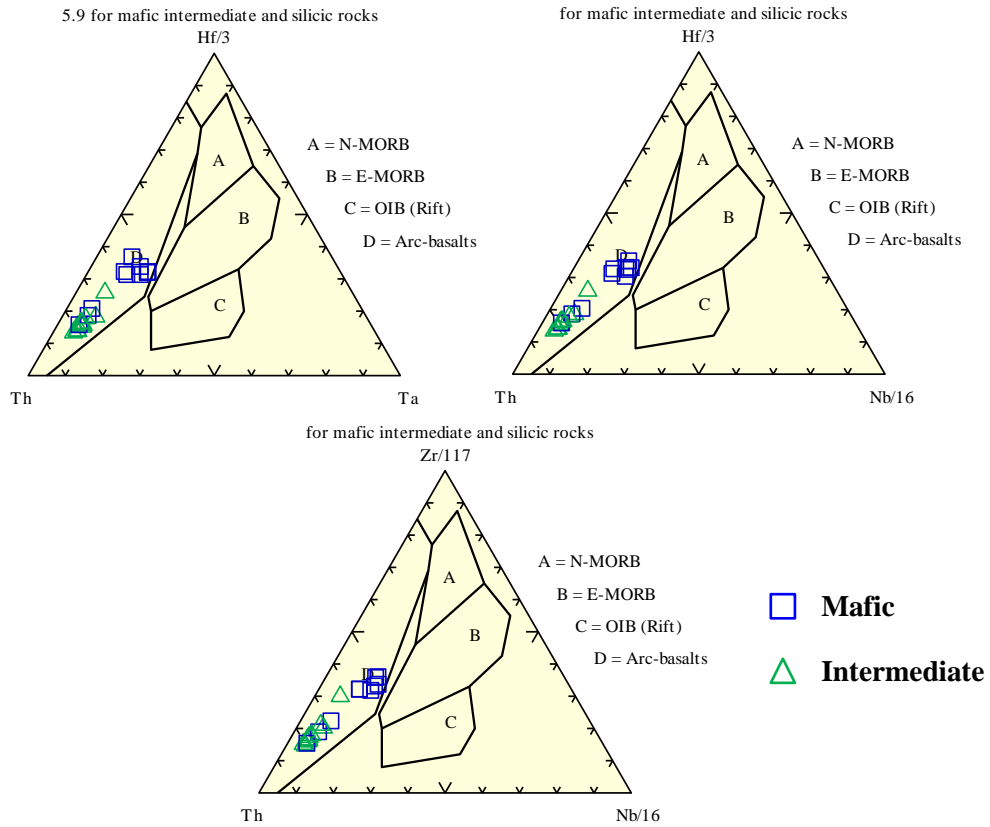
Figure D: Example trace element immobility tests for flows Maf1a and Maf3a.
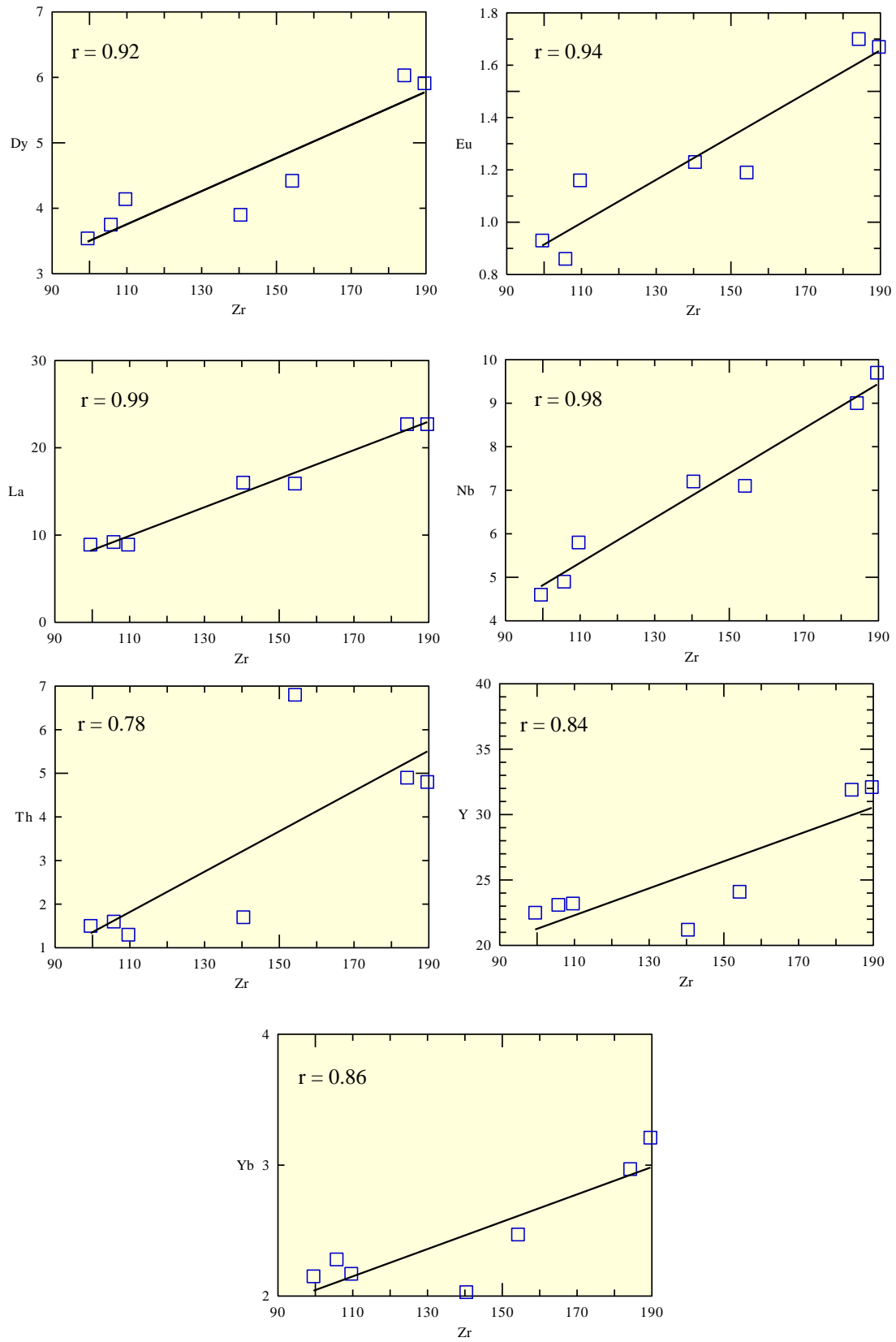
Figure E: Example trace element immobility tests for flow Intermediate 1.
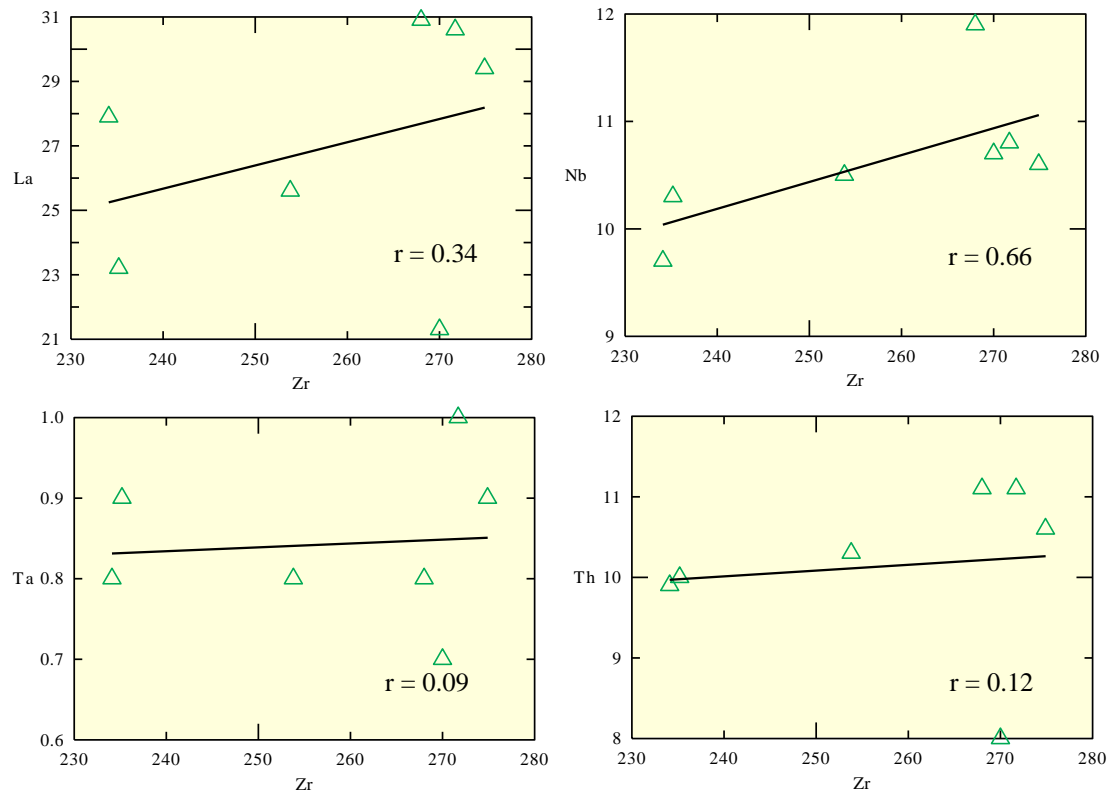
Appendix E

Table A: Mass changes in major oxides in the alteration of Maf2a-A to Maf6a-A based on Gresens calculations. All changes in ppm.

A) Isochemical alteration ($\Delta x_n = 0$)   **B) Isovolumetric alteration ($f_v = 1$)**

Component n	f_v	Component n	Δx_n
SiO_2	1.08	SiO_2	-4.29
TiO_2	1.12	TiO_2	-0.18
Al_2O_3	0.87	Al_2O_3	2.50
Fe_2O_3	1.17	Fe_2O_3	-1.40
MnO	1.87	MnO	-0.10
MgO	2.07	MgO	-1.98
CaO	0.36	CaO	12.00
Na_2O	10.35	Na_2O	-4.00
K_2O	0.42	K_2O	0.20
P_2O_5	1.17	P_2O_5	-0.04
LOI	0.01	LOI	4.37

C) Constant Al_2O_3 ($f_v = 0.87$)   **D) Constant TiO_2 ($f_v = 1.12$)**

Component n	Δx_n	Component n	Δx_n
SiO_2	-10.96	SiO_2	1.88
TiO_2	-0.38	Al_2O_3	4.77
Fe_2O_3	-2.50	Fe_2O_3	-0.38
MnO	-0.12	MnO	-0.09
MgO	-2.22	MgO	-1.76
CaO	9.55	CaO	14.27
Na_2O	-4.06	Na_2O	-3.95
K_2O	0.16	K_2O	0.25
P_2O_5	-0.06	P_2O_5	-0.01
LOI	3.79	LOI	4.90

Table B: Mass changes in major oxides in the alteration of Maf1a-A to Maf1a-C based on Gresens calculations. All changes in wt %.

A) Isochemical alteration ($\Delta x_n = 0$)

Component n	f_v
SiO_2	1.04
TiO_2	1.10
Al_2O_3	0.94
Fe_2O_3	1.06
MnO	0.79
MgO	1.12
CaO	0.93
Na_2O	1.06
K_2O	1.00
P_2O_5	1.06
LOI	0.59

B) Isovolumetric alteration ($f_v = 1$)

Component n	Δx_n
SiO_2	-2.28
TiO_2	-0.12
Al_2O_3	0.94
Fe_2O_3	-0.52
MnO	0.04
MgO	-0.67
CaO	0.62
Na_2O	-0.24
K_2O	-0.05
P_2O_5	-0.01
LOI	0.26

C) Constant Al_2O_3 ($f_v = 0.94$)

Component n	Δx_n
SiO_2	-5.52
TiO_2	-0.19
Fe_2O_3	-1.04
MnO	0.03
MgO	-1.00
CaO	0.11
Na_2O	-0.49
K_2O	-0.02
P_2O_5	-0.02
LOI	0.22

D) Constant TiO_2 ($f_v = 1.10$)

Component n	Δx_n
SiO_2	3.11
Al_2O_3	2.56
Fe_2O_3	0.34
MnO	0.06
MgO	-0.12
CaO	1.47
Na_2O	0.19
K_2O	0.03
P_2O_5	0.01
LOI	0.32

Table C: Mass changes in major oxides in the alteration of Int1-A to Int1-E based on Gresens calculations. All changes in wt %.

A) Isochemical alteration ($\Delta x_n = 0$)   **B) Isovolumetric alteration ($f_v = 1$)**

Component n	f_v	Component n	Δx_n
SiO_2	0.97	SiO_2	2.09
TiO_2	1.21	TiO_2	-0.23
Al_2O_3	1.23	Al_2O_3	-2.24
Fe_2O_3	2.87	Fe_2O_3	-7.94
MnO	1.25	MnO	-0.0303
MgO	11.78	MgO	-1.29
CaO	0.62	CaO	1.74
Na_2O	0.70	Na_2O	1.14
K_2O	18.00	K_2O	-2.19
P_2O_5	1.20	P_2O_5	-0.09
LOI	0.22	LOI	0.86

C) Constant Al_2O_3 ($f_v = 1.23$)   **D) Constant TiO_2 ($f_v = 1.21$)**

Component n	Δx_n	Component n	Δx_n
SiO_2	17.30	SiO_2	15.98
TiO_2	0.02	Al_2O_3	-0.22
Fe_2O_3	-6.96	Fe_2O_3	-7.05
MnO	0.00	MnO	-0.01
MgO	-1.26	MgO	-1.27
CaO	2.78	CaO	2.69
Na_2O	2.00	Na_2O	1.92
K_2O	-2.16	K_2O	-2.16
P_2O_5	0.02	P_2O_5	0.01
LOI	1.12	LOI	1.10

Table D: Mass changes >2 ppm in trace elements in the alteration of Maf2a-A to Maf6a-A based on Gresens calculations. All changes in ppm.

A) **Isochemical alteration ($\Delta x_n = 0$)**   B) **Isovolumetric alteration ($f_v = 1$)**

Component n	f_v	Component n	Δx_n
Ba	1.21	Ba	-33.45
Ce	1.21	Ce	-4.83
Co	1.12	Co	-5.66
Cu	0.52	Cu	32.56
Ga	0.46	Ga	18.33
Nd	1.17	Nd	-2.40
Ni	0.17	Ni	90.39
Rb	0.06	Rb	8.71
Sr	0.61	Sr	118.77
Y	1.34	Y	-6.54
Zn	0.51	Zn	5.77
Zr	1.16	Zr	-15.09

C) **Most likely volume factor ($f_v = 1.12$)**

Component n	Δx_n
Ba	-14.06
Ce	-2.12
Cu	40.75
Ga	22.43
Ni	103.41
Rb	9.83
Sr	155.08
V	33.55
Y	-4.23
Zn	7.18
Zr	-3.67

Table E: Mass changes >2 ppm in trace elements in the alteration of Maf1a-A to Maf1a-C based on Gresens calculations. All changes in ppm.

A) **Isochemical alteration ($\Delta x_n = 0$)**

Component n	f_v
Ba	0.90
Ce	0.91
Co	0.94
Cu	0.96
Mo	0.02
Ni	0.43
Rb	1.20
Sr	0.83
V	1.03
Zn	0.56
Zr	0.94

B) **Isovolumetric alteration ($f_v = 1$)**

Component n	Δx_n
Ba	9.84
Ce	1.87
Co	2.43
Cu	2.21
Mo	7.99
Ni	16.45
Rb	-1.31
Sr	27.23
V	-7.46
Zn	10.96
Zr	6.02

C) **Most likely volume factor ($f_v = 1.05$)**

Component n	Δx_n
Ba	14.73
Ce	2.87
Co	4.57
Cu	4.76
Ga	1.36
Mo	8.40
Nd	1.54
Ni	17.90
Sr	35.30
V	6.27
Y	1.71
Zn	12.21
Zr	11.30

Table F: Mass changes >2 ppm in trace elements in the alteration of Int1-A to Int1-E based on Gresens calculations. All changes in ppm.

A) Isochemical alteration ($\Delta x_n = 0$)			B) Isovolumetric alteration ($f_v = 1$)	
Component n	**Fv**		**Component n**	**Δxn**
Ba	7.67		Ba	-675.75
Ce	1.35		Ce	-16.16
Co	0.91		Co	1.51
Cs	66.27		Cs	-6.01
Cu	0.01		Cu	248.90
Ga	1.39		Ga	-5.01
La	1.43		La	-9.25
Mo	0.16		Mo	4.08
Nd	1.35		Nd	-7.99
Ni	0.03		Ni	26.81
Pb	2.00		Pb	-4.05
Rb	42.54		Rb	-72.65
Sr	1.27		Sr	-32.37
V	1.21		V	-3.35
Y	1.21		Y	-7.43
Zn	1.97		Zn	-58.17
Zr	1.26		Zr	-55.22

C) Most likely volume factor ($f_v = 1.25$)

Component n	Δx_n
Ba	-650.44
Ce	-4.72
Co	5.81
Cs	-5.98
Cu	311.63
Ga	-1.81
La	-3.91
Mo	5.30
Nd	-2.24
Ni	33.72
Pb	-3.04
Rb	-72.21
Sr	-2.09
Y	1.33
Zn	-43.22
Zr	-1.10

Figure A: Graphical comparison of major oxide results from Gresens calculations with the data treated under the assumption of constant volume (A), constant Al_2O_3 (B), constant TiO_2 (C), and with the calculated most likely volume factor (f_v) for each reaction (D). All changes in wt %.

C) Constant TiO₂
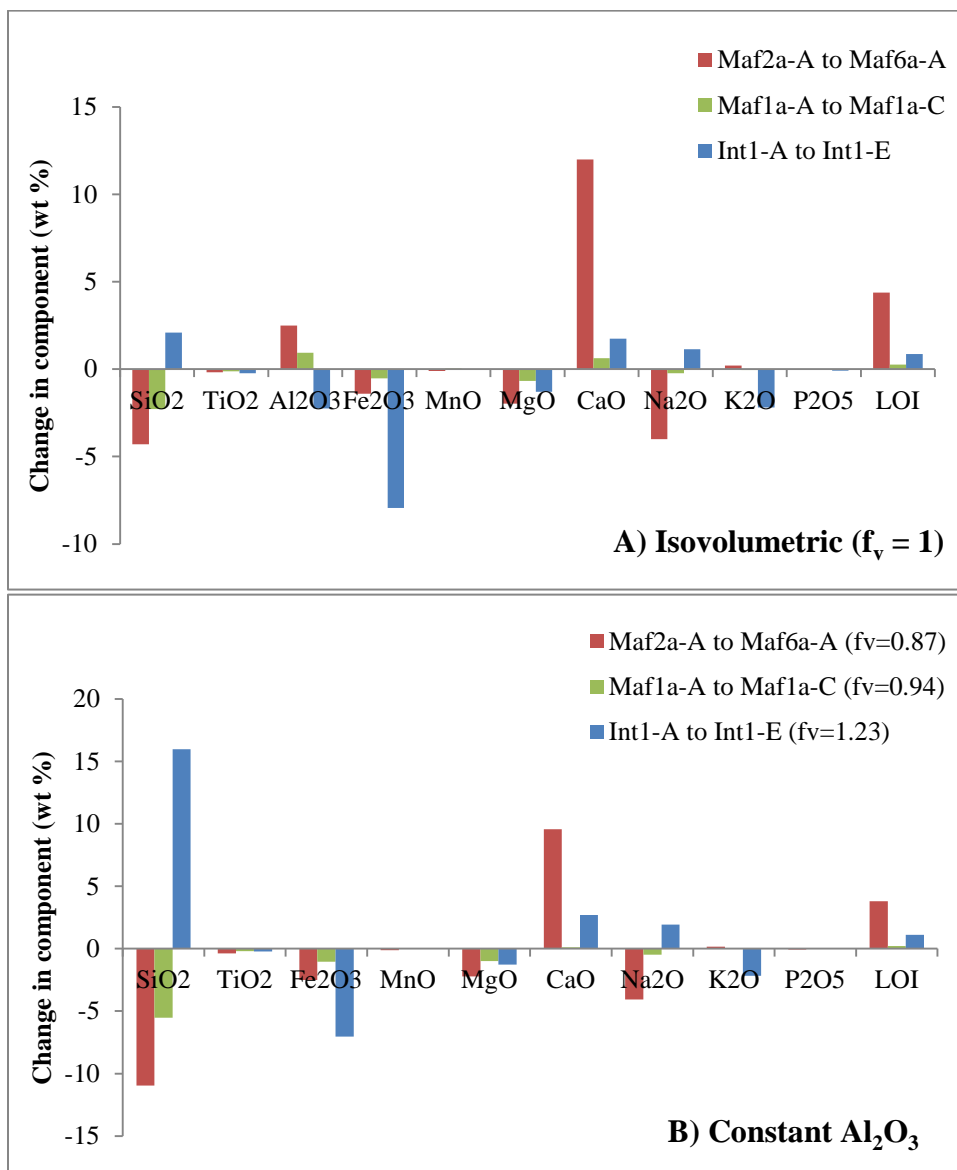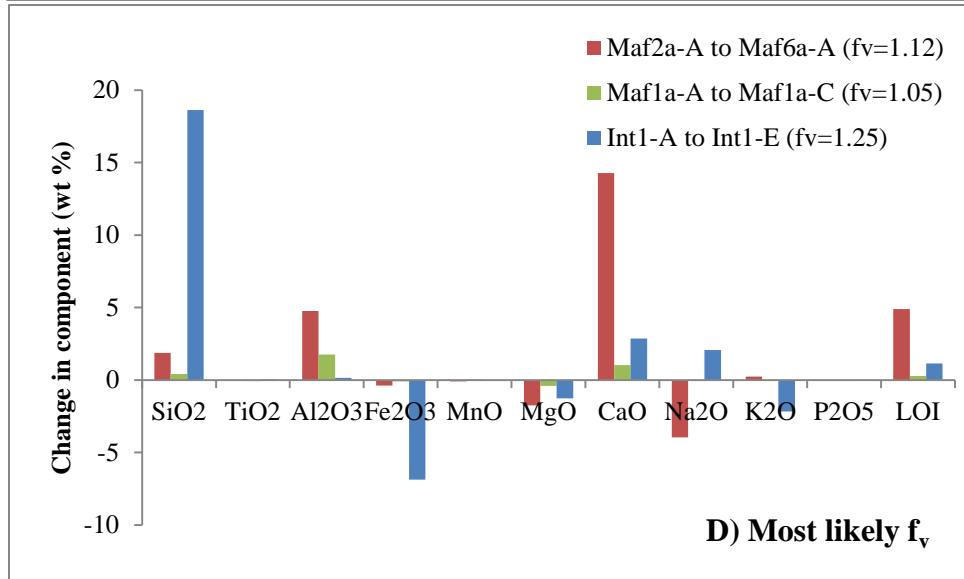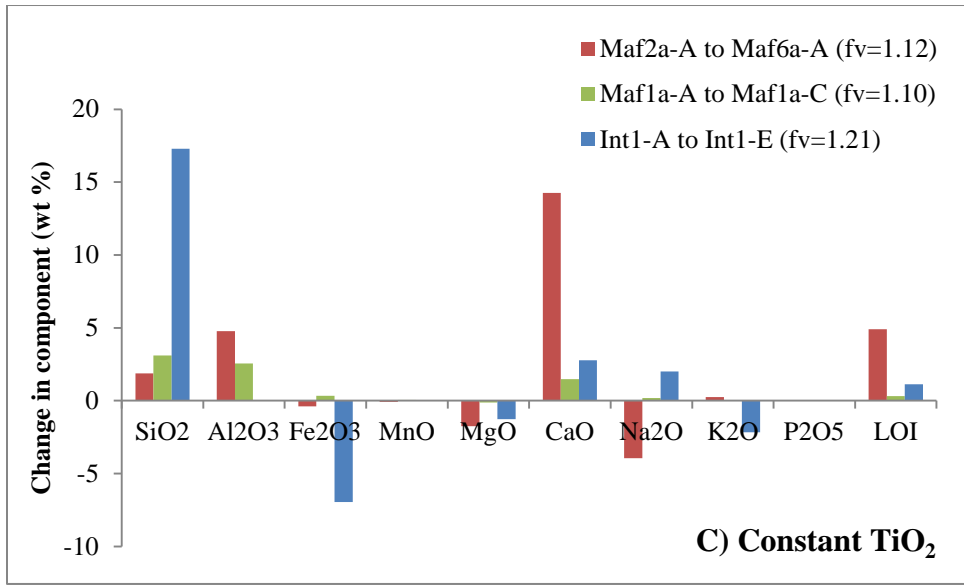
D) Most likely fᵥ

Figure B: Graphical comparison of trace element results from Gresens calculations for the alteration of Maf2a-A to Maf6a-A with the data treated under the assumption of constant volume (A), and with the calculated most likely volume factor ($f_v=1.12$) (B). All changes in ppm.
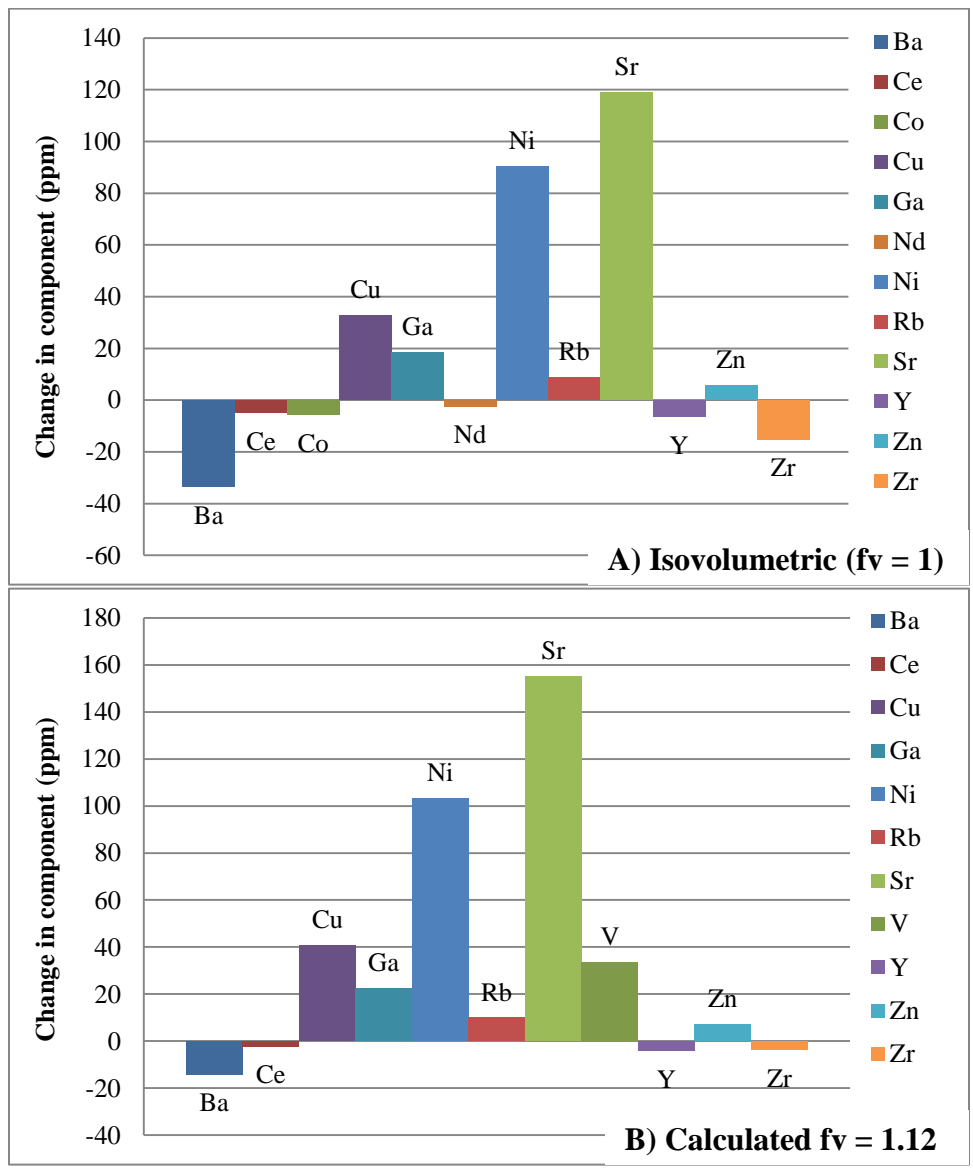
Figure C: Graphical comparison of trace element results from Gresens calculations for the alteration of Maf1a-A to Maf1a-C with the data treated under the assumption of constant volume (A), and with the calculated most likely volume factor (f_v=1.05) (B). All changes in ppm.

Figure D: Graphical comparison of trace element results from Gresens calculations for the alteration of Int1-A to Int1-E with the data treated under the assumption of constant volume (A), and with the calculated most likely volume factor (f_v=1.25) (B). All changes in ppm.

Table G: Mass balance calculations using Al, Ti, and Zr ratios of $X_{leastAlt}/X_{alt}$ as correction factors for the alteration of Maf2a-A to Maf6a-A.

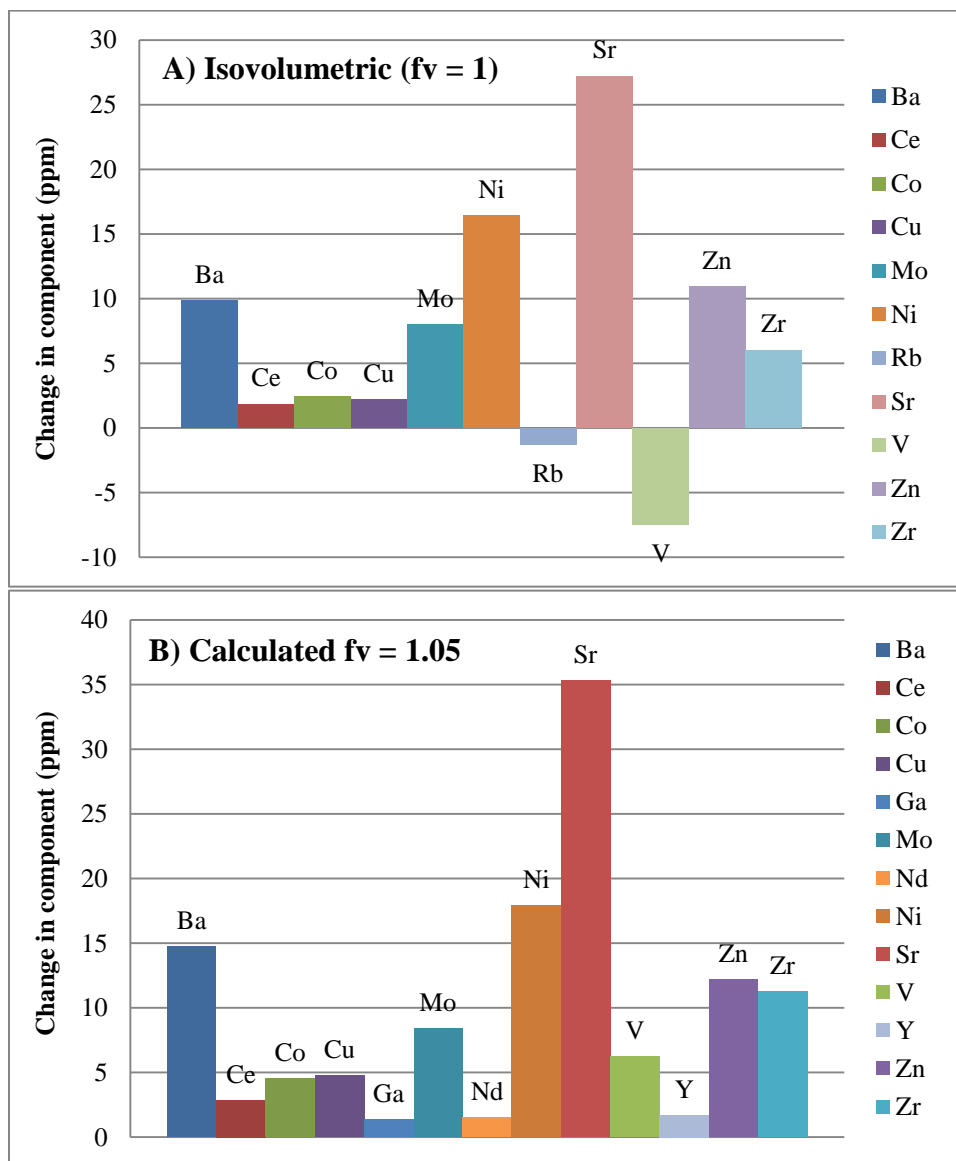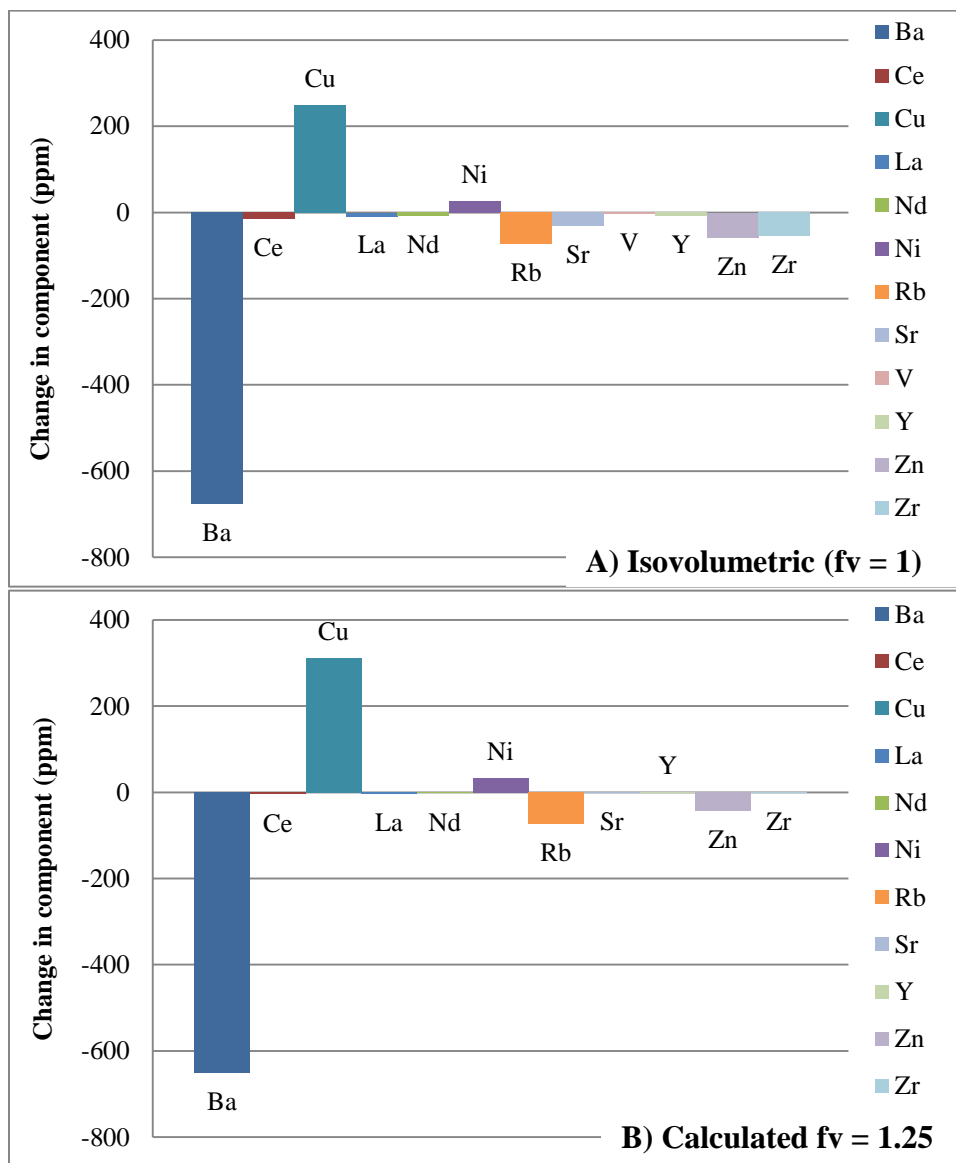| Major-element geochemical data for least altered and most altered samples (Appendix C)											
	SiO_2	Al_2O_3	TiO_2	Fe_2O_3	MgO	MnO	CaO	Na_2O	K_2O	P_2O_5	Zr
	%	%	%	%	%	%	%	%	%	%	ppm
Maf2a-A	55.63	16.37	1.67	9.85	3.83	0.22	6.87	4.43	0.15	0.25	110.2
Maf6a-A	47.99	17.64	1.39	7.90	1.73	0.11	17.64	0.40	0.33	0.20	88.9
normalized											
	Al	*Ti*	*Zr*								
	1.00	1.00	1.00								
	0.93	1.20	1.24								
Al_2O_3											
reconstruct	SiO_2	Al_2O_3	TiO_2	Fe_2O_3	MgO	MnO	CaO	Na_2O	K_2O	P_2O_5	Zr
Maf2a-A-Al	55.63	16.37	1.67	9.85	3.83	0.22	6.87	4.43	0.15	0.25	110.20
Maf6a-A-Al	44.53	16.37	1.29	7.33	1.61	0.10	16.37	0.37	0.31	0.19	82.50
change (%)	SiO_2	Al_2O_3	TiO_2	Fe_2O_3	MgO	MnO	CaO	Na_2O	K_2O	P_2O_5	Zr
Maf2a-A-Al	0.00		0.00	0.00	0.00	0.00	0.00	0.00	0.00	0.00	0.00
Maf6a-A-Al	3.46		0.10	0.57	0.12	0.01	1.27	0.03	0.02	0.01	6.40
TiO_2											
Reconstruct	SiO_2	Al_2O_3	TiO_2	Fe_2O_3	MgO	MnO	CaO	Na_2O	K_2O	P_2O_5	Zr
Maf2a-A-Ti	55.63	16.37	1.67	9.85	3.83	0.22	6.87	4.43	0.15	0.25	110.20
Maf6a-A-Ti	57.66	21.19	1.67	9.49	2.08	0.13	21.19	0.48	0.40	0.24	106.81
change (%)	SiO_2	Al_2O_3	TiO_2	Fe_2O_3	MgO	MnO	CaO	Na_2O	K_2O	P_2O_5	Zr
Maf2a-A-Ti	0.00	0.00		0.00	0.00	0.00	0.00	0.00	0.00	0.00	0.00
Maf6a-A-Ti	-9.67	-3.55		-1.59	-0.35	-0.02	-3.55	-0.08	-0.07	-0.04	-17.91
Zr											
Reconstruct	SiO_2	Al_2O_3	TiO_2	Fe_2O_3	MgO	MnO	CaO	Na_2O	K_2O	P_2O_5	Zr
Maf2a-A-Zr	55.63	16.37	1.67	9.85	3.83	0.22	6.87	4.43	0.15	0.25	110.20
Maf6a-A-Zr	59.49	21.87	1.72	9.79	2.14	0.14	21.87	0.50	0.41	0.25	110.20
change (%)	SiO_2	Al_2O_3	TiO_2	Fe_2O_3	MgO	MnO	CaO	Na_2O	K_2O	P_2O_5	Zr
Maf2a-A-Zr	0.00	0.00	0.00	0.00	0.00	0.00	0.00	0.00	0.00	0.00	
Maf6a-A-Zr	-11.50	-4.23	-0.33	-1.89	-0.41	-0.03	-4.23	-0.10	-0.08	-0.05	

Table H: Mass balance calculations using Al, Ti, and Zr ratios of $X_{leastAlt}/X_{alt}$ as correction factors for the alteration of Maf1a-A to Maf1a-C.

Major-element geochemical data for least altered and most altered samples (Appendix C)										
	SiO$_2$	Al$_2$O$_3$	TiO$_2$	Fe$_2$O$_3$	MgO	MnO	CaO	Na$_2$O	K$_2$O	P$_2$O$_5$	Zr
	%	%	%	%	%	%	%	%	%	%	Ppm
Maf1a-A	56.23	15.25	1.33	9.12	6.14	0.15	7.89	4.51	0.28	0.19	99.5
Maf1a-C	54.04	16.22	1.21	8.61	5.48	0.19	8.52	4.28	0.28	0.18	105.7

normalized

	Al	Ti	Zr
	1.0000	1.00	1.00
	0.9402	1.10	0.94

Al$_2$0$_3$

reconstruct	SiO$_2$	Al$_2$O$_3$	TiO$_2$	Fe$_2$O$_3$	MgO	MnO	CaO	Na$_2$O	K$_2$O	P$_2$O$_5$	Zr
Maf1a-A-Al	56.23	15.25	1.33	9.12	6.14	0.15	7.89	4.51	0.28	0.19	99.50
Maf1a-C-Al	50.81	15.25	1.14	8.10	5.15	0.18	8.01	4.02	0.26	0.17	99.38

change (%)	SiO$_2$	Al$_2$O$_3$	TiO$_2$	Fe$_2$O$_3$	MgO	MnO	CaO	Na$_2$O	K$_2$O	P$_2$O$_5$	Zr
Maf1a-A-Al	0.00		0.00	0.00	0.00	0.00	0.00	0.00	0.00	0.00	0.00
Maf1a-C-Al	3.23		0.07	0.51	0.33	0.01	0.51	0.26	0.02	0.01	6.32

TiO$_2$

reconstruct	SiO$_2$	Al$_2$O$_3$	TiO$_2$	Fe$_2$O$_3$	MgO	MnO	CaO	Na$_2$O	K$_2$O	P$_2$O$_5$	Zr
Maf1a-A-Ti	56.23	15.25	1.33	9.12	6.14	0.15	7.89	4.51	0.28	0.19	99.50
Maf1a-C-Ti	59.40	17.83	1.33	9.46	6.02	0.21	9.36	4.70	0.31	0.20	116.18

change (%)	SiO$_2$	Al$_2$O$_3$	TiO$_2$	Fe$_2$O$_3$	MgO	MnO	CaO	Na$_2$O	K$_2$O	P$_2$O$_5$	Zr
Maf1a-A-Ti	0.00	0.00		0.00	0.00	0.00	0.00	0.00	0.00	0.00	0.00
Maf1a-C-Ti	-5.36	-1.61		-0.85	-0.54	-0.02	-0.84	-0.42	-0.03	-0.02	-10.48

Zr

reconstruct	SiO$_2$	Al$_2$O$_3$	TiO$_2$	Fe$_2$O$_3$	MgO	MnO	CaO	Na$_2$O	K$_2$O	P$_2$O$_5$	Zr
Maf1a-A-Zr	56.23	15.25	1.33	9.12	6.14	0.15	7.89	4.51	0.28	0.19	99.50
Maf1a-C-Zr	50.87	15.27	1.14	8.10	5.16	0.18	8.02	4.03	0.26	0.17	99.50

change (%)	SiO$_2$	Al$_2$O$_3$	TiO$_2$	Fe$_2$O$_3$	MgO	MnO	CaO	Na$_2$O	K$_2$O	P$_2$O$_5$	Zr
Maf1a-A-Zr	0.00	0.00	0.00	0.00	0.00	0.00	0.00	0.00	0.00	0.00	
Maf1a-C-Zr	3.17	0.95	0.07	0.51	0.32	0.01	0.50	0.25	0.02	0.01	

Table I: Mass balance calculations using Al, Ti, and Zr ratios of $X_{leastAlt}/X_{alt}$ as correction factors for the alteration of Int1-A to Int1-E.

Major-element geochemical data for least altered and most altered samples (Appendix C)										
	SiO_2	Al_2O_3	TiO_2	Fe_2O_3	MgO	MnO	CaO	Na_2O	K_2O	P_2O_5	Zr
	%	%	%	%	%	%	%	%	%	%	ppm
Int1-A	64.03	11.84	1.33	12.17	1.41	0.15	2.79	2.62	2.32	0.55	271.70
Int1-E	71.84	10.43	1.19	4.60	0.13	0.13	4.92	4.08	0.14	0.50	235.20

normalized

	Al	*Ti*	*Zr*
	1.00	1.00	1.00
	1.14	1.12	1.16

Al_2O_3

reconstruct	SiO_2	Al_2O_3	TiO_2	Fe_2O_3	MgO	MnO	CaO	Na_2O	K_2O	P_2O_5	Zr
Int1-A-Al	64.03	11.84	1.33	12.17	1.41	0.15	2.79	2.62	2.32	0.55	271.70
Int1-E-Al	81.55	11.84	1.35	5.22	0.15	0.15	5.59	4.63	0.16	0.57	267.00

change (%)	SiO_2	Al_2O_3	TiO_2	Fe_2O_3	MgO	MnO	CaO	Na_2O	K_2O	P_2O_5	Zr
Int1-A-Al	0.00		0.00	0.00	0.00	0.00	0.00	0.00	0.00	0.00	0.00
Int1-E-Al	-9.71		-0.16	-0.62	-0.02	-0.02	-0.67	-0.55	-0.02	-0.07	-31.80

TiO_2

reconstruct	SiO_2	Al_2O_3	TiO_2	Fe_2O_3	MgO	MnO	CaO	Na_2O	K_2O	P_2O_5	Zr
Int1-A-Ti	64.03	11.84	1.33	12.17	1.41	0.15	2.79	2.62	2.32	0.55	271.70
Int1-E-Ti	80.29	11.66	1.33	5.14	0.15	0.15	5.50	4.56	0.16	0.56	262.87

change (%)	SiO_2	Al_2O_3	TiO_2	Fe_2O_3	MgO	MnO	CaO	Na_2O	K_2O	P_2O_5	Zr
Int1-A-Ti	0.00	0.00		0.00	0.00	0.00	0.00	0.00	0.00	0.00	0.00
Int1-E-Ti	-8.45	-1.23		-0.54	-0.02	-0.02	-0.58	-0.48	-0.02	-0.06	-27.67

Zr

reconstruct	SiO_2	Al_2O_3	TiO_2	Fe_2O_3	MgO	MnO	CaO	Na_2O	K_2O	P_2O_5	Zr
Int1-A-Zr	64.03	11.84	1.33	12.17	1.41	0.15	2.79	2.62	2.32	0.55	271.70
Int1-E-Zr	82.99	12.05	1.37	5.31	0.15	0.15	5.68	4.71	0.16	0.58	271.70

change (%)	SiO_2	Al_2O_3	TiO_2	Fe_2O_3	MgO	MnO	CaO	Na_2O	K_2O	P_2O_5	Zr
Int1-A-Zr	0.00	0.00	0.00	0.00	0.00	0.00	0.00	0.00	0.00	0.00	
Int1-E-Zr	-11.15	-1.62	-0.18	-0.71	-0.02	-0.02	-0.76	-0.63	-0.02	-0.08	

Appendix F

<u>**Table A:**</u> Specific gravity calculations using the Jolly balance, calibrated using a quartz crystal. Correction value (measured value of SG_{qtz} - reported value of SG_{qtz}) calculated as 0.053. Specific gravities corrected by subtracting the correction value from the calculated SG.

Sample ID	SG	Corrected SG
Qtz	2.7	2.7
Int1-A	2.9	2.8
Int1-B	2.9	2.9
Int1-C	2.9	2.9
Int1-D	2.7	2.6
Int1-E	2.7	2.6
Int1-G	2.8	2.8
Int2-A	2.9	2.8
Int2-B	2.8	2.8
Int3-A	2.8	2.7
Int4-A	2.6	2.6
Maf1a-A	2.9	2.8
Maf1a-B	2.9	2.9
Maf1a-C	2.9	2.8
Maf2a-A	2.9	2.8
Maf2a-B	2.8	2.8
Maf3a-A	2.9	2.8
Maf3a-B	2.9	2.9
Maf4a-A	2.8	2.8
Maf5a-A	3.0	2.9
Maf6a-A (altered core)	3.0	3.0
Maf6a-A (mafic rim)	3.1	3.0